



OPEN

Tailoring electronic and optical properties of hBN/InTe and hBN/GaTe heterostructures through biaxial strain engineering

A. Šolajić^{1✉} & J. Pešić^{1,2}

In this research study, we systematically investigate the electronic and optical properties of van der Waals heterostructures (HSs) consisting of InTe (GaTe) and hBN monolayers, subjected to controlled biaxial strain. Our analysis demonstrates that the application of strain induces noteworthy alterations in the electronic band structure, enabling precise manipulation of the band gap and augmentation of the absorption properties of these structures. Employing density functional theory, we conduct a comprehensive examination of the influence of strain on the electronic and optical characteristics of these HSs. Our investigation showcases the remarkable potential of strain engineering in rendering these heterostructures into efficient and robust wide-range absorbers, particularly optimised for the visible spectrum, underscoring their relevance in various photonic and optoelectronic applications, paving the way for integration into advanced nanodevices.

Van der Waals (vdW) heterostructures (HSs), a class of materials composed of stacked two-dimensional materials held together by van der Waals forces, have attracted significant attention in recent years due to their unique electronic and optical properties^{1–3}. A noteworthy advantage inherent to vdW HSs is their remarkable amenability to precise manipulation and customisation. The weak nature of vdW forces allows the layers to be easily separated and manipulated, allowing the creation of an unlimited number of different structures with precise control over the electronic, optical, and mechanical properties. This makes it possible to design and fabricate materials with specific desired characteristics, offering countless new possibilities for their applications in modern nanodevices⁴. With their high-performance electronic and optical properties, novel HSs can be used for transistors⁵, solar cells^{6,7}, lithium ion batteries^{8,9}, light emitting devices^{10,11}, photodetectors^{12–15}, various sensors^{16–18}, and many more. Recent research has further illuminated their promising potential as candidates for quantum computing applications¹⁹.

Delving deeper into the mechanisms of manipulation for vdW HSs not only enhances their properties but also unlocks a wider array of possibilities for applications in devices that fulfil the growing demands of today's market, such as sensors and switches. The modulation of electrical properties in such structures can be achieved in many ways, with the most common approaches being doping, strain application, or the use of external electric or magnetic field. The study of strain in 2D materials and vdW HSs represents a dynamically evolving research frontier, granting us an additional level of precision in controlling material properties^{20–22}.

Group III–VI monochalcogenide-based HSs have emerged as focal points of research attention, offering substantial promise for a broad spectrum of cutting-edge device applications. They find utility as Schottky barriers, high-performance 2D and flexible electronics, sensors, photodetectors, and more. Materials within the class of two-dimensional III–VI monochalcogenides are known for their high electron mobility, broad absorption spectra, and favourable elastic properties. Notably, the single-layer InTe is predicted to exhibit exceptional thermoelectric performance due to its remarkably low thermal conductance, boasting the highest merit figure, $ZT = 2.03$ at 300 K, among the III–VI monochalcogenide family²³. Recent study was discussing electronic transport and thermoelectric properties of doped InTe, showing that p-type InTe doped with Bi, Ag, Mn, Sn or Sb exhibits the enhanced thermoelectric performance, mainly induced by reduced thermal conductivity²⁴. Additionally, the InTe monolayer demonstrates a broad absorption spectrum, covering the ultraviolet to visible regions, with an absorption coefficient of up to 10^{-5} cm^{-1} . In most recent report, two-dimensional InTe

¹Laboratory for 2D materials, Center for Solid State Physics and New Materials, Institute of Physics Belgrade, University of Belgrade, Pregrevica 118, 11080 Belgrade, Serbia. ²Chair of Physics, Department Physics, Mechanics and Electrical Engineering, Montanuniversität Leoben, 8700 Leoben, Austria. ✉email: solajic@ipb.ac.rs

was synthesized in large-scale samples, as centimeter-scale 2D films on SiO₂/Si substrates²⁵. InTe also exists in tetragonal phase, and its electronic band structure has a highly anisotropic character²⁶, marking it of high interest for electronic and thermoelectric applications. In that phase, structure has quasi-one-dimensional form, where one-dimensional In¹⁺ chains are observed, and additionally, the presence of In¹⁺ induces a localized gap state, responsible for the high intrinsic p-type doping of InTe²⁷. Similarly to InTe, the monolayer GaTe exhibits comparable absorbing properties²⁸, along with excellent UV light absorption. In the realm of single-layer materials, each member of this material family exhibits remarkable and distinctive properties. Nonetheless, single layer III–VI monochalcogenides possess one noteworthy limitation in their pristine form. The majority of these materials display sensitivity to oxidation upon exposure to ambient air^{29–31}, especially in their single layer form, and need adequate material for passivation and mechanical protection. Non-reactive with most chemicals, stable in air and resistant to oxidation, hBN is already known as an effective coating material in the form of thin films or monolayers^{32–34}, and has been demonstrated successful for protection against oxidation and even for improving the electronic and optical properties of few-layered InSe and GaSe³⁵.

Motivated by these results, in our previous work, we designed and investigated two novel heterostructures, hBN/InTe and hBN/GaTe, as detailed in³⁶. These heterostructures displayed favourable electronic properties and an excellent broad absorption spectrum, enhanced and protected by the hBN layer, making them promising candidates for applications in photodetectors or field-effect transistors. Given the experimentally favourable binding energies and stacking versatility of both hBN/InTe and hBN/GaTe heterostructures, this study further delves into the intriguing potential of fine-tuning their properties through the application of controlled strain. In the following sections, we present a computational study of hBN/InTe and hBN/InTe under biaxial strain. The application of uniform biaxial strain does not alter the symmetry of the structure; instead, it allows us to tune the band structure and optical absorption.

Computational methods

Calculations were carried out using density functional theory (DFT), as implemented in the Quantum Espresso (QE) software package³⁷, based on plane waves and pseudopotentials. In all calculations, the Perdew–Burke–Ernzerhof (PBE) exchange correlation functional³⁸ is used, along with norm-conserving pseudopotentials. The energy cutoff of 80 Ry was set for both structures after the convergence tests.

The Monkhorst pack of $16 \times 16 \times 1$ mesh for k-point sampling is used in geometric optimisation, total energy, and phonon calculations. For calculations of p-DOS and optical properties, a refined $64 \times 64 \times 1$ mesh is used. The band structure is calculated on 440 k-points along Γ -M-K- Γ direction. To simulate the 2D structure, a vacuum of 20 Å was added along the z-direction to avoid interactions between the layers. Geometry optimisation of the positions of the atoms and the lattice parameters is performed using the BFGS algorithm, with criteria for the maximum forces allowed between atoms of 10^{-6} Ry/Å. To properly account for van der Waals force effects, the Grimme-D2 correction^{39,40} was included to obtain more accurate lattice constants and forces. The optical properties were calculated using the epsilon.x code in QE software, based on the random phase approximation (RPA).

Results and discussion

As discussed in our previous work³⁶, the unit cells of InTe and GaTe monolayer are $a = 4.371$ Å and $a = 4.048$ Å, respectively. The unit cell of hBN is $a = 2.515$ Å, and for both structures, constructing the heterostructure consisting of a $\sqrt{3} \times \sqrt{3}$ supercell of hBN rotated for 30° on top of 1×1 unit cell of InTe or GaTe provides an excellent match. After complete optimisation of the lattice parameters and atom positions within the unit cell, the obtained unit cell is hexagonal, with a lattice constant of $a = 4.336$ Å for hBN/InTe and $a = 4.309$ Å for hBN/GaTe. Resulting unit cell of hBN/InTe has induced strain of 0.8% on InTe layer and 0.3% on hBN layer, showing that HS constructed as described is almost an ideal match. The resulting unit cell of hBN/GaTe induces strain of 6% on GaTe and 0.8% on hBN which is slightly less perfect than hBN/InTe HS, but still agreeable. The top view of the structures is presented in Fig. 1. With all three types of stacking being energetically close to each other, we consider H-top stacking (the In(Ga) atom above the centre of the hBN hexagon), which has slightly lower total energy and binding energy compared to the B-top and N-top types. All constituting materials (hBN, InTe, GaTe) exhibit outstanding mechanical properties, demonstrating the ability to withstand significant biaxial strain strengths of more than 10%^{23,28,41}. From an experimental standpoint, achieving a controllable and precise strain beyond a few percent in complex structures like van der Waals (vdW) heterostructures is often challenging, if not impossible. Taking this into account, we chose to set the maximum absolute strain values at 5% even though both systems theoretically possess the capacity for higher strain tolerance. The uniform biaxial strain of -5 to 5% is applied to both structures, with the step of 1%, and the geometry optimisation of the positions of the atoms within the unit cell is performed for all strained structures. The binding energies E_b are calculated for all structures as follows:

$$E_b = E_{\text{heterostr.}} - E_{\text{In(Ga)Te}} - E_{\text{hBN}}, \quad (1)$$

where $E_{\text{heterostr.}}$, $E_{\text{In(Ga)Te}}$ and E_{hBN} represent the total energy of hBN/In(Ga)Te heterostructure, InTe or GaTe monolayer and hBN monolayer, respectively. Total and binding energies, E_{tot} and E_b , along with the distance between the hBN and In(Ga)Te layers d and the width of the layer h are given in Table in the Supplementary file. First, the binding energies are negative in all cases, suggesting that all strained structures are experimentally feasible. It can be seen from and Fig. 2 that the total energy is lowest for HS without strain and increases exponentially with both positive and negative strains, as expected, since the initial system without strain was fully relaxed with respect to the lattice constants and atom positions within the unit cell. The distance between layers and the bond lengths change with different values of applied strain. Although the bonds in the InTe (GaTe) layer are slightly shortened when compressive strain is applied (mainly the In(Ga)–Te bonds), a significant difference

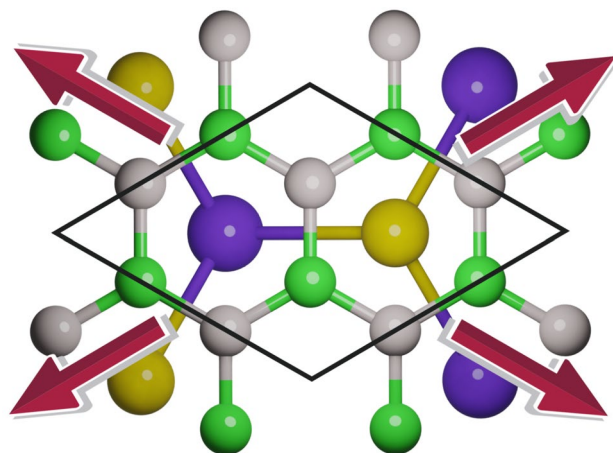


Figure 1. Top view of heterostructures, with arrows showing the tensile biaxial strain. B and N atoms are represented with a grey and green colour, In/Ga and Te atoms are coloured purple and yellow.

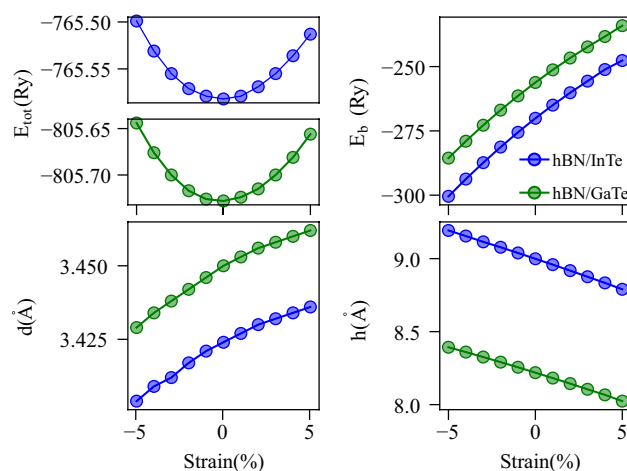


Figure 2. Dependence of total energy E_{tot} , binding energy E_b , distance between the layers d and the thickness of HSS h on applied strain. The blue lines and markers correspond to hBN/InTe, and green lines and markers correspond to hBN/GaTe.

is present in the angle of the In(Ga)–Te bond with respect to the horizontal plane, so the In(Ga)Te layer width is increased, and the inner Te atoms are positioned slightly closer to the hBN layer. In the case of tensile strain, the In(Ga)Te bonds are stretched, causing the layer width to decrease and the distance between the inner Te atoms and the hBN layer to increase. The complete data are given in Table 1 in the Supplementary file.

Before the introduction of strain into any structure, it is essential to conduct a thorough analysis of its mechanical characteristics. We used the Thermo pw code⁴² to compute the elastic constants. The code calculates the non-zero components of the stress tensor for a set of strains and obtains the elastic constants from the first derivative of the stress with respect to the strain. In this way, we can gain a solid basis to understand the relationship between strain and the mechanical reaction of the structure. For 2D systems, nonzero elastic constants follows the Hooke's law under plane stress conditions:

$$\begin{bmatrix} \sigma_1 \\ \sigma_2 \\ \sigma_3 \end{bmatrix} = \begin{bmatrix} c_{11} & c_{12} & 0 \\ 0 & c_{22} & 0 \\ 0 & 0 & c_{66} \end{bmatrix} \cdot \begin{bmatrix} \varepsilon_1 \\ \varepsilon_2 \\ \varepsilon_3 \end{bmatrix}. \quad (2)$$

For a hexagonal lattice, $C_{11} = C_{22}$ and $C_{12} = C_{21}$, $C_{66} = (C_{11} - C_{22})/2$, so there are only two independent elastic constants. In that case, Young's modulus, Poisson's ratio, and shear modulus are obtained from the following relations:

$$E_Y = C_{11} - \frac{C_{12}^2}{C_{11}}, \quad \nu_{xy} = \frac{C_{12}}{C_{11}}, \quad G_{xy} = C_{66}. \quad (3)$$

For hexagonal 2D systems, layer modulus that represents the resistance of a sheet to stretching is calculated by following⁴³:

$$\gamma^{2D} = \frac{C_{11} + C_{12}}{2}.$$

(4)

Calculated elastic constants and moduli are given in Table 1. Obtained elastic constants of single layer InTe and GaTe are in range of other III–VI monochalcogenides⁴⁴. Constants $C_{11} = 45.36$ N/m and $C_{12} = 11.76$ N/m for InTe are close to constants of single layer InSe, and $C_{11} = 65.62$ N/m and $C_{12} = 15.30$ N/m for GaTe close to results for single layer GaSe. We calculated the elastic constants of hBN in order to validate our results, and obtained values are in agreement with the literature^{43,45}. When the HSs are formed, all constants and moduli are significantly increased. Elastic constants C_{11} and C_{12} for hBN/InTe are $C_{11} = 338.3$ N/m and $C_{12} = 72.08$ N/m; $C_{11} = 340$ N/m and $C_{12} = 75.48$ for hBN/GaTe, and their values are roughly similar to the sum of individual constants of each layer in the heterostructure. Young modulus is increased to 323 N/m in HSs, which are high almost as in graphene (342–366 N/m for Young modulus and 206–212 N/m for layer modulus, according to the literature^{43,46}), indicating high resistance to unidirectional compression as well to stretching. The results suggest that the presence of the hBN layer in our heterostructures not only shields the delicate monochalcogenide layers from oxidation but also provides effective mechanical protection, at the same time rendering the system more robust and resistant to deformations.

In our investigation, we computed the band structures of both heterostructures (HSs) under various compressive and tensile strain conditions, building upon the foundation laid out in our previous study³⁶. The band structures for HSs under – 4%, 0% and 4% strain are visually represented in Fig. 3. The band structures for all values of strain, from – 5 to 5%, are represented in Figures S1 and S2 in supplementary file. In their pristine, unstrained states, hBN/InTe and hBN/GaTe exhibit band gaps of $E_g = 1.53$ eV and $E_g = 0.76$ eV, respectively. Notably, both HSs display an indirect band gap configuration, with the valence band maximum (VBM) positioned near the Γ point and the conduction band minimum (CBM) precisely at the Γ point.

When the application of strain is introduced, significant alterations occur in both the band gap and the shape of the bands within the heterostructures. In the case of the hBN/GaTe heterostructure subjected to compressive strain, the band gap widens as the strain magnitude increases, reaching a maximum value of $E_g = 1.49$ eV at –5% strain. Importantly, the valence band retains its shape while shifting downward to lower energy levels. In contrast, the conduction band exhibits distinct behaviour: the Γ -valley expands, whereas the energy level of the M-valley remains relatively stable. This results in both valleys having nearly identical energies at –4% strain. Conversely, the introduction of tensile strain leads to a contrasting effect. The upper region of the valence band near the Γ point shifts upward, while the lower region of the conduction band at the Γ point experiences a substantial descent. Consequently, at + 5% strain, the band gap narrows to only 0.24 eV.

The relationship between band gap and strain is systematically explored and plotted in Fig. 6. Remarkably, across the entire range of applied strains, from –5 to + 5%, the dependence closely approximates a linear decrease.

Turning our attention to the hBN/InTe heterostructure, we observe similar trends in band gap modulation under strain. However, a significant disparity arises in the conduction band behaviour, particularly under compressive strain. Here, the valence band also shifts downward as compressive strain intensifies, eventually falling below the group of bands situated around –0.5 eV at the Γ point. Initially, in the relaxed state, the conduction band minimum (CBM) resides at the Γ point, while the bottom of the M valley maintains nearly the same energy. However, as compressive strain is applied, the Γ -valley remains relatively stable in terms of energy, while the M-valley experiences a downward shift. Consequently, the CBM transitions from the Γ to the M-point as strain surpasses –1%. This intricate interplay between the valence and conduction bands results in a band gap expansion, peaking at $E_g = 1.69$ eV at –2% strain before gradually reducing to 1.39 eV at –5% strain.

In the case of tensile strain, the behaviour mirrors that of the hBN/GaTe heterostructure. The valence band shifts upward, and the CBM descends with increasing tensile strain, leading to a reduced band gap, which ultimately reaches a minimum of 0.70 eV at + 5% strain.

The shifts in the position of valleys within the conduction band in response to varying strain values are not uncommon and have been observed in InTe and GaTe monolayers subjected to biaxial strain^{28,47,48}. Furthermore, our analysis of the density of states (DOS) reveals that the bands closest to the Fermi level predominantly arise from the In(Ga) and Te states. DOS for HSs with – 4%, 0% and 4% strain are presented in Figs. 4 and 5. Complete

1	InTe	GaTe	hBN	hBN/InTe	hBN/GaTe
C_{11}	45.36	65.62	290.77	338.30	340.00
C_{12}	11.76	15.30	63.93	72.08	75.48
C_{66}	16.52	25.16	113.42	132.94	132.26
E_y	42.31	62.05	276.41	322.94	323.24
ν_{xy}	0.26	0.23	0.22	0.21	0.22
G_{xy}	16.52	25.16	113.42	132.94	132.26
γ^{2D}	28.56	40.46	177.35	205.19	207.74

Table 1. Elastic constants, Young modulus, Poisson ratio, shear modulus and layer modulus for HSs and pristine InTe and GaTe monolayers. Units are given in N/m.

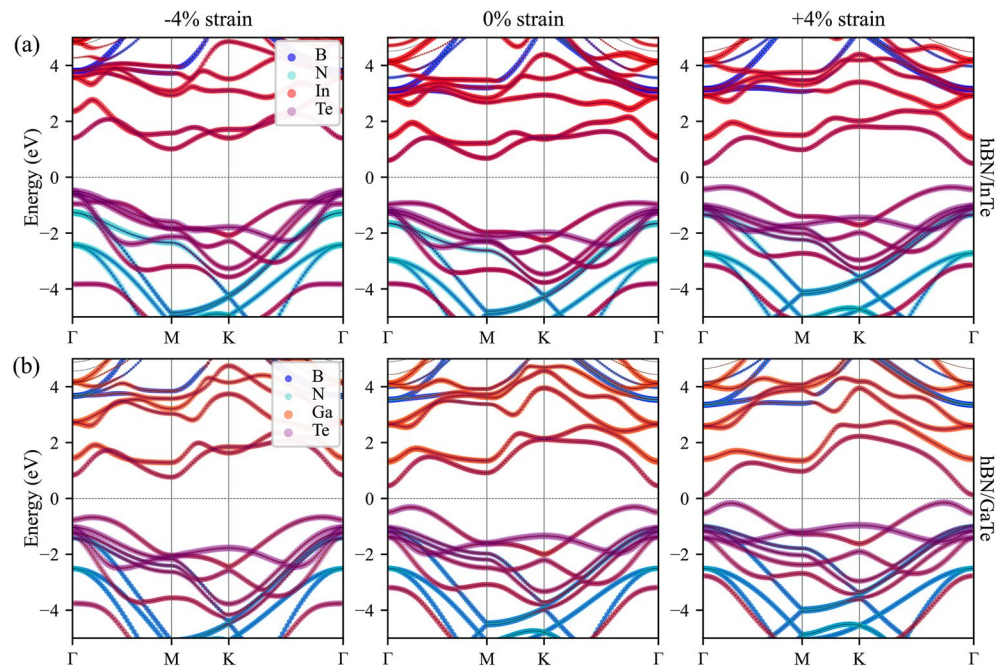


Figure 3. Band structure of (a) hBN/InTe HS and (b) hBN/GaTe. The width of the lines is proportional to the contribution of different atoms/states. The line width is proportional to the magnitude of projections of wavefunctions over atomic orbitals. The contributions from different atomic orbitals are presented in different colours, as shown in the legend.

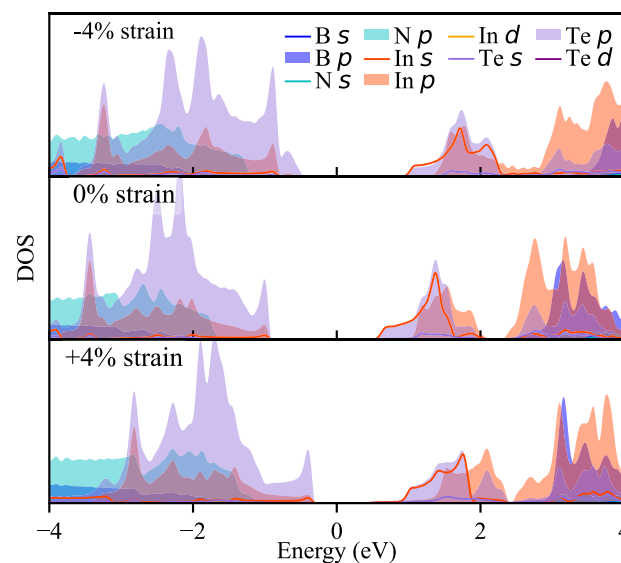


Figure 4. Projected density of states of hBN/InTe HS. Contributions from different atoms and states are represented with colours as in legend.

data with DOS for all strain values are shown in Figure S3 in supplementary file. The uppermost bands below the Fermi level primarily originate from the Te states, while the bands above comprise a combination of In(Ga) and Te states. Consequently, it can be inferred that the changes in the conduction band shape predominantly result from the influence of strain on the InTe(GaTe) layer itself, rather than being an inherent characteristic of the formed heterostructure. These findings underscore the profound influence of strain engineering on the electronic properties of these heterostructures, offering a promising avenue for precise control and modulation of their behaviour for tailored optoelectronic applications.

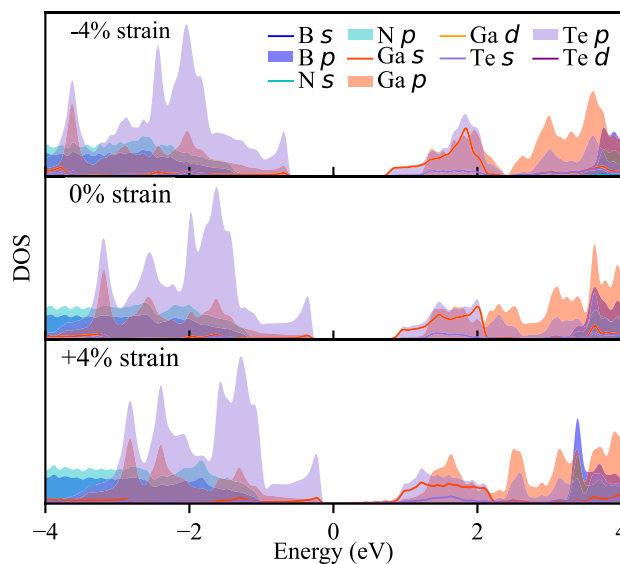


Figure 5. Projected density of states of hBN/GaTe HS. Contributions from different atoms and states are represented with colours as in legend.

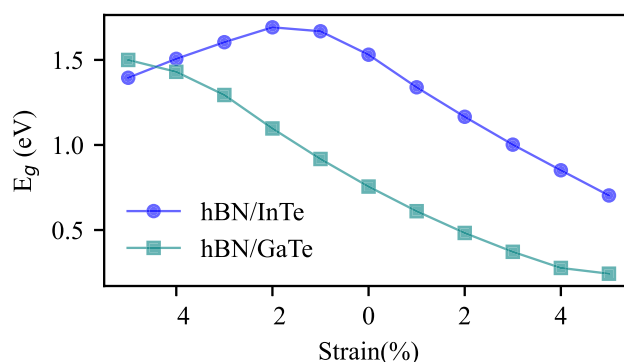


Figure 6. Band gap of hBN/InTe (indicated as blue line and circles) and hBN/GaTe (indicated as green line and squares) as a function of applied strain.

Significant variations in both the band gap and the shape of the bands can drastically alter dielectric function and absorption. The complex dielectric function $\epsilon(\omega) = \epsilon_R(\omega) + i\epsilon_I(\omega)$ is obtained from DFT calculations in the RPA framework. The absorption coefficient $\alpha(\omega)$ is obtained directly from the dielectric function as follows:

$$\alpha(\omega) = \sqrt{2} \frac{\omega}{c} \sqrt{\epsilon_R^2(\omega) + \epsilon_I^2(\omega) - \epsilon_I(\omega)}. \quad (5)$$

Calculation of optical properties were performed within RPA. Optical properties of group III monochalcogenide members and similar structures as well of hBN were previously studied both with GW and RPA based methods, and it is shown that RPA can provide reasonably good results of dielectric function and its qualitative description^{49–53}. In⁵⁴, heterostructure of InSe with silicene, germanene and antimonene, imaginary part of the dielectric function calculated both with RPA over GGA and GW, and main difference observed is the shift of the dielectric function for 0.5–1 eV due to larger calculated band gap. The absorption coefficients of both HSs under different strain strengths are presented in Figs. 7 and 8, respectively. The band gap width variations induced by strain strength exhibit a notable influence on the absorption properties of both HSs. Specifically, compressive strain causes the absorption function to shift towards higher energies, while tensile strain results in a shift towards lower energies, a behaviour consistently observed in both HSs. However, the most striking disparity in absorption behaviour occurs in hBN/InTe, where the application of compressive strain induces the formation of a pronounced peak at approximately 3 eV for z-polarisation. This striking alteration is attributed to the significant reduction of the M-valley in hBN/InTe and is absent in hBN/GaTe under similar strain conditions. This study highlights the intricate interplay between strain and the optical properties of these heterostructures. The observed differences in absorption behaviour underscore the nuanced effects that strain engineering can exert, offering a pathway towards fine-tuning the optical characteristics of these materials for tailored optoelectronic applications.

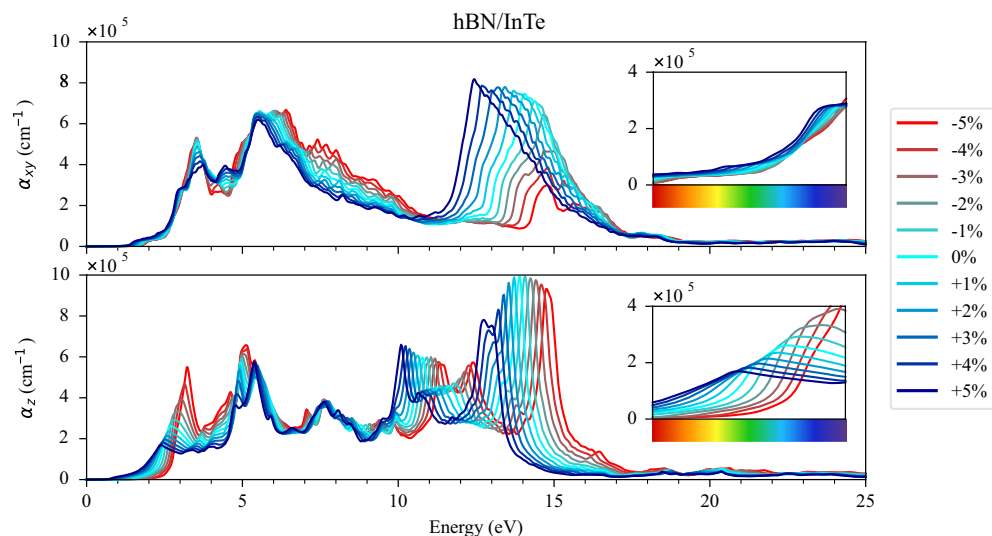


Figure 7. Absorption function of hBN/InTe HS for (a) in-plane (α_{xy}) and (b) out-of-plane (α_z) polarisations. Each colour represents a different value of the induced strain, from red (− 5% of strain) to blue (+ 5% of strain). The visible part of the spectrum is enlarged in the inset.

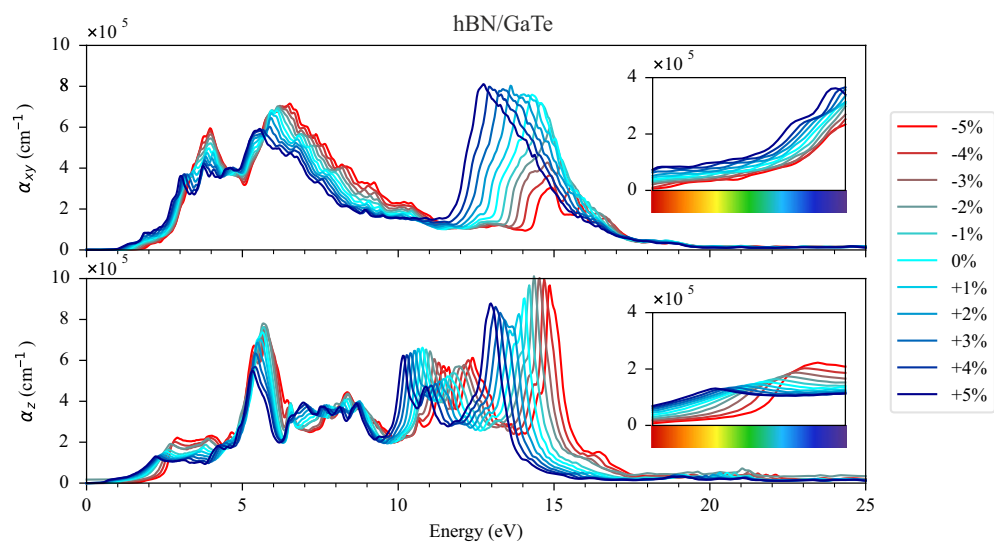


Figure 8. Absorption function of hBN/GaTe HS for (a) in-plane (α_{xy}) and (b) out-of-plane (α_z) polarisations. Each colour represents a different value of the induced strain, from red (− 5% of strain) to blue (+ 5% of strain). The visible part of the spectrum is enlarged in the inset.

Conclusions

In this study, we systematically investigated the impact of biaxial strain on recently designed HSs composed of InTe (GaTe) and hBN monolayers using DFT. All the considered strained structures were found to be experimentally feasible, characterised by negative binding energies. Our band structure analysis revealed that strain offers a powerful tool for the precise manipulation of the band gap in these structures.

In the case of hBN/GaTe, we observed an almost linear relationship between band gap and strain, with band gap values increasing under compressive strain and decreasing under tensile strain. Specifically, the largest band gap of $E_g = 1.49$ eV was achieved at − 5% strain, while it reduced to 0.24 eV at + 5% strain. In hBN/InTe, the manipulation of strain led to a decrease in the M-valley's energy, effectively positioning it below the Γ -valley. This resulted in a band gap that decreased under strain stronger than − 2%, with band gap energies falling within the range of 0.70–1.69 eV.

Additionally, we examined the optical properties by calculating the dielectric functions and found that tensile strain substantially enhanced absorption in the low-energy spectrum, particularly in the visible spectrum.

On the contrary, compressive strain increased absorption at 3 eV, but shifted the absorption function towards higher energies.

Our findings underscore the pivotal role of strain engineering in these HSs, offering precise control over their electronic and optical properties. Furthermore, these tunable properties open up possibilities for their utilisation in various sensor and switch applications.

Data availability

The datasets used and/or analysed during the current study are available from the corresponding author on reasonable request.

Received: 27 October 2023; Accepted: 3 January 2024

Published online: 11 January 2024

References

- Geim, A. K. & Grigorieva, I. V. Van der waals heterostructures. *Nature* **499**, 419–425 (2013).
- Novoselov, K., Mishchenko, O. A., Carvalho, O. A. & Neto, A. C. 2d materials and van der waals heterostructures. *Science* **353**, 25 (2016).
- Liu, Y. *et al.* Van der waals heterostructures and devices. *Nat. Rev. Mater.* **1**, 1–17 (2016).
- Liang, S.-J., Cheng, B., Cui, X. & Miao, F. Van der waals heterostructures for high-performance device applications: Challenges and opportunities. *Adv. Mater.* **32**, 1903800 (2020).
- Huo, N. *et al.* Novel and enhanced optoelectronic performances of multilayer MOS2-WS2 heterostructure transistors. *Adv. Funct. Mater.* **24**, 7025–7031 (2014).
- Furchi, M. M. *et al.* Device physics of van der waals heterojunction solar cells. *NPJ 2D Mater. Appl.* **2**, 1–7 (2018).
- Zheng, X. *et al.* Pn/pas-wse2 van der waals heterostructures for solar cell and photodetector. *Sci. Rep.* **10**, 1–9 (2020).
- Zhou, W. *et al.* Epitaxial growth of branched α -fe2o3/sno2 nano-heterostructures with improved lithium-ion battery performance. *Adv. Funct. Mater.* **21**, 2439–2445 (2011).
- Chen, C. *et al.* Mos2-on-mxene heterostructures as highly reversible anode materials for lithium-ion batteries. *Angew. Chem. Int. Ed.* **57**, 1846–1850 (2018).
- Withers, F. *et al.* Light-emitting diodes by band-structure engineering in van der waals heterostructures. *Nat. Mater.* **14**, 301–306 (2015).
- Zong, X. *et al.* Black phosphorus-based van der waals heterostructures for mid-infrared light-emission applications. *Light Sci. Appl.* **9**, 1–8 (2020).
- Qin, S. *et al.* Robust, flexible and broadband photodetectors based on van der waals graphene/c60 heterostructures. *Carbon* **167**, 668–674 (2020).
- Dong, T., Simoes, J. & Yang, Z. Flexible photodetector based on 2d materials: Processing, architectures, and applications. *Adv. Mater. Interfaces* **7**, 1901657 (2020).
- Chen, Y. *et al.* High-performance photovoltaic detector based on mote2/mos2 van der waals heterostructure. *Small* **14**, 1703293 (2018).
- Cui, B. *et al.* Ultrahigh photoresponsive photodetector based on graphene/sns2 van der waals heterostructure. *Phys. Status Solidi (a)* **218**, 2100228 (2021).
- Stutzmann, M. *et al.* Gan-based heterostructures for sensor applications. *Diam. Relat. Mater.* **11**, 886–891 (2002).
- Bag, A. & Lee, N.-E. Gas sensing with heterostructures based on two-dimensional nanostructured materials: A review. *J. Mater. Chem. C* **7**, 13367–13383 (2019).
- Hou, H.-L., Anichini, C., Samori, P., Criado, A. & Prato, M. 2d van der waals heterostructures for chemical sensing. *Adv. Funct. Mater.* **20**, 2207065 (2022).
- Scappucci, G., Taylor, P., Williams, J., Ginley, T. & Law, S. Crystalline materials for quantum computing: Semiconductor heterostructures and topological insulators exemplars. *MRS Bull.* **46**, 596–606 (2021).
- Xiong, P. *et al.* Strain engineering of two-dimensional multilayered heterostructures for beyond-lithium-based rechargeable batteries. *Nat. Commun.* **11**, 1–12 (2020).
- Zhang, J., Lang, X., Zhu, Y. & Jiang, Q. Strain tuned inse/mos 2 bilayer van der waals heterostructures for photovoltaics or photocatalysis. *Phys. Chem. Chem. Phys.* **20**, 17574–17582 (2018).
- Postorino, S. *et al.* Strain-induced effects on the electronic properties of 2d materials. *Nanomater. Nanotechnol.* **10**, 1847980420902569 (2020).
- Li, M.-S., Chen, K.-X., Mo, D.-C. & Lyu, S.-S. Predicted high thermoelectric performance in a two-dimensional indium telluride monolayer and its dependence on strain. *Phys. Chem. Chem. Phys.* **21**, 24695–24701 (2019).
- Song, L., Zhang, J., Mamakhel, A. & Iversen, B. B. Crystal structure, electronic transport, and improved thermoelectric properties of doped inte. *ACS Appl. Electron. Mater.* <https://doi.org/10.1021/acsaelm.3c01064> (2023).
- Yang, Z. *et al.* Large-scale synthesis of two-dimensional indium telluride films for broadband photodetectors. *Mater. Design* **233**, 112218. <https://doi.org/10.1016/j.matdes.2023.112218> (2023).
- Kremer, G. *et al.* Direct observation of highly anisotropic electronic and optical nature in indium telluride. *Phys. Rev. Mater.* **7**, 074601. <https://doi.org/10.1103/PhysRevMaterials.7.074601> (2023).
- Bouaziz, M. *et al.* Intrinsic defects and mid-gap states in quasi-one-dimensional indium telluride. *Phys. Rev. Res.* **5**, 033152. <https://doi.org/10.1103/PhysRevResearch.5.033152> (2023).
- Vi, V. T., Hieu, N. N., Hoi, B. D., Binh, N. T. & Vu, T. V. Modulation of electronic and optical properties of gate monolayer by biaxial strain and electric field. *Superlattices Microstruct.* **140**, 106435 (2020).
- Rahaman, M., Rodriguez, R. D., Monecke, M., Lopez-Rivera, S. A. & Zahn, D. R. T. GaSe oxidation in air: From bulk to monolayers. *Semicond. Sci. Technol.* **32**, 105004 (2017).
- Guo, Y., Zhou, S., Bai, Y. & Zhao, J. Defects and oxidation of group-iii monochalcogenide monolayers. *J. Chem. Phys.* **147**, 104709 (2017).
- Guo, Y., Zhou, S. & Zhao, J. Oxidation behaviors of two-dimensional metal chalcogenides. *ChemNanoMat* **6**, 838–849 (2020).
- Tang, X. *et al.* Direct growth of hexagonal boron nitride nanofilms on stainless steel for corrosion protection. *ACS Appl. Nano Mater.* **4**, 12024–12033 (2021).
- Liu, Z. *et al.* Ultrathin high-temperature oxidation-resistant coatings of hexagonal boron nitride. *Nat. Commun.* **4**, 2541 (2013).
- Li, X., Yin, J., Zhou, J. & Guo, W. Large area hexagonal boron nitride monolayer as efficient atomically thick insulating coating against friction and oxidation. *Nanotechnology* **25**, 105701 (2014).
- Arora, H. *et al.* Effective hexagonal boron nitride passivation of few-layered inse and gase to enhance their electronic and optical properties. *ACS Appl. Mater. Interfaces* **11**, 43480–43487 (2019).

36. Šolajić, A. & Pešić, J. Novel wide spectrum light absorber heterostructures based on hbn/in (ga) te. *J. Phys. Condens. Matter* **34**, 345301 (2022).
37. Giannozzi, P. *et al.* Quantum espresso: A modular and open-source software project for quantum simulations of materials. *J. Phys. Condensed Matter* **21**(395502), 19 (2009).
38. Perdew, J. P., Burke, K. & Ernzerhof, M. Generalized gradient approximation made simple. *Phys. Rev. Lett.* **77**, 3865–3868. <https://doi.org/10.1103/PhysRevLett.77.3865> (1996).
39. Grimme, S. Semiempirical gga-type density functional constructed with a long-range dispersion correction. *J. Comput. Chem.* **27**, 1787–1799 (2006).
40. Barone, V. *et al.* Role and effective treatment of dispersive forces in materials: Polyethylene and graphite crystals as test cases. *J. Comput. Chem.* **30**, 934–939 (2009).
41. Falin, A. *et al.* Mechanical properties of atomically thin boron nitride and the role of interlayer interactions. *Nat. Commun.* **8**, 15815 (2017).
42. Dal Corso, A. Thermopw: A python package to calculate the electronic thermal conductivity from first principles. https://dalcorso.github.io/thermo_pw/ (2023). Accessed 6 Oct 2023.
43. Andrew, R. C., Mapasha, R. E., Ukpong, A. M. & Chetty, N. Mechanical properties of graphene and boronitrene. *Phys. Rev. B* **85**, 125428. <https://doi.org/10.1103/PhysRevB.85.125428> (2012).
44. Li, W. & Li, J. Piezoelectricity in two-dimensional group-iii monochalcogenides. *Nano Res.* **8**, 3796–3802 (2015).
45. Peng, Q., Ji, W. & De, S. Mechanical properties of the hexagonal boron nitride monolayer: Ab initio study. *Comput. Mater. Sci.* **56**, 11–17 (2012).
46. Singh, S., Espejo, C. & Romero, A. H. Structural, electronic, vibrational, and elastic properties of graphene/mos 2 bilayer heterostructures. *Phys. Rev. B* **98**, 155309 (2018).
47. Touski, S. B., Ariapour, M. & Hosseini, M. Electrical and electronic properties of strained mono-layer inte. *Physica E* **118**, 113875 (2020).
48. Huang, L., Chen, Z. & Li, J. Effects of strain on the band gap and effective mass in two-dimensional monolayer gax (x = s, se, te). *RSC Adv.* **5**, 5788–5794 (2015).
49. Shang, J. *et al.* Tunable electronic and optical properties of inse/inte van der waals heterostructures toward optoelectronic applications. *J. Mater. Chem. C* **6**, 7201–7206 (2018).
50. Do, T.-N., Vi, V. T., Binh, N. T., Hieu, N. N. & Hieu, N. V. Computational study on strain and electric field tunable electronic and optical properties of inte monolayer. *Superlattices Microstruct.* **151**, 106816. <https://doi.org/10.1016/j.spmi.2021.106816> (2021).
51. Jalilian, J. & Safari, M. Electronic and optical properties of α -inx (x=s, se and te) monolayer: Under strain conditions. *Phys. Lett. A* **381**, 1313–1320. <https://doi.org/10.1016/j.physleta.2017.01.024> (2017).
52. Liao, Y., Liu, H., Yuan, G., Huang, Z. & Qi, X. Electronic and optical properties of novel graphene-like inte monolayer: First principle calculations. *Cryst. Res. Technol.* **55**, 2000102 (2020).
53. Zólyomi, V., Drummond, N. D. & Fal'ko, V. I. Electrons and phonons in single layers of hexagonal indium chalcogenides from ab initio calculations. *Phys. Rev. B* **89**, 205416. <https://doi.org/10.1103/PhysRevB.89.205416> (2014).
54. Sengupta, A., Dominguez, A. & Frauenheim, T. Photo-absorption properties of van der waals heterostructure of monolayer inse with silicene, germanene and antimonene. *Appl. Surf. Sci.* **475**, 774–780. <https://doi.org/10.1016/j.apsusc.2019.01.054> (2019).

Acknowledgements

The authors acknowledge funding provided by the Institute of Physics Belgrade through the Grant by the Ministry of Science, Technological Development and Innovations of the Republic of Serbia, and by Austrian Science Fund (FWF der Wissenschaftsfonds) through START Grant number Y1298-N. DFT calculations were performed using computational resources at Johannes Kepler University (Linz, Austria).

Author contributions

A.Š. did the calculations and prepared figures. Both authors wrote the main manuscript text and reviewed the manuscript.

Competing interests

The authors declare no competing interests.

Additional information

Supplementary Information The online version contains supplementary material available at <https://doi.org/10.1038/s41598-024-51303-4>.

Correspondence and requests for materials should be addressed to A.Š.

Reprints and permissions information is available at www.nature.com/reprints.

Publisher's note Springer Nature remains neutral with regard to jurisdictional claims in published maps and institutional affiliations.



Open Access This article is licensed under a Creative Commons Attribution 4.0 International License, which permits use, sharing, adaptation, distribution and reproduction in any medium or format, as long as you give appropriate credit to the original author(s) and the source, provide a link to the Creative Commons licence, and indicate if changes were made. The images or other third party material in this article are included in the article's Creative Commons licence, unless indicated otherwise in a credit line to the material. If material is not included in the article's Creative Commons licence and your intended use is not permitted by statutory regulation or exceeds the permitted use, you will need to obtain permission directly from the copyright holder. To view a copy of this licence, visit <http://creativecommons.org/licenses/by/4.0/>.

© The Author(s) 2024



Strain-induced modulation of electronic and optical properties in hBN/InSe heterostructure

Andrijana Šolajić¹ · Jelena Pešić¹

Received: 31 December 2023 / Accepted: 13 March 2024 / Published online: 16 June 2024
© The Author(s), under exclusive licence to Springer Science+Business Media, LLC, part of Springer Nature 2024

Abstract

Our study delves into the nuanced effects of strain on hBN/InSe heterostructures, known for their exceptional wide-spectrum absorption capabilities. Employing uniform biaxial strain in the range of -6% to 6% , our investigation reveals a powerful method for manipulating the band gap. Notably, intense tensile strain leads to the near-complete elimination of the band gap—an outcome with profound implications. Comparison with hBN/InTe and hBN/GaTe heterostructures underscores the unique behaviour of hBN/InSe, showing a striking resemblance to hBN/GaTe but achieving lower band gap values under tensile strain. These findings provide crucial insights for experimental work and serve as a guide for more intricate theoretical explorations. With its outstanding electronic properties, tunable band gap, and remarkable absorption characteristics, hBN/InSe emerges as a key player in the development of future novel devices.

Keywords VdW heterostructures · DFT · InSe · Electronic structure · Optical properties · 2D

1 Introduction

Two-dimensional (2D) materials and van der Waals (vdW) heterostructures (HSs) have captured immense attention within the scientific community in recent years, owing to their distinctive physical properties that distinguish them from their bulk counterparts (Novoselov et al. 2016; Geim and Grigorieva 2013; Liu et al. 2016). Their remarkable electronic, optical, and mechanical attributes open up numerous possibilities for applications in modern devices. The exhaustive research in this field has underscored the special advantage of 2D materials and vdW heterostructures—they offer a plenty of options for customization and precise manipulation of their properties, enabling their use in a wide array of applications including transistors, solar cells, lithium-ion batteries, photodetectors (Liang et al.

✉ Andrijana Šolajić
solajic@ipb.ac.rs

Jelena Pešić
yelena@ipb.ac.rs

¹ Laboratory for 2D materials, Center for Solid State Physics and New Materials, Institute of Physics Belgrade, University of Belgrade, Pregrevica 118, 11080 Belgrade, Serbia

2020; Huo et al. 2014; Furchi et al. 2018; Zhou et al. 2011; Withers et al. 2015; Bag and Lee 2019). The current needs of nanoelectronics, optoelectronics and spintronics necessitate use of materials and components with diverse characteristics, coupled with the imperative of their minimization. In this context, 2D materials and vdW heterostructures emerge as promising contributors to fulfilling these demands.

As for tuning their properties, various effective methods have emerged, including doping and controlled introduction of defects, application of external electric or magnetic fields, and the utilization of strain. Notably, strain has proven exceptionally efficient for the precise control of the electronic and optical properties of 2D materials, offering a means to tailor these properties without fundamentally altering the material's characteristics (Xiong et al. 2020; Postorino et al. 2020). In the realm of van der Waals (vdW) materials and heterostructures, in-plane strain is commonly employed to modulate the electronic band structure. However, its utility extends beyond this, as it has been demonstrated to influence spin-orbit coupling (Zhuang et al. 2016), alter magnetic ordering (Šiškins et al. 2020; Wang et al. 2020; Webster and Yan 2018), and introduce various other novel effects (Miao et al. 2021). This multidimensional impact of strain, giving rise to the evolving field of straintronics, has sparked a new wave of research in the manipulation and optimization of material properties for advanced applications.

Within the 2D materials landscape, group III monochalcogenides have emerged as a focal point of extensive research, distinguished by their unique and promising properties. Recent investigations highlight their high electron mobility, a critical parameter for electronic devices, surpassing $10^3 \text{ cm}^2 \text{ V}^{-1} \text{ s}^{-1}$ (Chen et al. 2019). Notably, their band gap is easily tunable by adjusting the number of layers or applying strain Song et al. (2018); Li et al. (2018); Ma et al. (2013). Moreover, these materials exhibit substantial optical absorption across the UV, visible, and infrared regions (Wang et al. 2019; Lei et al. 2013; Hu et al. 2012), showcasing their potential in photonic applications. The nonlinear optical properties of group III monochalcogenides have been explored (Jie et al. 2015; Zhou et al. 2015), adding another layer of versatility to their applications. A significant advantage lies in their ease of exfoliation through mechanical or chemical methods (Yang et al. 2017; Aitzhanov et al. 2022; Qi et al. 2021; Harvey et al. 2015; Yang et al. 2023). Notably, InSe, one of the pioneering members, has been extensively studied, revealing a plethora of extraordinary properties. For instance, InSe demonstrates excellent thermoelectric performance (Hung et al. 2017) and high electron mobility (Bandurin et al. 2017; Sucharitakul et al. 2015; Feng et al. 2014), underlining its significance in the realm of 2D materials and beyond.

The exploration of heterostructures based on group III monochalcogenides is a thriving area of research. When combined with graphene, these heterostructures demonstrate exceptional tunable Schottky diode characteristics (Kim et al. 2016; Pham et al. 2019; Zhang et al. 2020). Specifically, InSe/InTe heterostructures exhibit enhanced optical absorption intensity compared to isolated monolayers (Shang et al. 2018). Another noteworthy application is observed in Sb/InSe heterostructures, where practical utilization allows for dipole control of Rashba spin splitting. The incorporation of hBN layers in these heterostructures goes beyond enhancing the inherent properties of monochalcogenides. It provides robust mechanical protection and passivation for the fragile monochalcogenides (Tang et al. 2021; Liu et al. 2013; Li et al. 2014), which are susceptible to oxidation when exposed to air (Guo et al. 2017, 2020). This engineering approach not only improves the performance of the HSs but also ensures the stability and longevity of the delicate monochalcogenide components.

Computational predictions suggest that encapsulating an InSe layer between two hBN capping layers significantly boosts electron mobility compared to pristine InSe films (Kang

et al. 2017). The high mobility and on/off ratio exhibited by InSe/hBN/graphite heterostructures, especially when integrated onto flexible substrates, make them compelling candidates for flexible electronics (Wu et al. 2020).

The theoretical exploration of InSe/hBN heterostructures extends beyond their electrical properties to their optical characteristics. Studies indicate that the construction of the heterostructure enhances absorption, concurrently reducing the band gap (Shen et al. 2022) - The band gap of bulk InSe lies in range from 1.3 to 1.4 eV (Gürbulak et al. 2014; Politano et al. 2017; Sang et al. 2019), but in monolayer, the gap is increased to 2.37 eV (Lei et al. 2014; Zhuang and Hennig 2013), resulting in limited applications for optoelectronic devices, as it is too large to be usable for absorbing IR and visible part of the spectrum. This dual enhancement in optical properties further underscores the multifaceted advantages offered by InSe/hBN heterostructures, making them compelling candidates for diverse applications.

Leveraging these insights, our work aims to comprehensively investigate the impact of strain on InSe/hBN heterostructures. Furthermore, the theoretical findings on the optical properties of InSe/hBN heterostructures, indicating enhanced absorption and a reduced band gap, inspire our exploration into the nuanced effects of strain. Understanding how strain influences the electronic and optical properties of InSe/hBN heterostructures is pivotal for optimizing their performance and unlocking their full potential for future technological applications.

2 Computational Methods

Density functional theory (DFT) were performed in the Quantum Espresso (QE) software package (Giannozzi 2009), based on plane waves and pseudopotentials. The Perdew-Burke-Ernzerhof (PBE) exchange correlation functional (Perdew et al. 1996) is used along with norm-conserving pseudopotentials. The energy cutoff of 90 Ry was set after the convergence tests.

The Monkhorst pack of 16x16x1 mesh for k-point sampling is used in geometric optimisation and total energy calculations. For calculations of p-DOS and optical properties, a refined 48x48x1 mesh is used. The band structure is calculated on 440 k-points along Γ -M-K- Γ direction. A vacuum of 20 Å is added along the z-direction to avoid interactions between the layers and simulate 2D structure. Geometry optimisation of the positions of the atoms and the lattice parameters is performed using the BFGS algorithm, with criteria for the maximum forces allowed between atoms of 10^{-6} Ry/Å. To properly account for van der Waals force effects, the Grimme-D2 correction (Grimme 2006; Barone et al. 2009) was included to obtain more accurate lattice constants and forces. The optical properties were calculated using the epsilon.x code in QE software, based on the random phase approximation (RPA).

3 Results

Similarly to hBN/InTe and hBN/GaTe HSs reported in our previous work (Šolajić and Pešić 2022; Šolajić and Pešić 2023), hBN/InSe HS is modelled as supercell composed of 1x1 unit cell of InSe, with $\sqrt{3} \times \sqrt{3}$ supercell of hBN rotated for 30° on top of InSe. Drawing parallels with our previous studies, this approach ensures consistency in our methodology.

For hBN, the unit cell's lattice constant (a) is 2.51\AA , while the constructed $\sqrt{3} \times \sqrt{3}$ supercell has a lattice constant of 4.34\AA . Comparatively, the calculated lattice constant for InSe is 4.03\AA , closely mirroring the values obtained for GaTe in our earlier research (Šolajić and Pešić 2022), where $a = 4.05\text{\AA}$.

Searching for an energetically most favourable configuration, the constructed heterostructure undergoes relaxation, adjusting both the lattice parameter and atomic positions within the unit cell. The optimized lattice parameter for the hBN/InSe heterostructure converges to $a = 4.29\text{\AA}$. Notably, this relaxation induces a 1% strain on the hBN layer and a 6% strain on InSe. This pattern aligns with observations in our studies of hBN/GaTe and hBN/InTe, where the preference is for GaTe (InTe) to experience more significant strain than the hBN layer. Such strain variation arise from the different elastic properties inherent in the combined materials, providing valuable insights into the mechanical interplay within these heterostructures. Namely, the elastic constants of hBN are roughly 3 times larger than ones of InSe, as well the Young and layer modulus (Li and Li 2015; Šolajić and Pešić 2022), similar as in GaTe, leading to different strain strengths induced in each layer.

The application of uniform tensile and compressive biaxial strain, with a maximum amplitude of 6%, to the heterostructure induces significant transformations in its structural parameters. In the unstrained, relaxed configuration, the distance between the hBN layer and InSe, denoted as d , measures 3.29\AA . Under compressive strain, d slightly decreases, reaching 3.26\AA for -6% strain, while under tensile strain, it increases, peaking at 3.30\AA for 6% . The bond lengths also undergo alterations with strain. In the absence of strain, the In-In bond length is 2.82\AA , the In-Se bond is 2.73\AA , and the In-Se-In angle is 103° . Under compressive strain, these bond lengths reduce: the In-In bond shortens to 2.79\AA , the In-Se bond contracts to 2.66\AA , and the In-Se-In angle decreases to 98.7° . Conversely, tensile strain leads to elongation of bonds and widening of angles. At 6% strain, the In-In bond extends to 2.85\AA , the In-Se bond increases to 2.80\AA , and the angle expands to 108° . These variations in geometry and covalent bond distances are anticipated to exert a profound influence on the heterostructure's band structure and band gap, providing crucial insights into the structural modifications induced by strain.

3.1 Electronic structure

In the absence of applied strain, representing the relaxed structure, band gap of hBN/InSe heterostructure is calculated to be $E_g = 0.56\text{ eV}$, which is less than the band gaps observed in both the hBN/InTe and hBN/GaTe heterostructures. To validate our results, we also calculated the band gap of the InSe monolayer, obtaining $E_g = 1.49\text{ eV}$, consistent with previous results using the same methodology (Hu et al. 2017). It is important to note that DFT calculations with standard functionals such as PBE often underestimate the band gap in semiconductors. For a more accurate assessment of the band gap, hybrid functionals (e.g. HSE06) are commonly employed. However, it has been observed that in group III monochalcogenides and related structures, the difference in band structures obtained using PBE and hybrid functionals primarily stems from variations in the width of the band gap, which tends to be larger (and more accurate) with hybrids. Notably, the valence bands remain largely unchanged within both methods, while the conduction bands are shifted upwards, largely preserving their shape. Taking into account the qualitatively similar band structures obtained using both methods, we opted for the PBE functional in this manuscript for our calculations. This decision was made due to the significant computational demands associated with calculations employing hybrid

functionals, especially in studies of systems under strain, where a large number of calculations are necessitated. The estimated error introduced in band gaps in our research is approximately in the range of 0.6–0.9 eV. Specifically, our calculations yield a band gap of 1.49 eV in InSe monolayer and 0.56 eV in hBN/InSe heterostructure without introduced strain; when hybrid functionals are used, band gaps of 2.37 eV and 1.16 eV are obtained for monolayer InSe and hBN/InSe heterostructure, respectively. A similar deviation in the band structure is expected in strained structures.

Figure 1 illustrates the relationship between band gap and strain for the hBN/InSe heterostructure, alongside the previously studied hBN/InTe and hBN/GaTe heterostructures for comparative analysis. In contrast to the behaviour observed in hBN/InTe, where the band gap enlarges up to 2% strain before declining, the band gap in hBN/InSe mirrors the trend observed in hBN/GaTe. Notably, it exhibits an almost linear dependence on applied strain. The widest band gap, $E_g = 1.37$ eV, is achieved under -6% strain. Conversely, tensile strain diminishes the band gap, reaching near-zero values at 6% strain. At this point, the energy level at the bottom of the valley in the Γ point of the valence band aligns closely with the energy level at the top of the conduction band valleys located between the Γ and M point, and between K and Γ point, leaving only the indirect gap between the valleys.

Analysing deeper the behaviour of bands proximate to the Fermi level and the composition of associated states reveals several key features, we present the band structure for different strain values illustrated in Fig. 2. Band structure is calculated along the Γ -M-K- Γ direction, and given that heterostructure consisted only of single-layered hBN and InSe is essentially two dimensional, hence the Brillouin zone is practically flat, and negligible contribution exist in the out-of-plane directions. Primarily, the valence band predominantly comprises states contributed by In and Se. Under compressive strain, the valley in the Γ point expands, while under tensile strain, it contracts, influencing the entire band. The conduction band behaviour is more peculiar. For tensile strain, the top of the conduction band rises, and the band closest to the Fermi level is predominantly composed from In and Se states. Conversely, with compressive strain, where top of the conduction band located between the Γ and M/K points is decreasing, at -4% strain, top of the conduction band relocates to the Γ point, and is predominantly composed of N states.

The projected density of states illustrated in Fig. 3 is showing more clear picture of atoms/states composition near the Fermi level. Near the Fermi level we predominantly

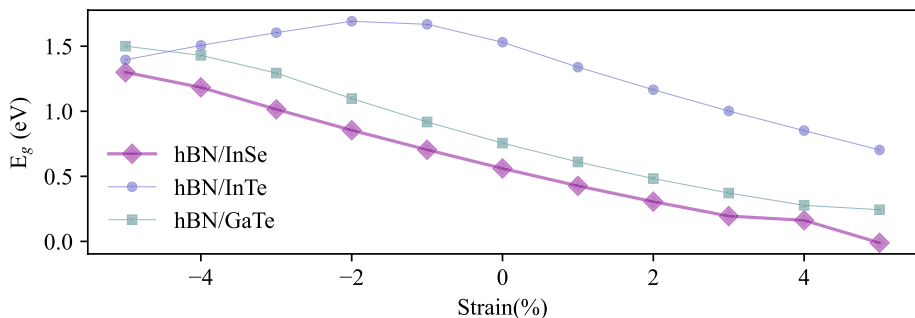


Fig. 1 Band gap as a function of strain for hBN/InSe (purple line with rhomboid markers), along with hBN/InTe (green line and square markers) and hBN/GaTe (blue line, circle markers) for comparison

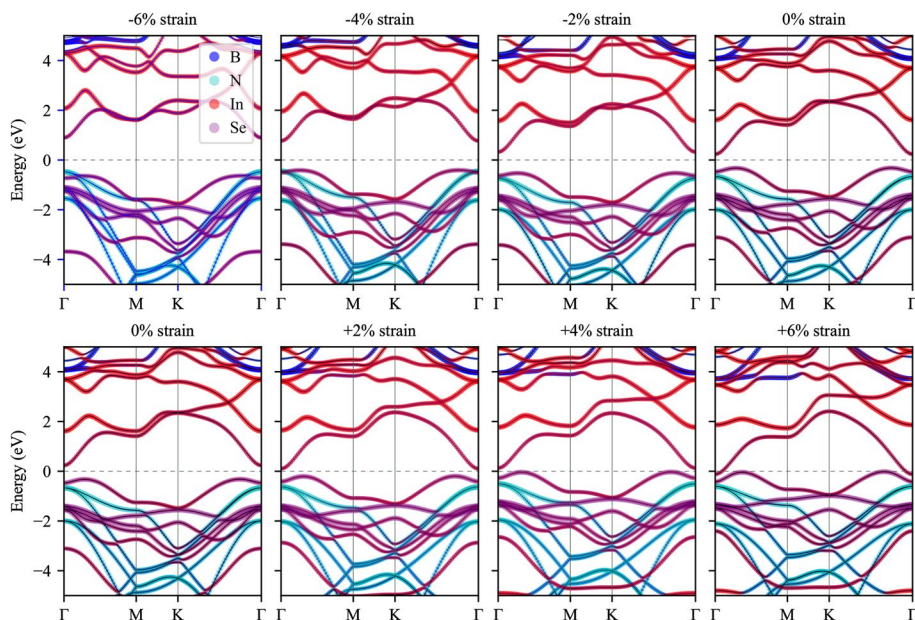


Fig. 2 Projected bandstructure of hBN/InSe HS for different values of applied strain, from -6% to $+6\%$. Contribution from different atoms/states are represented in different colours as in legend

observe Se p and In s states, for strain strengths in range of -4% to $+6\%$. For compressive strain of -4% and stronger, N p states are dominant below the Fermi level, and above the Fermi level, group of In p states is moved closer to the bottom of valence band.

3.2 Optical properties

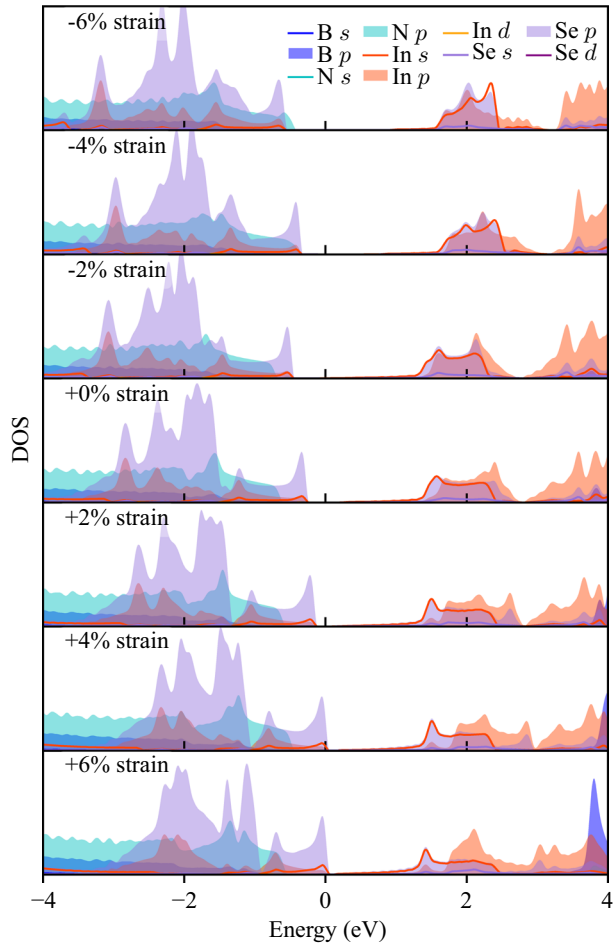
Consistent with our previous research, the optical properties were calculated within the random phase approximation (RPA). We were mostly interested to study how does the strain influence the absorption of heterostructure, and RPA was previously displayed as good performer for qualitative description of optical properties (Jalilian and Safari 2017; Liao et al. 2020; Zólyomi et al. 2014; Shang et al. 2018; Do et al. 2021; Sengupta et al. 2019). The complex dielectric function $\epsilon(\omega) = \epsilon_R(\omega) + i\epsilon_I(\omega)$ is calculated first. From there, we can get the absorption function as follows:

$$\alpha(\omega) = \sqrt{2} \frac{\omega}{c} \sqrt{\epsilon_R^2(\omega) + \epsilon_I^2(\omega)} - \epsilon_I(\omega). \quad (1)$$

Real and imaginary part of dielectric function are presented in Figs. 4 and 5.

In general, both the real and imaginary components of the dielectric function undergo shifts to the right under negative strain and to the left under positive strain, accompanied by alterations in peak amplitudes. However, notable deviations become evident. Under positive strain, specifically at $+4\%$ and beyond, the imaginary part of the dielectric function diverges to infinity at 0 eV. Concurrently, at the same energy, the real part of the dielectric function diverges towards $-\infty$, indicative of a transition towards a metallic character. In

Fig. 3 Projected density of states of hBN/InSe for different strain values. States from different atoms are presented as in legend



the case of z polarization, additional peaks in the imaginary part of $\epsilon(\omega)$ emerge above +4% strain at approximately 0.5 eV, subsequently dropping to zero at 1.25 eV and 3.75 eV. These distinct features in the dielectric response under strain provide valuable insights into the evolving electronic structure and the potential transition towards metallic behaviour.

Building on prior investigations of hBN/InSe (Shen et al. 2022), which showcased exceptional absorption across a broad spectrum comparable to hBN/InTe and hBN/GaTe, our focus turns to manipulating these properties through strain-induced enhancements. Figure 6 presents the absorption profile of the hBN/InSe heterostructure, considering in-plane (xy) and out-of-plane (z) polarizations. The observed behavior is in agreement with our findings in previously studied heterostructures. Our results affirm the outstanding wide-spectrum absorptive capabilities of hBN/InSe, consistent with the reported values in (Shen et al. 2022), where absorption peaks reach up to $8 \times 10^5 \text{ cm}^{-1}$, as well with hBN/In(Ga) Te HSs which showcase similar magnitude. In the xy polarization, compressive strain enhances absorption in the part of UV spectrum (6 eV to 11 eV), while the peak at 15 eV slowly diminishes. Conversely, tensile strain shifts this peak towards the left without losing its amplitude. Notably, tensile strains of +5% and above introduce a small peak in

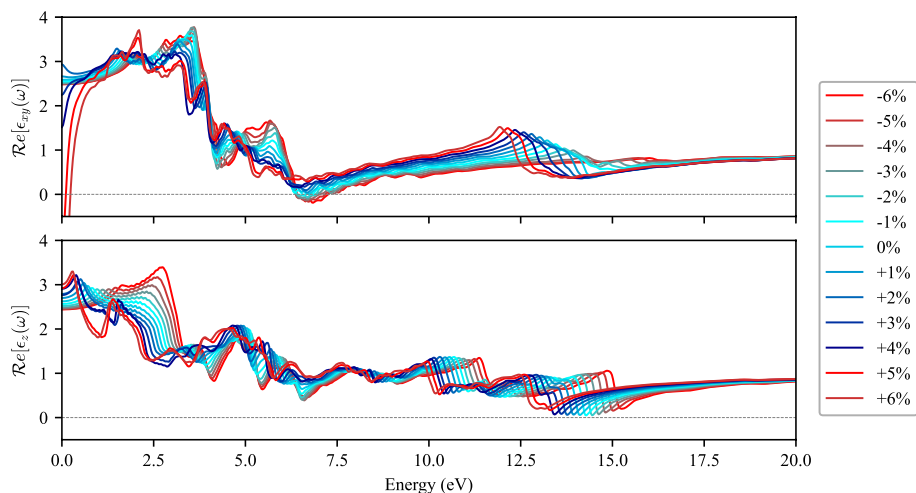


Fig. 4 Real part of complex dielectric function for (a) xy and (b) z polarization, for different values of strain

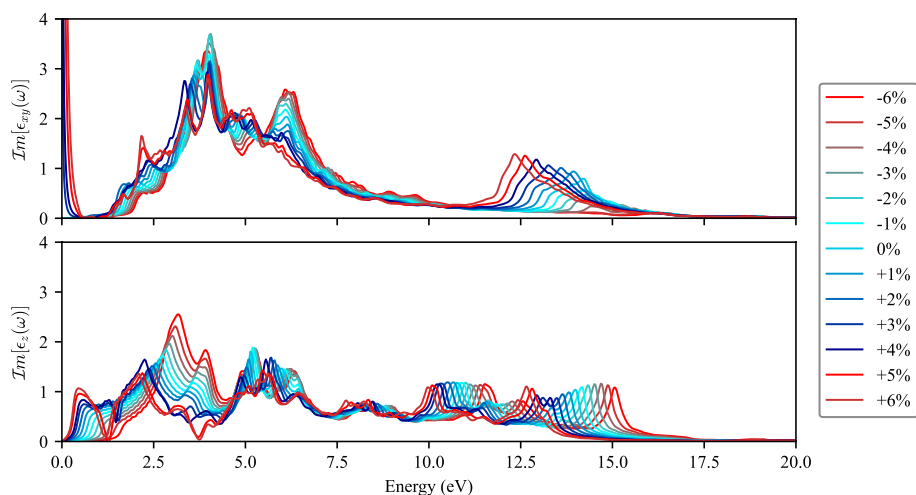


Fig. 5 Imaginary part of complex dielectric function for (a) xy and (b) z polarization, for different values of strain

the IR spectrum and enhance absorption in the visible range. In out-of-plane polarization, tensile strain shifts the absorption function leftward, slightly improving absorption in the visible spectrum, while compressive strains enhance the 2.5 eV to 4.5 eV region. However, stronger tensile strains of 5% and 6% result in a drop to zero absorption at 1.5 eV and 3.8 eV, a feature which is not observed in previously studied HSs. Most of those effects are ascribed to the change in the band gap as a function of strain, but also to different behaviour of specific band and the shape of their valleys, e.g. rising of Np states near the Fermi level at strong compressive strain. These substantial changes in absorption as a function of

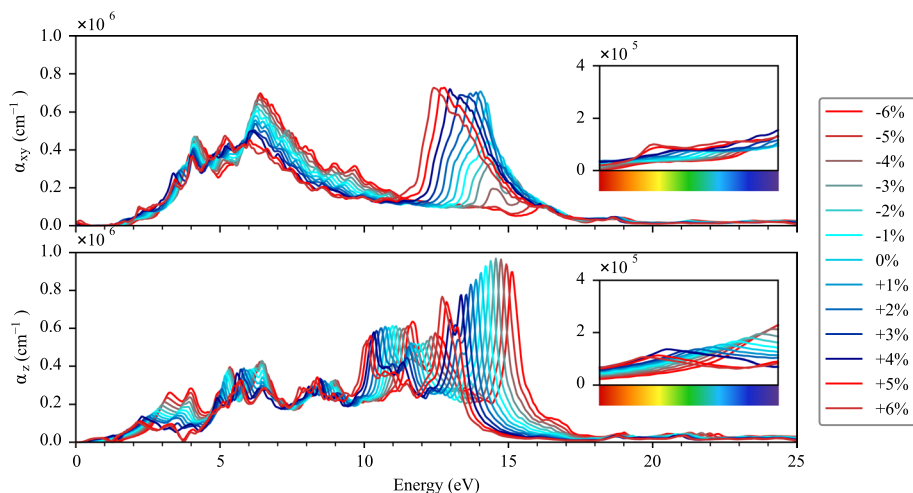


Fig. 6 Absorption function of hBN/InSe for xy and z polarization, for different values of strain. The inset shows the enlarged part within the visible-light part of the spectrum

strain offer a promising avenue for tailoring the properties of hBN/InSe for specific applications, particularly in the development of sensors and detectors.

4 Conclusion

In conclusion, we systematically explored the impact of strain on hBN/InSe heterostructures—an already established exceptional wide-spectrum absorber. Recognized for its promising electronic and mechanical properties, hBN/InSe emerges as a strong contender for future electronic and optoelectronic devices. Applying uniform biaxial strain in the range of -6% to 6% , our results unveil a highly effective method for manipulating the band gap, showcasing a particularly noteworthy outcome: near-complete elimination of the band gap under intense tensile strain. Comparing our findings with previous investigations on strain effects in hBN/InTe and hBN/GaTe heterostructures, hBN/InSe exhibits a striking resemblance to hBN/GaTe. However, the hBN/InSe system demonstrates a distinct trend of reaching lower band gap values under tensile strain, concurrently enhancing absorption in the low-energy spectrum. These outcomes bear considerable significance for guiding subsequent experimental endeavours and serve as a roadmap for more intricate theoretical explorations. With its established outstanding electronic and transport properties, coupled with highly tunable band gap and remarkable absorption characteristics, hBN/InSe stands poised to make a substantial impact on the advancement of future novel devices.

Acknowledgements The authors acknowledge funding provided by the Institute of Physics Belgrade through the grant by the Ministry of Science, Technological Development and Innovations of the Republic of Serbia, and European Cooperation in Science and Technology (COST) Action CA21159 PhoBioS. DFT calculations were performed using computational resources at Johannes Kepler University (Linz, Austria).

Author's contribution AS performed calculations and prepared figures. Both authors wrote and reviewed the manuscript.

Funding The authors acknowledge funding provided by the Institute of Physics Belgrade through the grant by the Ministry of Science, Technological Development and Innovations of the Republic of Serbia.

Data availability Statement The datasets generated during and/or analysed during the current study are available from the corresponding author on request.

Declarations

Conflict of interest The authors have no relevant financial or non-financial interests to disclose.

References

- Aitzhanov, M., Guseinov, N., Nemkayeva, R., Sagidolda, Y., Tolepov, Z., Prikhodko, O., Mukhametkarimov, Y.: Growth and liquid-phase exfoliation of gase1- xss crystals. *Materials* **15**(20), 7080 (2022)
- Bag, A., Lee, N.-E.: Gas sensing with heterostructures based on two-dimensional nanostructured materials: a review. *J. Mater. Chem. C* **7**(43), 13367–13383 (2019)
- Bandurin, D.A., Tyurnina, A.V., Geliang, L.Y., Mishchenko, A., Zólyomi, V., Morozov, S.V., Kumar, R.K., Gorbachev, R.V., Kudrynskyi, Z.R., Pezzini, S.: High electron mobility, quantum hall effect and anomalous optical response in atomically thin inse. *Nat. Nanotechnol* **12**(3), 223–227 (2017)
- Barone, V., Casarin, M., Forrer, D., Pavone, M., Sami, M., Vittadini, A.: Role and effective treatment of dispersive forces in materials: Polyethylene and graphite crystals as test cases. *J. Comput. Chem.* **30**(6), 934–939 (2009)
- Chen, J., Tan, X., Lin, P., Sa, B., Zhou, J., Zhang, Y., Wen, C., Sun, Z.: Comprehensive understanding of intrinsic mobility in the monolayers of iii–vi group 2d materials. *Phys. Chem. Chem. Phys.* **21**(39), 21898–21907 (2019)
- Do, T.-N., Vi, V.T.T., Binh, N.T.T., Hieu, N.N., Hieu, N.V.: Computational study on strain and electric field tunable electronic and optical properties of inte monolayer . *Superlatt. Microstruct.* **151**, 106816 (2021). <https://doi.org/10.1016/j.spmi.2021.106816>
- Feng, W., Zheng, W., Cao, W., Hu, P.: Back gated multilayer inse transistors with enhanced carrier mobilities via the suppression of carrier scattering from a dielectric interface. *Adv. Mater.* **26**(38), 6587–6593 (2014)
- Furchi, M.M., Höller, F., Dobusch, L., Polyushkin, D.K., Schuler, S., Mueller, T.: Device physics of van der waals heterojunction solar cells . *npj 2D Mater. Appl.* **2**(1), 1–7 (2018)
- Geim, A.K., Grigorieva, I.V.: Van der waals heterostructures. *Nature* **499**(7459), 419–425 (2013)
- Giannozzi, P.: Quantum espresso: a modular and open-source software project for quantum simulations of materials. *J. Phys. Condensed Matter* **21**(39), 395502–395519 (2009)
- Grimme, S.: Semiempirical gga-type density functional constructed with a long-range dispersion correction. *J. Comput. Chem.* **27**(15), 1787–1799 (2006)
- Guo, Y., Zhou, S., Bai, Y., Zhao, J.: Defects and oxidation of group-iii monochalcogenide monolayers. *J. Chem. Phys.* **147**(10), 104709 (2017)
- Guo, Y., Zhou, S., Zhao, J.: Oxidation behaviors of two-dimensional metal chalcogenides. *ChemNanoMat* **6**(6), 838–849 (2020)
- Gürbulak, B., Şata, M., Dogan, S., Duman, S., Ashkhasi, A., Keskenler, E.F.: Structural characterizations and optical properties of inse and inse: Ag semiconductors grown by bridgman/stockbarger technique. *Phys. E Low-dimensional Syst. Nanostruct.* **64**, 106–111 (2014)
- Harvey, A., Backes, C., Gholamvand, Z., Hanlon, D., McAteer, D., Nerl, H.C., McGuire, E., Seral-Ascaso, A., Ramasse, Q.M., McEvoy, N.: Preparation of gallium sulfide nanosheets by liquid exfoliation and their application as hydrogen evolution catalysts. *Chem. Mater.* **27**(9), 3483–3493 (2015)
- Hu, P., Wen, Z., Wang, L., Tan, P., Xiao, K.: Synthesis of few-layer gase nanosheets for high performance photodetectors. *ACS Nano* **6**(7), 5988–5994 (2012)
- Hu, T., Zhou, J., Dong, J.: Strain induced new phase and indirect-direct band gap transition of monolayer inse. *Phys. Chem. Chem. Phys.* **19**(32), 21722–21728 (2017)
- Hung, N.T., Nugraha, A.R., Saito, R.: Two-dimensional inse as a potential thermoelectric material. *Appl. Phys. Lett.* **111**(9) (2017)
- Huo, N., Kang, J., Wei, Z., Li, S.-S., Li, J., Wei, S.-H.: Novel and enhanced optoelectronic performances of multilayer mos2-ws2 heterostructure transistors. *Adv. Funct. Mater.* **24**(44), 7025–7031 (2014)
- Jalilian, J., Safari, M.: Electronic and optical properties of α -inx ($x = s, se$ and te) monolayer: Under strain conditions. *Phys. Lett. A* **381**(15), 1313–1320 (2017). <https://doi.org/10.1016/j.physleta.2017.01.024>

- Jie, W., Chen, X., Li, D., Xie, L., Hui, Y.Y., Lau, S.P., Cui, X., Hao, J.: Layer-dependent nonlinear optical properties and stability of non-centrosymmetric modification in few-layer gase sheets. *Angewandte Chemie International Edition* **54**(4), 1185–1189 (2015)
- Kang, P., Michaud-Rioux, V., Kong, X., Yu, G., Guo, H.: Calculated carrier mobility of h-bn/ γ -inse/h-bn van der waals heterostructures. *2D Mater.* **4**(4), 045014 (2017)
- Kim, W., Li, C., Chaves, F.A., Jiménez, D., Rodríguez, R.D., Susoma, J., Fenner, M.A., Lipsanen, H., Riikonen, J.: Tunable graphene-gase dual heterojunction device. *Adv. Mater.* **28**(9), 1845–1852 (2016)
- Lei, S., Ge, L., Liu, Z., Najmaei, S., Shi, G., You, G., Lou, J., Vajtai, R., Ajayan, P.M.: Synthesis and photoresponse of large gase atomic layers. *Nano Lett.* **13**(6), 2777–2781 (2013)
- Lei, S., Ge, L., Najmaei, S., George, A., Kappera, R., Lou, J., Chhowalla, M., Yamaguchi, H., Gupta, G., Vajtai, R.: Evolution of the electronic band structure and efficient photo-detection in atomic layers of inse. *ACS Nano* **8**(2), 1263–1272 (2014)
- Li, Y., Wang, T., Wu, M., Cao, T., Chen, Y., Sankar, R., Ulaganathan, R.K., Chou, F., Wetzel, C., Xu, C.-Y., : Ultrasensitive tunability of the direct bandgap of 2d inse flakes via strain engineering. *2D Mater.* **5**(2), 021002 (2018)
- Li, W., Li, J.: Piezoelectricity in two-dimensional group-iii monochalcogenides. *Nano Res.* **8**, 3796–3802 (2015)
- Li, X., Yin, J., Zhou, J., Guo, W.: Large area hexagonal boron nitride monolayer as efficient atomically thick insulating coating against friction and oxidation. *Nanotechnology* **25**(10), 105701 (2014)
- Liang, S.-J., Cheng, B., Cui, X., Miao, F.: Van der waals heterostructures for high-performance device applications: challenges and opportunities. *Adv. Mater.* **32**(27), 1903800 (2020)
- Liao, Y., Liu, H., Yuan, G., Huang, Z., Qi, X.: Electronic and optical properties of novel graphene-like inte monolayer: first principle calculations. *Crystal Res. Technol.* **55**(12), 2000102 (2020)
- Liu, Z., Gong, Y., Zhou, W., Ma, L., Yu, J., Idrobo, J.C., Jung, J., MacDonald, A.H., Vajtai, R., Lou, J.: Ultrathin high-temperature oxidation-resistant coatings of hexagonal boron nitride. *Nat. Commun.* **4**(1), 2541 (2013)
- Liu, Y., Weiss, N.O., Duan, X., Cheng, H.-C., Huang, Y., Duan, X.: Van der waals heterostructures and devices. *Nat. Rev. Mater.* **1**(9), 1–17 (2016)
- Ma, Y., Dai, Y., Guo, M., Yu, L., Huang, B.: Tunable electronic and dielectric behavior of gas and gase monolayers. *Phys. Chem. Chem. Phys.* **15**(19), 7098–7105 (2013)
- Miao, F., Liang, S.-J., Cheng, B.: Straintronics with van der waals materials. *npj Quant. Mater.* **6**(1), 59 (2021)
- Novoselov, K., Mishchenko, O.A., Carvalho, O.A., Neto, A.C.: 2d materials and van der waals heterostructures. *Science* **353**(6298) (2016)
- Perdew, J.P., Burke, K., Ernzerhof, M.: Generalized gradient approximation made simple. *Phys. Rev. Lett.* **77**, 3865–3868 (1996) <https://doi.org/10.1103/PhysRevLett.77.3865>
- Pham, K.D., Vu-Quang, H., Nguyen, C.V.: Modulation of electronic properties and schottky barrier in the graphene/gase heterostructure by electric gating. *Phys. B Condensed Matter* **555**, 69–73 (2019)
- Politano, A., Campi, D., Cattelan, M., Ben Amara, I., Jaziri, S., Mazzotti, A., Barinov, A., Gürbulak, B., Duman, S., Agnoli, S.: Indium selenide: an insight into electronic band structure and surface excitations. *Sci. Rep.* **7**(1), 3445 (2017)
- Postorino, S., Grassano, D., D'Alessandro, M., Pianetti, A., Pulci, O., Palummo, M.: Strain-induced effects on the electronic properties of 2d materials. *Nanomater. Nanotechnol.* **10**, 1847980420902569 (2020)
- Qi, X., Gao, M., Ding, C., Zhang, W., Qu, R., Guo, Y., Gao, H., Zhang, Z.: Simple exfoliation of bulk gallium selenide to single/few layers by a temperature-adjustment bath-ultrasonic treatment. *Status Solidi (RRL) Rapid Res. Lett.* **15**(8), 2100052 (2021)
- Sang, D.K., Wang, H., Qiu, M., Cao, R., Guo, Z., Zhao, J., Li, Y., Xiao, Q., Fan, D., Zhang, H.: Two dimensional β -inse with layer-dependent properties: band alignment, work function and optical properties. *Nanomaterials* **9**(1), 82 (2019)
- Sengupta, A., Dominguez, A., Frauenheim, T.: Photo-absorption properties of van der waals heterostructure of monolayer inse with silicene, germanene and antimonene. *Appl. Surf. Sci.* **475**, 774–780 (2019). <https://doi.org/10.1016/j.apsusc.2019.01.054>
- Shang, J., Pan, L., Wang, X., Li, J., Deng, H.-X., Wei, Z.: Tunable electronic and optical properties of inse/ inte van der waals heterostructures toward optoelectronic applications. *J. Mater. Chem. C* **6**(27), 7201–7206 (2018)
- Shen, N.-f., Yang, X.-d., Wang, X.-x., Wang, G.-h., Wan, J.-g.: Two-dimensional van der waals heterostructure of indium selenide/hexagonal boron nitride with strong interlayer coupling. *Chem. Phys. Lett.* **749**, 137430 (2020)

- Šiškins, M., Lee, M., Mañas-Valero, S., Coronado, E., Blanter, Y.M., Zant, H.S., Steeneken, P.G.: Magnetic and electronic phase transitions probed by nanomechanical resonators. *Nat. Commun.* **11**(1), 2698 (2020)
- Šolajić, A., Pešić, J.: Tailoring electronic and optical properties of /in te and hbn /gate heterostructures through biaxial strain engineering. PREPRINT (2023). Version 1
- Šolajić, A., Pešić, J.: Novel wide spectrum light absorber heterostructures based on hbn/in (ga) te. *J. Phys. Condensed Matter* **34**(34), 345301 (2022)
- Song, C., Fan, F., Xuan, N., Huang, S., Zhang, G., Wang, C., Sun, Z., Wu, H., Yan, H.: Largely tunable band structures of few-layer in se by uniaxial strain. *ACS Appl. Mater. Interfaces* **10**(4), 3994–4000 (2018)
- Sucharitakul, S., Goble, N.J., Kumar, U.R., Sankar, R., Bogorad, Z.A., Chou, F.-C., Chen, Y.-T., Gao, X.P.: Intrinsic electron mobility exceeding 103 cm²/(v s) in multilayer in se fets. *Nano Lett.* **15**(6), 3815–3819 (2015)
- Tang, X., Wang, H., Liu, C., Zhu, X., Gao, W., Yin, H.: Direct growth of hexagonal boron nitride nanofilms on stainless steel for corrosion protection. *ACS Appl. Nano Mater.* **4**(11), 12024–12033 (2021)
- Wang, H., Qin, G., Yang, J., Qin, Z., Yao, Y., Wang, Q., Hu, M.: First-principles study of electronic, optical and thermal transport properties of group iii–vi monolayer mx (m = ga, in; x = s, se). *J. Appl. Phys.* **125**(24) (2019)
- Wang, Y., Wang, C., Liang, S.-J., Ma, Z., Xu, K., Liu, X., Zhang, L., Admasu, A.S., Cheong, S.-W., Wang, L.: Strain-sensitive magnetization reversal of a van der waals magnet. *Adv. Mater.* **32**(42), 2004533 (2020)
- Webster, L., Yan, J.-A.: Strain-tunable magnetic anisotropy in monolayer CrCl₃, CrBr₃, and CrI₃. *Phys. Rev. B* **98**(14), 144411 (2018)
- Withers, F., Del Pozo-Zamudio, O., Mishchenko, A., Rooney, A., Gholinia, A., Watanabe, K., Taniguchi, T., Haigh, S., Geim, A., Tartakovskii, A.: Light-emitting diodes by band-structure engineering in van der waals heterostructures. *Nat. Mater.* **14**(3), 301–306 (2015)
- Wu, L., Shi, J., Zhou, Z., Yan, J., Wang, A., Bian, C., Ma, J., Ma, R., Liu, H., Chen, J.: In se/hbn/graphite heterostructure for high-performance 2D electronics and flexible electronics. *Nano Res.* **13**, 1127–1132 (2020)
- Xiong, P., Zhang, F., Zhang, X., Wang, S., Liu, H., Sun, B., Zhang, J., Sun, Y., Ma, R., Bando, Y.: Strain engineering of two-dimensional multilayered heterostructures for beyond-lithium-based rechargeable batteries. *Nat. Commun.* **11**(1), 1–12 (2020)
- Yang, Z., Jie, W., Mak, C.-H., Lin, S., Lin, H., Yang, X., Yan, F., Lau, S.P., Hao, J.: Wafer-scale synthesis of high-quality semiconducting two-dimensional layered in se with broadband photoresponse. *ACS Nano* **11**(4), 4225–4236 (2017)
- Yang, Z., Guo, J., Li, H., Du, X., Zhao, Y., Chen, H., Chen, W., Zhang, Y.: Large-scale synthesis of two-dimensional indium telluride films for broadband photodetectors. *Mater. Des.* **233**, 112218 (2023)
- Zhang, W., Shi, C., He, C., Bai, M.: External-strain induced transition from schottky to ohmic contact in graphene/in se and graphene/janus in₂se₂ heterostructures. *J. Solid State Chem.* **289**, 121511 (2020)
- Zhou, W., Cheng, C., Liu, J., Tay, Y.Y., Jiang, J., Jia, X., Zhang, J., Gong, H., Hng, H.H., Yu, T.: Epitaxial growth of branched α -fe₂o₃/sno₂ nano-heterostructures with improved lithium-ion battery performance. *Adv. Funct. Mater.* **21**(13), 2439–2445 (2011)
- Zhou, X., Cheng, J., Zhou, Y., Cao, T., Hong, H., Liao, Z., Wu, S., Peng, H., Liu, K., Yu, D.: Strong second-harmonic generation in atomic layered gase. *J. Am. Chem. Soc.* **137**(25), 7994–7997 (2015)
- Zhuang, H.L., Hennig, R.G.: Single-layer group-iii monochalcogenide photocatalysts for water splitting. *Chem. Mater.* **25**(15), 3232–3238 (2013)
- Zhuang, H.L., Kent, P., Hennig, R.G.: Strong anisotropy and magnetostriction in the two-dimensional stoner ferromagnet fe₃ gete₂. *Phys. Rev. B* **93**(13), 134407 (2016)
- Zólyomi, V., Drummond, N.D.: Fal'ko, V.I.: Electrons and phonons in single layers of hexagonal indium chalcogenides from ab initio calculations. *Phys. Rev. B* **89**, 205416 (2014). <https://doi.org/10.1103/PhysRevB.89.205416>

Publisher's Note Springer Nature remains neutral with regard to jurisdictional claims in published maps and institutional affiliations.

Springer Nature or its licensor (e.g. a society or other partner) holds exclusive rights to this article under a publishing agreement with the author(s) or other rightsholder(s); author self-archiving of the accepted manuscript version of this article is solely governed by the terms of such publishing agreement and applicable law.

Spin-phonon interaction and short-range order in $\text{Mn}_3\text{Si}_2\text{Te}_6$

S. Djurdjić Mijin,¹ A. Šolajić,¹ J. Pešić^{1,*}, Y. Liu^{2,†}, C. Petrovic², M. Bockstedte,³ A. Bonanni,⁴
Z. V. Popović,^{1,5} and N. Lazarević¹

¹*Institute of Physics Belgrade, University of Belgrade, Pregrevica 118, 11080 Belgrade, Serbia*

²*Condensed Matter Physics and Materials Science Department, Brookhaven National Laboratory, Upton, New York 11973-5000, USA*

³*Institute for Theoretical Physics, Johannes Kepler University Linz, Altenbergerstrasse 69, 4040 Linz, Austria*

⁴*Institute of Semiconductor and Solid-State Physics, Johannes Kepler University Linz, Altenbergerstrasse 69, 4040 Linz, Austria*

⁵*Serbian Academy of Sciences and Arts, Knez Mihailova 35, 11000 Belgrade, Serbia*



(Received 7 September 2022; revised 31 January 2023; accepted 3 February 2023; published 21 February 2023)

The vibrational properties of ferrimagnetic $\text{Mn}_3\text{Si}_2\text{Te}_6$ single crystals are investigated using Raman spectroscopy and density functional theory calculations. Eighteen Raman-active modes are identified, 14 of which are assigned according to the trigonal symmetry. Four additional peaks, obeying the A_{1g} selection rules, are attributed to the overtones. The unconventional temperature evolution of the A_{1g}^5 mode self-energy suggests a competition between different short-range magnetic correlations that significantly impact the spin-phonon interaction in $\text{Mn}_3\text{Si}_2\text{Te}_6$. The research provides comprehensive insight into the lattice properties, studies their temperature dependence, and shows arguments for the existence of competing short-range magnetic phases in $\text{Mn}_3\text{Si}_2\text{Te}_6$.

DOI: [10.1103/PhysRevB.107.054309](https://doi.org/10.1103/PhysRevB.107.054309)

I. INTRODUCTION

Layered magnetic van der Waals materials have lately received widespread attention due to their potential application in spintronics, magnetoelectronics, data storage, and biomedicine [1–7]. Recent experimental confirmation of a long-range magnetism persisting down to a monolayer in CrI_3 [8] further affirmed these materials as a platform for magneto-optoelectronic devices [9], and as candidates for studying low-dimensional magnetism [10].

$\text{Mn}_3\text{Si}_2\text{Te}_6$ single crystals were first synthesized in 1985 [11]. However, few studies were carried out on this compound since. It was only recently that the attention has shifted to them, mainly through comparisons with quasi-two-dimensional materials, specifically CrSiTe_3 . The vast majority of recent studies were focused on explaining the magnetism in $\text{Mn}_3\text{Si}_2\text{Te}_6$ and determining its crystal structure. It was revealed that $\text{Mn}_3\text{Si}_2\text{Te}_6$ crystallizes in a trigonal structure described by the $P\bar{3}1c$ (No. 163) space group [11,12]. According to various magnetization studies, $\text{Mn}_3\text{Si}_2\text{Te}_6$ is an insulating ferrimagnetic with Curie temperature T_c between 74 and 78 K [12–15]. First-principles calculations suggested a competition between the ferrimagnetic ground state and three additional magnetic configurations, originating from the antiferromagnetic exchange for the three nearest Mn-Mn pairs [15]. Additionally, both magnetization and diffuse neutron scattering experiments point at the existence of strong spin correlations well above T_c , which may be associated with

short-range order or to the preserved correlated excitations in the paramagnetic region [12,15].

Here, we present an experimental and theoretical Raman scattering study of $\text{Mn}_3\text{Si}_2\text{Te}_6$ single crystals, with the focus on phonon properties in the temperature range from 80 to 320 K. Out of 18 observed modes, 14 ($5A_{1g} + 9E_g$) are identified and assigned in agreement with the $P\bar{3}1c$ space group. Phonon energies are in a good agreement with the theoretical predictions. Two most prominent Raman modes, A_{1g}^4 and A_{1g}^5 , are used to study the temperature evolution of phonon properties, and reveal three subsequent phase transitions at $T_1 = 142.5$ K, $T_2 = 190$ K, and $T_3 = 285$ K. Furthermore, the A_{1g}^5 mode exhibits strong asymmetry, most likely originating from enhanced spin-phonon coupling. Interestingly, the A_{1g}^5 phonon line is symmetric in the temperature range T_1 – T_2 , while becoming more asymmetric above T_3 , potentially indicating that the strength of spin-phonon interaction changes with temperature. We speculate that the observed phenomenon, shown in the A_{1g}^5 phonon, originates from the shift in dominance between competing magnetic states, that are found to be very close in energy [15].

II. EXPERIMENTAL AND COMPUTATIONAL DETAILS

The $\text{Mn}_3\text{Si}_2\text{Te}_6$ single-crystal samples used in this study are prepared according to the procedure described in Ref. [12]. The Raman spectra have been obtained with a Tri Vista 557 spectrometer (Teledyne Princeton Instruments, Trenton, NJ, USA) with a 1800/1800/2400 grooves/mm diffraction grating combination in a backscattering configuration. The 514-nm line of a Coherent Ar^+/Kr^+ ion laser (Coherent, Santa Clara, CA, USA) is utilized as the excitation source. The direction of the incident (scattered) light coincides with

*Corresponding author: jelena.pesic@ipb.ac.rs

†Present address: Los Alamos National Laboratory, Los Alamos, New Mexico 87545, USA.

TABLE I. Wyckoff positions of atoms and their contributions to the Γ -point phonons together with the corresponding Raman tensors for the $P\bar{3}1c$ space group of $\text{Mn}_3\text{Si}_2\text{Te}_6$.

Space group: $P\bar{3}1c$	
Atoms	Irreducible representations
Mn ($2c$)	$A_{2g} + A_{2u} + E_g + E_u$
Mn ($4f$)	$A_{1g} + A_{1u} + A_{2g} + A_{2u} + 2E_g + 2E_u$
Si ($4e$)	$A_{1g} + A_{1u} + A_{2g} + A_{2u} + 2E_g + 2E_u$
Te ($12i$)	$3A_{1g} + 3A_{1u} + 3A_{2g} + 3A_{2u} + 6E_g + 6E_u$
Raman tensors	
$A_{1g} = \begin{pmatrix} a & & \\ & a & \\ & & b \end{pmatrix}$	
${}^1E_g = \begin{pmatrix} c & & \\ & -c & d \\ & d & \end{pmatrix}$	${}^2E_g = \begin{pmatrix} & & \\ & -c & -d \\ d & & \end{pmatrix}$

the crystallographic c axis. Laser-beam focusing is achieved through a microscope objective with $50\times$ magnification. The temperature-dependent Raman scattering measurements have been performed under high vacuum (10^{-6} mbar), with the sample being placed inside of a KONTI CryoVac continuous helium flow cryostat (CryoVac GmbH & Co. KG, Troisdorf, Germany) with a 0.5-mm-thick window. The samples are cleaved in air before being placed into the cryostat. The obtained Raman spectra are corrected by a Bose factor. The spectrometer resolution is comparable to a Gaussian width of 1 cm^{-1} .

The calculations are based on the density functional theory (DFT) formalism as implemented in the Vienna *ab initio* simulation package (VASP) [16–19], with the plane-wave basis truncated at a kinetic energy of 520 eV, using the Perdew-Burke-Ernzerhof (PBE) exchange-correlation functional [20] and projector augmented-wave (PAW) method [19,21]. The Monkhorst and Pack scheme of k -point sampling is employed to integrate over the first Brillouin zone with $12 \times 12 \times 10$ at the Γ -centered grid. The convergence criteria for energy and force have been set to 10^{-6} eV and 0.001 eV \AA^{-1} , respectively. The DFT-D2 method of Grimme is employed for van der Waals (vdW) corrections [22]. The vibrational modes are calculated using density functional perturbation theory implemented in VASP and PHONOPY [23]. Previous DFT results found the energy of the ferrimagnetic state to be well above an eV per Mn below that of the nonmagnetic state [15], thus this configuration is considered in this study.

III. RESULTS AND DISCUSSION

A. Polarization measurements

$\text{Mn}_3\text{Si}_2\text{Te}_6$ crystallizes in a trigonal $P\bar{3}1c$ crystal structure [11,12]. The Wyckoff positions of the atoms and their contributions to the Γ -point phonons, together with the corresponding Raman tensors, are listed in Table I. In total, there are 16 Raman-active modes ($5A_{1g} + 11E_g$) and 17 infrared-active modes ($6A_{2u} + 11E_u$). According to the Raman tensors presented in Table I, in our scattering configuration and with

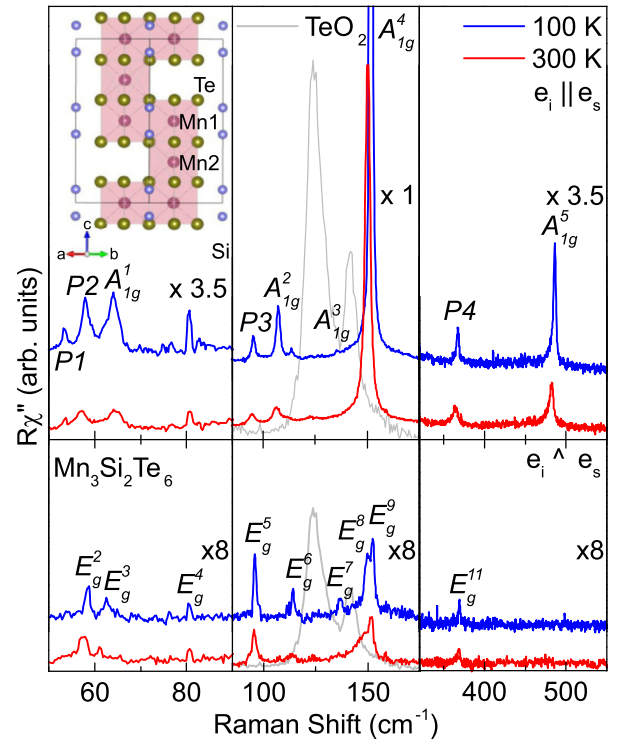


FIG. 1. Raman spectra of $\text{Mn}_3\text{Si}_2\text{Te}_6$ single crystal measured in two scattering geometries at $T = 100\text{ K}$ (blue solid line) and $T = 300\text{ K}$ (red solid lines) with incident light being directed along $[100]$. Peaks observed in both geometries are identified as E_g modes, whereas peaks observed only for the parallel polarization configuration are assigned as A_{1g} modes. Gray line: TeO_2 spectrum at 300 K , scaled for clarity. The crystal structure of $\text{Mn}_3\text{Si}_2\text{Te}_6$ viewed laterally along the c axis is presented in the inset.

Raman scattering events within the crystallographic ab plane, E_g symmetry modes can be observed in the Raman spectra measured in both parallel and crossed polarization configurations, whereas A_{1g} modes arise only for those in parallel polarization configuration.

As depicted in Fig. 1, nine phonon lines are observed in a parallel polarization configuration only, and identified as A_{1g} symmetry modes. According to the symmetry analysis only five A_{1g} symmetry modes are expected, resulting in four excess modes at 53.3 , 57.9 , 95.3 , and 366.7 cm^{-1} . These modes may arise from infrared/silent phonons activated by disorder and from the relaxation of the symmetry selection rules [24–27]. However, it is more likely they are overtones. Overtones, which are always observable in A symmetries, but can also be observed in other symmetries, can become observable in Raman spectra due to disorder and/or enhanced coupling of the phonons to other excitations such as in the case of spin-phonon coupling [28].

Aside from the discussed A_{1g} symmetry modes, our spectra host nine modes which obey the E_g selection rules. Therefore, nine out of the expected 11 E_g modes have been singled out and identified. The absence of two E_g modes might be attributed to their low intensity and/or the finite resolution of the spectrometer.

Calculated and experimental phonon energies are collected in Table II, and are found to be in good agreement with each

TABLE II. Phonon symmetries and phonon frequencies of $\text{Mn}_3\text{Si}_2\text{Te}_6$ phonons. The experimental values are determined at 100 K. All calculations have been performed at zero 0 K. The experimental uncertainty is 0.3 cm^{-1} .

Space group $P\bar{3}1c$			
n_0	Symm.	Expt. (cm^{-1})	Calc. (cm^{-1})
1	E_g^1		53.1
2	$P1$	53.3	
3	$P2$	57.9	
4	E_g^2	58.7	58.5
5	E_g^3	62.6	61.8
6	A_{1g}^1	64.2	62.3
7	E_g^4	80.4	82.7
8	$P3$	95.3	
9	E_g^5	95.9	90.3
10	A_{1g}^2	107.3	104.3
11	E_g^6	114.0	106.5
12	A_{1g}^3	135.4	134.2
13	E_g^7	136.6	136.1
14	E_g^8	149.8	143.4
15	A_{1g}^4	151.8	147.3
16	E_g^9	152.6	146.6
17	E_g^{10}		352.7
18	$P4$	366.7	
19	E_g^{11}	368.7	354.5
20	A_{1g}^5	486.7	475.8

other, with the discrepancy being below 8% for all observed modes.

Our data significantly differ from those presented in Ref. [14] where two Raman-active modes were reported, one at 118.4 cm^{-1} and the other at 136.9 cm^{-1} , assigned as E_g and A_{1g} , respectively. The E_g and A_{1g} modes in our spectra closest (in terms of energy) to those reported in Ref. [14] are the peaks at ~ 114.3 and 135.4 cm^{-1} (Table II). Although the discrepancy in phonon energy is not significant, the observed phonon linewidths strongly deviate from those presented in Ref. [14]. A possible explanation for the discrepancy is the presence of TeO_2 in samples presented in Ref. [14], as the peaks reported there match rather well with the Raman response of TeO_2 (Fig. 1). In order to avoid potential contamination in our study, measurements have been repeated on multiple crystals, and no oxide traces have been identified in the spectra.

B. Temperature dependence

Some of the modes represented in Fig. 1 exhibit an asymmetric line shape. Although the appearance of a mode asymmetry can be attributed to the presence of defects [29], this would have a significant impact also on the linewidths of other modes in the spectrum, which is not the case here. The asymmetry may arise from coupling between the phonon and other elementary excitations [30–32]. The line shape originating from such a coupling is given by the Fano

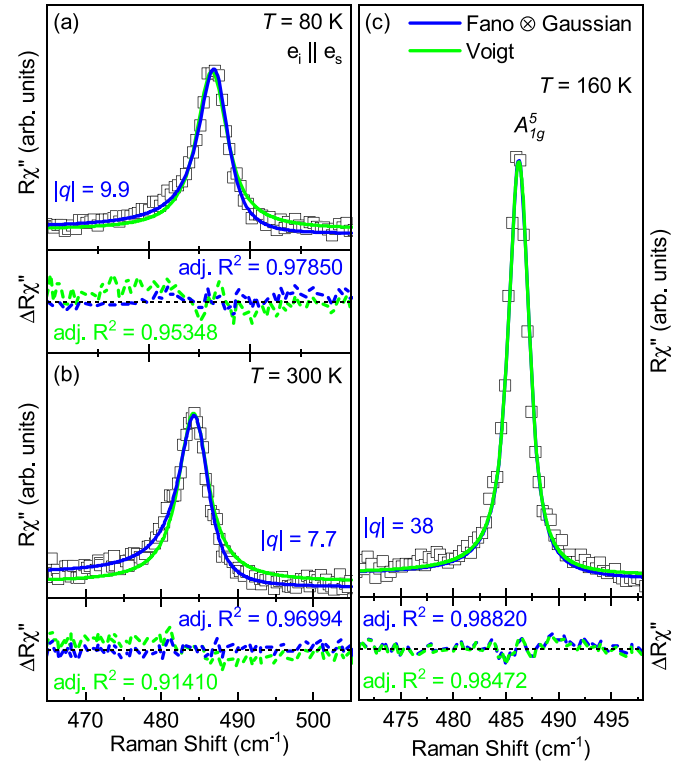


FIG. 2. Raman response as a function of the Raman shift. Quantitative analysis of the A_{1g}^5 mode at temperatures as indicated. (a) and (b) The blue solid lines represent the line shape obtained as a convolution of Fano profiles and Gaussian, whereas the green solid lines represent Voigt profiles. (c) Comparison between asymmetric (deep blue) and symmetric (light blue) line shapes obtained as a Fano-Gaussian convolution and a Voigt profile. Experimental data are represented by open squares.

profile [33–36]

$$I(\omega) = I_0 \frac{(q + \epsilon)^2}{1 + \epsilon^2},$$

where $\epsilon(\omega) = 2(\omega - \omega_0)/\Gamma$. Here, ω_0 is the phonon frequency in the absence of interaction, Γ is the full width at half maximum (FWHM), I_0 is the amplitude, and q is the Fano parameter. The Fano parameter and FWHM depend on the interaction strength between the phonon and the elementary excitation, and therefore can be used as its indicator. To include the finite spectral resolution of the experimental setup, the Fano profile is convoluted with a Gaussian function as demonstrated in Ref. [28].

The high-intensity peak at 486.7 cm^{-1} , identified as the A_{1g}^5 symmetry mode, does not overlap with any other mode. The quantitative analysis of this peak is performed using both the symmetric Voigt profile and the Fano-Gaussian convolution mentioned above. The comparison between the two models and the experimental data at 80 and 300 K are presented in Figs. 2(a) and 2(b), respectively. The asymmetric line shapes provide a satisfactory description of the measured phonon line shape, suggesting the presence of an additional scattering mechanism in $\text{Mn}_3\text{Si}_2\text{Te}_6$.

The spectral region of the A_{1g}^5 Raman-active mode in the temperature range of interest is presented in Fig. 3(a). The

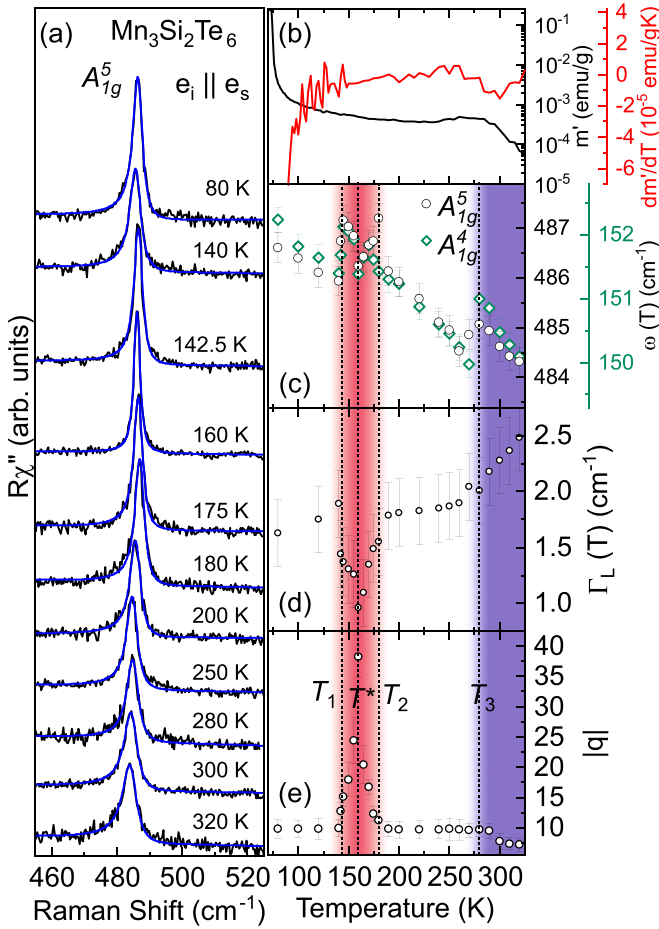


FIG. 3. (a) The spectral region of the A_{1g}^5 Raman-active mode of $Mn_3Si_2Te_6$ at indicated temperatures measured in the parallel polarization configuration. Green solid lines represent line shapes obtained as a convolution of the Fano line shape and Gaussian, calculated to fit the experimental data. (b) Temperature dependence of ac susceptibility real part $m'(T)$ and its temperature derivative plotted as a function of temperature with $\mathbf{H} \parallel \mathbf{ab}$. Temperature dependence of (c) the energy of the A_{1g}^4 and A_{1g}^5 as well as (d) the linewidth, and (e) the Fano parameter $|q|$ of the A_{1g}^5 mode.

blue solid lines represent fits to the experimental data obtained using the Fano-Gaussian line shape. The temperature dependence of the phonon energy, linewidth, and the Fano parameter $|q|$ of the A_{1g}^5 mode are depicted in Figs. 3(c)–3(e), respectively. By increasing the temperature above 80 K, the A_{1g}^5 mode broadens and softens up to $T_1 = 142.5$ K, where it abruptly narrows and shifts to higher energies followed by further softening and narrowing up to $T^* = 160$ K. Additional heating leads to a broadening and hardening before the drop in phonon energy at $\sim T_2 = 190$ K. In the region T_2 the mode softens and broadens with an additional jump in phonon energy at $T_3 = 285$ K. A similar trend is also observed for the A_{1g}^4 mode, as evidenced in Fig. 3(b).

This intriguing temperature dependence is also manifested in the asymmetry, i.e., the Fano parameter $|q|$ [Fig. 3(d)] of the A_{1g}^5 peak. At the lowest experimental temperature, 80 K, the A_{1g}^5 mode exhibits strong asymmetry with a Fano parameter $|q| = 9.9$. Upon heating the sample to $\sim T_1$ a Fano parameter

remains nearly constant before the significant increase in the temperature range between T_1 and T^* resulting in a symmetric line shape [$|q| = 38$, Fig. 3(c)]. A further temperature increase leads to a strong decrease of $|q|$ up to T_2 , where the asymmetry is restored ($|q| = 9.9$), remaining almost constant up to T_3 . At higher temperatures, the line shape becomes more asymmetric, reaching $|q| \sim 8$ at the highest experimentally accessible temperature $T = 320$ K.

While the ferrimagnetic order in $Mn_3Si_2Te_6$ is established only at $T_c = 78$ K [12,14], the asymmetry of the mode can be observed at all experimental temperatures. Based on the research done on $Mn_3Si_2Te_6$ and related materials, the most probable scenario is the one in which the observed asymmetry can be traced to an enhanced spin-phonon interaction related to short-range correlations, that can survive up to temperatures well above T_c [24,37–39]. We may speculate, according to the results presented in Ref. [15], that these short-range correlations are likely in terms of the antiferromagnetic exchange interaction between the three nearest Mn-Mn pairs (as depicted in Fig. 1) in the paramagnetic background. However, this alone cannot explain sudden changes in the properties of the A_{1g}^5 phonon mode. Rather, the existence of competing short-range magnetic phases may be responsible for the observed behavior of the phonon modes. The first phonon mode anomaly at $T_3 = 285$ K corresponds to the anomaly in $m'(T)_{ab}$ [Fig. 3(b)] and can be seen as the outlet of additional short-range order in the paramagnetic domains [40] and possibly change of their nature of previously established ones. The onset in temperature with the magnetization anomaly near 330 K [14,41] is likely the consequence of local disorder. At T_2 , $Mn_3Si_2Te_6$ becomes locally magnetically frustrated, resulting in the change in magnetostriction and a rapid decrease of the spin-phonon interaction that is manifested in the strong evolution of the phonon self-energy (Fig. 3). At this temperature both the magnetoresistance and nonlinearity of Hall resistance become observable [41]. In this scenario, by further lowering the temperature, at T_1 a new short-range magnetic order and the strong spin-phonon interaction are established. The new magnetic order is most likely antiferromagnetic [15]. In order to fully understand the complex evolution of the short-range magnetic correlation in $Mn_3Si_2Te_6$ that is manifested through the anomalous temperature development of the A_{1g}^5 mode, further investigations are required.

IV. CONCLUSION

The lattice dynamic in single-crystalline $Mn_3Si_2Te_6$ using Raman spectroscopy is analyzed. Five A_{1g} modes and nine E_g modes are observed and assigned according to the $P\bar{3}1c$ symmetry group. Four additional peaks to the ones assigned to the $P\bar{3}1c$ symmetry group, obeying A_{1g} selection rules, are attributed to overtones. There is a pronounced asymmetry of the A_{1g}^5 phonon mode at 100 and 300 K. The unconventional temperature evolution of the A_{1g}^5 Raman mode reveals three successive, possibly magnetic, phase transitions that may significantly impact the strength of the spin-phonon interaction in $Mn_3Si_2Te_6$. These are likely caused by the competition between the various magnetic states, close in energy. This paper provides comprehensive insight into the lattice properties, their temperature dependence, and shows arguments

for the existence of competing short-range magnetic phases in $\text{Mn}_3\text{Si}_2\text{Te}_6$.

ACKNOWLEDGMENTS

The authors acknowledge funding provided by the Institute of Physics Belgrade, through a grant from the Ministry of Science, Technological Development and Innovations of the Republic of Serbia, the Serbian Academy of Sciences and Arts - Project No. F-134, the Science Fund of the Republic of

Serbia, PROMIS, 6062656, StrainedFeSC, Austrian Science Fund (FWF) through Project No. P31423, and the support of Austrian Academy of Sciences' Joint Excellence in Science and Humanities (JESH) Program (J.P.). DFT calculations were performed using computational resources at Johannes Kepler University (Linz, Austria). Materials synthesis was supported by the U.S. DOE-BES, Division of Materials Science and Engineering, under Contract No. DE-SC0012704 (BNL). The authors would like to thank Dr. Rudi Hackl for useful discussions that contributed to the finalized version of the manuscript.

- [1] Z. Guguchia, Unconventional magnetism in layered transition metal dichalcogenides, *Condensed Matter* **5**, 42 (2020).
- [2] Q. H. Wang, K. Kalantar-Zadeh, A. Kis, J. N. Coleman, and M. S. Strano, Electronics and optoelectronics of two-dimensional transition metal dichalcogenides, *Nat. Nanotechnol.* **7**, 699 (2012).
- [3] W. Han, R. K. Kawakami, M. Gmitra, and J. Fabian, Graphene spintronics, *Nat. Nanotechnol.* **9**, 794 (2014).
- [4] W. Zhang, R. Mazzarello, M. Wuttig, and E. Ma, Designing crystallization in phase-change materials for universal memory and neuro-inspired computing, *Nat. Rev. Mater.* **4**, 150 (2019).
- [5] C. Zhu, G. Yang, H. Li, D. Du, and Y. Lin, Electrochemical sensors and biosensors based on nanomaterials and nanostructures, *Anal. Chem.* **87**, 230 (2015).
- [6] X. J. Zhou, Magnetism in medicine: A handbook, second completely revised and enlarged edition, *Med. Phys.* **34**, 4978 (2007).
- [7] Q. H. Wang, A. Bedoya-Pinto, M. Blei, A. H. Dismukes, A. Hamo, S. Jenkins, M. Koperski, Y. Liu, Q.-C. Sun, E. J. Telford, H. H. Kim, M. Augustin, U. Vool, J.-X. Yin, L. H. Li, A. Falin, C. R. Dean, F. Casanova, R. F. L. Evans, M. Chshiev *et al.*, The magnetic genome of two-dimensional van der Waals materials, *ACS Nano* **16**, 6960 (2022).
- [8] B. Huang, G. Clark, E. Navarro-Moratalla, D. R. Klein, R. Cheng, K. L. Seyler, D. Zhong, E. Schmidgall, M. A. McGuire, D. Cobden, W. Yao, D. Xiao, P. Jarillo-Herrero, and X. Xu, Layer-dependent ferromagnetism in a van der Waals crystal down to the monolayer limit, *Nature (London)* **546**, 270 (2017).
- [9] S. Jiang, L. Li, Z. Wang, K. F. Mak, and J. Shan, Controlling magnetism in 2D CrI_3 by electrostatic doping, *Nat. Nanotechnol.* **13**, 549 (2018).
- [10] N. Sethulakshmi, A. Mishra, P. Ajayan, Y. Kawazoe, A. K. Roy, A. K. Singh, and C. S. Tiwary, Magnetism in two-dimensional materials beyond graphene, *Mater. Today* **27**, 107 (2019).
- [11] H. Vincent, D. Leroux, and D. Bijaoui, Crystal structure of $\text{Mn}_3\text{Si}_2\text{Te}_6$, *J. Solid State Chem.* **63**, 349 (1986).
- [12] Y. Liu and C. Petrovic, Critical behavior and magnetocaloric effect in $\text{Mn}_3\text{Si}_2\text{Te}_6$, *Phys. Rev. B* **98**, 064423 (2018).
- [13] R. Rimet, C. Schlenker, and H. Vincent, A new semiconducting ferrimagnet: A silicon manganese telluride, *J. Magn. Magn. Mater.* **25**, 7 (1981).
- [14] L. M. Martinez, H. Iturriaga, R. Olmos, L. Shao, Y. Liu, T. T. Mai, C. Petrovic, A. R. Hight Walker, and S. R. Singamaneni, Enhanced magnetization in proton irradiated $\text{Mn}_3\text{Si}_2\text{Te}_6$ van der Waals crystals, *Appl. Phys. Lett.* **116**, 172404 (2020).
- [15] A. F. May, Y. Liu, S. Calder, D. S. Parker, T. Pandey, E. Cakmak, H. Cao, J. Yan, and M. A. McGuire, Magnetic order and interactions in ferrimagnetic $\text{Mn}_3\text{Si}_2\text{Te}_6$, *Phys. Rev. B* **95**, 174440 (2017).
- [16] G. Kresse and J. Hafner, *Ab initio* molecular dynamics for liquid metals, *Phys. Rev. B* **47**, 558 (1993).
- [17] G. Kresse and J. Furthmüller, Efficiency of ab-initio total energy calculations for metals and semiconductors using a plane-wave basis set, *Comput. Mater. Sci.* **6**, 15 (1996).
- [18] G. Kresse and J. Furthmüller, Efficient iterative schemes for *ab initio* total-energy calculations using a plane-wave basis set, *Phys. Rev. B* **54**, 11169 (1996).
- [19] G. Kresse and D. Joubert, From ultrasoft pseudopotentials to the projector augmented-wave method, *Phys. Rev. B* **59**, 1758 (1999).
- [20] J. P. Perdew, K. Burke, and M. Ernzerhof, Generalized Gradient Approximation Made Simple, *Phys. Rev. Lett.* **77**, 3865 (1996).
- [21] P. E. Blöchl, Projector augmented-wave method, *Phys. Rev. B* **50**, 17953 (1994).
- [22] S. Grimme, Semiempirical GGA-type density functional constructed with a long-range dispersion correction, *J. Comput. Chem.* **27**, 1787 (2006).
- [23] A. Togo and I. Tanaka, First principles phonon calculations in materials science, *Scr. Mater.* **108**, 1 (2015).
- [24] F. Jin, N. Lazarević, C. Liu, J. Ji, Y. Wang, S. He, H. Lei, C. Petrovic, R. Yu, Z. V. Popović, and Q. Zhang, Phonon anomalies and magnetic excitations in $\text{BaFe}_2\text{Se}_2\text{O}$, *Phys. Rev. B* **99**, 144419 (2019).
- [25] M. Moskovits and D. Dilella, Surface-enhanced Raman spectroscopy of benzene and benzene- d_6 adsorbed on silver, *J. Chem. Phys.* **73**, 6068 (1980).
- [26] A. Dubroka, J. Humlíček, M. V. Abrashev, Z. V. Popović, F. Sapiña, and A. Cantarero, Raman and infrared studies of $\text{La}_{1-y}\text{Sr}_y\text{Mn}_{1-x}\text{M}_x\text{O}_3$ ($M = \text{Cr, Co, Cu, Zn, Sc, or Ga}$): Oxygen disorder and local vibrational modes, *Phys. Rev. B* **73**, 224401 (2006).
- [27] A. G. Souza Filho, J. L. B. Faria, I. Guedes, J. M. Sasaki, P. T. C. Freire, V. N. Freire, J. Mendes Filho, M. M. Xavier, F. A. O. Cabral, J. H. de Araújo, and J. A. P. da Costa, Evidence of magnetic polaronic states in $\text{La}_{0.70}\text{Sr}_{0.30}\text{Mn}_{1-x}\text{Fe}_x\text{O}_3$ manganites, *Phys. Rev. B* **67**, 052405 (2003).
- [28] A. Baum, A. Milosavljević, N. Lazarević, M. M. Radonjić, B. Nikolić, M. Mitschek, Z. I. Maranloo, M. Šćepanović, M. Grujić-Brojčin, N. Stojilović, M. Opel, A. Wang, C. Petrovic,

- Z. V. Popović, and R. Hackl, Phonon anomalies in FeS, *Phys. Rev. B* **97**, 054306 (2018).
- [29] N. Lazarević, M. Radonjić, M. Šćepanović, H. Lei, D. Tanasković, C. Petrovic, and Z. V. Popović, Lattice dynamics of KNi_2Se_2 , *Phys. Rev. B* **87**, 144305 (2013).
- [30] M. Balkanski, K. P. Jain, R. Beserman, and M. Jouanne, Theory of interference distortion of Raman scattering line shapes in semiconductors, *Phys. Rev. B* **12**, 4328 (1975).
- [31] D. Olego and M. Cardona, Self-energy effects of the optical phonons of heavily doped p -GaAs and p -Ge, *Phys. Rev. B* **23**, 6592 (1981).
- [32] E. H. Hasdeo, A. R. T. Nugraha, M. S. Dresselhaus, and R. Saito, Breit-Wigner-Fano line shapes in Raman spectra of graphene, *Phys. Rev. B* **90**, 245140 (2014).
- [33] U. Fano, Effects of configuration interaction on intensities and phase shifts, *Phys. Rev.* **124**, 1866 (1961).
- [34] P. H. M. van Loosdrecht, J. P. Boucher, G. Martinez, G. Dhalenne, and A. Revcolevschi, Inelastic Light Scattering from Magnetic Fluctuations in CuGeO_3 , *Phys. Rev. Lett.* **76**, 311 (1996).
- [35] M. Braden, B. Hennion, W. Reichardt, G. Dhalenne, and A. Revcolevschi, Spin-Phonon Coupling in CuGeO_3 , *Phys. Rev. Lett.* **80**, 3634 (1998).
- [36] J. W. Ager, W. Walukiewicz, M. McCluskey, M. A. Plano, and M. I. Landstrass, Fano interference of the Raman phonon in heavily boron-doped diamond films grown by chemical vapor deposition, *Appl. Phys. Lett.* **66**, 616 (1995).
- [37] S. Djurdjić Mijin, A. M. M. Abeykoon, A. Šolajić, A. Milosavljević, J. Pešić, Y. Liu, C. Petrovic, Z. V. Popović, and N. Lazarević, Short-range order in VI_3 , *Inorg. Chem.* **59**, 16265 (2020).
- [38] L. J. Sandilands, Y. Tian, K. W. Plumb, Y.-J. Kim, and K. S. Burch, Scattering Continuum and Possible Fractionalized Excitations in α - RuCl_3 , *Phys. Rev. Lett.* **114**, 147201 (2015).
- [39] A. Milosavljević, A. Šolajić, J. Pešić, Y. Liu, C. Petrovic, N. Lazarević, and Z. V. Popović, Evidence of spin-phonon coupling in CrSiTe_3 , *Phys. Rev. B* **98**, 104306 (2018).
- [40] Y. Liu, Z. Hu, M. Abeykoon, E. Stavitski, K. Attenkofer, E. D. Bauer, and C. Petrovic, Polaronic transport and thermoelectricity in $\text{Mn}_3\text{Si}_2\text{Te}_6$ single crystals, *Phys. Rev. B* **103**, 245122 (2021).
- [41] Y. Ni, H. Zhao, Y. Zhang, B. Hu, I. Kimchi, and G. Cao, Colossal magnetoresistance via avoiding fully polarized magnetization in the ferrimagnetic insulator $\text{Mn}_3\text{Si}_2\text{Te}_6$, *Phys. Rev. B* **103**, L161105 (2021).

PAPER

Novel wide spectrum light absorber heterostructures based on hBN/In(Ga)Te

To cite this article: A Šolajić and J Pešić 2022 *J. Phys.: Condens. Matter* **34** 345301

View the [article online](#) for updates and enhancements.

You may also like

- [Temperature-induced phase transition of two-dimensional semiconductor GaTe](#)
Xiaoyu Wang, , Xue Wang et al.
- [Stacking effect on the electronic structures of hexagonal GaTe](#)
Kang Lai and Jiayu Dai
- [Effects of interlayer interactions on the nanoindentation response of freely suspended multilayer gallium telluride](#)
Jin Zhang, Yan Zhou, Penghua Ying et al.

Novel wide spectrum light absorber heterostructures based on hBN/In(Ga)Te

A Šolajić*  and J Pešić 

Center for Solid State Physics and New Materials, Institute of Physics Belgrade, University of Belgrade, Pregrevica 118, 11080 Belgrade, Serbia

E-mail: solajic@ipb.ac.rs

Received 20 April 2022, revised 2 June 2022

Accepted for publication 16 June 2022

Published 28 June 2022



CrossMark

Abstract

Two-dimensional group III monochalcogenides have recently attracted quite attention for their wide spectrum of optical and electric properties, being promising candidates for optoelectronic and novel electrical applications. However, in their pristine form they are extremely sensitive and vulnerable to oxygen in air and need good mechanical protection and passivization. In this work we modeled and studied two newly designed van der Waals (vdW) heterostructures based on layer of hexagonal boron nitride (hBN) and GaTe or InTe monolayer. Using density functional theory, we investigate electronic and optical properties of those structures. Their moderate band gap and excellent absorption coefficient makes them ideal candidate for broad spectrum absorbers, covering all from part of IR to far UV spectrum, with particularly good absorption of UV light. The hBN layer, which can be beneficial for protection of sensitive GaTe and InTe, does not only preserve their optical properties but also enhances it by changing the band gap width and enhancing absorption in low-energy part of spectrum. Calculated binding energies prove that all three stacking types are possible to obtain experimentally, with H-top as the preferable stacking position. Moreover, it is shown that type of stacking does not affect any relevant properties and bandstructure does not reveal any significant change for each stacking type.

Keywords: heterostructures, hBN, 2D materials, InTe, GaTe, light absorption, DFT

(Some figures may appear in colour only in the online journal)

1. Introduction

Enormous attention given to the exploration and researching of two-dimensional materials in the past decade has started a whole new era in materials science and countless possibilities for novel devices emerged. After successful exfoliation and experimental confirmation of graphene's extraordinary properties, many van der Waals (vdW) layered materials were regaining the attention, being extensively exploited in order to find more possible 2D structures [1]—hexagonal boron nitride [2, 3], silicene [4, 5], germanene [6, 7], transition

metal dichalcogenides (TMD's) [8–13], MXenes [14, 15]. As a result, many possibilities emerged for more innovations and research of more complex systems such are 2D vdW heterostructures. Those layered structures often have new rich physics and enhanced properties, particularly attractive for countless applications in nanoelectronic [16–18] and optoelectronic devices such are Light-emitting diodes based on vdW heterostructures [19], solar cells [20, 21] and flexible broad-spectrum photodetectors [22, 23].

In last few years, two-dimensional group IIIa monochalcogenides have been extensively researched [24–27]. In their bulk form, they are layered structures with weak vdW binding forces, suitable for mechanical exfoliation down to a single layer. With a wide spectrum of exceptional electronic and

* Author to whom any correspondence should be addressed.

optical properties in their two dimensional form, they became very desirable candidates for further research and applications. One of the most outstanding materials in this 2D family, InSe, exhibits very high electron mobility [28] and superb optical properties. Previous work revealed it as very promising material for a highly stable field effect transistors [29]. Excellent absorption properties mark InSe favorable for use in broad spectrum flexible photodetectors, covering wide range from UV to the near IR region [30]. With the idea to further enhance their properties to be more suitable for particular devices, research of vdW heterostructures based on 2D group IIIa monochalcogenides brought notable attention. Various combinations of group III monochalcogenides and graphene emerged as an effective and tunable Schottky barrier [31–35] with many possible ways to precisely control the electronic properties—via electric field, external strain or controlling the interlayer distance. Recent work on heterostructures based on InSe/hBN revealed them as excellent absorbers of the visible and UV part of spectrum.

Two members of group III monochalcogenides were more recently explored and theoretically proposed as new 2D structures—monolayers of InTe and GaTe. Both materials are indirect band gap semiconductors with moderate band gaps of 1.29 and 1.75 eV, respectively. In addition to good electrical and optical properties [36–40], those materials also excel in elastic properties, being able to sustain considerable values of both tensile and compressive strain [36, 40, 41], which is already proven as very effective and convenient way to precisely tune electronic and optical properties of 2D materials [42–44]. Suitable for various applications in novel electronic and optoelectronic devices, research of heterostructures based on those materials is very attractive, with huge expectations for achieving new effects or enhancing desired properties of the 2D structures alone. However, pristine monochalcogenides, especially in form of thin films or as a single layer, are very sensitive and vulnerable to oxygen in air—many studies reveal that single layers are oxidized almost instantly after exposure to the air [45–48]. The issue of their challenging stability can be overcome by passivation with adequate material which would ensure the safe encapsulation of monochalcogenides as well as good mechanical protection. One of materials particularly good and widely used for this purpose is hexagonal boron nitride (hBN). Experimental studies confirmed it as effective for protection and passivation of few layers InSe and GaSe, while their electronic and optical properties are preserved or even enhanced [49] hence the similar effects can be expected for different members of the group III monochalcogenide family.

In the next sections, we present newly designed heterostructures, hBN/GaTe and hBN/InTe, based on a single layer of GaTe or InTe and a layer of hBN. Using the density functional theory (DFT), we explore their electronic and optical properties and analyze the influence of hBN layer on GaTe and InTe. Given the facts stated in previous paragraphs, our motivation was to model stable, mechanically protected structures based on those materials, which would excel in their electronic and optical properties in broad spectrum. Based on their lattice

parameters, we expect to obtain structures with good lattice matching, suitable for experimental realization.

2. Theoretical methods

Results are obtained using DFT implemented in Quantum Espresso (QE) software package [50], based on plane waves and pseudopotentials. Perdew–Burke–Ernzerhof (PBE) functional [51] and PAW pseudopotentials [52] were used in all calculations. After convergence tests, the energy cutoff for the wavefunction and the charge density were set to 44 Ry and 364 Ry for hBN/InTe heterostructure, and 60 Ry and 480 Ry for hBN/GaTe heterostructure. The Monkhorst–Pack of $16 \times 16 \times 1$ mesh for k-point sampling is used in geometric optimization, total energy and phonon calculations. For calculations of p-DOS and optical properties, refined mesh of $64 \times 64 \times 1$ is used. The bandstructure is calculated on 440 k-points along Γ –M–K– Γ direction. In order to simulate 2D structure, a vacuum of 20 Å was added along the z-direction to avoid interactions between the layers. Geometry optimization of both atom positions and lattice parameters is performed using BFGS algorithm, with criteria for maximum allowed forces between atoms of 10^{-6} Ry Å⁻¹. As the GGA functionals do not take into consideration long range forces as the van der Waals force, Grimme-D2 correction was included to obtain more accurate lattice constants and forces. Optical properties were calculated using epsilon.x code in QE software, based on the random phase approximation (RPA).

3. Results and discussion

Both GaTe (InTe) and hBN have hexagonal lattices with D_{3h}^1 symmetry. Lattice constants obtained after the geometric optimizations of $a = 4.371$ Å for InTe, $a = 4.047$ Å for GaTe and 2.515 Å for hBN are in agreement with previous reports [25, 37, 40, 53]. The unit cell of In(Ga)Te/hBN heterostructure is modeled as a supercell which contain one layer of InTe(1×1) or GaTe(1×1) on top of layer of hBN($\sqrt{3} \times \sqrt{3}$) supercell, resulting in hexagonal unit cell with C_3^1 symmetry. The lattice constant of $\sqrt{3} \times \sqrt{3}$ supercell of hBN is $a = 4.347$ Å. In case of hBN/InTe heterostructure, lattice constants of InTe and hBN supercell are excellent matches with close values of 4.371 and 4.347 Å. After geometric optimization, obtained lattice constant of formed heterostructure is $a = 4.336$ Å. That results in almost ideal lattice matching with induced strain of 0.8% on InTe layer and 0.3% on hBN layer, making this heterostructure a great candidate for experimental realization. With lattice constant of $a = 4.047$ Å, monolayer of GaTe is a less perfect match with $a = 4.347$ Å of hBN supercell. However, the obtained lattice constant of formed hBN/GaTe heterostructure is $a = 4.309$ Å which induces strains of 6.1% on GaTe layer and 0.8% on hBN, making them still possible for fabrication. Hence, both heterostructures are promising in terms of lattice matching and can be modeled with proposed supercell. Phonon dispersion for both heterostructures is also calculated and presented in figure 1 in order to

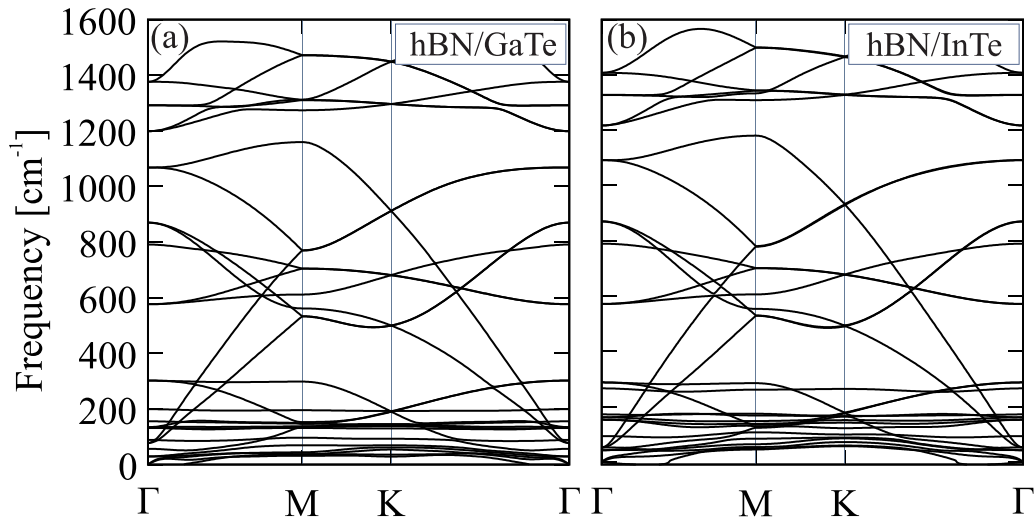


Figure 1. Phonon dispersion of (a) hBN/InTe and (b) hBN/GaTe.

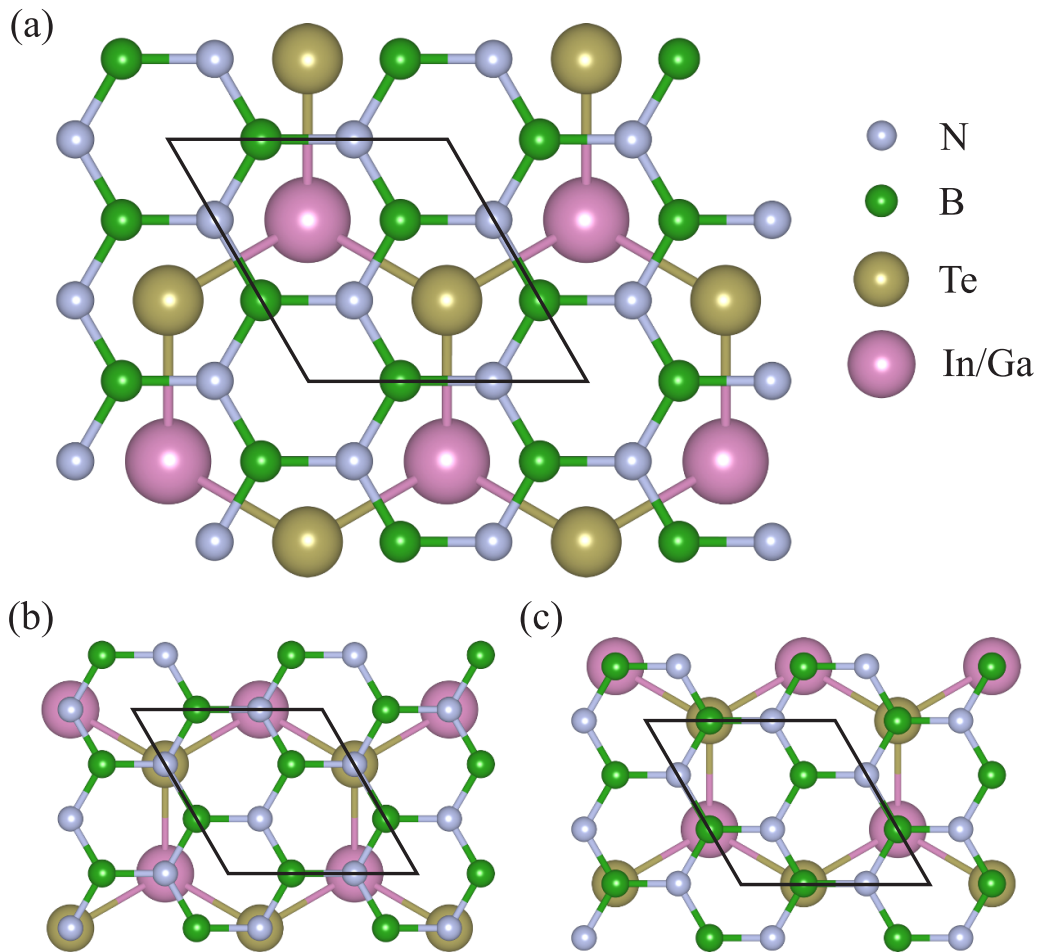


Figure 2. Top view of three possible stacking types, (a) H-top, (b) N-top and (c) B-top.

confirm the structural stability. We do not observe imaginary frequencies, except the small kinks near the Gamma point with low negative values, which are often emerging in calculations of phonons in 2D materials, being a numerical issue and not the real instabilities.

Three possible stacking types are presented in figure 2, the H-top (In/Ga atom being in the center of hBN hexagon), B-top

(In/Ga atom above the B atom of hBN) and N-top (In/Ga atom above the N atom of hBN). We investigated all three types of structure in order to determine the favorable stacking, as well whether the properties are affected by type of stacking, e.g. bandstructure. The optimal distance between the hBN layer and InTe(GaTe) layers (*d*) for both heterostructures and each of their stacking types are obtained previously during the

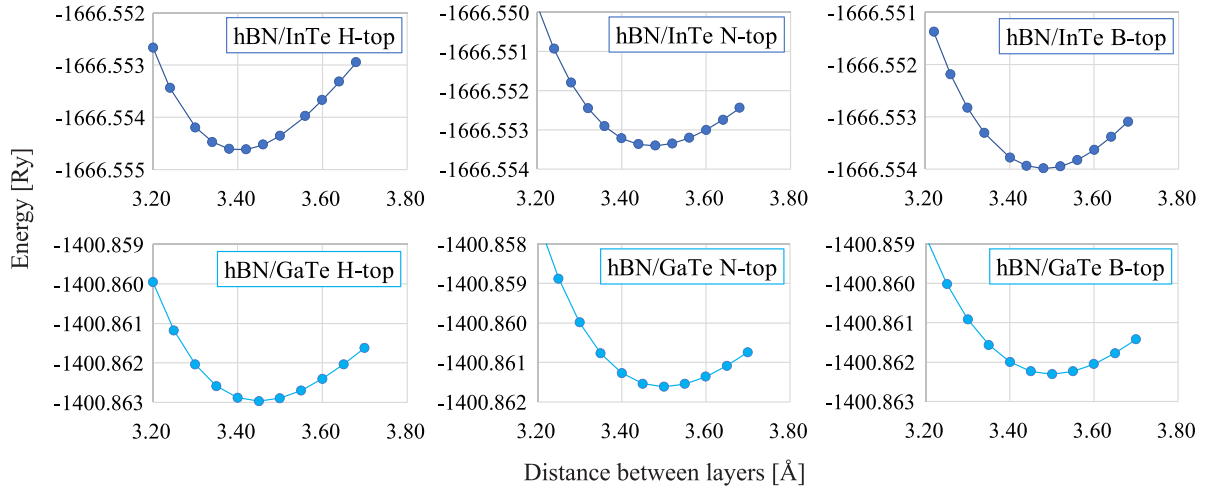


Figure 3. Total energy of the system as a function of the distance between hBN and InTe(GaTe) for different stacking types for hBN/InTe and hBN/GaTe.

geometry optimization, with resulting distances of 3.43–3.52 Å for different stacking positions of hBN/InTe and 3.45–3.52 Å for hBN/GaTe. Total energy of the structure in function of the interlayer distance is shown in figure 3.

In order to confirm the stability of the structures and prove they can be experimentally obtained, we calculated their binding energies (E_b) by the following equation:

$$E_b = E_{\text{heterostr.}} - E_{\text{In(Ga)Te}} - E_{\text{hBN}}, \quad (1)$$

where $E_{\text{heterostr.}}$, $E_{\text{In(Ga)Te}}$ and E_{hBN} represent the total energy of hBN/In(Ga)Te heterostructure, InTe or GaTe monolayer and hBN monolayer, respectively. Binding energies, interlayer distance and lattice parameters obtained for each configuration of hBN/InTe and hBN/GaTe heterostructures are summarized in table 1. Negative values of binding energies suggest that both heterostructures are energetically feasible in all stacking configurations. The favorable stacking type for both hBN/InTe and hBN/GaTe heterostructures is H-top with the lowest value of binding energy, but also the total energy of H-top configuration for both heterostructures is ≈ 8 and ≈ 17 meV lower than in N-top and B-top configurations, respectively. However, the total and binding energies for H-top, N-top and B-top stacking configurations differ just for 10 meV, making all systems convenient for fabrication.

From our calculations, both InTe and GaTe monolayers have an indirect band gap of $E_g = 1.38$ eV and $E_g = 1.75$ eV respectively, while hBN has a large direct band gap of 4.63 eV. These results are in agreement with previous theoretical results obtained using the PBE functional [24, 36, 37, 40]. As the PBE functional underestimates the band gap in semiconductors, hybrid functionals such as Heyd–Scuseria–Ernzerhof (HSE) must be used in order to obtain accurate electronic properties. Reports on similar structures show that employing the HSE functional does not change the bandstructure qualitatively, the most significant difference comes from shifted bands above the Fermi level and thus an enlargement of the band gap. Large difference in band gap of InTe(GaTe) and hBN

Table 1. Lattice parameters, distance between hBN and In(Ga)Te layers (d) and binding energy for all three possible stacking types of hBN/InTe and hBN/GaTe.

	hBN/InTe		
	H-top	N-top	B-top
a (Å)	4.346	4.337	4.337
d (Å)	3.429	3.523	3.479
E_b (meV)	−269.64	−255.49	−259.63
	hBN/GaTe		
	H-top	N-top	B-top
a (Å)	4.309	4.309	4.311
d (Å)	3.451	3.516	3.503
E_b (meV)	−255.62	−241.76	−246.61

as well their alignment of bands make both systems a type-I heterojunctions. This can be also confirmed from the density of states of pristine single layer hBN, InTe and GaTe and projected density of states for both heterostructures, presented in figure 4. As in similar heterostructures [54], the bandstructure does not change with the stacking almost at all—zones near the Fermi level are nearly identical, the band gap does not change and only minor differences can be observed e.g. slightly changed position of some zones below the Fermi level and far above the Fermi level. Bandstructure plots for all three stacking types are shown in figure 5. In further discussion we will focus on the H-top stacking in both hBN/InTe and hBN/GaTe heterostructures.

Atom-decomposed bandstructures of hBN/InTe and hBN/GaTe are presented in figures 6 and 7, alongside their pristine monolayer compounds, InTe and GaTe for easier comparison. Fermi level is set to zero and shown in green line in all figures. Both GaTe and InTe pristine monolayers are indirect band gap semiconductors with valence band maxima close to the Γ point and conduction band minima (CBM) at the M point for GaTe

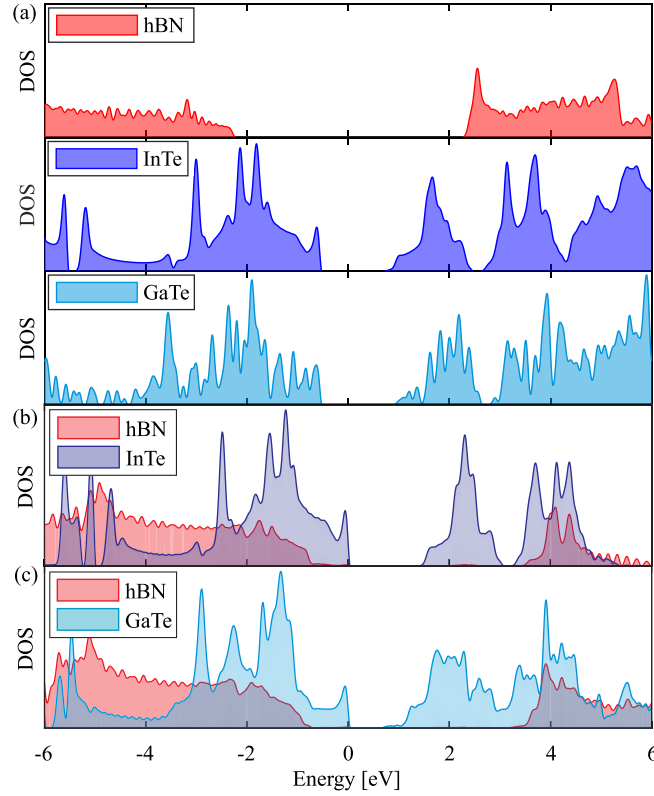


Figure 4. Projected density of states for (a) single layer hBN, InTe and GaTe, (b) hBN/InTe heterostructure and (c) hBN/GaTe heterostructure. The contribution from hBN is shown in red lines and red shaded area, while dark blue and turquoise lines and area represent contribution from InTe and GaTe, respectively.

and Γ and M points for InTe. After stacking into heterostructure, the band gap is slightly changed from original GaTe and InTe structures. CBM are shifted to the Γ point in both heterostructures. In the hBN/InTe band gap is slightly enlarged, from 1.38 eV in pure InTe monolayer to 1.54 eV in the heterostructure. This change in band gap is barely visible and bands near the Fermi level have the same shape as in pristine InTe. Hence, upon forming the hBN/InTe heterostructure, there are no important differences in the band structure. States around the Fermi level are almost completely formed by InTe, while the hBN contributions are observed below -2 eV and above 3 eV, similar as in pristine hBN.

More changes can be observed in the second structure—gap of single layer GaTe is 1.59 eV, but after the heterostructure is formed, band gap is reduced to just 0.79 eV. Upon forming the heterostructure, in the vicinity of the Γ point, there are many mixed states around -1 eV, originated from 5p states of Te atoms and 2p states of N atoms, as result of interaction between the hBN and GaTe layers. In addition, valence band is heavily lifted, separating previously grouped states around the Γ point for more than 0.5 eV and significantly reducing the band gap.

The reduction of band gap along with interfacial states can be useful for applications in optoelectronics so we proceeded to analyze the optical properties of these heterostructures. We calculated the absorption coefficients, expecting both structures to have good absorption properties. The

complex dielectric function $\epsilon(\omega) = \epsilon_R(\omega) + i\epsilon_I(\omega)$ is obtained from calculations in the RPA framework. From these results, we can obtain the absorption coefficient $\alpha(\omega)$ as the following:

$$\alpha(\omega) = \sqrt{2} \frac{\omega}{c} \sqrt{\epsilon_R^2(\omega) + \epsilon_I^2(\omega) - \epsilon_I(\omega)}. \quad (2)$$

Results are shown in figure 8 for hBN/InTe and figure 9 for hBN/GaTe heterostructures, both plotted alongside their pristine monolayer compounds. Both structures have very good absorption properties, being able to absorb visible, near and far UV spectrum—the absorption of hBN/GaTe even slightly extends to the IR spectrum. As the PBE functional underestimates band gap, some shift in energy would be noticed compared to HSE calculations. The results though would not be significantly changed, only the reduction in capabilities of absorbing the IR and red part of the visible light is expected.

The highest peaks in absorption function are near 6 eV, primarily originating from the InTe/GaTe, at 11 and at 14 eV as a contribution from hBN layer, with peaks up to $8 \times 10^5 \text{ cm}^{-1}$. As a result of smaller band gap in hBN/GaTe heterostructure, slightly enhanced absorption is observed in very low energy region of 1–2 eV. The difference is though, not significant, which is not unexpected as the bandstructures of hBN/InTe and hBN/GaTe do not differ much qualitatively, and band gap

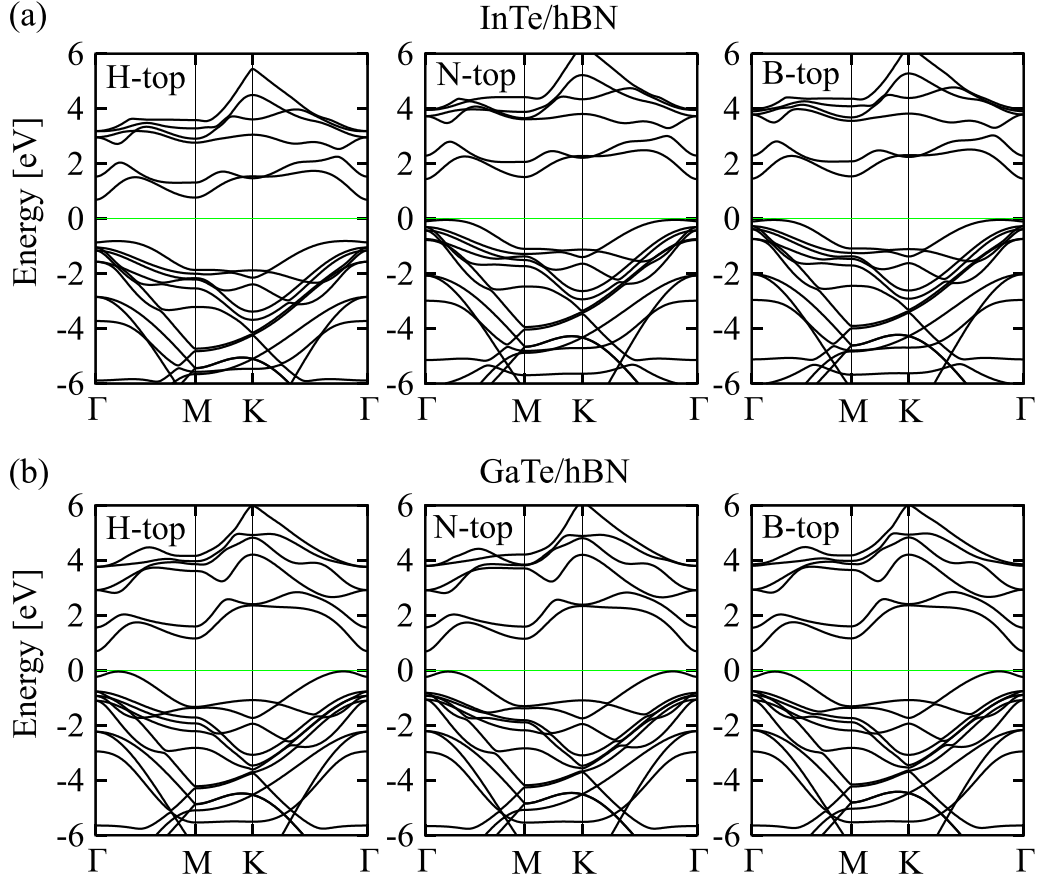


Figure 5. Bandstructure for different types of stacking for (a) hBN/InTe and (b) hBN/GaTe heterostructure.

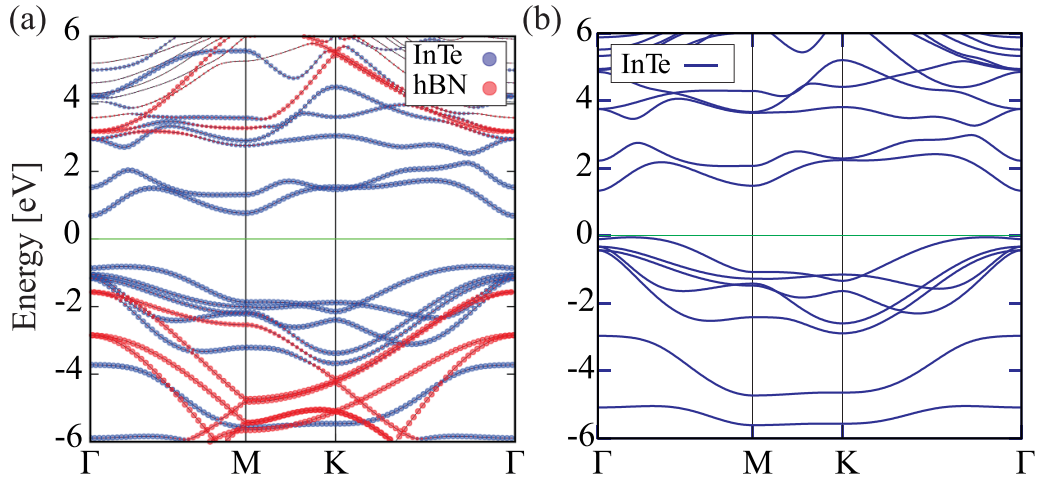


Figure 6. (a) Projected bandstructure of hBN/InTe heterostructure and (b) bandstructure of InTe monolayer. The size of circles on the left graph indicate the magnitude of projections of wavefunctions over atomic orbitals—contribution from different atomic orbitals are presented in different colors as shown in the legend.

in GaTe/hBN is primarily reduced due to one single shifted band below the Fermi level. In addition, results obtained using RPA calculations have contribution just from transitions in ground state, any exciton effects cannot be observed. In energy range from 3 to 15 eV, both heterostructures have exceptional values of absorption of $2\text{--}8 \times 10^5 \text{ cm}^{-1}$, giving them a huge potential for light absorbers in near and far UV spectrum. This makes both heterostructures excellent candidates for

light absorption-relevant photoelectric applications, such as modern photodetectors. Further, we calculated the reflectance for our heterostructures. The real and imaginary part of dielectric function are related with a complex index of refraction $n^*(\omega) = n(\omega) + i\kappa(\omega)$ by:

$$\epsilon_R = 2n\kappa, \epsilon_I = n^2 - \kappa^2. \quad (3)$$

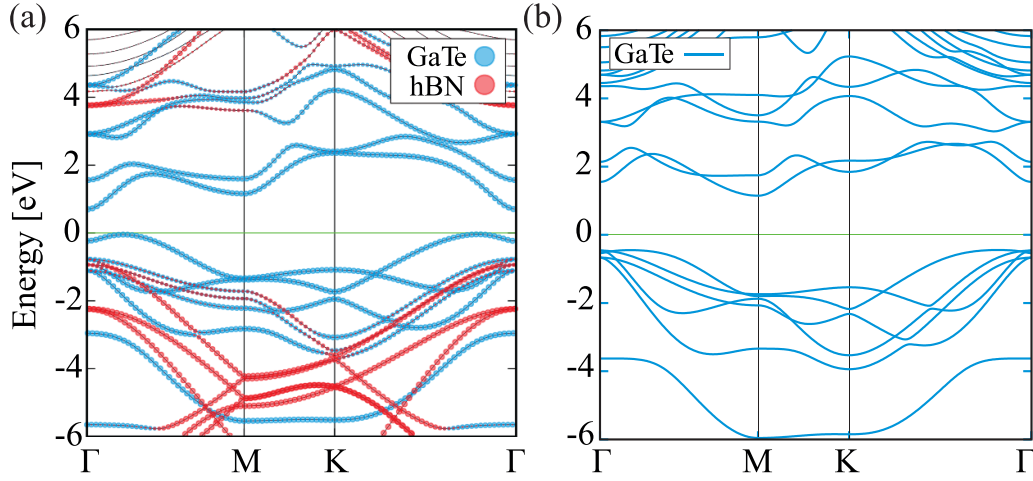


Figure 7. (a) Projected bandstructure of hBN/GaTe heterostructure and (b) bandstructure of GaTe monolayer. The size of circles on the left graph indicate the magnitude of projections of wavefunctions over atomic orbitals—contribution from different atomic orbitals are presented in different colors as shown in the legend.

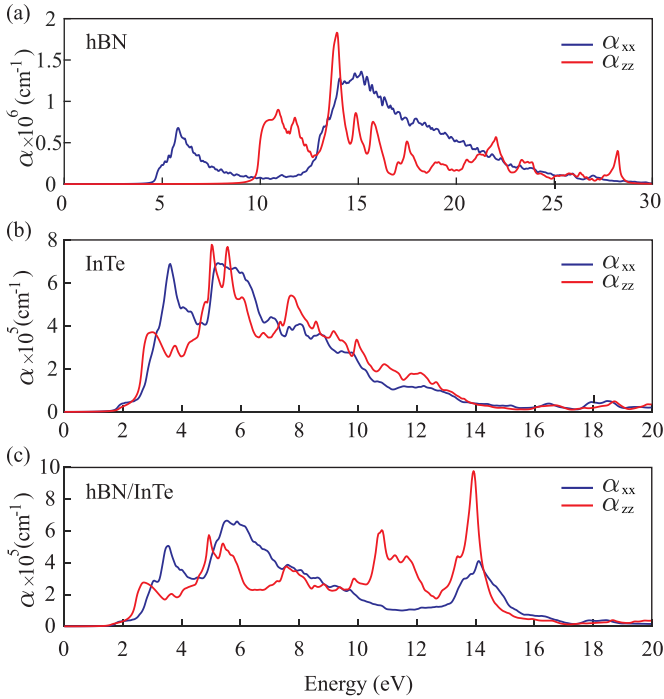


Figure 8. Absorption coefficient of (a) hBN, (b) InTe, (c) hBN/InTe heterostructure for in-plane (α_{xx}) and out-of-plane (α_{zz}) polarizations.

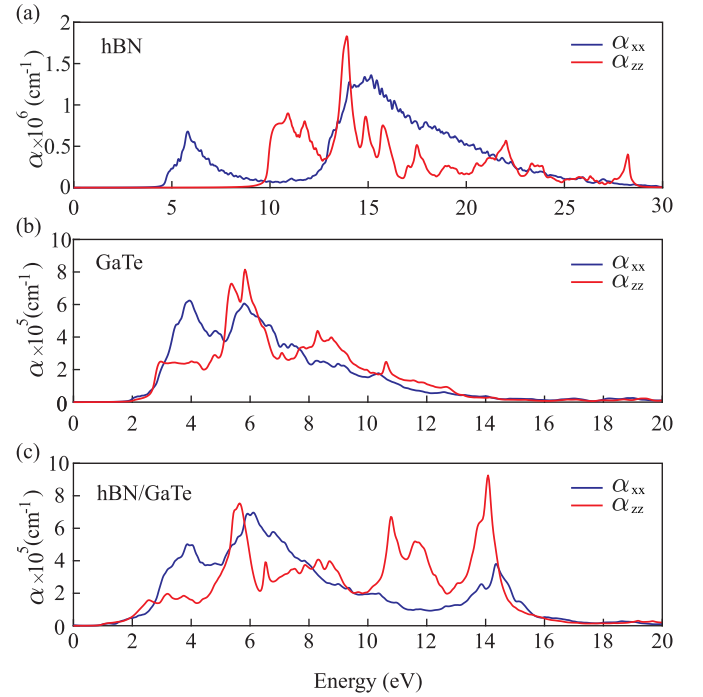


Figure 9. Absorption coefficient of (a) hBN, (b) GaTe, (c) hBN/GaTe heterostructure for in-plane (α_{xx}) and out-of-plane (α_{zz}) polarizations.

The reflectance is now given by:

$$\frac{(n-1)^2 + \kappa^2}{(n+1)^2 + \kappa^2}. \quad (4)$$

Figure 10 presents calculated reflectance of hBN/InTe and hBN/GaTe heterostructures. Reflectance of both materials are no larger than 30% for any energy, and are especially low in the low-energy region with 10%, confirming that only a

small amount of light is being reflected at any incidence angle. As both heterostructures have qualitatively similar bandstructures, their reflectances are not much different. However, for z polarization, the small peak at 2.5 eV is flattened in hBN/GaTe dropping to nearly constant values of around 10% in region up to 5 eV, while the peak at 6 eV is narrowed and higher than in hBN/InTe. That can be ascribed as a result of differences in shape and positions of certain bands and different values of band gap.

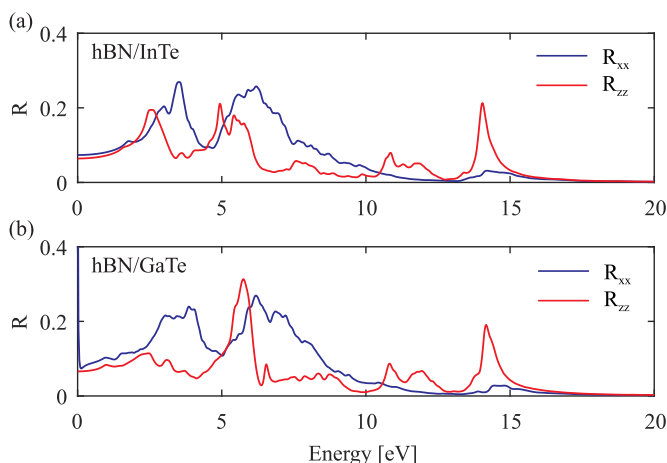


Figure 10. Reflectance of (a) hBN/InTe heterostructure and (b) hBN/GaTe, for in-plane (α_{xx}) and out-of-plane (α_{zz}) polarizations.

4. Conclusions

We report the study of two new heterostructures based on hexagonal boron nitride and InTe/GaTe, by employing first principle calculations. We confirm the structural stability of those systems and show that stacking type does not affect any of the relevant properties and all types of stacking are feasible for fabrication. We investigate their electronic and optical properties, showing the benefit of forming heterostructures of InTe/GaTe with hBN layer. Formation of heterostructure slightly changes the band gap in comparison with pristine monolayer InTe and GaTe, which also enhances absorption in the low-energy region of the spectrum. Both heterostructures have good broad spectrum absorption, with exceptionally good absorbing of the UV light. Hence, their electronic and optical properties reveal them as excellent candidates for field effect transistors based on vdW heterostructures, or modern optoelectronic devices such as flexible broad spectrum photodetectors, solar cells. From the previous studies, the hBN layer is also proven to be beneficial for mechanical protection of sensitive and vulnerable single layers of monochalcogenides like InTe and GaTe, while as we showed, electronic and optical properties are not only preserved but even enhanced. Of special interest is hBN/InTe heterostructure for its remarkably good lattice constant matching between InTe and hBN layers which yields less than 1% of induced strain between the layers. This places hBN/InTe beneficial over similar studied heterostructures with comparable electronic and absorption properties (e.g. hBN/InSe) with significant advantage for future fabrication and experiments as well for their further mechanical manipulation. As both InTe (GaTe) and hBN can withstand a moderate strain, electronic and optical properties can be tuned by applying the strain on the heterostructure or by including electric field, giving these materials a huge value for further research and applications.

Data availability statement

All data that support the findings of this study are included within the article (and any supplementary files).

Acknowledgments

The authors acknowledge funding provided by the Institute of Physics Belgrade through the grant by the Ministry of Education, Science and Technological Development of the Republic of Serbia. DFT calculations were performed using computational resources at Johannes Kepler University (Linz, Austria).

ORCID iDs

A Šolajić  <https://orcid.org/0000-0002-0553-0858>

J Pešić  <https://orcid.org/0000-0002-8600-7187>

References

- [1] Liu B and Zhou K 2019 *Prog. Mater. Sci.* **100** 99–169
- [2] Zhang K, Feng Y, Wang F, Yang Z and Wang J 2017 *J. Mater. Chem. C* **5** 11992–2022
- [3] Song L *et al* 2010 *Nano Lett.* **10** 3209–15
- [4] Kara A, Enriquez H, Seitsonen A P, Voon L L Y, Vizzini S, Aufray B and Oughaddou H 2012 *Surf. Sci. Rep.* **67** 1–18
- [5] Zhao J *et al* 2016 *Prog. Mater. Sci.* **83** 24–151
- [6] Acun A *et al* 2015 *J. Phys.: Condens. Matter* **27** 443002
- [7] Derivaz M, Dentel D, Stephan R, Hanf M C, Mehdaoui A, Sonnet P and Pirri C 2015 *Nano Lett.* **15** 2510–6
- [8] Fu Q *et al* 2021 *Adv. Mater.* **33** 1907818
- [9] Li Y, Wang H, Xie L, Liang Y, Hong G and Dai H 2011 *J. Am. Chem. Soc.* **133** 7296–9
- [10] Splendiani A, Sun L, Zhang Y, Li T, Kim J, Chim C Y, Galli G and Wang F 2010 *Nano Lett.* **10** 1271–5
- [11] Li H, Zhang Q, Yap C C R, Tay B K, Edwin T H T, Olivier A and Baillargeat D 2012 *Adv. Funct. Mater.* **22** 1385–90
- [12] Zhao W, Ghorannevis Z, Chu L, Toh M, Kloc C, Tan P H and Eda G 2013 *ACS Nano* **7** 791–7
- [13] Li H, Lu G, Wang Y, Yin Z, Cong C, He Q, Wang L, Ding F, Yu T and Zhang H 2013 *Small* **9** 1974–81
- [14] Anasori B, Lukatskaya M R and Gogotsi Y 2017 *Nat. Rev. Mater.* **2** 1–17
- [15] Pang J, Mendes R G, Bachmatiuk A, Zhao L, Ta H Q, Gemming T, Liu H, Liu Z and Rummeli M H 2019 *Chem. Soc. Rev.* **48** 72–133
- [16] Geim A K and Grigorieva I V 2013 *Nature* **499** 419–25
- [17] Novoselov K, Mishchenko A, Carvalho A and Neto A C 2016 *Science* **353** 14
- [18] Liu Y, Weiss N O, Duan X, Cheng H C, Huang Y and Duan X 2016 *Nat. Rev. Mater.* **1** 1–17
- [19] Withers F *et al* 2015 *Nat. Mater.* **14** 301–6
- [20] Furchi M M, Höller F, Dobusch L, Polyushkin D K, Schuler S and Mueller T 2018 *npj 2D Mater. Appl.* **2** 1–7
- [21] Zheng X, Wei Y, Pang K, Kaner Tolbert N, Kong D, Xu X, Yang J, Li X and Li W 2020 *Sci. Rep.* **10** 1–9
- [22] Qin S, Du Q, Dong R, Yan X, Liu Y, Wang W and Wang F 2020 *Carbon* **167** 668–74
- [23] Dong T, Simoes J and Yang Z 2020 *Adv. Mater. Interfaces* **7** 1901657

- [24] Ren C, Wang S, Tian H, Luo Y, Yu J, Xu Y and Sun M 2019 *Sci. Rep.* **9** 1–6
- [25] Demirci S, Avazl N, Durgun E and Cahangirov S 2017 *Phys. Rev. B* **95** 115409
- [26] Yang Z and Hao J 2019 *Adv. Mater. Technol.* **4** 1900108
- [27] Chen J, Cai S, Xiong R, Sa B, Wen C, Wu B and Sun Z 2020 *Phys. Chem. Chem. Phys.* **22** 7039–47
- [28] Bandurin D A *et al* 2017 *Nat. Nanotechnol.* **12** 223–7
- [29] Jiang J, Li J, Li Y, Duan J, Li L, Tian Y, Zong Z, Zheng H, Feng X, Li Q 2019 *npj 2D Mater. Appl.* **3** 1–8
- [30] Tamalampudi S R, Lu Y-Y, Rajesh Kumar U, Sankar R, Liao C-D, Cheng C-H, Chou F C and Chen Y-T 2014 *Nano Lett.* **14** 2800–6
- [31] Li H, Zhou Z and Wang H 2020 *Nanotechnology* **31** 335201
- [32] Li H, Zhou Z, Zhang K and Wang H 2019 *Nanotechnology* **30** 405207
- [33] Pham K D, Vu-Quang H and Nguyen C V 2019 *Physica B* **555** 69–73
- [34] Pham K D, Hieu N N, Phuc H V, Fedorov I, Duque C, Amin B and Nguyen C V 2018 *Appl. Phys. Lett.* **113** 171605
- [35] Gao X, Shen Y, Ma Y, Wu S and Zhou Z 2019 *Comput. Mater. Sci.* **170** 109200
- [36] Touski S B, Ariapour M and Hosseini M 2020 *Physica E* **118** 113875
- [37] Liao Y, Liu H, Yuan G, Huang Z and Qi X 2020 *Cryst. Res. Technol.* **55** 2000102
- [38] Li K, Xian X, Wang J and Yu N 2019 *Appl. Surf. Sci.* **471** 18–22
- [39] Ariapour M and Touski S B 2019 *Mater. Res. Express* **6** 076402
- [40] Vi V T, Hieu N N, Hoi B D, Binh N T and Vu T V 2020 *Superlattices Microstruct.* **140** 106435
- [41] Jalilian J and Safari M 2017 *Phys. Lett. A* **381** 1313–20
- [42] Zhang J, Lang X, Zhu Y and Jiang Q 2018 *Phys. Chem. Chem. Phys.* **20** 17574–82
- [43] Xiong P *et al* 2020 *Nat. Commun.* **11** 1–12
- [44] Postorino S, Grassano D, D'Alessandro M, Pianetti A, Pulci O and Palummo M 2020 *Nanomater. Nanotechnol.* **10** 1847980420902569
- [45] Rahaman M, Rodriguez R D, Monecke M, Lopez-Rivera S A and Zahn D R T 2017 *Semicond. Sci. Technol.* **32** 105004
- [46] Guo Y, Zhou S and Zhao J 2020 *ChemNanoMat* **6** 838–49
- [47] Guo Y, Zhou S, Bai Y and Zhao J 2017 *J. Chem. Phys.* **147** 104709
- [48] Afaneh T, Fryer A, Xin Y, Hyde R H, Kapuruge N and Gutierrez H R 2020 *ACS Appl. Nano Mater.* **3** 7879–87
- [49] Arora H, Jung Y, Venanzi T, Watanabe K, Taniguchi T, Hubner R, Schneider H, Helm M, Hone J C and Erbe A 2019 *ACS Appl. Mater. Interfaces* **11** 43480–7
- [50] Giannozzi P *et al* 2009 *J. Phys.: Condens. Matter* **21** 395502
- [51] Perdew J P, Burke K and Ernzerhof M 1996 *Phys. Rev. Lett.* **77** 3865–8
- [52] Dal Corso A 2014 *Comput. Mater. Sci.* **95** 337–50
- [53] Wickramaratne D, Weston L and Van de Walle C G 2018 *J. Phys. Chem. C* **122** 25524–9
- [54] Shen N F, Yang X D, Wang X X, Wang G H and Wan J G 2020 *Chem. Phys. Lett.* **749** 137430

Evolution of lattice, spin, and charge properties across the phase diagram of $\text{FeSe}_{1-x}\text{S}_x$

N. Lazarević^{1,*}, A. Baum^{2,3,*}, A. Milosavljević¹, L. Peis^{2,3,†}, R. Stumberger^{2,3,‡}, J. Bekaert⁴, A. Šolajić¹, J. Pešić¹, Aifeng Wang⁵, M. Šćepanović¹, A. M. Milinda Abeykoon⁶, M. V. Milošević⁴, C. Petrovic⁷, Z. V. Popović^{1,8} and R. Hackl^{2,3,9}

¹Center for Solid State Physics and New Materials, Institute of Physics Belgrade,

University of Belgrade, Pregrevica 118, 11080 Belgrade, Serbia

²Walther Meissner Institut, Bayerische Akademie der Wissenschaften, 85748 Garching, Germany

³Fakultät für Physik, Technische Universität München, 85478 Garching, Germany

⁴Department of Physics, University of Antwerp, Groenenborgerlaan 171, B-2020 Antwerp, Belgium

⁵School of Physics, Chongqing University, Chongqing 400044, China

⁶National Synchrotron Light Source II, Brookhaven National Laboratory, Upton, New York 11973, USA

⁷Condensed Matter Physics and Materials Science Department, Brookhaven National Laboratory, Upton, New York 11973-5000, USA

⁸Serbian Academy of Sciences and Arts, Kneza Mihaila 35, 11000 Belgrade, Serbia

⁹IFW Dresden, Helmholtzstr. 20, 01069 Dresden, Germany



(Received 9 March 2022; revised 27 July 2022; accepted 26 August 2022; published 19 September 2022)

A Raman scattering study covering the entire substitution range of the $\text{FeSe}_{1-x}\text{S}_x$ solid solution is presented. Data were taken as a function of sulfur concentration x for $0 \leq x \leq 1$, of temperature and of scattering symmetry. All types of excitations including phonons, spins, and charges are analyzed in detail. It is observed that the energy and width of the iron-related B_{1g} phonon mode vary continuously across the entire range of sulfur substitution. The A_{1g} chalcogenide mode disappears above $x = 0.23$ and reappears at a much higher energy for $x = 0.69$. In a similar way the spectral features appearing at finite doping in A_{1g} symmetry vary discontinuously. The magnetic excitation centered at approximately 500 cm^{-1} disappears above $x = 0.23$ where the A_{1g} lattice excitations exhibit a discontinuous change in energy. The low-energy mode associated with fluctuations displays maximal intensity at the nematic structural transition and thus tracks the phase boundary.

DOI: [10.1103/PhysRevB.106.094510](https://doi.org/10.1103/PhysRevB.106.094510)

I. INTRODUCTION

Iron-based compounds are widely believed to host unconventional superconductivity, thus being similar to cuprates or heavy fermion systems. All are characterized by competing phases including magnetism, crystal symmetry breaking or nematicity, and fluctuations of charge and spin prior to superconductivity [1–3]. While long-range magnetic ordering was found in the majority of the compounds, it is absent in the binary compound FeSe . Yet a nematic and structural phase transition occurs simultaneously at 90 K [4–6]. Below $T_c = 9 \text{ K}$ superconductivity is observed [7]. Upon applied pressure T_c increases to approximately 37 K [8]. By substituting sulfur for selenium, the transition temperature to the nematic phase is suppressed to zero for $x \sim 0.2$ [9], suggesting the existence of a quantum critical point (QCP), and a depression of T_c to approximately 2 K. For $x > 0.2$, T_c increases again and

reaches 5 K at $x = 1$ [10]. Surprisingly enough, FeS displays a metallic variation of the resistivity and a high residual resistivity ratio RRR of approximately 30, and neither structural nor nematic phase transitions occur [11]. Thus, $\text{FeSe}_{1-x}\text{S}_x$ uniquely offers access to instabilities and critical points and the disappearance thereof while superconductivity survives.

FeSe and FeS are isostructural, thus providing us with the opportunity to probe the evolution of competing order by isoelectronic substitution. We wish to address the question as to which extent the properties and, specifically, superconductivity are interrelated with the other instabilities and how the electronic properties affect the phonons. We employ inelastic light scattering to probe evolution with composition of lattice spin and charge excitations in $\text{FeSe}_{1-x}\text{S}_x$ [12]. We identify the A_{1g} and B_{1g} modes, a two-phonon scattering process as well as additional modes that can be traced to either defect-induced or second-order scattering. The obtained experimental results are in good agreement with numerical calculations. Phonons self-energy temperature dependence supports the results reported in Refs. [13,14] where emerging short-range magnetic order at approximately 20 K was reported.

II. EXPERIMENT

Single crystals of $\text{FeSe}_{1-x}\text{S}_x$ were synthesized as described elsewhere [15]. Before the experiment the samples were cleaved in air.

Inelastic light scattering on phonons was performed using a Tri Vista 557 Raman spectrometer with the first

*These authors contributed equally to this work.

†Present Address: IFW Dresden, Helmholtzstr. 20, 01069 Dresden, Germany.

‡Present Address: Robert Bosch GmbH, Robert-Bosch-Platz 1, 70839 Gerlingen, Germany.

Published by the American Physical Society under the terms of the Creative Commons Attribution 4.0 International license. Further distribution of this work must maintain attribution to the author(s) and the published article's title, journal citation, and DOI.

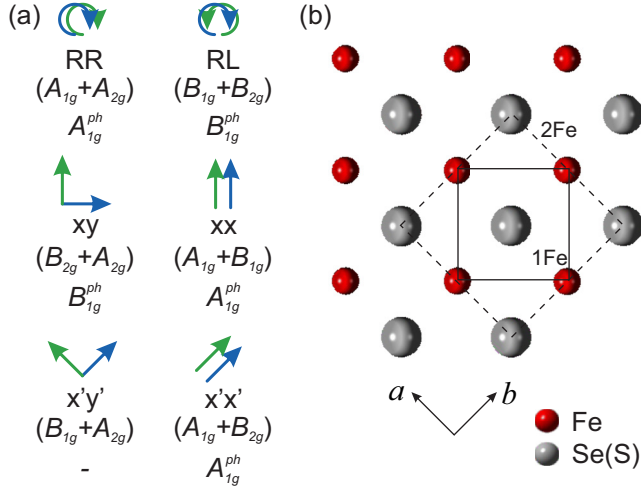


FIG. 1. Crystal structure and selection rules for FeSe(S). Solid and dashed lines represent the 1-Fe and the crystallographic 2-Fe unit cell, respectively. The crystallographic axes are *a* and *b*. In FeSe and FeS only one A_{1g} and one B_{1g} phonon is expected as indicated by A_{1g}^{ph} and B_{1g}^{ph}, respectively. The symmetries projected with the polarizations indicated symbolically with respect to the 1-Fe cell are relevant for electronic and spin excitations. The symmetries of the phonons are in brackets.

two monochromators coupled subtractively and the grating combination 1800/1800/2400 grooves/mm. For excitation a Coherent Verdi G solid state laser was used emitting at 532 nm. The samples were mounted in a KONTI CryoVac continuous helium flow cryostat having a 0.5-mm-thick window. The vacuum was pumped to the range of 10⁻⁶ mbar using a turbo molecular pump. The laser was focused to a spot size of approximately 8 μm using a microscope objective lens with ×50 magnification. The power absorbed by the sample was *P_a* = 0.75 mW. In backscattering configuration as used here, the incident and scattered photons propagate parallel to the crystallographic *c* axis. All Raman spectra were divided by the Bose factor.

Fluctuations and two magnon excitations were probed with a calibrated scanning spectrometer. The samples were attached to the cold finger of a He-flow cryostat having a vacuum of better than 10⁻⁶ mbar. A diode-pumped solid state laser emitting at 575 nm (Coherent GENESIS) was used as an excitation source. The laser beam was focused on the sample at an angle of incidence of 66° to a spot of 2*r_f* ≈ 50 μm. Polarization and power of the incoming light were adjusted in a way that the light inside the sample had the proper polarization state and a power of *P_a* = 4 mW independent of polarization. The ratio *P_a*/*r_f* is similar for the μ setup and thus the local heating for both experiments can be estimated to be in the range 3–5 K. All four symmetries of the *D*_{4h} group, A_{1g}, A_{2g}, B_{1g}, and B_{2g}, can be accessed using appropriate in-plane polarizations of the incident and scattered light.

The selection rules are dictated by the crystal structure. Here, only polarizations in the *ab* plane are relevant, as shown in Fig. 1, with solid and dashed lines representing 1-Fe and 2-Fe unit cells, respectively. For the tetragonal system there are six principal scattering geometries and each probes two symmetry channels. We align our laboratory system with the

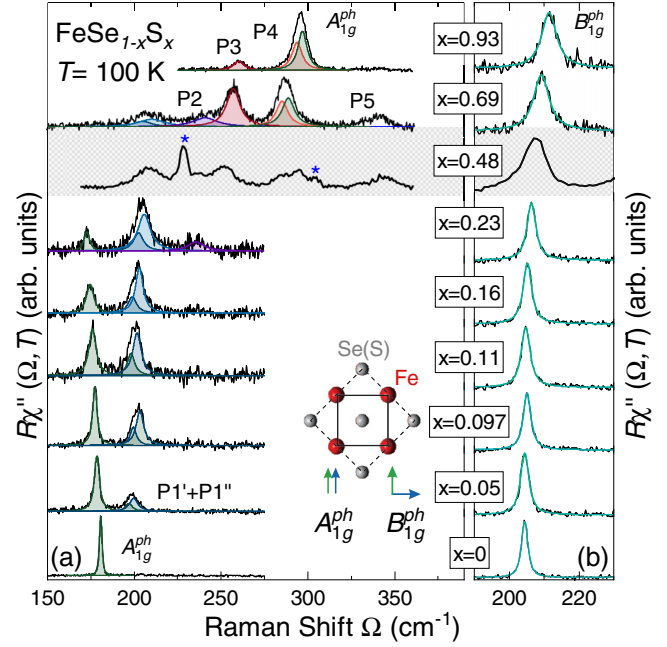


FIG. 2. Phonon spectra of FeSe_{1-x}S_x measured at 100 K. We show *xx* and *xy* spectra where *x* and *y* are rotated by 45° with respect to the 2-Fe unit cell, as indicated in the inset, and project A_{1g}^{ph} and B_{1g}^{ph}, respectively. (a) A_{1g}^{ph} spectra. Only for pure FeSe (*x* = 0), a single line is observed at the A_{1g} energy of 165 cm⁻¹ expected from lattice dynamics. Above *x* = 0.23 the Se(S) vibration becomes unobservable and reappears only for *x* ≥ 0.69 at a much higher energy of approximately 290 cm⁻¹ similar to that in pure FeS. The spectrum at *x* = 0.48 was measured on the scanning spectrometer and is therefore shaded. There may be an indication of the A_{1g}^{ph} phonon at about 290 cm⁻¹. The peaks other than Raman-active phonons are labeled P1–P5 with increasing energy. Those with asterisks correspond to maxima in the phonon density of states (Fig. 6). Solid lines represent the best fits to the data using Voigt profiles. (b) B_{1g}^{ph} spectra. Energy and linewidth vary continuously with sulfur content.

1-Fe unit cell. As a consequence, the B_{1g} phonon (B_{1g}^{ph}) is observable in the *xy* configuration which corresponds to the B_{2g} symmetry channel in the 2-Fe cell (Fig. 1). We decided to use this orientation since our main focus here is electronic and spin excitations for which the 1-Fe unit cell is more appropriate. A_{1g}^{ph} is the fully symmetric in-phase Se(S) mode with elongations along the *c* axis; B_{1g}^{ph} corresponds to the out-of-phase vibration of the Fe atoms parallel to the *c* axis.

III. RESULTS AND DISCUSSION

A. Lattice excitations

First, the focus is placed on lattice excitations observable in the *xx* and *xy* scattering configuration projecting A_{1g}^{ph} and B_{1g}^{ph} in the spectral range characteristic for phonons. Figure 2 shows the evolution of the spectra with doping *x*, where *x* indicates the sulfur concentration. Additional spectra for *x* = 0.48 and, for convenience, *x* = 1 are shown in Fig. 7. In order to minimize the thermal broadening of the modes while staying above the nematic phase transition, the spectra

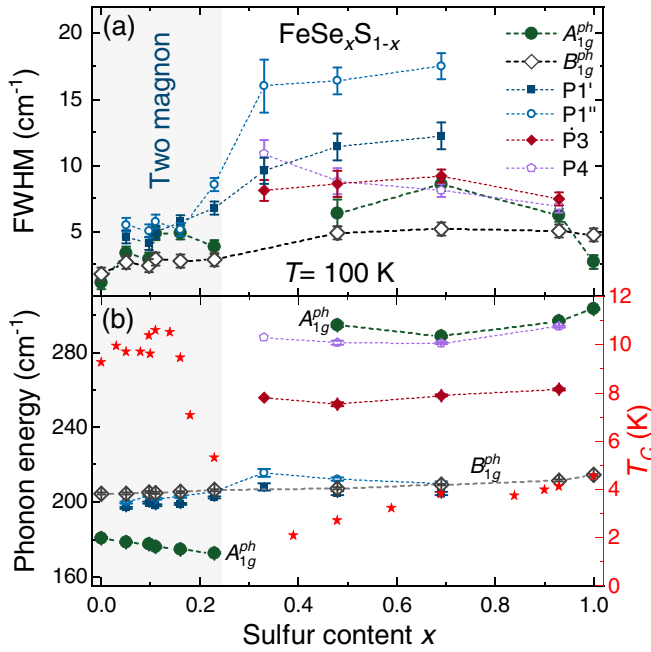


FIG. 3. Energies and linewidths of the Raman-active modes and T_c in $\text{FeSe}_{1-x}\text{S}_x$ as a function of sulfur content x at 100 K. (a) Peak widths (FWHM) and (b) energies as obtained from the fits (left axis). The T_c values of the corresponding solid solution are taken from Ref. [16].

were recorded at 100 K. In pure stoichiometric compounds only one A_{1g}^{ph} and one B_{1g}^{ph} phonon mode is expected (see Fig. 1). This is indeed the case for FeSe [Fig. 2(a), bottom] as described by Gnezdilov *et al.* [17] and corroborated here. In contrast, in pure FeS ($x = 1$) additional modes exist in the xx spectrum which were assigned to two-phonon scattering (265 cm^{-1}) and a projection of the phonon density of states (PDOS) ($\sim 300 \text{ cm}^{-1}$) [18] as reproduced in Fig. 7(b). The xy spectra show only the B_{1g}^{ph} mode for all doping levels displayed here [see also Fig. 7(a)]. It hardens monotonously and exhibits a weak maximum of the linewidth at $x = 0.69$ and $x = 0.93$ highlighting the effect of disorder as summarized in Figs. 3(a) and 3(b).

The xx spectra display a much more complex doping dependence. Upon substituting only a small amount of sulfur ($x = 0.05$) for selenium an additional structure appears at about 200 cm^{-1} [Fig. 2(a)]. Closer inspection of the $\text{FeSe}_{0.95}\text{S}_{0.05}$ spectra reveals that this feature consists of two peaks denoted as $P1'$ and $P1''$. With increasing x , these structures gain intensity and harden slightly, whereas the A_{1g} phonon softens, gradually loses intensity, and becomes undetectable at concentrations above $x = 0.23$. It reappears as a clear peak only for $x \geq 0.69$ at a much higher energy characteristic for FeS [18] and possibly as a remnant structure in the spectrum for $x = 0.48$ [Fig. 7(a)]. As in FeS the A_{1g}^{ph} peak overlaps with a weaker structure which is compatible with the PDOS (P4). At $x = 0.69$ P4 is approximately as strong as the A_{1g} phonon. Here [and at $x = 0.48$, Fig. 7(a)] there is also a broad feature at 340 cm^{-1} (P5). For $x = 0.93$ similar to $x = 1$ there is another structure at 250 cm^{-1} (P3) which gains intensity toward $x = 0.69$ where it has a weak companion at

235 cm^{-1} (P2) being present down to $x = 0.23$. As expected, the increase of crystalline disorder due to substitution leads to a broadening of all observed modes to some maximum value before the trend reverses for compositions close to pure FeS. The widths and energies of the stronger modes are summarized in Fig. 3. As opposed to the B_{1g}^{ph} phonon in xy configuration, all modes in xx polarization including the Raman-active phonon depend quasidiscontinuously on substitution.

This dichotomy of the substitution dependence of the phonon part in xx and xy configuration is the most remarkable effect of this study. Whereas the continuous evolution of the Fe B_{1g} line by and large tracks the degree of disorder and lattice contraction, the Se/S A_{1g} mode varies counterintuitively. Naively one would expect a continuous (not necessarily trivial) increase in the phonon frequency and maximal broadening for doping levels around $x = 0.5$ similar to what is observed in isotopically substituted semiconductors [19]. However, the line disappears after a continuous loss of intensity at approximately $x = 0.23$ and 172 cm^{-1} and reappears (presumably) at $x = 0.48$ slightly below 300 cm^{-1} . At low doping the A_{1g} energy decreases by 4% although S is lighter than Se by a factor of 2.13 and the lattice contracts. Above $x = 0.48$ the energy of the A_{1g} phonon varies as expected [see Fig. 3(b)].

The structures appearing in addition to the allowed phonons are rather difficult to interpret in detail. There are essentially two possibilities for intensity to appear in addition to the phonons: defect-induced scattering projecting the PDOS on the site of the defect or overtone (combination) scattering [20]. In FeS one of the peaks (P3) is in the gap between the acoustic and the optical branches and was therefore assigned to an overtone, whereas P4 may originate from the PDOS [18]. The two features depend in the same fashion on doping as the A_{1g} phonon, and the assignment may be maintained. This is plausible on the basis of the PDOS (Fig. 6) although the PDOS of a solid solution cannot be calculated straightforwardly. If we argue that the extra lines vary as discontinuously as the phonon, $P1'$ and $P1''$ would have both an overtone and a PDOS component. Interestingly, $P1'$ and $P1''$ have the expected doping dependence [see Fig. 3(b)].

The anomalous doping dependence of the A_{1g} phonon may indicate an enhanced electron-phonon coupling which manifests itself also in the linewidth (on top of the inhomogeneous broadening) [Fig. 3(a)]. The slightly enhanced electron-phonon coupling may boost T_c a little bit until the structure becomes unstable and T_c decreases rapidly for $x > 0.16$. There is, in fact, a kink in the c/a ratio at $x = 0.23$ which may be related to the structural instability [15]. In a recent preprint the collapse of T_c is almost precipitous and coincides with the end of the nematic phase [21], and one may speculate about the position of the quantum critical point and its impact. Yet, further work is necessary to finally clarify the issue.

B. Spin excitations and fluctuations

Second, we focus on the electronic B_{1g} symmetry channel projected in the $x'y'$ (1-Fe) configuration. Figure 4 shows the doping dependence of the high-energy Raman spectra at approximately 4 K. The A_{2g} contribution can be neglected in these materials [22]. A broad excitation centered at about

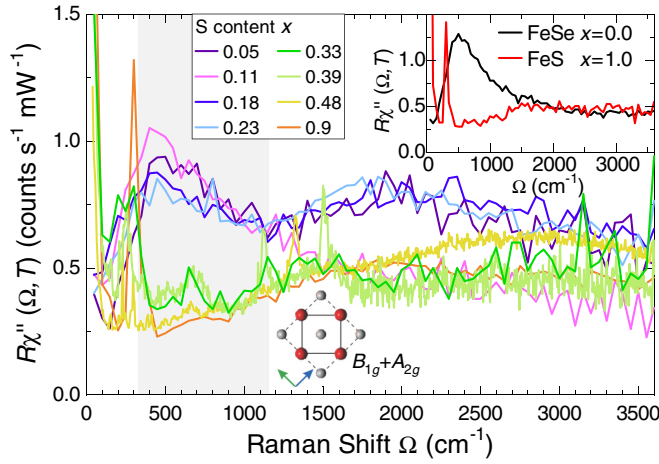


FIG. 4. Doping dependence of the high-energy spectra of $\text{FeSe}_{1-x}\text{S}_x$ in xy (2-Fe) configuration at 4 K, except for $x = 0.33$, $x = 0.39$, and $x = 0.48$ which were obtained at 100 K. For the electronic unit cell (full line in Fig. 1) relevant here the B_{1g} and A_{2g} symmetries are projected where A_{2g} is negligibly weak. The doping levels are indicated. The inset compares the high-energy spectra of pure FeSe [22] and FeS. The maximum in the range 500 cm^{-1} is compatible with two-magnon scattering [23], whereas the broad shoulder around 2000 cm^{-1} appearing in three out of ten (including all doping levels) spectra was identified as luminescence by using various laser lines for excitation. The peaks in the range $700\text{--}1550\text{ cm}^{-1}$ observed only for the doping levels $x = 0.33$, $x = 0.39$, and $x = 0.48$ may originate from either overtones of the phonon density of states [20,24] or from magnetic excitations in the paramagnetic state above the magnetic phase which was observed recently below $20\text{--}40\text{ K}$ [25,26]. Since the measuring temperature is well above the magnetic transition the former is more likely.

500 cm^{-1} dominates the spectrum at $x = 0$ which was interpreted in terms of two-magnon scattering [22]. Since the ratio of the nearest to the next-nearest-neighbor exchange coupling J_1 and J_2 is close to 0.5 [27] the system is a nearly frustrated antiferromagnet. Consequently the two-magnon Raman peak is pushed to energies well below $3J_1$ [23]. No comparable feature is observed in FeS (see inset in Fig. 4).

Upon doping, the two-magnon peak remains relatively robust up to $x = 0.23$ and is absent for higher doping levels. This goes in line with the fact that for $x = 0$, the Fermi velocity in the d_{xy} band, $v_F^{(xy)}$, is significantly smaller than $v_F^{(xz)}$ or $v_F^{(yz)}$ and increases by only 10% for $x \leq 0.20$. For $x > 0.20$ $v_F^{(xy)}$ increases significantly towards FeS [28]. Generally, $v_F^{(xy)}$ in FeSe is smaller than $v_F^{(xy)}$ in $\text{Ba}(\text{Fe}_{1-x}\text{Co}_x)_2\text{As}_2$ for instance [29], in agreement with theoretical predictions [30–32]. Thus FeSe is close to the localization limit, and the two-magnonlike response may result from the rather slow carriers on the d_{xy} band. In contrast, the more itinerant carriers in the pnictides condense into a stripelike spin density wave (SDW) which becomes manifest in a gap and a coherence peak [22,33].

In the energy region $\Omega < 200\text{ cm}^{-1}$ extra intensity is observed for low temperatures. In FeSe it becomes clearly visible below 200 K and fills the spectral gap below the magnon at 500 cm^{-1} . Below approximately 100 K an isolated

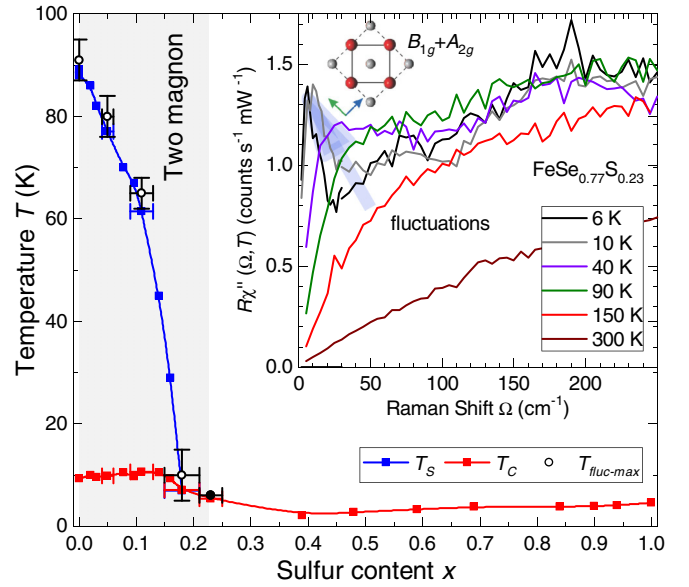


FIG. 5. Phase diagram of $\text{FeSe}_{1-x}\text{S}_x$ with $T_{\text{fluct,max}}$ tracing T_S in the region where the two-magnon feature was observed in the Raman scattering experiment. T_c taken from Ref. [15]. The full circle represents the lowest accessible temperature. Inset: Low-energy Raman spectrum showing the temperature dependence of the fluctuation contribution at $x = 0.23$. Spectra for all doping levels $0 \leq x \leq 0.23$ are shown in Fig. 8.

peak may be observed for $x = 0$ which continuously softens above the structural transformation at $T_s = 90\text{ K}$, fades away below T_s , and almost vanishes at 21 K [22,34]. The line shape and the temperature dependence above T_s can be described quantitatively in terms of critical fluctuations in a similar fashion as in $\text{Ba}(\text{Fe}_{1-x}\text{Co}_x)_2\text{As}_2$ [22,33,35]. For increasing doping, this extra intensity starts to develop at lower temperatures. However, remarkably enough the temperature where this peak's intensity is maximal, $T_{\text{fluct,max}}$, always coincides with the respective transition temperature $T_s(x)$. At $x = 0.23$ the fluctuation response gains intensity down to the lowest accessible temperatures as presented in the inset of Fig. 5. Thus, the phase transition line of the nematic phase can also be tracked by the Raman response. For $x = 0.33$ (the next available doping level) the fluctuation response cannot be observed any further. Concomitantly, the two-magnon excitation at 500 cm^{-1} becomes unobservable. The most likely explanation of this coincidence is that the two phenomena have the same origin and result from spin excitations. However, there is no consensus on that view in the literature, and Zhang *et al.* [36] and Chibani *et al.* [34] interpret the same experimental observation in terms of quadrupolar charge fluctuations. Yet, one certainly has to answer the question as to why the fluctuations are not found in the simulations [23].

Most probably, the length scale the simulations can deal with limits the applicability of the exact diagonalization method. Since it was intended to study the temperature dependence the cluster had to be sufficiently small (4×4) to keep the time for the simulations finite [23]. For the two-magnon excitations, the 4×4 cluster is sufficient because only nearest-neighbor spins are important. However, close to

the transition the correlation length of fluctuations diverges making them inaccessible for the small clusters tractable numerically. Actually, well above the transition there is a shoulder on the low-energy side of the two-magnon peak which may be associated with the fluctuations but the shoulder is lost close to T_s . Thus, although there are experimental arguments in favor of spin fluctuations at low energy there is no theoretical support for this conjecture.

The last question we wish to address concerns the origin of possible local or quasilocal spin order in $\text{FeSe}_{1-x}\text{S}_x$ for $x < 0.3$. It was observed a while ago that the width of the various bands derived from the orbitals close to the Fermi surface varies by approximately a factor of 3 or more. There are itinerant yz and xz bands crossing the Fermi surface at E_F and a weakly dispersing xy band just below E_F [29] on which the nearly localized spins may reside [30,32]. It is an important question to which extent the fluctuations at low energy are related to these spins. As a matter of fact, Ba122 displays itinerant SDW magnetism as manifested by a gap and a coherence peak along with fluctuations [22,33], whereas FeSe exhibits signatures of local spins and also fluctuations at low energies as shown here. In $\text{FeSe}_{1-x}\text{S}_x$ both phenomena disappear together above $x > 0.23$.

IV. CONCLUSION

Raman results covering the entire substitution range $0 \leq x \leq 1$ in $\text{FeSe}_{1-x}\text{S}_x$ were presented. The main goal was the study of the physics around the QCP where the nematic instability approached zero transition temperature in the range $0.16 \leq x \leq 0.23$. We find a striking signature of this transition in both the phonon and the electronic spectra. Whereas the B_{1g} phonon varies continuously with S substitution, the A_{1g} phonon and all structures in the xx spectra show a discontinuity above $x = 0.23$. Similarly, the electronic spectra dominated by spin excitations change abruptly here. Both the two-magnon excitations and the low-energy fluctuations disappear. We argue that they are interrelated. Since we could not observe gap excitation for $x > 0$, statements about the evolution of the superconducting pairing are currently not possible. Another issue is the exact position of the quantum critical transition and its sharpness.

ACKNOWLEDGMENTS

We acknowledge valuable discussions with T. Böhm and D. Jost. The authors acknowledge funding provided by the Institute of Physics Belgrade through a grant by the Ministry of Education, Science and Technological Development of the Republic of Serbia and and SASA Project No. F-134. The work was supported by the Science Fund of the Republic of Serbia, PROMIS, No. 6062656, StrainedFeSC, by Research Foundation-Flanders (FWO), and COST actions CA16218 and CA21144. Further support came from the German research foundation (DFG) via projects Ha2071/8-1, Ha2071/12-1, and 107745057-TRR 80 and from the DAAD via the project-related personal exchange program PPP with Serbia Grant No. 57449106. J.B. is Senior Postdoctoral Fellow of the FWO, and further acknowledges the Erasmus+ program for staff mobility and training (KA107, 2018) for a

research stay at the Institute of Physics Belgrade. The computational resources and services used for the first-principles calculations in this work were provided by the VSC (Flemish Supercomputer Center), funded by the FWO and the Flemish Government, department EWI. Work at Brookhaven National Laboratory is supported by the U.S. DOE under Contract No. DESC0012704 (materials synthesis).

APPENDIX A: PHONON DISPERSION AND DENSITY OF STATES

We have performed density functional theory (DFT) calculations as implemented in the ABINIT package [38]. We have used the Perdew-Burke-Ernzerhof functional tailored for solids [39] and optimized norm-conserving pseudopotentials [40,41], where Fe $3s^2 3p^6 3d^6 4s^2$, S $3s^2 3p^4$, and Se $3d^{10} 4s^2 4p^4$ are treated as valence electrons. The energy cutoff for the plane-wave basis was set to 50 Ha. The lattice parameters and atomic positions used in the calculations were directly obtained from our x-ray diffraction measurements (performed at 300 K). Following previous first-principles studies on phonons in, for example, FeS [18], the crystal structures were not further relaxed, to achieve optimal characterization of the phonon frequencies. Here, both FeS and FeSe adopt the simple tetragonal space group $P4/nmm$ (No. 129), where Fe occupies Wyckoff position $2a$ and S/Se position $2c$. The latter comprises an additional degree of freedom, namely, the height of the chalcogen atoms S and Se with respect to the Fe plane, denoted as z . An overview of the lattice parameters that were used in the calculations is provided in Table I.

Subsequently, the phonon dispersions were obtained from density functional perturbation theory (DFPT) calculations, also within ABINIT. Here, we have used a $15 \times 15 \times 9$ k -point grid for the electron wave vectors and a $5 \times 5 \times 3$ q -point grid for the phonon wave vectors. For the electronic occupation we employed Fermi-Dirac smearing with broadening factor $\sigma = 0.01$ Ha.

The results of these calculations are shown in Fig. 6. FeS is found to have phonon frequencies stretching up to 344 cm^{-1} [Fig. 6(a)], which is significantly higher than the maximum phonon value of 273 cm^{-1} obtained for FeSe [Fig. 6(b)], owing to the higher atomic mass of Se compared to S. The atom-resolved phonon densities of states (DOS) of both compounds reveal a mixture of iron and chalcogen contribution throughout the entire phonon spectrum [Figs. 6(c) and 6(d)]. Interestingly, there is a change of dominant phonon character, with the lower modes dominated by Fe in FeS, while the lower modes have predominant Se character in FeSe. This reversal can be understood from the fact that the atomic number of Fe ($Z = 26$) lies in between those of S ($Z = 16$) and Se ($Z = 34$). These differences in atomic masses lead moreover

TABLE I. Lattice parameters, obtained from x-ray diffraction measurements, used in the DFT and DFPT calculations.

Compound	a (Å)	c (Å)	z (units of c)
FeS	3.6795	5.0321	0.2578
FeSe	3.7707	5.5202	0.2671

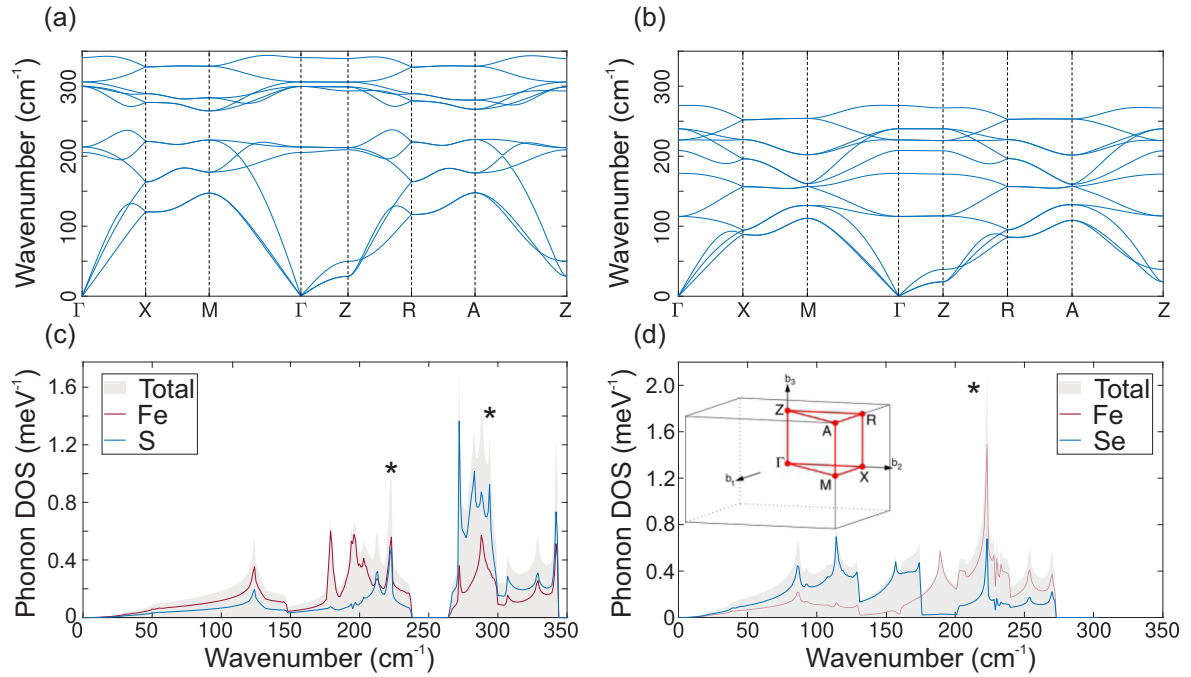


FIG. 6. Calculated phonon band structures of (a) FeS and (b) FeSe. Phonon DOS of (c) FeS and (d) FeSe, including partial contributions from Fe and S/Se. The Brillouin zone of both structures depicted in black is shown in the inset of (d), with the irreducible Brillouin zone, along which the band structures are plotted, in red [37]. The energies of the extra peaks in Fig. 7 are also indicated here by asterisks.

to a small energy gap between Fe- and S-dominated modes in FeS (between 238 and 265 cm^{-1}), which is entirely absent in FeSe.

APPENDIX B: $\text{FeSe}_{0.52}\text{S}_{0.48}$ AND FeS

For convenience we show here additional doping levels in Fig. 7. The spectrum for $x = 1$ in panel (b) was already published elsewhere [18]. Note that for $x'x'$ both A_{1g}^{ph} and B_{1g}^{ph} are projected and that the labels for the symmetry-forbidden peaks P3 and P4 are different from those in the earlier paper [18]. $x = 0.48$ [Fig. 7(a)] is in the middle between FeSe and FeS, and one can therefore expect the strongest contribution from defect-induced scattering. This interpretation is supported by the presence of structures in both configurations. All peaks resolved at $x = 0.69$ in xx configuration are also observed here. In addition there are two lines marked by asterisks which appear only at $x = 0.48$. Since they appear also for $x'x'$ we interpret them in terms of contributions from the PDOS as shown in Fig. 6 where the respective energies correspond to a high DOS of either FeSe or FeS. Structure P5 may be related to the high-energy part of FeS.

APPENDIX C: FLUCTUATION RESPONSE

The Raman response from fluctuations was studied by various authors [22,36,42]. While the experiments agree by and large, the interpretation is still controversial. Here we show that the fluctuations appear along with the two-magnon excitations at approximately 500 cm^{-1} from a frustrated spin system [22,23]. Above $x = 0.23$ we could neither observe fluctuations nor two-magnon excitations (see Fig. 4). We cannot entirely exclude that the fluctuations are masked by in-

sufficient stray-light rejection in the more disordered samples but consider it unlikely.

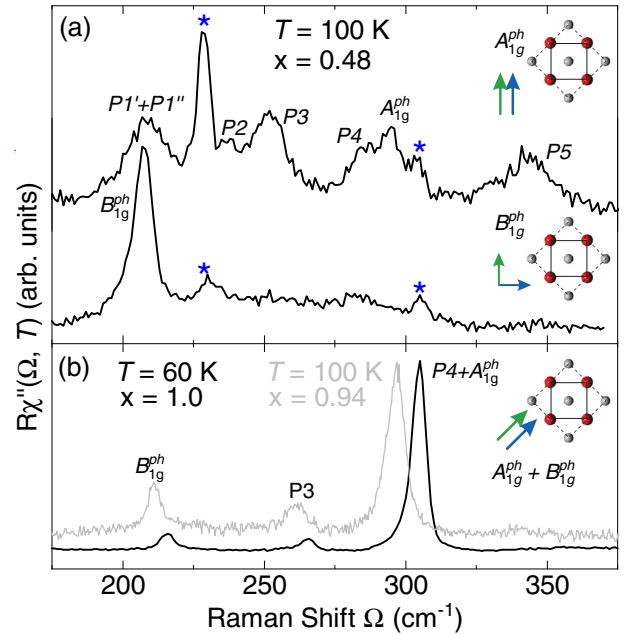


FIG. 7. $\text{FeSe}_{1-x}\text{S}_x$ for $x = 0.48$, $x = 0.94$, and $x = 1$. (a) A_{1g}^{ph} (xx) and B_{1g}^{ph} (xy) spectra for $\text{FeSe}_{0.52}\text{S}_{0.48}$. In addition to the phonons and the structures observed at the other doping levels there are two relatively sharp lines (marked by asterisks) which we associate with the PDOS. They may also arise from a nearly ordered superstructure close to 50% doping.

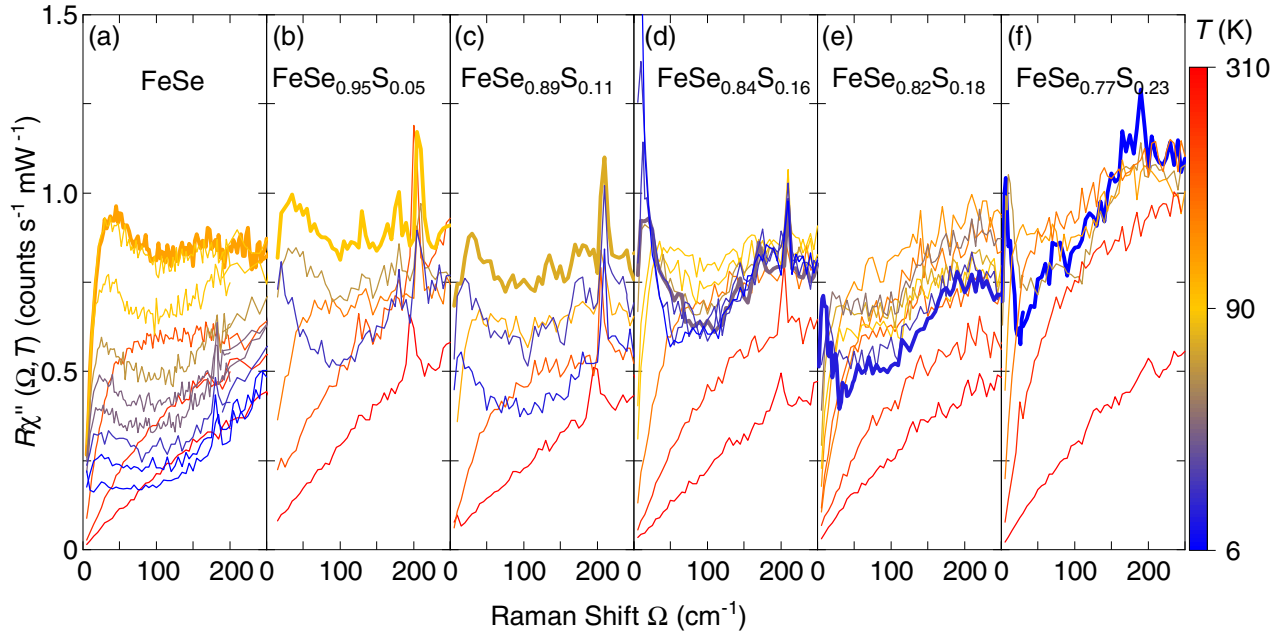


FIG. 8. Fluctuation response of $\text{FeSe}_{1-x}\text{S}_x$ for $0 \leq x \leq 0.23$. The spectra with the maximal intensity in the fluctuations are highlighted. The respective temperatures are (a) 91 K, (b) 80 K, (c) 65 K, (d) 25 K, (e) 10 K, and (f) 6 K, where 6 K was the lowest accessible temperature. The temperatures are compiled in Fig. 5 and track the transition to the nematic phase.

If excitations are very close to zero energy one encounters two difficulties: (1) The experimentally accessible quantity is the differential cross section, $d^2\sigma/(d\Omega d\omega) \propto S(q=0, \omega)$. The dynamical structure factor or Van Hove function $S(q=0, \omega)$ is related to the imaginary part of the Raman response function $\text{Im}\chi(q=0, \omega)$ through the fluctuation-dissipation theorem as $S(q=0, \omega) = \pi^{-1}\{1 + n(\omega, T)\}\text{Im}\chi(q=0, \omega)$ [43]. The Bose factor $1 + n(\omega, T)$ increases rapidly towards $\omega = 0$ for $\hbar\omega < k_B T$ and conceals all spectral features below $k_B T$. Since the fluctuation-dissipation theorem is derived on purely statistical arguments the response function contains exactly the same information as the structure factor but makes features at low energy visible. Thus it is sensible to show $\text{Im}\chi(q=0, \omega)$ rather than $S(q=0, \omega)$. (2) If the surface is not atomically flat there is stray light from insufficient rejection of the laser. The problem is aggravated

when atoms of the residual gas accumulate on the surface at low temperature. In panels (a), (b), and (d) of Fig. 8 this effect can be observed. Fortunately, it can be distinguished from the desired response which always goes through zero linearly for causality reasons. (a) In FeSe only the spectra at 10 K show a slight increase which, however, is separated from the fluctuation peak at finite energy. (b) The increase at 10 K is partially resulting from stray light but the maximal intensity is already observed at 80 K. (c) There is little contribution from stray light. (d) Here the stray light becomes strong below 20 K. In (e) and (f) the stray light is negligible.

Remarkably, the overall intensity of all spectra is approximately the same, whereas the maximal intensity in the fluctuation peak is observed at different temperatures as indicated in Fig. 8. These temperatures compare well with the boundary of the nematic phase as shown in Fig. 5.

-
- [1] D. J. Scalapino, A common thread: The pairing interaction for unconventional superconductors, *Rev. Mod. Phys.* **84**, 1383 (2012).
 - [2] E. Fradkin, S. A. Kivelson, and J. M. Tranquada, *Colloquium: Theory of intertwined orders in high temperature superconductors*, *Rev. Mod. Phys.* **87**, 457 (2015).
 - [3] S. Lederer, Y. Schattner, E. Berg, and S. A. Kivelson, Enhancement of Superconductivity near a Nematic Quantum Critical Point, *Phys. Rev. Lett.* **114**, 097001 (2015).
 - [4] A. E. Böhrer, T. Arai, F. Hardy, T. Hattori, T. Iye, T. Wolf, H. v. Löhneysen, K. Ishida, and C. Meingast, Origin of the Tetragonal-to-Orthorhombic Phase Transition in FeSe: A Combined Thermodynamic and NMR Study of Nematicity, *Phys. Rev. Lett.* **114**, 027001 (2015).
 - [5] T. M. McQueen, A. J. Williams, P. W. Stephens, J. Tao, Y. Zhu, V. Ksenofontov, F. Casper, C. Felser, and R. J. Cava, Tetragonal-to-Orthorhombic Structural Phase Transition at 90 K in the Superconductor $\text{Fe}_{1.01}\text{Se}$, *Phys. Rev. Lett.* **103**, 057002 (2009).
 - [6] M. D. Watson, T. K. Kim, A. A. Haghighirad, N. R. Davies, A. McCollam, A. Narayanan, S. F. Blake, Y. L. Chen, S. Ghannadzadeh, A. J. Schofield *et al.*, Emergence of the nematic electronic state in FeSe, *Phys. Rev. B* **91**, 155106 (2015).
 - [7] F.-C. Hsu, J.-Y. Luo, K.-W. Yeh, T.-K. Chen, T.-W. Huang, P. M. Wu, Y.-C. Lee, Y.-L. Huang, Y.-Y. Chu, D.-C. Yan, and M.-K. Wu, Superconductivity in the PbO-type structure α -FeSe, *Proc. Natl. Acad. Sci. USA* **105**, 14262 (2008).

- [8] S. Medvedev, T. M. McQueen, I. A. Troyan, T. Palasyuk, M. I. Erements, R. J. Cava, S. Naghavi, F. Casper, V. Ksenofontov, G. Wortmann, and C. Felser, Electronic and magnetic phase diagram of β -Fe_{1.01}Se with superconductivity at 36.7 K under pressure, *Nat. Mater.* **8**, 630 (2009).
- [9] Y. Sato, S. Kasahara, T. Taniguchi, X. Xing, Y. Kasahara, Y. Tokiwa, Y. Yamakawa, H. Kontani, T. Shibauchi, and Y. Matsuda, Abrupt change of the superconducting gap structure at the nematic critical point in FeSe_{1-x}S_x, *Proc. Natl. Acad. Sci. USA* **115**, 1227 (2018).
- [10] X. Lai, H. Zhang, Y. Wang, X. Wang, X. Zhang, J. Lin, and F. Huang, Observation of superconductivity in tetragonal FeS, *J. Am. Chem. Soc.* **137**, 10148 (2015).
- [11] U. Pachmayr, N. Fehn, and D. Johrendt, Structural transition and superconductivity in hydrothermally synthesized FeX (X = S, Se), *Chem. Commun.* **52**, 194 (2016).
- [12] N. Lazarević and R. Hackl, Fluctuations and pairing in Fe-based superconductors: Light scattering experiments, *J. Phys.: Condens. Matter* **32**, 413001 (2020).
- [13] S. Hohenstein, U. Pachmayr, Z. Guguchia, S. Kamusella, R. Khasanov, A. Amato, C. Baines, H.-H. Klauss, E. Morenzoni, D. Johrendt, and H. Luetkens, Coexistence of low-moment magnetism and superconductivity in tetragonal FeS and suppression of T_c under pressure, *Phys. Rev. B* **93**, 140506(R) (2016).
- [14] F. K. K. Kirschner, F. Lang, C. V. Topping, P. J. Baker, F. L. Pratt, S. E. Wright, D. N. Woodruff, S. J. Clarke, and S. J. Blundell, Robustness of superconductivity to competing magnetic phases in tetragonal FeS, *Phys. Rev. B* **94**, 134509 (2016).
- [15] A. Wang, A. Milosavljevic, A. M. M. Abeykoon, V. Ivanovski, Q. Du, A. Baum, E. Stavitski, Y. Liu, N. Lazarevic, K. Attenkofer *et al.*, Suppression of superconductivity and nematic order in Fe_{1-y}Se_{1-x}S_x ($0 \leq x \leq 1$; $y \leq 0.1$) crystals by anion height disorder, *Inorg. Chem.* **61**, 11036 (2022).
- [16] A. Wang, L. Wu, V. N. Ivanovski, J. B. Warren, J. Tian, Y. Zhu, and C. Petrovic, Critical current density and vortex pinning in tetragonal FeS_{1-x}Se_x ($x = 0, 0.06$), *Phys. Rev. B* **94**, 094506 (2016).
- [17] V. Gnezdilov, Y. G. Pashkevich, P. Lemmens, D. Wulferding, T. Shevtsova, A. Gusev, D. Chareev, and A. Vasiliev, Interplay between lattice and spin states degree of freedom in the FeSe superconductor: Dynamic spin state instabilities, *Phys. Rev. B* **87**, 144508 (2013).
- [18] A. Baum, A. Milosavljević, N. Lazarević, M. M. Radonjić, B. Nikolić, M. Mitschek, Z. I. Maranloo, M. Šćepanović, M. Grujić-Brojčin, N. Stojilović *et al.*, Phonon anomalies in FeS, *Phys. Rev. B* **97**, 054306 (2018).
- [19] M. Cardona and M. L. W. Thewalt, Isotope effects on the optical spectra of semiconductors, *Rev. Mod. Phys.* **77**, 1173 (2005).
- [20] G. Turrell, *Infrared and Raman Spectra of Crystals* (Academic, London/New York, 1972).
- [21] Y. Mizukami, M. Haze, O. Tanaka, K. Matsuura, D. Sano, J. Böker, I. Eremin, S. Kasahara, Y. Matsuda, and T. Shibauchi, Thermodynamics of transition to BCS-BEC crossover superconductivity in FeSe_{1-x}S_x, [arXiv:2105.00739](https://arxiv.org/abs/2105.00739).
- [22] A. Baum, H. N. Ruiz, N. Lazarević, Y. Wang, T. Böhm, R. Hosseinian Ahangharnejhad, P. Adelman, T. Wolf, Z. V. Popović *et al.*, Frustrated spin order and stripe fluctuations in FeSe, *Commun. Phys.* **2**, 14 (2019).
- [23] H. Ruiz, Y. Wang, B. Moritz, A. Baum, R. Hackl, and T. P. Devereaux, Frustrated magnetism from local moments in FeSe, *Phys. Rev. B* **99**, 125130 (2019).
- [24] W. Spengler and R. Kaiser, First and second order Raman scattering in transition metal compounds, *Solid State Commun.* **18**, 881 (1976).
- [25] F. Nabeshima, Y. Kawai, N. Shikama, Y. Sakishita, A. Suter, T. Prokscha, S. E. Park, S. Komiya, A. Ichinose, T. Adachi, and A. Maeda, Sulfur-induced magnetism in FeSe_{1-x}S_x thin films on LaAlO₃ revealed by muon spin rotation/relaxation, *Phys. Rev. B* **103**, 184504 (2021).
- [26] X. Yi, X. Xing, L. Qin, J. Feng, M. Li, Y. Zhang, Y. Meng, N. Zhou, Y. Sun, and Z. Shi, Hydrothermal synthesis and complete phase diagram of FeSe_{1-x}S_x ($0 \leq x \leq 1$) single crystals, *Phys. Rev. B* **103**, 144501 (2021).
- [27] J. K. Glasbrenner, I. I. Mazin, H. O. Jeschke, P. J. Hirschfeld, R. M. Fernandes, and R. Valentí, Effect of magnetic frustration on nematicity and superconductivity in iron chalcogenides, *Nat. Phys.* **11**, 953 (2015).
- [28] A. I. Coldea, Electronic nematic states tuned by isoelectronic substitution in bulk FeSe_{1-x}S_x, *Frontiers Phys.* **8**, 594500 (2021).
- [29] M. Yi, Z.-K. Liu, Y. Zhang, R. Yu, J.-X. Zhu, J. Lee, R. Moore, F. Schmitt, W. Li, S. Riggs *et al.*, Observation of universal strong orbital-dependent correlation effects in iron chalcogenides, *Nat. Commun.* **6**, 7777 (2015).
- [30] Z. P. Yin, K. Haule, and G. Kotliar, Kinetic frustration and the nature of the magnetic and paramagnetic states in iron pnictides and iron chalcogenides, *Nat. Mater.* **10**, 932 (2011).
- [31] K. M. Stadler, Z. P. Yin, J. von Delft, G. Kotliar, and A. Weichselbaum, Dynamical Mean-Field Theory Plus Numerical Renormalization-Group Study of Spin-Orbital Separation in a Three-Band Hund Metal, *Phys. Rev. Lett.* **115**, 136401 (2015).
- [32] S. L. Skornyakov, V. I. Anisimov, D. Vollhardt, and I. Leonov, Effect of electron correlations on the electronic structure and phase stability of FeSe upon lattice expansion, *Phys. Rev. B* **96**, 035137 (2017).
- [33] F. Kretzschmar, T. Böhm, U. Karahasanović, B. Muschler, A. Baum, D. Jost, J. Schmalian, S. Caprara, M. Grilli, C. Di Castro *et al.*, Critical spin fluctuations and the origin of nematic order in Ba(Fe_{1-x}Co_x)₂As₂, *Nat. Phys.* **12**, 560 (2016).
- [34] S. Chibani, D. Farina, P. Massat, M. Cazayous, A. Sacuto, T. Urata, Y. Tanabe, K. Tanigaki, A. E. Böhrer, P. C. Canfield *et al.*, Lattice-shifted nematic quantum critical point in FeSe_{1-x}S_x, *npj Quantum Mater.* **6**, 37 (2021).
- [35] U. Karahasanovic, F. Kretzschmar, T. Böhm, R. Hackl, I. Paul, Y. Gallais, and J. Schmalian, Manifestation of nematic degrees of freedom in the Raman response function of iron pnictides, *Phys. Rev. B* **92**, 075134 (2015).
- [36] W. Zhang, S. Wu, S. Kasahara, T. Shibauchi, Y. Matsuda, and G. Blumberg, Quadrupolar charge dynamics in the nonmagnetic FeSe_{1-x}S_x superconductors, *Proc. Natl. Acad. Sci. USA* **118**, e2020585118 (2021).
- [37] W. Setyawan and S. Curtarolo, High-throughput electronic band structure calculations: Challenges and tools, *Comput. Mater. Sci.* **49**, 299 (2010).
- [38] X. Gonze, B. Amadon, G. Antonius, F. Arnardi, L. Baguet, J.-M. Beuken, J. Bieder, F. Bottin, J. Bouchet, E. Bousquet *et al.*, The ABINIT project: Impact, environment and recent developments, *Comput. Phys. Commun.* **248**, 107042 (2020).

- [39] J. P. Perdew, A. Ruzsinszky, G. I. Csonka, O. A. Vydrov, G. E. Scuseria, L. A. Constantin, X. Zhou, and K. Burke, Restoring the Density-Gradient Expansion for Exchange in Solids and Surfaces, *Phys. Rev. Lett.* **100**, 136406 (2008).
- [40] D. R. Hamann, Optimized norm-conserving Vanderbilt pseudopotentials, *Phys. Rev. B* **88**, 085117 (2013).
- [41] M. van Setten, M. Giantomassi, E. Bousquet, M. Verstraete, D. Hamann, X. Gonze, and G.-M. Rignanese, The PseudoDojo: Training and grading a 85 element optimized norm-conserving pseudopotential table, *Comput. Phys. Commun.* **226**, 39 (2018).
- [42] P. Massat, D. Farina, I. Paul, S. Karlsson, P. Strobel, P. Toulemonde, M.-A. Méasson, M. Cazayous, A. Sacuto, S. Kasahara *et al.*, Charge-induced nematicity in FeSe, *Proc. Natl. Acad. Sci. USA* **113**, 9177 (2016).
- [43] L. D. Landau and E. M. Lifshitz, *Electrodynamics of Continuous Media* (Pergamon, Oxford, 1960), p. 377.



Structural and optical characterization of titanium–carbide and polymethyl methacrylate based nanocomposite

Jelena Pešić¹ · Andrijana Šolajić¹ · Jelena Mitrić¹ · Martina Gilić¹ · Ivan Pešić² · Novica Paunović¹ · Nebojša Romčević¹

Received: 11 October 2021 / Accepted: 10 March 2022 / Published online: 12 May 2022

© The Author(s), under exclusive licence to Springer Science+Business Media, LLC, part of Springer Nature 2022

Abstract

The rich chemistries and unique morphologies of titanium carbide MXenes, made them strong candidates for many applications like sensors and electronic device materials. During the synthesis procedure, chemical etching, oxidation occurs and residual materials, like titanium-dioxide nanocrystals and nanosheets are often present in resulting material. As titanium-carbide MXenes are suggested to be used as additive in organic polymer matrices for production of nanocomposites, it is essential to consider the presence of the oxides and other residuals together with MXene flakes in synthesis results, and consequently in produced nanocomposite. In this study we present structural and optical characterization of such polymer nanocomposite titanium carbide/PMMA (Polymethyl methacrylate) consisting of Ti_3C_2 , TiC_2 MXenes and TiC , and TiO_2 residues of synthesis in PMMA matrix, as a multicomponent nanocomposite. Using XRD, infra-red and Raman spectroscopy, followed by comparative study on the vibrational properties using density functional theory calculations, we characterize this nanocomposite. Further, the SEM measurements are performed, demonstrating the produced titanium-carbide-based flakes in nanocomposite are well defined and separated to nanosized grains, allowing us to use Maxwell–Garnet model to analyse infrared spectrum. This enables us to determine the presence of the optical modification of polymer matrices corresponding to a volume fraction of 0.25.

Keywords Titanium-carbide nanoparticles · PMMA composite · Multicomponent nanocomposite

This article is part of the Topical Collection on Photonics:Current Challenges and Emerging Applications.

Guest edited by Jelena Radovanovic, Dragan Indjin, Maja Nesic, Nikola Vukovic and Milena Milosevic.

✉ Jelena Pešić
yelena@ipb.ac.rs

¹ Institute of Physics Belgrade, University of Belgrade, Pregrevica 118, Belgrade 11080, Serbia

² Faculty of Technology and Metallurgy, University of Belgrade, Belgrade 11000, Serbia

1 Introduction

Nanocomposites are the combination of two or more different materials where a minimum of one of the components has dimension less than 100 nm Twardowski (2007). The polymer nanocomposites are made of organic polymer matrix (in this research, polymethyl methacrylate—PMMA) and inorganic components (titanium carbide nanoparticles). The properties of the obtained nanocomposites depend on the individual properties of each component, morphology and the interface characteristics. In an attempt to improve the properties of conventional polymer materials and extend the fields of their applications, functionalization has emerged as important method in improvement of their not satisfactory electronic, thermal and mechanical properties Tamborra et al. (2004); Hussain et al. (2006). In addition to typical advantages of polymers (such are light-weight, low cost, and good processability), the improvement of electrical properties (e.g., electrical conductivity) with the addition of a small amount of conductive fillers into polymer matrices have promoted polymer nanocomposites into versatile multifunctional materials. Many applications like household electronics, memory and microwave devices are potentially available with addition of metal oxide nanoparticles to polymer. This enables the modification of the polymer's physical properties as well as the implementation of new features in the polymer matrix creating new type of materials known as the polymer nanocomposites. PMMA as a thermoplastic polymer, has many extraordinary properties, like great transparency and ultraviolet resistance, high abrasion resistance, hardness and stiffness and making it widely used in many applications ranging from everyday items to high tech devices. Further, PMMA is nondegradable and biocompatible which makes it an excellent candidate in medical applications like tissue engineering with typical applications such as fracture fixation, intraocular lenses and dentures Peppas and Langer (1994).

Multicomponent nanocomposites based of layered and 2D materials have drawn significant attention in past decade with promises of various applications. Reduction of dimensionality of the system to the truly atomic-scale 2D is related to the occurrence of all new amazing properties in low-dimensional material, since the reduction of available phase space and decreased screening lead to enhancement of quantum effects and increased correlations. Low-dimensional materials have been studied intensively both for their fundamental properties and insight in basic principles of matter but as well for their colossal potential for applications. A discovery of true two-dimensional material graphene Novoselov et al. (2004) and its remarkable properties like and experimental observation of Klein tunnelling, quantum Hall effect and superconductivity Novoselov et al. (2004); Katsnelson et al. (2006); Zhang et al. (2005); Durajski et al. (2019); Pešić et al. (2014); Margine et al. (2016); Durajski et al. (2020) paved the way for investigation of a new family of materials in low-dimensional physics. The new field of two-dimensional materials research has arose and investigated not only graphene but many more crystal structures where, just like in graphene, cells are connected in at least one direction by the van der Waals' forces Novoselov et al. (2016).

Transition metal carbides are important group of materials for applications since they possess some desired characteristics such as thermal stability, wear and corrosion resistance, electronic, magnetic as well as catalytic properties. Titanium-carbide powders are generally used for manufacturing cutting tools, used in treatment of metals and as abrasive-resistant materials. In 2011 Naguib et al. (2011), the group of early transition metal carbides and/or carbo-nitrides labeled as MXenes. MXenes are produced by the etching out of the A layers from MAX phases Naguib et al. (2011, 2012, 2013). Name MAX phase

comes from its chemical composition: $M_{n+1}AX_n$, where M is an early transition metal, A is mainly a group IIIA or IVA (i.e., groups 13 or 14) element, X is carbon and/or nitrogen, and $n = 1, 2$, or 3 .

During the synthesis of titanium-carbide MXenes by chemical etching, oxidation can occur which results in presence of TiO_2 consisted of nanosheets and numerous TiO_2 nanocrystals Naguib et al. (2014). There are several studies Zhu et al. (2016); Gao et al. (2015) whose researched is focused in possible applications of TiO_2 -MXene structures. It is demonstrated the joint effects of Ti_3C_2 and TiO_2 endowed TiO_2 - Ti_3C_2 nanocomposites with excellent properties and improved functionalities Zhu et al. (2016). In this work we investigate the structural and optical properties of polymer nanocomposites prepared by the incorporation of titanium-carbide nanoparticles consisting of Ti_3C_2 , TiC_2 TiC and TiO_2 into the matrices of polymer PMMA. The sample of nanocomposite material was prepared, the PMMA matrix with titanium-carbide particles, PMMA/ TiC . As for similar materials Shan et al. (2021, 2020, 2021); Tan et al. (2021); Jafari et al. (2020); Tan et al. (2021) proper understanding of composition of materials used in composite is crucial and XRD analysis for the titanium-carbide flakes. The structural and morphology studies of the nanocomposites were carried out by SEM and Raman spectroscopy. Infrared spectroscopy is a very powerful technique in analysis of various nanoparticle and nanocomposite materials prepared in various techniques Dastan (2015); Dastan and Chaure (2014); Dastan et al. (2014); Dastan and Chaure (2017). To further understand properties of our inhomogeneous nanocomposite we used infrared spectroscopy with Maxwell–Garnet model. To further support optical characterization, calculations based on density functional theory were performed.

2 Samples preparation and structural characterization

2.1 Titan-carbide/PMMA composite synthesis

In this work, titanium-carbide/PMMA nanocomposite sample was made from mixture of MXene based titanium-carbide nanoflakes in PMMA matrix. Production of layered titanium-carbide flakes is based on MXene synthesis by selective etching of Al atomic layers from Ti_3AlC_2 MAX phase, we used the so-called 'mild' method with lithium fluoride (LiF) and hydrochloric acid (HCl) Tu et al. (2018). This method was described in Naguib et al. (2011). Procedure of composite preparation is described in Fig. 1.

Commercially available PMMA Acryrex CM205 (Chi Mei Corp. Korea, ($M_w \approx 90400$ g/mol, $n = 1.49$, $\lambda = 633$ nm) pellets were used as a matrix for sample preparation. Ti_3AlC_2 MAX phase was processed and kindly donated from Layered Solids Group, Drexel University. Titanium-carbide flakes were obtained by sonification in the water and drying the supernatant in a Petri dish in the oven for 30 minutes on $90^\circ C$.

Composite was prepared with 10 wt% PMMA solution in acetone (Carlo Erbe Reagents, Spain) and added dried titanium-carbide flakes. After stirring the solution was poured in Petri dish Cao et al. (2017) and dried in oven 24h on $40^\circ C$. Content of titanium-carbide flakes in the sample was 1.7 wt%.

The morphology of the produced composite has been investigated by FESEM using high resolution electron microscope MIRA3 TESCAN. Samples display separated nano-sized grains. Fig. 2a presents FESEM image of MXene flakes delaminated in water showing morphology of obtained flakes, b FESEM image of the PMMA/titanium-carbide

Fig. 1 Schematic describing the synthesis process of MXenes from MAX phases and preparation of composite

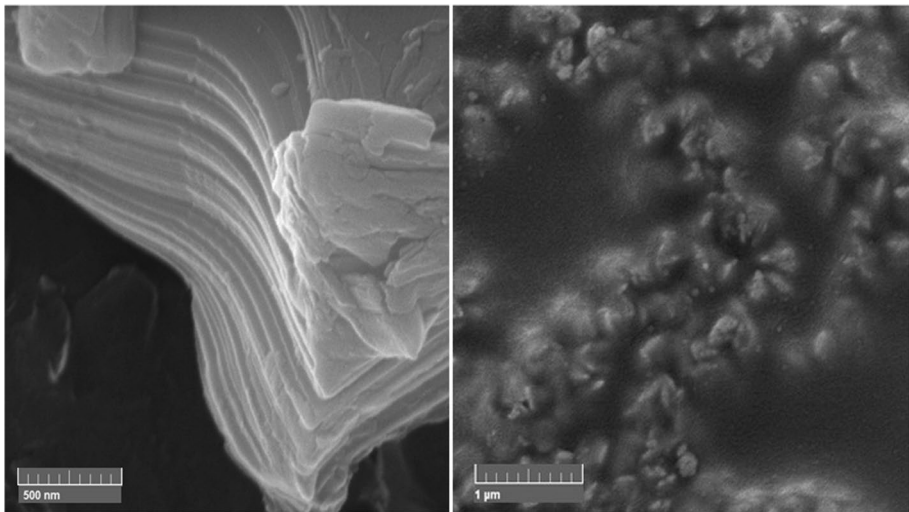
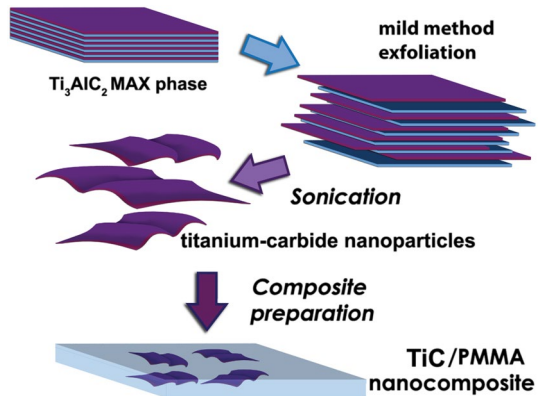


Fig. 2 FESEM photos of **a** Flakes delaminated in water; **b** PMMA composite prepared with titanium-carbide flakes

nanocomposite. Characteristic layered structure of MXenes is visible on FESEM image and confirming success of delamination and exfoliation procedures. Obtained flakes demonstrate multilayered structure with few μm in diameter. In Fig. 2b typical accordion like structure can be indicated in nanosize grain-like structures, clustered in PMMA matrix.

2.2 XRD

X-ray diffraction powder (XRD) technique was used to determine structural characteristics of titanium-carbide based flakes to be used in composites. Philips PW 1050 diffractometer equipped with a PW 1730 generator was used. The same conditions were used for all samples, 40 kV \times 20 mA, using Ni filtered Co $K\alpha$ radiation of 0.1778897 nm at room temperature. Measurements were carried out in the 2θ range of 20–80° with a scanning step

Fig. 3 XRD pattern for titanium-carbide flakes, starting material for PMMA/TiC composite

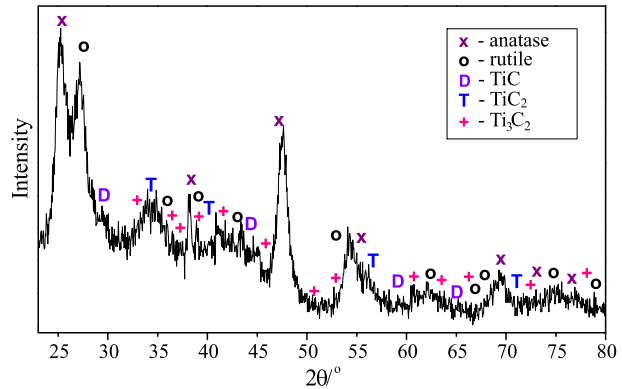
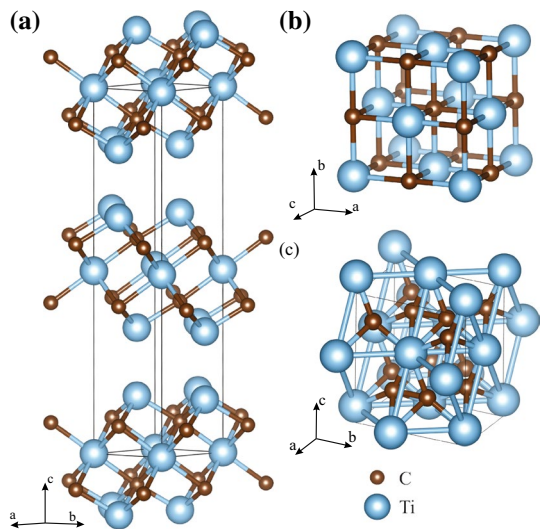


Fig. 4 Schematic representation of Titanium-carbide structures present at composite **a** Ti_3C_2 , **b** TiC and **c** TiC_2



of 0.05° and 10 s scanning time per step. In Fig. 3 is presented XRD pattern for titanium-carbide flakes, starting material for composite. The different phases of titanium carbide can be noticed from diffractogram— Ti_3C_2 , TiC and TiC_2 together with TiO_2 . TiO_2 is widely present as anatase and rutile and it is confirmed that they belong to space groups $P6_3/mmc$ (194), $Fm\bar{3}m$ (225) $Fm2m$ (42), $I4_1/amd$ (141), $P4_2/mnm$ (136), respectively. The unit cells of MXene structures Ti_3C_2 , TiC and TiC_2 are presented in Fig. 4. These structures were further used in DFT analysis of optical spectroscopy results in Sect. 3.3.

3 Results and discussion

3.1 Raman spectroscopy

The micro-Raman spectra were taken in the backscattering configuration and analyzed by the TriVista 557 system equipped with a nitrogen cooled charge-coupled-device

detector. As an excitation source, we used the 532 nm line of Ti:Sapphire laser. Excitation energy is in the off-resonance regime for all the considered materials. The Raman spectra of the PMMA, PMMA/TiC, and titanium-carbide flakes, measured in the spectral range of 100–1100 cm^{-1} at room temperature, are presented in Fig. 5.

The Raman spectrum of PMMA is presented in Fig. 5a. Intense modes at 235, 300, 362, 400, 484, 560, 603, 660, 733, 815, 839, 864, 911, 967, 985, 1063 and 1091 cm^{-1} were detected. The obtained results are in a good agreement with the values given in the literature Willis et al. (1969); Thomas et al. (2008); Ćurčić et al. (2020).

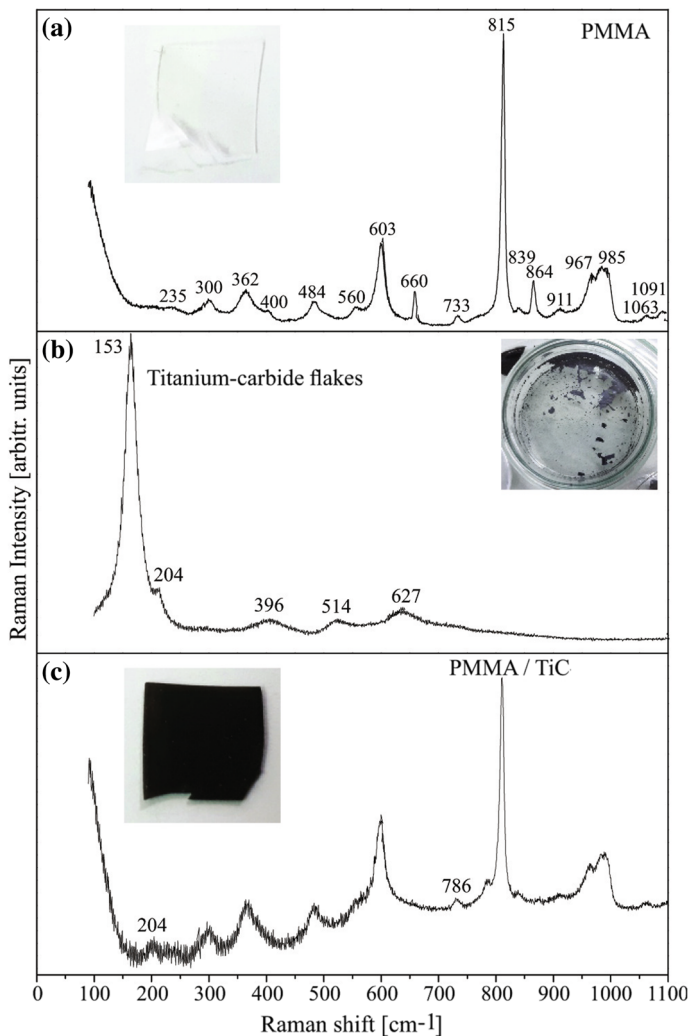


Fig. 5 Raman spectra with photo of the sample of **a** PMMA, **b** Titanium-carbide flakes, **c** PMMA/TiC composite. Only titanium-carbide related peaks are marked in this spectrum. Unassigned peaks correspond to PMMA from **a** spectrum

In Fig. 5b spectrum of titanium-carbide flakes after etching procedure is presented. Several characteristic peaks can be distinguished on 153 cm^{-1} , 204 cm^{-1} , 396 cm^{-1} , 514 cm^{-1} and 627 cm^{-1} . Peaks at 153 cm^{-1} and 627 cm^{-1} correspond to doubly degenerated E_{2g} modes of Ti_3C_2 . The frequency associated with E_{2g} modes is calculated to be at 161 cm^{-1} for the bare Ti_3C_2 . Since their main contribution is from in-plane vibrations of Ti and C atoms, it can be influenced by the vibrations of the terminal atoms (as a residue of synthesis procedure) weaken the in-plane motion of the Ti and C atoms, hence there is shift to lower frequency. The terminal groups play significant roles for the vibrational modes: the terminal atoms weakening the motions in which the surface Ti atoms are involved while strengthening the out-of-plane vibration of the C atoms; the corresponding vibrational frequencies dramatically change with the various terminal atoms Zhao et al. (2016). This is consistent with XRD results suggesting significant amount of TiO_2 as a residue of synthesis procedure as described in introduction. This can be also visible in Raman spectrum of titanium-carbide flakes on 204 cm^{-1} and 514 cm^{-1} . The doubly degenerated modes at 621 cm^{-1} correspond to the in-plane vibration of the C atoms Hu et al. (2015). In Fig. 5c spectrum of PMMA/TiC is presented, only titanium-carbide related peaks at 204 and 786 cm^{-1} are marked in this spectrum. Unassigned peaks correspond to PMMA peaks marked on a) panel.

As XRD analysis demonstrated, obtained flakes contain both MXene flakes and titanium-dioxide as the residue of synthesis procedure. To further understand and assign this spectra we performed theoretical analysis of all materials identified in XRD pattern using density functional theory calculations. Calculations provided us a guide for identification of peaks and all results are summarized in Table 1.

3.2 Far-infrared spectroscopy

Far-infrared reflection spectra were measured at room temperature in the spectral range from 40 to 600 cm^{-1} , carried out with a BOMEM DA 8 spectrometer. The experimental data are represented at Fig. 6a and by circles at Fig. 6b–d. As expected, the reflection spectra of nanocomposites are by intensity placed between the starting composites. In order to analyse far-infrared spectra we have used the classical oscillator model with free carrier contribution, as a base for Maxwell–Garnet effective medium approximation Abstreiter (1984); Carter and Bate (1971). The low-frequency dielectric properties of single crystals are described by classical oscillators corresponding to the TO modes, to which the Drude part is superimposed to take into account the free carrier contribution:

$$\epsilon_s(\omega) = \epsilon_\infty + \sum_{k=1}^l \frac{\epsilon_\infty S_k}{\omega_{TOk}^2 - \omega^2 - i\gamma_{TOk}\omega} - \frac{\epsilon_\infty \omega_p^2}{\omega(\omega + i\Gamma_p)}, \quad (1)$$

where ϵ_∞ is the bound charge contribution and it is assumed to be a constant, ω_{TOk}^2 is the transverse optical-phonon frequency, ω_p^2 the plasma frequency, γ_{TOk} is damping, Γ_p is the plasmon mode damping coefficient, and S_k is the oscillator strength.

In general, the optical properties of an inhomogeneous material are described by the complex dielectric function that depends on 3D distribution of constituents. The investigated mixture consists of two materials with two different dielectric components. One is treated as a host, and the other as the inclusions. The characterization of the inhomogeneous material by the two dielectric functions is not useful, since one need to know the exact geometrical arrangement of the constituents of the material. However, if the wavelength of

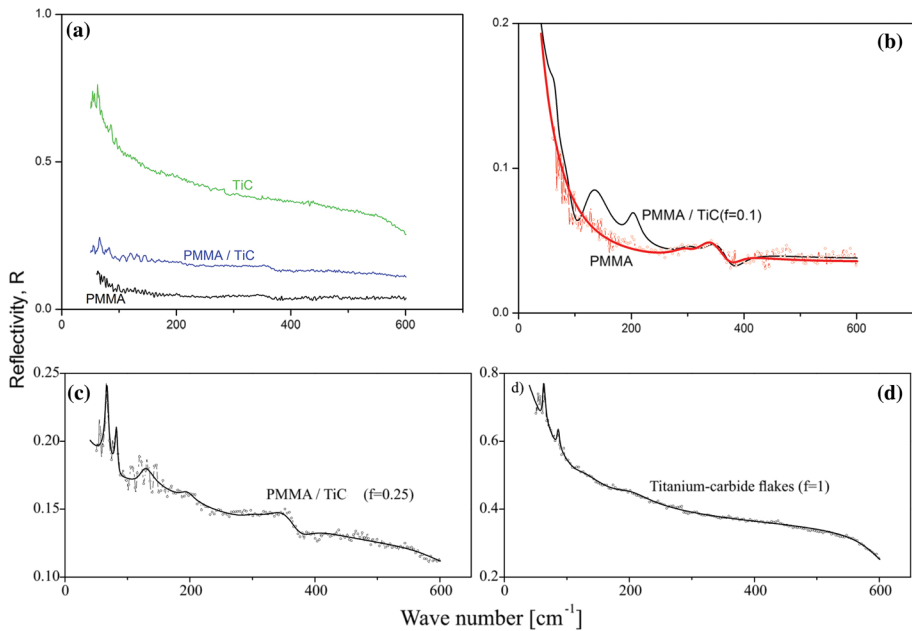


Fig. 6 Infrared analysis: **a** Infrared spectra of Titanium-carbide flakes (green) and composites PMMA/TiC (blue) and pure PMMA (black), **b**, **c**, and **d** circles represent experimental data and solid lines are fit obtained by Maxwell–Garnet model as described in Sect. 3.2

Table 1 Raman and infrared spectrum analysis and modes assignation for synthesized titanium-carbide flakes and PMMA/TiC composite

Titanium-carbide flakes		PMMA/TiC		Description
Raman	IR	Raman	IR	
ω_1	62.4	66		E_u , Ti_3C_2
ω_2	85.8	81		B_1 , TiO_2 rutile
ω_3	119	127		A_{2u} , Ti_3C_2 and B_1 TiC_2
ω_4	153			E_g , Ti_3C_2
ω_5	204	204	195	E , TiO_2 anatase
ω_6	396			A_2 , TiC_2 ; E , TiO_2 anatase
ω_7	514			A_1 , TiO_2 anatase
ω_8	620		615	E_u , Ti_3C_2
ω_9	627			E_g , Ti_3C_2
ω_{10}		786		A_g , TiO_2 rutile
ω_p	80		150	
f	1		0.25	

Infrared modes fit is obtained by Maxwell–Garnet model. Modes assignation is performed using values obtained in DFT calculations

the electromagnetic radiation is much larger than the size of inclusions, classical theories of inhomogeneous material presume that the material can be treated as a homogeneous substance with an effective dielectric function. In the literature, many mixing models can

be found for the effective permittivity of such mixture. Some are present in ref Sihvola (1999). Optical properties of such materials depend upon the properties of constituents, as well as their volume fraction. Since our samples are well defined and separated nanosized grains (as demonstrated on FESEM images, Fig. 2), we used Maxwell–Garnet model for present case. For the spherical inclusions case, the prediction of the effective permittivity of mixture, ϵ_{eff} , according to the Maxwell–Garnet mixing rule is Garnett (1904):

$$\epsilon_{eff} = \epsilon_1 + 3f\epsilon_1 \frac{\epsilon_2 - \epsilon_1}{\epsilon_2 + 2\epsilon_1 - f(\epsilon_2 - \epsilon_1)} \quad (2)$$

Here, spheres of permittivity ϵ_2 (Titanium-carbide) are located randomly in homogeneous environment ϵ_1 (PMMA) and occupy a volume fraction f .

Solid lines in Fig. 6 are calculated spectra obtained by a fitting procedure based on the previously presented model. The agreement of the theoretical model obtained in this manner with the experimental results is excellent.

To demonstrate the model, together with the infrared spectrum of PMMA, Fig. 6b is given the theoretical spectrum of PMMA/TiC nanocomposites for $f = 0.1$. The properties of TiC structures are clearly visible. A larger share of TiC structures leads to the spectrum in Fig 6c, which was obtained for $f = 0.25$. In Fig. 6d, for $f=1$ of course there is no effect from PMMA.

3.3 Discussion

In Table 1 are summarized results from spectroscopic measurements of obtained nanocomposites. As stated above, for infrared measurements the agreement of the theoretical model with obtained spectra is excellent and best fit parameters are presented in this table.

To further support our results we performed DFT based calculations and calculated vibrational frequencies in Γ point for all materials present after titanium-carbide flakes exfoliation, which we determined are present using XRD, Fig. 3. Obtained values are compared to experimental Raman and infrared spectrum and modes have been assigned. Results are summarized in Table 1. We presented only modes that can be assigned to peaks from the spectra. In infrared spectra we can notice good agreement with theoretical calculations, specially for low-energy E_u and A_{2u} mode of Ti_3C_2 which is present the composite spectrum (Fig. 6b, c) as in starting titanium-carbide material (Fig. 6d). As shown in XRD we notice peaks originating from TiO_2 and TiC_2 in mid-energy region. High-energy mode E_u on 620 cm^{-1} is present in spectrum of PMMA/TiC. In Table 2 are summarized calculated optical modes for Ti_3C_2 with symmetry 194 group used in analysis.

DFT calculations were performed using the Quantum Espresso software package Gianozzi (2009), based on the plane waves and pseudopotentials. The PBE (Perdew, Burke and Ernzerhof) Perdew et al. (1996) exchange-correlation functional was employed and PAW (Projector augmented waves) pseudopotentials were used. Energy cutoff for wavefunctions and charge density were set to 52 Ry and 575 Ry to ensure the convergence. The Brillouin zone was sampled using the Monkhorst-Pack scheme, with $8 \times 8 \times 8$ k-points mesh for TiC_2 , $8 \times 8 \times 4$ for Ti_3C_2 , $12 \times 12 \times 12$ for TiC, and $8 \times 8 \times 8$ for TiO_2 (Rutile and Anatase structures). Phonon frequencies are calculated within the DPFT (Density Functional Perturbation Theory) implemented in Quantum Espresso Baroni et al. (2001). In order to obtain the lattice parameters more accurately, van der Waals forces were treated using the Grimme-D2 correction Grimme (2006)

Table 2 Vibrational modes for Ti_3C_2 with symmetry group 194, calculated from the measured data

Ti_3C_2 (P6 ₃ /mmc)		
cm^{-1}	Symmetry	Raman or IR active
65.0	E_u	I
135.2	A_{2u}	I
160.6	E_g	R
161.4	E_g	R
229.9	A_{1g}	R
269.3	A_{1g}	R
271.1	E_u	I
271.7	E_u	I
371.4	A_{2u}	I
382.4	A_{2u}	I
549.1	A_{2u}	I
554.4	A_{2u}	I
611.2	E_g	R
620.4	E_g	R
624.1	E_u	I
626.4	E_u	I
653.2	A_{1g}	R
658.3	A_{1g}	R

Optical spectroscopy results supported with the DFT numerical calculation confirm that produced composites PMMA/TiC show optical modification comparing to pure PMMA. Our X-ray diffraction investigation of synthesized nanomaterials identified presence of Ti_3C_2 and TiC_2 MXenes and residual TiO_2 and TiC from the synthesis procedure, which can be also supported from the optical spectroscopy results.

4 Conclusion

In this paper, we present results of optical and structural investigation of composite based on titanium-carbide nanoflakes (Ti_3C_2 , TiC_2 TiC and TiO_2) in PMMA matrix. X-ray diffraction (XRD) investigation of synthesized nanomaterials identified presence of Ti_3C_2 and TiC_2 MXenes and residual TiO_2 and TiC from the synthesis procedure. The optical properties were studied by Raman and infrared spectroscopy at room temperature. The analysis of the Raman spectra was made by the fitting procedure. For analysis of infrared spectra we used Maxwell–Garnet model. In order to identify and assign vibrational modes, vibrational frequencies of all identified materials were calculated using density functional theory, and compared with experimental results. We confirmed optical modification in composite structure compared to pure PMMA. Further analysis that goes beyond the scope of this publication studies mechanical properties of composite materials, confirming improvements compared to pure PMMA. The obtained composite showed enhanced hardness, elastic modulus and tensile strength compared with pure PMMA Pesic et al. (2019).

Acknowledgements The authors acknowledge funding provided by the Institute of Physics Belgrade and Faculty of Technology and Metallurgy, through the grant by the Ministry of Education, Science and Technological Development of the Republic of Serbia. All calculations were performed using computational resources at Johannes Kepler University, Linz, Austria.

Author Contributions Conceptualization, JP and NR; investigation JP, AŠ, JM, MG, IP, NP; validation, JP, NP, NR; formal analysis, JP, AŠ, JM, MG, NP, NR; writing JP and AŠ; writing–review and editing, JP, AŠ, NP, NR; visualization, AŠ; supervision, NR; project administration, NR; funding acquisition, NR. All authors have read and agreed to the published version of the manuscript.

Funding The authors acknowledge funding provided by the Institute of Physics Belgrade and Faculty of Technology and Metallurgy, through the grant by the Ministry of Education, Science and Technological Development of the Republic of Serbia.

Data availability All additional material is available at authors on request.

Code availability Not applicable.

Declarations

Conflict of interest The Authors declare no conflict of interest.

Ethical approval Not applicable.

Informed consent Not applicable.

Consent for publication All authors consent to publication results presented in manuscript.

References

- Abstreiter, G.: Light Scattering in Solids IV. Springer, New York (1984)
- Baroni, S., de Gironcoli, S., Dal Corso, A., Giannozzi, P.: Phonons and related crystal properties from density-functional perturbation theory. *Rev. Mod. Phys.* **73**, 515–562 (2001)
- Cao, Y., Deng, Q., Liu, Z., Shen, D., Wang, T., Huang, Q., Du, S., Jiang, N., Lin, C.-T., Yu, J.: Enhanced thermal properties of poly (vinylidene fluoride) composites with ultrathin nanosheets of mxene. *RSC Adv.* **7**(33), 20494–20501 (2017)
- Carter, D.L., Bate, R.T.: The Physics of Semimetals and Narrow-gap Semiconductors: Proceedings, vol. 32. Pergamon, Texas, USA (1971)
- Ćurčić, M., Hadžić, B., Gilić, M., Radojević, V., Bjelajac, A., Radović, I., Timotjević, D., Romčević, M., Trajić, J., Romcevic, N.: Surface optical phonon (sop) mode in ZnS/poly (methylmethacrylate) nanocomposites. *Physica E* **115**, 113708 (2020)
- Dastan, D.: Nanostructured anatase titania thin films prepared by sol-gel dip coating technique. *J. Atom. Mol. Condens. Matter Nano Phys.* **2**, 109–114 (2015)
- Dastan, D., Chaure, N.B.: Influence of surfactants on TiO₂ nanoparticles grown by sol-gel technique. *Int. J. Mater. Mech. Manuf.* **2**, 21 (2014)
- Dastan, D., Chaure, N.: Kartha: Surfactants assisted solvothermal derived titania nanoparticles: synthesis and simulation. *J. Mater. Sci.* **28**, 7784–7796 (2017)
- Dastan, D., Londhe, P.U., Chaure, N.B.: Characterization of TiO₂ nanoparticles prepared using different surfactants by sol-gel method. *J. Mater. Sci.* **25**, 3473–3479 (2014)
- Durajski, A.P., Skoczylas, K.M., Szczaniak, R.: Superconductivity in bilayer graphene intercalated with alkali and alkaline earth metals. *Phys. Chem. Chem. Phys.* **21**, 5925–5931 (2019). <https://doi.org/10.1039/C9CP00176J>
- Durajski, A.P., Augusciak, A.E., Szczaniak, R.: Tunable electronic and magnetic properties of substitutionally doped graphene. *Physica E* **119**, 113985 (2020). <https://doi.org/10.1016/j.physe.2020.113985>
- Gao, Y., Wang, L., Zhou, A., Li, Z., Chen, J., Bala, H., Hu, Q., Cao, X.: Hydrothermal synthesis of TiO₂/Ti₃C₂ nanocomposites with enhanced photocatalytic activity. *Mater. Lett.* **150**, 62–64 (2015)

- Garnett, J.M.: XII. Colours in metal glasses and in metallic films. *Philosoph. Trans. R. Soc. Lond. Ser. A* **203**, 385–420 (1904)
- Giannozzi, P., et al.: QUANTUM ESPRESSO: a modular and open-source software project for quantum simulations of materials. *J. Phys. Condens. Matter* **21**(39), 395502 (2009)
- Grimme, S.: Semiempirical GGA-type density functional constructed with a long-range dispersion correction. *J. Comput. Chem.* **27**(15), 1787–1799 (2006)
- Hu, T., Wang, J., Zhang, H., Li, Z., Hu, M., Wang, X.: Vibrational properties of ti_3c_2 and $\text{ti}_3\text{c}_2\text{t}_2$ ($\text{t} = \text{o}, \text{f}, \text{oh}$) monosheets by first-principles calculations: a comparative study. *Phys. Chem. Chem. Phys.* **17**(15), 9997–10003 (2015)
- Hussain, F., Hojjati, M., Okamoto, M., Gorga, R.E.: Review article: polymer-matrix nanocomposites, processing, manufacturing, and application: an overview. *J. Compos. Mater.* **40**(17), 1511–1575 (2006). <https://doi.org/10.1177/0021998306067321>
- Jafari, A., Tahani, K., Dastan, D., Asgary, S., Shi, Z., Yin, X.-T., Zhou, W.-D., Garmestani, H.: Ştefan Ţălu: Ion implantation of copper oxide thin films; statistical and experimental results. *Surf. Interfaces* **18**, 100463 (2020)
- Katsnelson, M.I., Novoselov, K.S., Geim, A.K.: Chiral tunnelling and the Klein paradox in graphene. *Nat. Phys.* **2**, 620–625 (2006)
- Margine, E.R., Lambert, H., Giustino, F.: Electron-phonon interaction and pairing mechanism in superconducting ca-intercalated bilayer graphene. *Sci. Rep.* **6**, 21414 (2016)
- Naguib, M., Kurtoglu, M., Presser, V., Lu, J., Niu, J., Heon, M., Hultman, L., Gogotsi, Y., Barsoum, M.W.: Two-dimensional nanocrystals produced by exfoliation of ti_3alc_2 . *Adv. Mater.* **23**(37), 4248–4253 (2011). <https://doi.org/10.1002/adma.201102306>
- Naguib, M., Mashtalir, O., Carle, J., Presser, V., Lu, J., Hultman, L., Gogotsi, Y., Barsoum, M.W.: Two-dimensional transition metal carbides. *ACS Nano* **6**(2), 1322–1331 (2012). <https://doi.org/10.1021/nn204153h>
- Naguib, M., Halim, J., Lu, J., Cook, K.M., Hultman, L., Gogotsi, Y., Barsoum, M.W.: New two-dimensional niobium and vanadium carbides as promising materials for li-ion batteries. *J. Am. Chem. Soc.* **135**(43), 15966–15969 (2013). <https://doi.org/10.1021/ja405735d>
- Naguib, M., Mashtalir, O., Lukatskaya, M.R., Dyatkin, B., Zhang, C., Presser, V., Gogotsi, Y., Barsoum, M.W.: One-step synthesis of nanocrystalline transition metal oxides on thin sheets of disordered graphitic carbon by oxidation of mxenes. *Chem. Commun.* **50**, 7420–7423 (2014)
- Novoselov, K.S., Geim, A.K., Morozov, S.V., Jiang, D., Zhang, Y., Dubonos, S.V., Grigorieva, I.V., Firsov, A.A.: Electric field effect in atomically thin carbon films. *Science* **306**(5696), 666–669 (2004). <https://doi.org/10.1126/science.1102896>
- Novoselov, K.S., Mishchenko, A., Carvalho, A., Castro Neto, A.H.: 2d materials and van der Waals heterostructures. *Science* **353**, 6298 (2016). <https://doi.org/10.1126/science.aac9439>
- Peppas, N., Langer, R.: New challenges in biomaterials. *Science* **263**(5154), 1715–1720 (1994). <https://doi.org/10.1126/science.8134835>
- Perdew, J.P., Burke, K., Ernzerhof, M.: Generalized gradient approximation made simple. *Phys. Rev. Lett.* **77**, 3865–3868 (1996)
- Pesic, I., Radojevic, V., Barsoum, N. M. Tomic, Romcevic, N.: Preparation, characterization and mechanical properties of mxene/pmma composite. *TechConnect World Innovation Conference and Expo*, Boston, MA, USA. <https://www.techconnectworld.com/World2019/wednesday.htmlW6.26> (2019)
- Pešić, J., Gajić, R., Hingerl, K., Belić, M.: Strain-enhanced superconductivity in li-doped graphene. *EPL (Europhys. Lett.)* **108**(6), 67005 (2014). <https://doi.org/10.1209/0295-5075/108/67005>
- Shan, K., Yi, Z.-Z., Yin, X.-T., Dastan, D., Dadkhah, S., Coates, B.T., Garmestani, H.: Mixed conductivities of a-site deficient Y, Cr-doubly doped srTiO_3 as novel dense diffusion barrier and temperature-independent limiting current oxygen sensors. *Adv. Powder Technol.* **31**(12), 4657–4664 (2020)
- Shan, K., Yi, Z.-Z., Yin, X.-T., Cui, L., Dastan, D., Garmestani, H., Alamgir, F.M.: Diffusion kinetics mechanism of oxygen ion in dense diffusion barrier limiting current oxygen sensors. *J. Alloy. Compd.* **855**, 157465 (2021)
- Shan, K., Zhai, F., Yi, Z.-Z., Yin, X.-T., Dastan, D., Tajabadi, F., Jafari, A., Abbasi, S.: Mixed conductivity and the conduction mechanism of the orthorhombic CAZRO_3 based materials. *Surf. Interfaces* **23**, 100905 (2021)
- Sihvola, A.H.: *Electromagnetic Mixing Formulas and Applications*, vol. 47. IET, UK (1999)
- Tamborra, M., Striccoli, M., Comparelli, R., Curri, M., Petrella, A., Agostiano, A.: Optical properties of hybrid composites based on highly luminescent CDS nanocrystals in polymer. *Nanotechnology* **15**(4), 240 (2004)

- Tan, G.-L., Tang, D., Dastan, D., Jafari, A., Shi, Z., Chu, Q.-Q., Silva, J.P.B., Yin, X.-T.: Structures, morphological control, and antibacterial performance of tungsten oxide thin films. *Ceram. Int.* **47**(12), 17153–17160 (2021)
- Tan, G.-L., Tang, D., Dastan, D., Jafari, A., Silva, J.P.B., Yin, X.-T.: Effect of heat treatment on electrical and surface properties of tungsten oxide thin films grown by HFCVD technique. *Mater. Sci. Semicond. Process.* **122**, 105506 (2021)
- Thomas, K., Sheeba, M., Nampoori, V., Vallabhan, C., Radhakrishnan, P.: Raman spectra of polymethyl methacrylate optical fibres excited by a 532 nm diode pumped solid state laser. *J. Opt. A Pure Appl. Opt.* **10**(5), 055303 (2008)
- Tu, S., Jiang, Q., Zhang, X., Alshareef, H.N.: Large dielectric constant enhancement in mxene percolative polymer composites. *ACS Nano* **12**(4), 3369–3377 (2018)
- Twardowski, T.E.: *Introduction to Nanocomposite Materials: Properties, Processing, Characterization*, DEStech Publications Inc, Lancaster, USA (2007)
- Willis, H., Zichy, V., Hendra, P.: The laser-Raman and infra-red spectra of poly (methyl methacrylate). *Polymer* **10**, 737–746 (1969)
- Zhang, Y., Tan, Y.-W., Stormer, H.L., Kim, P.: Experimental observation of the quantum hall effect and Berry's phase in graphene. *Nature* **438**, 201–204 (2005)
- Zhao, T., Zhang, S., Guo, Y., Wang, Q.: TiC_2 : a new two-dimensional sheet beyond mxenes. *Nanoscale* **8**(1), 233–242 (2016)
- Zhu, J., Tang, Y., Yang, C., Wang, F., Cao, M.: Composites of TiO_2 nanoparticles deposited on Ti_3C_2 mxene nanosheets with enhanced electrochemical performance. *J. Electrochem. Soc.* **163**(5), 785–791 (2016)

Publisher's Note Springer Nature remains neutral with regard to jurisdictional claims in published maps and institutional affiliations.

Probing charge density wave phases and the Mott transition in 1T-TaS₂ by inelastic light scattering

S. Djurdjić Mijin,¹ A. Baum,² J. Bekaert,³ A. Šolajić,¹ J. Pešić,¹ Y. Liu,^{4,*} Ge He,² M. V. Milošević,³ C. Petrovic,⁴ Z. V. Popović,^{1,5} R. Hackl,² and N. Lazarević¹

¹Center for Solid State Physics and New Materials, Institute of Physics Belgrade, University of Belgrade, Pregrevica 118, RS-11080 Belgrade, Serbia

²Walther Meissner Institut, Bayerische Akademie der Wissenschaften, D-85748 Garching, Germany

³Department of Physics, University of Antwerp, Groenenborgerlaan 171, B-2020 Antwerp, Belgium

⁴Condensed Matter Physics and Materials Science Department, Brookhaven National Laboratory, Upton, New York 11973-5000, USA

⁵Serbian Academy of Sciences and Arts, Knez Mihailova 35, RS-11000 Belgrade, Serbia



(Received 10 March 2021; revised 14 June 2021; accepted 16 June 2021; published 22 June 2021)

We present a polarization-resolved, high-resolution Raman scattering study of the three consecutive charge density wave (CDW) regimes in 1T-TaS₂ single crystals, supported by *ab initio* calculations. Our analysis of the spectra within the low-temperature commensurate (C-CDW) regime shows $P\bar{3}$ symmetry of the system, thus excluding the previously proposed triclinic stacking of the “star-of-David” structure, and promoting trigonal or hexagonal stacking instead. The spectra of the high-temperature incommensurate (IC-CDW) phase directly project the phonon density of states due to the breaking of the translational invariance, supplemented by sizable electron-phonon coupling. Between 200 and 352 K, our Raman spectra show contributions from both the IC-CDW and the C-CDW phases, indicating their coexistence in the so-called nearly commensurate (NC-CDW) phase. The temperature dependence of the symmetry-resolved Raman conductivity indicates the stepwise reduction of the density of states in the CDW phases, followed by a Mott transition within the C-CDW phase. We determine the size of the Mott gap to be $\Omega_{\text{gap}} \approx 170\text{--}190$ meV, and track its temperature dependence.

DOI: [10.1103/PhysRevB.103.245133](https://doi.org/10.1103/PhysRevB.103.245133)

I. INTRODUCTION

Quasi-two-dimensional transition metal dichalcogenides (TMDs), such as the various structures of TaSe₂ and TaS₂, have been in the focus of various scientific investigations over the last 30 years, mostly due to the plethora of charge density wave (CDW) phases [1,2]. Among all TMD compounds 1T-TaS₂ stands out because of its unique and rich electronic phase diagram [3–6]. It experiences phase transitions at relatively high temperatures, making it easily accessible for investigation and, mainly for the hysteresis effects, attractive for potential applications such as data storage [7], information processing [8], or voltage-controlled oscillators [9].

The cascade of phase transitions as a function of temperature includes the transition from the normal metallic to the incommensurate CDW (IC-CDW) phase, the nearly commensurate CDW (NC-CDW) phase, and the commensurate CDW (C-CDW) phase occurring at around $T_{\text{IC}} = 554$ K, $T_{\text{NC}} = 355$ K, and in the temperature range from $T_{\text{C}\downarrow} = 180$ K to $T_{\text{C}\uparrow} = 230$ K, respectively. Recent studies indicate the possibility of yet another phase transition in 1T-TaS₂ at $T_H = 80$ K, named the hidden CDW state [10–12]. This discovery led to a new boost in attention for 1T-TaS₂.

Upon lowering the temperature to $T_{\text{IC}} = 554$ K, the normal metallic state structure, described by the space group $P\bar{3}m1$ (D_{3d}^d) [13], transforms into the IC-CDW state. As will be

demonstrated here, the IC-CDW domains shrink upon further temperature reduction until they gradually disappear, giving place to the C-CDW ordered state. This region in the phase diagram between 554 and roughly 200 K is characterized by the coexistence of the IC-CDW and C-CDW phases and is often referred to as NC-CDW. At the transition temperature T_C , IC-CDW domains completely vanish [14] and a new lattice symmetry is established. There is a general consensus about the formation of “star-of-David” clusters with in-plane $\sqrt{13}a \times \sqrt{13}a$ lattice reconstruction, whereby 12 Ta atoms are grouped around the 13th Ta atom [15,16]. In the absence of any external strain fields, this can be achieved in two equivalent ways (by either clockwise or counterclockwise rotations) thus yielding domains [17]. Despite extensive investigations, both experimental and theoretical, it remains an open question whether the stacking of star-of-David clusters is triclinic, trigonal, hexagonal, or a combination thereof [15,16,18–20]. The C-CDW phase is believed to be an insulator [3,21–23] with a gap of around 100 meV [13]. Very recent theoretical studies based on density-functional theory (DFT) find an additional ordering pattern along the crystallographic c axis. The related gap has a width of approximately 0.5 eV along k_z and becomes gapped at the Fermi energy E_F in the C-CDW phase [24,25].

Nearly all of the previously reported results for optical phonons in 1T-TaS₂ are based on Raman spectroscopy on the C-CDW phase and on temperature-dependent measurements in a narrow range around the NC-CDW to C-CDW phase transition [13,15,18–20]. In this paper we present temperature-dependent polarization-resolved Raman

*Present address: Los Alamos National Laboratory, Los Alamos, New Mexico 87545, USA.

measurements in the temperature range from 4 to 370 K covering all three CDW regimes of 1T-TaS₂. Our analysis of the C-CDW phase confirms the symmetry to be $P\bar{3}$, while the NC-CDW phase is confirmed as a mixed regime of commensurate and incommensurate domains. The Raman spectra of the IC-CDW phase mainly project the phonon density of states due to the breaking of translation invariance and sizable electron-phonon coupling. The growth of the CDW gap upon cooling, followed by the opening of the Mott gap, is traced via the initial slope of the symmetry-resolved spectra. The size of 170–190 meV and the temperature dependence of the Mott gap are directly determined from high-energy Raman data.

II. EXPERIMENTAL AND NUMERICAL METHODS

The preparation of the studied 1T-TaS₂ single crystals is described elsewhere [26–29]. Calibrated customized Raman scattering equipment was used to obtain the spectra. Temperature-dependent measurements were performed with the sample attached to the cold finger of a He-flow cryostat. The sample was cooled down to the lowest temperature and then heated. In either case the rates were less than ± 1 K/min. All measurements were performed in a high vacuum of approximately 5×10^{-5} Pa.

The 575-nm laser line of a diode-pumped Coherent GENESIS MX-SLM solid state laser was used as an excitation source. Additional measurements with the 458- and 514-nm laser lines were performed with a Coherent Innova 304C argon ion laser. The absorbed power was set at 4 mW. All spectra shown are corrected for the sensitivity of the instrument and the Bose factor, yielding the imaginary part of the Raman susceptibility $R\chi''$, where R is an experimental constant. An angle of incidence of $\Theta_i = 66.0 \pm 0.4^\circ$ and atomically flat cleaved surfaces enable us to measure at energies as low as 5 cm^{-1} without a detectable contribution from the laser line since the directly reflected light does not reach the spectrometer. The corresponding laser spot has an area of roughly $50 \times 100 \text{ }\mu\text{m}^2$ which prevents us from observing the possible emergence of the domains [17,30]. The inelastically scattered light is collected along the surface normal (crystallographic c axis) with an objective lens having a numerical aperture of 0.25. In the experiments presented here, the linear polarizations of the incident and scattered light are denoted as \mathbf{e}_i and \mathbf{e}_s , respectively. For \mathbf{e}_i horizontal to the plane of incidence there is no projection on the crystallographic c axis. For the low numerical aperture of the collection optics \mathbf{e}_s is always perpendicular to the c axis. Low-energy data up to 550 cm^{-1} were acquired in steps of $\Delta\Omega = 1 \text{ cm}^{-1}$ with a resolution of $\sigma \approx 3 \text{ cm}^{-1}$. The symmetric phonon lines were modeled using Voigt profiles where the width of the Gaussian part is given by σ . For spectra up to higher energies the step width and resolution were set at $\Delta\Omega = 50 \text{ cm}^{-1}$ and $\sigma \approx 20 \text{ cm}^{-1}$, respectively. The Raman tensors for the D_{3d} point group are given in Table I. Accordingly, parallel linear polarizations project both A_{1g} and E_g symmetries, while crossed linear polarizations only project E_g . The pure A_{1g} response then can be extracted by subtraction.

We have performed DFT calculations as implemented in the ABINIT package [31]. We have used the Perdew-Burke-Ernzerhof (PBE) functional, an energy cutoff of 50 Ha for the

TABLE I. Raman tensors for trigonal systems (point group D_{3d}).

$$A_{1g} = \begin{pmatrix} a & 0 & 0 \\ 0 & a & 0 \\ 0 & 0 & b \end{pmatrix} \quad {}^1E_g = \begin{pmatrix} c & 0 & 0 \\ 0 & -c & d \\ 0 & d & 0 \end{pmatrix} \quad {}^2E_g = \begin{pmatrix} 0 & -c & -d \\ -c & 0 & 0 \\ -d & 0 & 0 \end{pmatrix}$$

plane-wave basis, and we have included spin-orbit coupling by means of fully relativistic Goedecker pseudopotentials [32,33], where Ta- $5d^36s^2$ and S- $3s^23p^4$ states are treated as valence electrons. The crystal structure was relaxed so that forces on each atom were below $10 \text{ }\mu\text{eV}/\text{\AA}$ and the total stress on the unit cell below 1 bar, yielding lattice parameters $a = 3.44 \text{ \AA}$ and $c = 6.83 \text{ \AA}$. Subsequently, the phonons and the electron-phonon coupling (EPC) were obtained from density-functional perturbation theory (DFPT) calculations, also within ABINIT [34]. Here, we have used an $18 \times 18 \times 12$ \mathbf{k} -point grid for the electron wave vectors and a $6 \times 6 \times 4$ \mathbf{q} -point grid for the phonon wave vectors. For the electronic occupation we employed Fermi-Dirac smearing with broadening factor $\sigma_{\text{FD}} = 0.01 \text{ Ha}$, which is sufficiently high to avoid unstable phonon modes related to the CDW phases.

III. RESULTS AND DISCUSSION

A. Lattice dynamics of the charge-density wave regimes

Temperature-dependent symmetry-resolved Raman spectra of 1T-TaS₂ are presented in Fig. 1. It is obvious that their evolution with temperature is divided into three distinct ranges (IC-CDW, NC-CDW, and C-CDW) as indicated. The lattice dynamics for each of these ranges will be treated separately in the first part of the section. In the second part we address the electron dynamics.

1. C-CDW phase

At the lowest temperatures 1T-TaS₂ exists in the commensurate C-CDW phase. Here, the atoms form so-called star-of-David clusters. Different studies report either triclinic stacking of these clusters leading to $P\bar{1}$ unit cell symmetry [16], or trigonal or hexagonal stacking and $P\bar{3}$ unit cell symmetry [15,18–20]. A factor group analysis predicts 57 A_g Raman-active modes with an identical polarization dependence for $P\bar{1}$ unit cell symmetry, and alternatively 19 $A_g + 19 E_g$ Raman-active modes for $P\bar{3}$ unit cell symmetry [13]. Our polarized Raman scattering measurements at $T = 4 \text{ K}$, measured in two scattering channels, together with the corresponding cumulative fits are shown in Fig. 2. As it can be seen, we have observed modes of two different symmetries in the related scattering channels. This result indicates trigonal or hexagonal stacking of the star-of-David clusters. The symmetric phonon lines can be described by Voigt profiles, the best fit of which is shown as blue (for parallel light polarizations) and red (crossed polarizations) lines. After fitting Voigt profiles to the Raman spectra, 38 phonon modes were singled out. Following the selection rules for A_g and E_g symmetry modes, 19 were assigned as A_g and 19 as E_g symmetry, meaning all expected modes could be identified. The contribution from each mode to the cumulative fit is presented in Fig. 2 as green

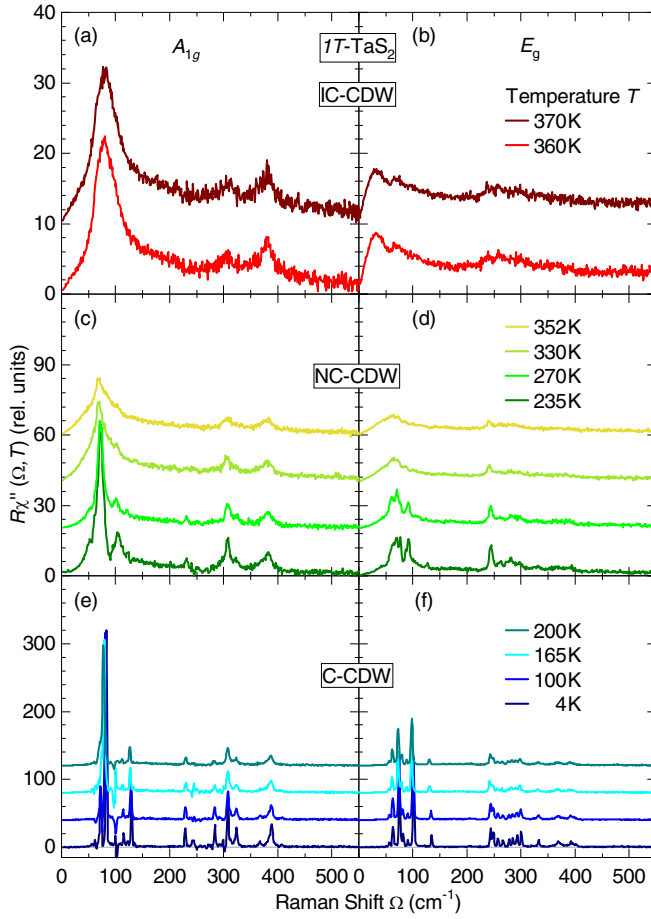


FIG. 1. Symmetry-resolved Raman spectra of 1T-TaS₂ at temperatures as indicated. Both C-CDW (blue lines) and IC-CDW (red lines) domains yield significant contributions to the Raman spectra of the NC-CDW phase (green lines).

TABLE II. A_{1g} and E_g Raman mode energies experimentally obtained at $T = 4$ K.

n_o	$\omega_{A_g} \text{ (cm}^{-1}\text{)}$	$\omega_{E_g} \text{ (cm}^{-1}\text{)}$
1	62.6	56.5
2	73.3	63.3
3	83.4	75.3
4	114.9	82.0
5	121.9	90.5
6	129.5	101.1
7	228.7	134.8
8	244.1	244.0
9	271.9	248.9
10	284.2	257.5
11	298.6	266.6
12	307.2	278.3
13	308.2	285.0
14	313.0	292.9
15	321.2	300.5
16	324.2	332.7
17	332.0	369.2
18	367.2	392.6
19	388.4	397.7

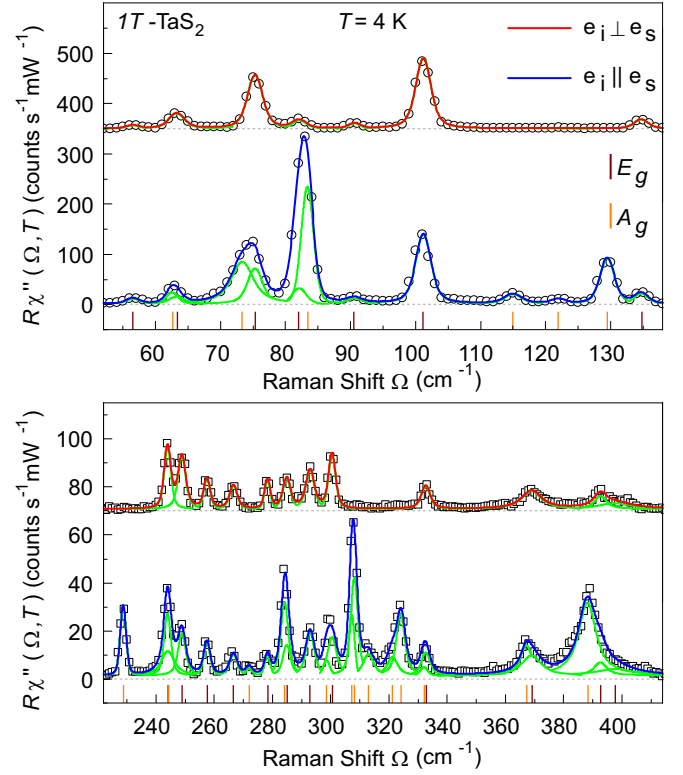


FIG. 2. Raman spectra at $T = 4$ K, i.e., in the C-CDW phase, for parallel and crossed light polarizations. Red and blue solid lines represent fits of the experimental data using Voigt profiles. Spectra are offset for clarity. The short vertical lines depict central frequencies obtained from the data analysis. The exact energy values are presented in Table II.

lines, whereas the complete list of the corresponding phonon energies can be found in Table II.

2. IC-CDW phase

At the highest experimentally accessible temperatures 1T-TaS₂ adopts the IC-CDW phase. Data collected by Raman scattering at $T = 370$ K, containing all symmetries, are shown as a blue solid line in Fig. 3. As 1T-TaS₂ is metallic in this phase [25] we expect the phonon lines to be superimposed on a continuum of electron-hole excitations which we approximate using a Drude spectrum shown as a dashed line [35,36].

Since the IC-CDW phase arises from the normal metallic phase, described by space group $P\bar{3}m1$ [13,37], it is interesting to compare our Raman results on the IC-CDW phase to an *ab initio* calculation of the phonon dispersion in the normal phase, shown as an inset in Fig. 3. Four different optical modes were obtained at Γ : E_u at 189 cm⁻¹ (double degenerate), E_g at 247 cm⁻¹ (double degenerate), A_{2u} at 342 cm⁻¹, and A_{1g} at 346 cm⁻¹. A factor group analysis shows that two of these are Raman active, namely E_g and A_{1g} [13].

We observe that the calculated phonon eigenvalues of the simple metallic phase at Γ do not closely match the observed peaks in the experimental spectra of the IC-CDW phase. Rather, these correspond better to the calculated phonon density of states (PDOS), depicted in Fig. 3. There are essentially three different ways to project the PDOS in a Raman

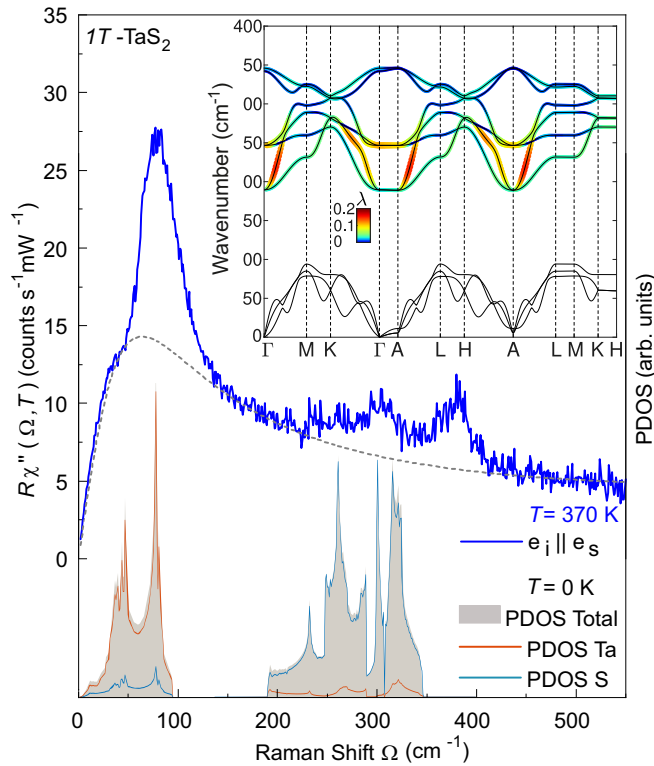


FIG. 3. Raman response for parallel light polarizations in the IC-CDW phase at 370 K (blue line). The dashed line depicts the possible electronic continuum. The contributions of the Ta (dark brown) and S atoms (light brown) to the calculated PDOS (gray area) are shown below. The inset shows the calculated phonon dispersion of 1T-TaS₂ in the simple metallic phase, with the electron-phonon coupling (λ) of the optical branches indicated through the color scale.

experiment and to overcome the $q \approx 0$ selection given by the small momentum of visible light: (i) scattering on impurities [38], (ii) enhanced electron-phonon coupling [39], and (iii) breaking of the translational symmetry in the IC-CDW phase. (i) We rule out chemical impurity scattering, expected to exist at all temperatures, as the low-temperature spectra (Fig. 2) show no signs thereof. (ii) The additional scattering channel may come from the electron-phonon coupling (EPC). The calculated EPC, λ , in the optical modes (inset of Fig. 3) is limited, yet not negligible, reaching maxima of ~ 0.2 in the lower optical branches around the Brillouin zone (BZ) points Γ and A. The calculated atom-resolved PDOS shows the acoustic modes to be predominantly due to Ta and the optical modes due to S, as a result of their difference in atomic mass. The acoustic modes display several dips that are signatures of the latent CDW phases, for which the EPC cannot be reliably determined. Significant EPC in the optical modes of 1T-TaS₂ is furthermore supported by experimental results linking a sharp increase in the resistivity above the IC-CDW transition temperature to the EPC [37]. It also corroborates calculated [14] and experimentally obtained [13] values of the CDW gap, which correspond to intermediate to strong EPC [37]. (iii) Although EPC certainly contributes we believe that the majority of the additional scattering channels can be traced back to the incommensurate breaking of the translational in-

variance upon entering IC-CDW. Thus the “weighted” PDOS is projected into the Raman spectrum [see Figs. 1(a) and 1(b)]. These “weighting” factors depend on the specific symmetries along the phonon branches as well as the “new periodicity” and go well beyond the scope of this paper.

3. NC-CDW phase

The nearly commensurate phase is seen as a mixed phase consisting of regions of commensurate and incommensurate CDWs [40,41]. This coexistence of high- and low-temperature phases is observable in our temperature-dependent data as shown in Fig. 1. The spectra for the IC-CDW (red curves) and C-CDW phase (blue curves) are distinctly different, as also visible in the data shown above (Figs. 2 and 3). The spectra of the NC-CDW phase ($235 \text{ K} < T < 352 \text{ K}$) comprise contributions from both phases. As 352 K is the highest temperature at which the contributions from the C-CDW phase can be observed in the spectra, we suggest that the phase transition temperature from IC-CDW to NC-CDW phase is somewhere in between 352 and 360 K. This conclusion is in good agreement with experimental results regarding this transition [4–6].

B. Gap evolution

The opening of a typically momentum-dependent gap in the electronic excitation spectrum is a fundamental property of CDW systems which has also been observed in 1T-TaS₂ [13,37,42]. Here, in addition to the CDW, a Mott transition at the onset of the C-CDW phase leads to an additional gap opening in the bands close to the Γ point [21,43]. Symmetry-resolved Raman spectroscopy can provide additional information here using the momentum resolution provided by the selection rules. To this end, we look at the initial slopes of the electronic part of the spectra.

As shown in Figs. 4(a)–4(c), different symmetries project individual parts of the BZ [36,44]. The vertices given by the hexagonal symmetry of 1T-TaS₂ are derived in Appendix C. The A_{1g} vertex mainly highlights the area around the Γ point while the E_g vertices predominantly project the BZ boundaries. The opening of a gap at the Fermi level reduces N_F , leading to an increase of the resistivity in the case of 1T-TaS₂. This reduction of N_F manifests itself also in the Raman spectra which, to zeroth order, are proportional to N_F [35,44]. As a result, the initial slope changes as shown Figs. 4(d) and 4(e), which zoom in on the low-energy region of the spectra from Fig. 1. The initial slope of the Raman response is $R \lim_{\Omega \rightarrow 0} \frac{\partial \chi''}{\partial \Omega} \propto N_F \tau_0$, where R incorporates only experimental factors [44]. The electronic relaxation $\Gamma_0^* \propto (N_F \tau_0)^{-1}$ is proportional to the dc resistivity $\rho(T)$ [45]. If a gap opens up there is vanishing intensity at $T = 0$ below the gap edge for an isotropic gap. At finite temperature there are thermally excited quasiparticles which scatter. Thus, there is a linear increase at low energies [35]. The black lines in Figs. 4(d)–4(g) represent the initial slopes and their temperature dependences. The lines comprise carrier relaxation and gap effects, and we focus only on the relative changes.

Starting in the IC-CDW phase at $T = 370 \text{ K}$ [Fig. 4(d)] the initial slope is higher for the E_g spectrum than for A_{1g} symmetry. While the CDW gap started to open already at

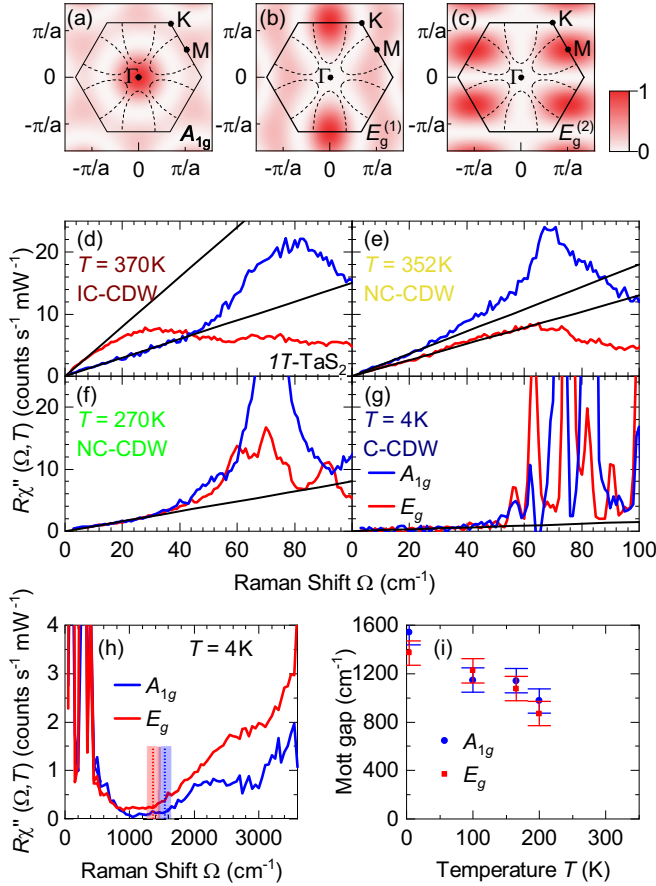


FIG. 4. Evolution of the gaps. (a)–(c) Squared Raman vertices and Fermi surface of 1T-TaS₂ for the indicated symmetries in the normal phase above T_C . The derivation of Raman vertices is presented in Appendix C. (d)–(g) Low-energy Raman spectra for A_{1g} symmetry (blue) and E_g symmetries (red) at temperatures as indicated. The spectra shown are zooms on the data shown in Fig. 1. The black lines highlight the initial slope of the spectra. (h) High-energy spectra at 4 K. Vertical dashed lines and colored bars indicate the approximate size and error bars of the Mott gap for the correspondingly colored spectrum. (i) Temperature dependence of the Mott gap Δ_μ ($\mu = A_{1g}, E_g$).

554 K around the M points [43], which are highlighted by the E_g vertex, the Fermi surface projected by the E_g vertex continues to exist. Thus, we may interpret the different slopes as a manifestation of a momentum-dependent gap in the IC-CDW phase and assume overall intensity effects to be symmetry independent for all temperatures. At $T = 352$ K [Fig. 4(e)] the slope for E_g symmetry is substantially reduced to below the A_{1g} slope due to a strong increase of the CDW gap in the commensurate regions [43] which emerge upon entering the NC-CDW phase. Further cooling also decreases the slope for the A_{1g} spectrum, as the Mott gap around the Γ point starts to open within the continuously growing C-CDW domains [40,41]. Below $T = 270$ K the initial slopes are identical for both symmetries and decrease with temperature. Apparently, the Mott gap opens up on the entire Fermi surface in direct correspondence with the increase of the resistivity by approximately an order of magnitude [3]. Finally, at the lowest temperature close to 4 K the initial slopes drop to almost zero

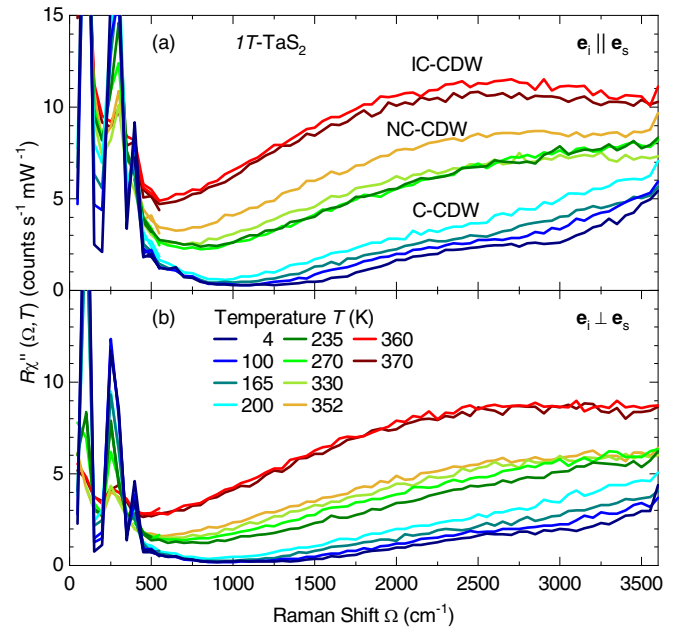


FIG. 5. Raman spectra up to high energies for (a) parallel and (b) crossed polarizations of the incident and scattered light at temperatures as given in the legend.

[Fig. 4(g)], indicating vanishing conductivity or fully gapped bands in the entire BZ.

Concomitantly, and actually more intuitive for the opening of a gap, we observe the loss of intensity in the Raman spectra below a threshold at an energy Ω_{gap} . Below 30 cm⁻¹ the intensity is smaller than 0.2 counts(mW s)⁻¹ [Fig. 4(g)] and still smaller than 0.3 counts(mW s)⁻¹ up to 1500 cm⁻¹ [Fig. 4(h)]. For a superconductor or a CDW system the threshold is given by 2Δ , where Δ is the single-particle gap, and a pileup of intensity for higher energies, $\Omega > 2\Delta$ [44]. A pileup of intensity cannot be observed here. Rather, the overall intensity is further reduced with decreasing temperature as shown in Figs. 5 and 6 in Appendixes A and B. In particular, the reduction occurs in distinct steps between the phases and continuous inside the phases with the strongest effect in the C-CDW phase below approximately 210 K (Fig. 5). In a system as clean as 1T-TaS₂ the missing pileup in the C-CDW phase is surprising and argues for an alternative interpretation.

In a Mott system, the gap persists to be observable but the pileup is not a coherence phenomenon and has not been observed yet. In fact, the physics is quite different, and the conduction band is split symmetrically about the Fermi energy E_F into a lower and a upper Hubbard band. Thus in the case of Mott-Hubbard physics the experimental signatures are more such as those expected for an insulator or semiconductor having a small gap, where at $T = 0$ there is a range without intensity and an interband onset with a band-dependent shape. At finite temperature there are thermal excitations inside the gap. For 1T-TaS₂ at the lowest accessible temperature, both symmetries exhibit a flat, nearly vanishing electronic continuum below a slightly symmetry-dependent threshold (superposed by the phonon lines at low energies). Above the threshold a weakly structured increase is observed. We interpret this onset as the distance of the lower

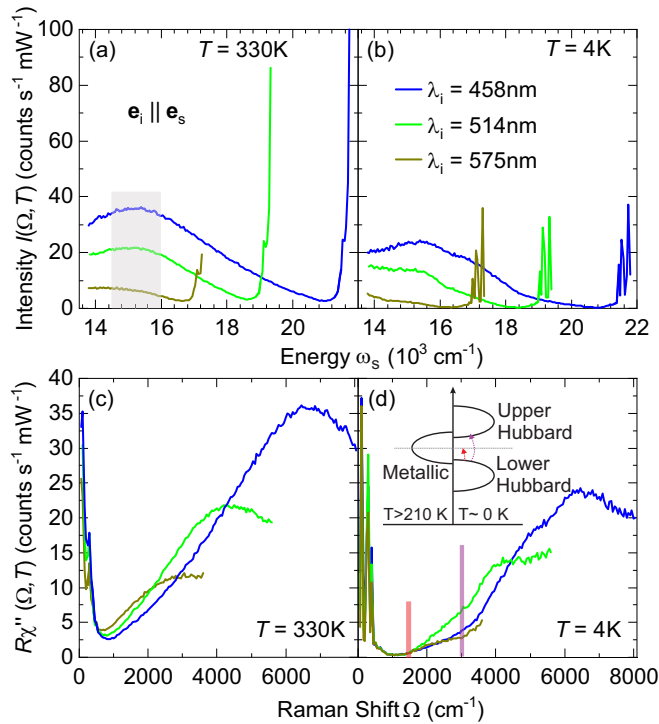


FIG. 6. Luminescence contribution to the Raman data. (a), (b) Intensity as a function of the absolute frequency for (a) $T = 330$ K and (b) $T = 4$ K. The approximate peak maximum of the contribution attributed to luminescence is highlighted by the gray shaded area. (c), (d) Raman susceptibility calculated from (a) and (b), respectively, shown as a function of frequency (Raman) shift. The luminescence peak appears at different Raman shifts depending on the wavelength of the laser light. At $T = 4$ K the spectra are identical up to 1600 cm^{-1} for all laser light wavelengths.

Hubbard band from the Fermi energy E_F or half of the distance between the lower and the upper Hubbard band, shown as vertical dashed lines at $1350\text{--}1550$ $\text{cm}^{-1} \equiv 170\text{--}190$ meV [Fig. 4(h)]. The energy is in good agreement with gap obtained from the in-plane angle-resolved photoemission spectroscopy (ARPES) [43], scanning tunneling spectroscopy [46], and infrared spectroscopy [13] which may be compared directly with our Raman results measured with in-plane polarizations. Upon increasing the temperature the size of the gap shrinks uniformly in both symmetries [Fig. 4(i)] and may point to an onset above the C-CDW phase transition, consistent with the result indicated by the initial slope. However, we cannot track the development of the gap into the NC-CDW phase as an increasing contribution of luminescence (see Appendix B) overlaps with the Raman data.

Recently, it was proposed on the basis of DFT calculations that $1T\text{-TaS}_2$ orders also along the c axis perpendicular to the planes in the C-CDW state [24,25]. This quasi-one-dimensional (1D) coupling is unexpectedly strong and the resulting metallic band is predicted to have a width of approximately 0.5 eV. For specific relative ordering of the star of David patterns along the c axis this band develops a gap of 0.15 eV at E_F [25], which is intriguingly close to the various experimental observations. However, since our light polarizations are strictly in plane, we have to conclude that the gap

observed here (and presumably in the other experiments) is an in-plane gap. Our experiment cannot detect an out-of-plane gap. Thus, neither a quasimetallic dispersion along the c axis nor a gap in this band along k_z may be excluded in the C-CDW phase. However, there is compelling evidence for a Mott-like gap in the layers rather than a CDW gap.

IV. CONCLUSIONS

We have presented a study of the various charge density wave regimes in $1T\text{-TaS}_2$ by inelastic light scattering, supported by *ab initio* calculations. The spectra of lattice excitations in the commensurate CDW (C-CDW) phase determine the unit cell symmetry to be $P\bar{3}$, indicating trigonal or hexagonal stacking of the “star-of-David” structure. The high-temperature spectra of the incommensurate CDW (IC-CDW) state are dominated by a projection of the phonon density of states caused by either a significant electron-phonon coupling or, more likely, the superstructure. The intermediate nearly commensurate (NC-CDW) phase is confirmed to be a mixed regime of commensurate and incommensurate regions contributing to the phonon spectra below an onset temperature $T_{\text{NC}} \approx 352\text{--}360$ K, in good agreement with previously reported values. At the lowest measured temperatures, the observation of a virtually clean gap without a redistribution of spectral weight from low to high energies below T_C argues for the existence of a Mott metal-insulator transition at a temperature of order 100 K. The magnitude of the gap is found to be $\Omega_{\text{gap}} \approx 170\text{--}190$ meV and has little symmetry, thus momentum, dependence, in agreement with earlier ARPES results [37]. At 200 K, on the high-temperature end of the C-CDW phase, the gap shrinks to $\sim 60\%$ of its low-temperature value. Additionally, the progressive filling of the CDW gaps by thermal excitations is tracked via the initial slope of the spectra, and indicates that the Mott gap opens primarily on the parts of the Fermi surface closest to the Γ point.

Our results demonstrate the potential of using inelastic light scattering to probe the momentum dependence and energy scale of changes in the electronic structure driven by low-temperature collective quantum phenomena. This opens perspectives to investigate the effect of hybridization on collective quantum phenomena in heterostructures composed of different 2D materials, e.g., alternating T and H monolayers as in the $4Hb\text{-TaS}_2$ phase [47].

ACKNOWLEDGMENTS

The authors acknowledge funding provided by the Institute of Physics Belgrade through the grant by the Ministry of Education, Science and Technological Development of the Republic of Serbia. The work was supported by the Science Fund of the Republic of Serbia, PROMIS, No. 6062656, StrainedFeSC, and by Research Foundation-Flanders (FWO). J.B. acknowledges support of a postdoctoral fellowship of the FWO, and of the Erasmus + program for staff mobility and training (KA107, 2018) for a research stay at the Institute of Physics Belgrade, during which part of the work was carried out. The computational resources and services used for the first-principles calculations in this work were provided by the VSC (Flemish Supercomputer Center), funded by the

FWO and the Flemish Government – department EWI. Work at Brookhaven is supported by the U.S. DOE under Contract No. DESC0012704. A.B. and R.H. acknowledge support by the German research foundation (DFG) via Projects No. Ha2071/12-1 and No. 107745057 – TRR 80 and by the DAAD via the project-related personal exchange program PPP with Serbia Grant No. 57449106.

APPENDIX A: RAW DATA

Figure 5 shows Raman spectra at temperatures ranging from $T = 4$ to 370 K for parallel [Fig. 5(a)] and crossed [Fig. 5(b)] in-plane light polarizations. The spectra were measured in steps of $\Delta\Omega = 50 \text{ cm}^{-1}$ and a resolution of $\sigma \approx 20 \text{ cm}^{-1}$. Therefore neither the shapes nor the positions of the phonon lines below 500 cm^{-1} may be resolved. All spectra reach a minimum in the range from 500 to 1600 cm^{-1} . At energies above 500 cm^{-1} the overall intensities are strongly temperature dependent and decreasing with decreasing temperature. Three clusters of spectra are well separated according to the phases they belong to.

In the C-CDW phase ($T \leq 200 \text{ K}$, blue lines) the spectra start to develop substructures at 1500 and 3000 cm^{-1} . The spectra at 200 K increase almost linearly with energy. The spectra of the NC- and IC-CDW phases exhibit a broad maximum centered in the region of $2200\text{--}3200 \text{ cm}^{-1}$ which may be attributed to luminescence (see Appendix B). For clarification we measured a few spectra with various laser lines for excitation.

APPENDIX B: LUMINESCENCE

Figure 6 shows Raman spectra measured with parallel light polarizations for three different wavelengths λ_i of the incident laser light. Figures 6(a) and 6(b) depict the measured intensity I (without the Bose factor) as a function of the absolute frequency $\tilde{\nu}$ of the scattered light.

At high temperature [$T = 330 \text{ K}$, Fig. 6(a)] a broad peak can be seen for all λ_i which is centered at a fixed frequency of $15\,200 \text{ cm}^{-1}$ of the scattered photons (gray shaded area). The peak intensity decreases for increasing λ_i (decreasing energy). Correspondingly, this peak's center depends on the laser wavelength in the spectra shown as a function of the Raman shift [Fig. 6(c)]. This behavior indicates that the origin of this excitation is likely to be luminescence where transitions at fixed absolute final frequencies are expected.

At low temperature [Fig. 6(b)] we can no longer find a structure at a fixed absolute energy. Rather, as already indicated in the main part, the spectra develop additional, yet weak, structures which are observable in all spectra but are particularly pronounced for blue excitation. For green and yellow excitation the spectral range of the spectrometer, limited to 732 nm, is not wide enough for a deeper insight into the luminescence contributions (at energies different from those at high temperature) and no maximum common to all three spectra is observed. If these spectra are plotted as a function of the Raman shift, the changes in slope at 1500 and 3000 cm^{-1} are found to be in the same position for all λ_i , values thus arguing for inelastic scattering rather than luminescence. Since we do currently not have the appropriate experimental

tools for an in-depth study, our interpretation is preliminary although supported by the observations in Fig. 6(d).

As shown in the inset of Fig. 6(d) we propose a scenario on the basis of Mott physics. In the C-CDW phase the reduced bandwidth is no longer the largest energy and the Coulomb repulsion U becomes relevant [22] and splits the conduction band into a lower and upper Hubbard band. We assume that the onset of scattering at 1500 cm^{-1} corresponds to the distance of the highest energy of the lower Hubbard band to the Fermi energy E_F . The second onset corresponds then to the distance between the highest energy of the lower Hubbard band and the lowest energy of the upper Hubbard band. An important question needs to be answered: Into which unoccupied states right above E_F does the first process scatter electrons? We may speculate that some DOS is provided by the metallic band dispersing along k_z or by the metallic domain walls between the different types of ordering patterns along the c axis observed recently by tunneling spectroscopy [46]. These quasi-1D domain walls would provide the states required for the onset of scattering at high energy but are topologically too small for providing enough density of states for a measurable intensity at low energy [Fig. 4(g)] in a location-integrated experiment such as Raman scattering.

APPENDIX C: DERIVATION OF THE RAMAN VERTICES

Phenomenologically, the Raman vertices can be derived based on lattice symmetry, which are proportional to the Brillouin zone harmonics. They are a set of functions that exhibit the symmetry and periodicity of the lattice structure proposed by Allen [48]. These functions make the k -space sums and energy integrals more convenient than that of the Cartesian basis or the spherical harmonics basis, especially for those materials who have anisotropic and/or multiple Fermi pockets. The three Cartesian components of the Fermi velocity v_k are recommended to generate this set of functions since they inherit the symmetry and periodicity of the crystal lattice naturally. However, in most cases, we do not know the details of band dispersion. A phenomenological method is needed to construct such a set of basis functions. Here, we demonstrate a method based on the group theory. The Brillouin zone harmonics can be obtained by the projection operation on specific trial functions.

For a certain group G with symmetry elements R and symmetry operators \hat{P}_R , it can be described by several irreducible representations Γ_n , where n labels the representation. For each irreducible representation, there are corresponding basis functions $\Phi_{\Gamma_n}^j$ that can be used to generate representation matrices for a particular symmetry. Here, j labels the component or partner of the representations. For an arbitrary function F , we have

$$F = \sum_{\Gamma_n} \sum_j f_j^{\Gamma_n} \Phi_{\Gamma_n}^j. \quad (\text{C1})$$

According to the group theory, we can always define a projection operator by the relation [49]

$$\hat{P}^{\Gamma_n} = \frac{d}{N} \sum_R \chi^{\Gamma_n}(R) * \hat{P}_R, \quad (\text{C2})$$

TABLE III. Symmetry operations \hat{P}_R and corresponding character table of the D_{3d} point group.

\hat{P}_R	x'	y'	z'	$\chi^{\Gamma_n}(R)$	
				A_{1g}	E_g
E	x	y	z	1	2
C_3^1	$-\frac{1}{2}x + \frac{\sqrt{3}}{2}y$	$-\frac{\sqrt{3}}{2}x - \frac{1}{2}y$	z	1	-1
C_3^{-1}	$-\frac{1}{2}x - \frac{\sqrt{3}}{2}y$	$\frac{\sqrt{3}}{2}x - \frac{1}{2}y$	z	1	-1
C_2'	x	$-y$	$-z$	1	0
C_2''	$-\frac{1}{2}x + \frac{\sqrt{3}}{2}y$	$\frac{\sqrt{3}}{2}x + \frac{1}{2}y$	$-z$	1	0
C_2'''	$-\frac{1}{2}x - \frac{\sqrt{3}}{2}y$	$-\frac{\sqrt{3}}{2}x + \frac{1}{2}y$	$-z$	1	0
I	$-x$	$-y$	$-z$	1	2
S_6^1	$\frac{1}{2}x - \frac{\sqrt{3}}{2}y$	$\frac{\sqrt{3}}{2}x + \frac{1}{2}y$	$-z$	1	-1
S_6^{-1}	$\frac{1}{2}x + \frac{\sqrt{3}}{2}y$	$-\frac{\sqrt{3}}{2}x + \frac{1}{2}y$	$-z$	1	-1
σ_v'	$-x$	y	z	1	0
σ_v''	$\frac{1}{2}x - \frac{\sqrt{3}}{2}y$	$-\frac{\sqrt{3}}{2}x - \frac{1}{2}y$	z	1	0
σ_v'''	$\frac{1}{2}x + \frac{\sqrt{3}}{2}y$	$\frac{\sqrt{3}}{2}x - \frac{1}{2}y$	z	1	0

that satisfies the relation

$$\hat{P}^{\Gamma_n} F = \sum_j f_j^{\Gamma_n} \Phi_{\Gamma_n}^j, \quad (C3)$$

where d is the dimensionality of the irreducible representation Γ_n , N is the number of symmetry operators in the group, and $\chi^{\Gamma_n}(R)$ is the character of the matrix of symmetry operator R in irreducible representation Γ_n . By projection operation on a certain irreducible representation Γ_n , we can directly get its basis functions $\Phi_{\Gamma_n}^j$.

The basis functions are not unique. In specific physical problems, it is useful to use physical insight to guess an appropriate arbitrary function to find the basis functions for specific

problems. $1T$ -TaS₂ belongs to the D_{3d} point group. There are 12 symmetry operators in this group, i.e., E , C_3^1 , C_3^{-1} , C_2' , C_2'' , C_2''' , I , S_6^1 , S_6^{-1} , σ_v' , σ_v'' , σ_v''' . The coordinate transformations after symmetry operations and the corresponding character table are listed in Table III.

In order to simulate the periodicity of the Brillouin zone, trigonometric functions are used as trial functions. According to the parity of the irreducible representations, we can choose an appropriate trigonometric function, e.g., a sine function for odd parity representation and cosine function for even parity representation. The combinations of them are also available.

Here, we use $F = \cos(k_x a)$ as a trial function, where a is the in-plane crystal constant. The basis function of A_{1g} can be derived as

$$\Phi_{A_{1g}}(\mathbf{k}) = \frac{1}{3} \left[\cos(k_x a) + 2 \cos\left(\frac{1}{2}k_x a\right) \cos\left(\frac{\sqrt{3}}{2}k_y a\right) \right]. \quad (C4)$$

With the same method, we obtain a basis function of E_g as

$$\Phi_{E_g^1}(\mathbf{k}) = \frac{2}{3} \left[\cos(k_x a) - \cos\left(\frac{1}{2}k_x a\right) \cos\left(\frac{\sqrt{3}}{2}k_y a\right) \right]. \quad (C5)$$

Since the E_g is a two-dimensional representation, the projection operation provides only one of the two basis functions of the corresponding subspace. The second function is found based on the subspace invariance under the symmetry operations (e.g., if we operate $\Phi_{E_g^1}$ with C_3^1 symmetry, the result can be presented as a linear combination of $\Phi_{E_g^1}$ and $\Phi_{E_g^2}$). Thus we obtain

$$\Phi_{E_g^2}(\mathbf{k}) = 2 \sin\left(\frac{1}{2}k_x a\right) \sin\left(\frac{\sqrt{3}}{2}k_y a\right). \quad (C6)$$

- [1] J. C. Tsang, J. E. Smith, M. W. Shafer, and S. F. Meyer, Raman spectroscopy of the charge-density-wave state in $1T$ - and $2H$ -TaSe₂, *Phys. Rev. B* **16**, 4239 (1977).
- [2] C. J. Sayers, H. Hedayat, A. Ceraso, F. Muser, M. Cattelan, L. S. Hart, L. S. Farrar, S. Dal Conte, G. Cerullo, C. Dallera, E. Da Como, and E. Carbone, Coherent phonons and the interplay between charge density wave and Mott phases in $1T$ -TaSe₂, *Phys. Rev. B* **102**, 161105(R) (2020).
- [3] A. J. Wilson, J. F. D. Salvo, and S. Mahajan, Charge-density waves and superlattices in the metallic layered transition metal dichalcogenides, *Adv. Phys.* **24**, 117 (1975).
- [4] C. B. Scruby, P. M. Williams, and G. S. Parry, The role of charge density waves in structural transformations of $1T$ -TaS₂, *Philos. Mag.* **31**, 255 (1975).
- [5] R. E. Thomson, B. Burk, A. Zettl, and J. Clarke, Scanning tunneling microscopy of the charge-density-wave structure in $1T$ -TaS₂, *Phys. Rev. B* **49**, 16899 (1994).
- [6] W. Wen, C. Dang, and L. Xie, Photoinduced phase transitions in two-dimensional charge-density-wave $1T$ -TaS₂, *Chin. Phys. B* **28**, 058504 (2019).
- [7] D. Svetin, I. Vaskivskiy, S. Brazovskii, Mertelj, and D. Mihailovic, Three-dimensional resistivity and switching between correlated electronic states in $1T$ -TaS₂, *Sci. Rep.* **7**, 46048 (2017).
- [8] D. Svetin, I. Vaskivskiy, P. Sutar, E. Goresnik, J. Gospodarcic, T. Mertelj, and D. Mihailovic, Transitions between photoinduced macroscopic quantum states in $1T$ -TaS₂ controlled by substrate strain, *Appl. Phys. Express* **7**, 103201 (2014).
- [9] G. Liu, B. Debnath, T. R. Pope, T. T. Salguero, R. K. Lake, and A. A. Balandin, A charge-density wave oscillator based on an integrated tantalum disulfide-boron nitride-graphene device operating at room temperature, *Nat. Nanotechnol.* **11**, 845 (2016).
- [10] R. Salgado, A. Mohammadzadeh, F. Kargar, A. Geremew, C.-Y. Huang, M. A. Bloodgood, S. Rumyantsev, T. T. Salguero, and A. A. Balandin, Low-frequency noise spectroscopy of charge-density-wave phase transitions in vertical quasi-2D $1T$ -TaS₂ devices, *Appl. Phys. Express* **12**, 037001 (2019).
- [11] Z. X. Wang, Q. M. Liu, L. Y. Shi, S. J. Zhang, T. Lin, T. Dong, D. Wu, and N. L. Wang, Photoinduced hidden CDW state and relaxation dynamics of $1T$ -TaS₂ probed by time-resolved terahertz spectroscopy, *arXiv:1906.01500*.
- [12] L. Stojchevska, I. Vaskivskiy, T. Mertelj, P. Kusar, D. Svetin, S. Brazovskii, and D. Mihailovic, Ultrafast switching to a stable

- hidden quantum state in an electronic crystal, *Science* **344**, 177 (2014).
- [13] L. V. Gasparov, K. G. Brown, A. C. Wint, D. B. Tanner, H. Berger, G. Margaritondo, R. Gaál, and L. Forró, Phonon anomaly at the charge ordering transition in $1T$ -TaS₂, *Phys. Rev. B* **66**, 094301 (2002).
- [14] O. R. Albertini, R. Zhao, R. L. McCann, S. Feng, M. Terrones, J. K. Freericks, J. A. Robinson, and A. Y. Liu, Zone-center phonons of bulk, few-layer, and monolayer $1T$ -TaS₂: Detection of commensurate charge density wave phase through Raman scattering, *Phys. Rev. B* **93**, 214109 (2016).
- [15] S. Uchida and S. Sugai, Infrared and raman studies on a commensurate CDW states in transition metal dichalcogenides, *Physica B+C* **105**, 393 (1981).
- [16] R. Brouwer and F. Jellinek, The low-temperature superstructures of $1T$ -TaSe₂ and $2H$ -TaSe₂, *Physica B+C* **99**, 51 (1980).
- [17] A. Zong, X. Shen, A. Kogar, L. Ye, C. Marks, D. Chowdhury, T. Rohwer, B. Freelon, S. Weathersby, R. Li, J. Yang, J. Checkelsky, X. Wang, and N. Gedik, Ultrafast manipulation of mirror domain walls in a charge density wave, *Sci. Adv.* **4**, eaau5501 (2018).
- [18] J. R. Duffay and R. D. Kirby, Raman scattering from $1T$ -TaS₂, *Solid State Commun.* **20**, 617 (1976).
- [19] T. Hirata and F. S. Ohuchi, Temperature dependence of the Raman spectra of $1T$ -TaS₂, *Solid State Commun.* **117**, 361 (2001).
- [20] S. L. L. M. Ramos, R. Plumadore, J. Boddison-Chouinard, S. W. Hla, J. R. Guest, D. J. Gosztola, M. A. Pimenta, and A. Luican-Mayer, Suppression of the commensurate charge density wave phase in ultrathin $1T$ -TaS₂ evidenced by Raman hyperspectral analysis, *Phys. Rev. B* **100**, 165414 (2019).
- [21] B. Sipos, A. F. Kusmartseva, A. Akrap, H. Berger, L. Forró, and E. Tutis, From Mott state to superconductivity in $1T$ -TaS₂, *Nat. Mater.* **7**, 960 (2008).
- [22] P. Fazekas and E. Tosatti, Electrical, structural and magnetic properties of pure and doped $1T$ -TaS₂, *Philos. Mag. B* **39**, 229 (1979).
- [23] E. Martino, A. Pisoni, L. Ćirić, A. Arakcheeva, H. Berger, A. Akrap, C. Putzke, P. J. W. Moll, I. Batistić, E. Tutiš, L. Forró, and K., Preferential out-of-plane conduction and quasi-one-dimensional electronic states in layered $1T$ -TaS₂, *npj 2D Mater. Appl.* **4**, 7 (2020).
- [24] P. Darancet, A. J. Millis, and C. A. Marianetti, Three-dimensional metallic and two-dimensional insulating behavior in octahedral tantalum dichalcogenides, *Phys. Rev. B* **90**, 045134 (2014).
- [25] S.-H. Lee, J. S. Goh, and D. Cho, Origin of the Insulating Phase and First-Order Metal-Insulator Transition in $1T$ -TaS₂, *Phys. Rev. Lett.* **122**, 106404 (2019).
- [26] Y. Ma, Y. Hou, C. Lu, L. Li, and C. Petrovic, Possible origin of nonlinear conductivity and large dielectric constant in the commensurate charge-density-wave phase of $1T$ -TaS₂, *Phys. Rev. B* **97**, 195117 (2018).
- [27] L. J. Li, W. J. Lu, X. D. Zhu, L. S. Ling, Z. Qu, and Y. P. Sun, Fe-doping induced superconductivity in the charge-density-wave system $1T$ -TaS₂, *Europhys. Lett.* **98**, 29902 (2012).
- [28] Y. Liu, R. Ang, W. J. Lu, W. H. Song, L. J. Li, and Y. P. Sun, Superconductivity induced by Se-doping in layered charge-density-wave system $1T$ -TaS_{2-x}Se_x, *Appl. Phys. Lett.* **102**, 192602 (2013).
- [29] R. Ang, Y. Miyata, E. Ieki, K. Nakayama, T. Sato, Y. Liu, W. J. Lu, Y. P. Sun, and T. Takahashi, Superconductivity and bandwidth-controlled Mott metal-insulator transition in $1T$ -TaS_{2-x}Se_x, *Phys. Rev. B* **88**, 115145 (2013).
- [30] M. Bovet, D. Popović, F. Clerc, C. Koitzsch, U. Probst, E. Bucher, H. Berger, D. Naumović, and P. Aebi, Pseudogapped Fermi surfaces of $1T$ -TaS₂ and $1T$ -TaSe₂: A charge density wave effect, *Phys. Rev. B* **69**, 125117 (2004).
- [31] X. Gonze, B. Amadon, P.-M. Anglade, J.-M. Beuken, F. Bottin, P. Boulanger, F. Bruneval, D. Caliste, R. Caracas, M. Côté, T. Deutsch, L. Genovese, P. Ghosez, M. Giantomassi, S. Goedecker, D. Hamann, P. Hermet, F. Jollet, G. Jomard, S. Leroux *et al.*, ABINIT: First-principles approach to material and nanosystem properties, *Comput. Phys. Commun.* **180**, 2582 (2009).
- [32] S. Goedecker, M. Teter, and J. Hutter, Separable dual-space Gaussian pseudopotentials, *Phys. Rev. B* **54**, 1703 (1996).
- [33] M. Krack, Pseudopotentials for H to Kr optimized for gradient-corrected exchange-correlation functionals, *Theor. Chem. Acc.* **114**, 145 (2005).
- [34] X. Gonze, D. C. Allan, and M. P. Teter, Dielectric Tensor, Effective Charges, and Phonons in α -Quartz by Variational Density-Functional Perturbation Theory, *Phys. Rev. Lett.* **68**, 3603 (1992).
- [35] A. Zawadowski and M. Cardona, Theory of Raman scattering on normal metals with impurities, *Phys. Rev. B* **42**, 10732 (1990).
- [36] N. Lazarević and R. Hackl, Fluctuations and pairing in Fe-based superconductors: Light scattering experiments, *J. Phys.: Condens. Matter* **32**, 413001 (2020).
- [37] K. Rossnagel, On the origin of charge-density waves in select layered transition-metal dichalcogenides, *J. Phys.: Condens. Matter* **23**, 213001 (2011).
- [38] R. Shuker and R. W. Gammon, Raman-Scattering Selection-Rule Breaking and the Density of States in Amorphous Materials, *Phys. Rev. Lett.* **25**, 222 (1970).
- [39] A. Baum, A. Milosavljević, N. Lazarević, M. M. Radonjić, B. Nikolić, M. Mitschek, Z. I. Maranloo, M. Šćepanović, M. Grujić-Brožčin, N. Stojilović, M. Opel, A. Wang, C. Petrovic, Z. V. Popović, and R. Hackl, Phonon anomalies in FeS, *Phys. Rev. B* **97**, 054306 (2018).
- [40] A. Spijkerman, J. L. de Boer, A. Meetsma, G. A. Wiegers, and S. van Smaalen, X-ray crystal-structure refinement of the nearly commensurate phase of $1T$ -TaS₂ in $(3+2)$ -dimensional superspace, *Phys. Rev. B* **56**, 13757 (1997).
- [41] R. He, J. Okamoto, Z. Ye, G. Ye, H. Anderson, X. Dai, X. Wu, J. Hu, Y. Liu, W. Lu, Y. Sun, A. N. Pasupathy, and A. W. Tsien, Distinct surface and bulk charge density waves in ultrathin $1T$ -TaS₂, *Phys. Rev. B* **94**, 201108(R) (2016).
- [42] G. Grüner, The dynamics of charge-density waves, *Rev. Mod. Phys.* **60**, 1129 (1988).
- [43] C. Sohrt, A. Stange, M. Bauer, and K. Rossnagel, How fast can a Peierls–Mott insulator be melted?, *Faraday Discuss.* **171**, 243 (2014).
- [44] T. P. Devereaux and R. Hackl, Inelastic light scattering from correlated electrons, *Rev. Mod. Phys.* **79**, 175 (2007).
- [45] M. Opel, R. Nemetschek, C. Hoffmann, R. Philipp, P. F. Müller, R. Hackl, I. Tüttő, A. Erb, B. Revaz, E. Walker, H. Berger, and L. Forró, Carrier relaxation, pseudogap, and superconducting

- gap in high- T_c cuprates: A Raman scattering study, [Phys. Rev. B **61**, 9752 \(2000\)](#).
- [46] J. Skolimowski, Y. Gerasimenko, and R. Žitko, Mottness Collapse without Metallization in the Domain Wall of the Triangular-Lattice Mott Insulator 1T-TaS₂, [Phys. Rev. Lett. **122**, 036802 \(2019\)](#).
- [47] A. Ribak, R. M. Skiff, M. Mograbi, P. K. Rout, M. H. Fischer, J. Ruhman, K. Chashka, Y. Dagan, and A. Kanigel, Chiral superconductivity in the alternate stacking compound 4Hb-TaS₂, [Sci. Adv. **6**, eaax9480 \(2020\)](#).
- [48] P. B. Allen, Fermi-surface harmonics: A general method for nonspherical problems. Application to Boltzmann and Eliashberg equations, [Phys. Rev. B **13**, 1416 \(1976\)](#).
- [49] M. S. Dresselhaus, G. Dresselhaus, and A. Jorio, *Group Theory* (Springer, Berlin, 2008).

PAPER

Peculiar symmetry-protected electronic dispersions in two-dimensional materials

To cite this article: V Damjanović *et al* 2020 *J. Phys.: Condens. Matter* **32** 485501

View the [article online](#) for updates and enhancements.

You may also like

- [Dynamics of an \$M\$ -level equidistant radiator in the presence of a thermal electromagnetic field](#)
N A Enaki and V I Koroli
- [A symmetry for the vanishing cosmological constant](#)
Recal Erdem
- [Hopf symmetry breaking and confinement in \(2+1\)-dimensional gauge theory](#)
Alexander F. Bais, Bernd J. Schroers and Joost K. Slingerland

Peculiar symmetry-protected electronic dispersions in two-dimensional materials

V Damljanović^{1,3} , N Lazić² , A Šolajić¹ , J Pešić¹ , B Nikolić²  and M Damjanović² 

¹ Institute of Physics Belgrade, University of Belgrade, Pregrevica 118, 11080 Belgrade, Serbia

² NanoLab, Faculty of Physics, University of Belgrade, PO Box 44, Belgrade 11001, Serbia

E-mail: damlja@ipb.ac.rs

Received 16 June 2020, revised 23 July 2020

Accepted for publication 30 July 2020

Published 8 September 2020



Abstract

Symmetry indicates that low energy spectra of materials could be richer than well-known Dirac, semi-Dirac, or quadratic, hosting some unusual quasiparticles. Performing the systematic study of exact forms of low energy effective Hamiltonians and dispersions in high-symmetry points with fourfold degeneracy of bands, we found new, previously unreported dispersion, which we named poppy flower (PF) after its shape. This massless fermion exists in non-magnetic two-dimensional (2D) crystals with spin-orbit coupling (SOC), which are invariant under one of the proposed ten noncentrosymmetric layer groups. We suggest real three-dimensional (3D) layered materials suitable for exfoliation, having layers that belong to these symmetry groups as candidates for realization of PF fermions. In 2D systems without spin-orbit interaction, fortune teller (FT)-like fermions were theoretically predicted, and afterward experimentally verified in the electronic structure of surface layer of silicon. Herein, we show that such fermions can also be hosted in 2D crystals with SOC, invariant under additional two noncentrosymmetric layer groups. This prediction is confirmed by density functional based calculation: layered BiIO_4 , which has been synthesized already as a 3D crystal, exfoliates to stable monolayer with symmetry $pb2_1a$, and FT fermion is observed in the band structure. Analytically calculated density of states (DOS) of the PF shows semimetallic characteristic, in contrast to metallic nature of FT having non-zero DOS at the bands contact energy. We indicate possibilities for symmetry breaking patterns which correspond to the robustness of the proposed dispersions as well as to the transition from Dirac centrosymmetric semimetal to PF.

Keywords: electronic dispersions, spin-orbit coupling, symmetry, new fermions

(Some figures may appear in colour only in the online journal)

1. Introduction

Electronic dispersion essentially determines crystal properties and it is well known that it is assigned by quantum numbers of the underlying symmetry group. These are space, layer (including wallpaper) or line groups, referring respectively to dimensionality of crystals: 3D, quasi-2D (Q2D), or quasi-1D. Probably the most famous example of a low-dimensional material is graphene (there are also related single layers, such as borophene [1], borophosphene [2], graphynes

[3], etc), which hosts Dirac like (linear in quasi-momentum) dispersion in the vicinity of high symmetry Dirac points. Such shape of energy bands, besides being responsible for some intriguing phenomena, provides material realization of relativistic electron. This triggered numerous investigations of the connection between symmetry of materials and appearance of Dirac and Weyl points in their band structures. These points are attributed to existence of rotational [4], nonsymmorphic [5], mirror [6], space-time inversion [7, 8], time-reversal plus fractional translation [9], and generalized chiral symmetry [10]. There are also results on the search for Weyl and Dirac

³ Author to whom any correspondence should be addressed.

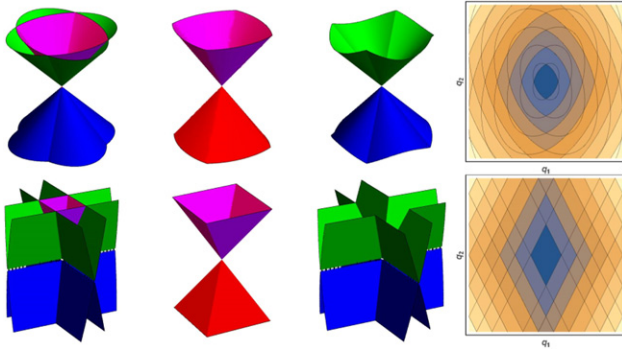


Figure 1. PF (up) and FT (bottom) dispersions (given by equations (3.1)): from left to right are all bands, bands $E_{\pm 1, +1}$, bands $E_{\pm 1, -1}$ and horizontal sections of the bands (iso-energetic lines).

points according to group theoretical criteria in Brillouin zones (BZs) of all space [11], layer [12–14] or wallpaper groups [15].

In addition, geometrical symmetries impose conditions that lead to the emergence of unconventional quasiparticles in condensed matter systems. In 3D materials, enforced by space groups, double Dirac points [16], three-component [17, 18] or hourglass fermions [19] are found, inspiring further theoretical and experimental research [20–25]. Concerning Q2D systems, besides Dirac (as in graphene [26]), there are also semi-Dirac (Dirac-like in one direction, and quadratic in the orthogonal one, as in black phosphorus [27]), quadratic (as in molybdenum disulphide [28]), and fortune teller (FT) dispersions [29], which corresponds to the coexistence of a nodal point and lines. Namely, symmetry analysis of the possible completely linear dispersions in non-magnetic, Q2D materials with negligible spin–orbit coupling (SOC) has shown that only completely massless fermions appearing in layers are Dirac and FT [29]. Recently, FT dispersion has been experimentally confirmed in a surface layer of silicon [30].

A question arises whether new types of fermions are possible in Q2D materials by inclusion of SOC? With help of layer double groups (LDGs) and time-reversal symmetry (TRS) (i.e. gray LDG), we made a quite general search for linear dispersions in the vicinity of high symmetry points (HSPs); since no reference to nonsymmorphic symmetries is made, the topological (hour-glass like) band crossing mechanisms are not *a priori* assumed, as it is usual. Indeed, it turns out that there are two peculiar types (figure 1) featuring twelve nonsymmorphic and noncentrosymmetric groups: two groups support previously predicted FT, and the remaining ones poppy flower (PF) dispersion (generalizing both FT and Dirac types).

After a brief overview of necessary group-theoretical methods, the obtained results are discussed on the basis of effective low-energy model, calculated densities of states and symmetry breaking patterns. Also, a list of material candidates supporting the new dispersions is provided. The predicted effect is justified by density functional based relaxation and band structure calculation in BiIO₄ monolayer. Synthesis of this layered 3D material was reported around a decade ago [31]. Numerical band structure con-

firms our group theoretical prediction, which may be the motivation for future laboratory synthesis of this material as monolayer.

2. Method

Symmetry determines Bloch Hamiltonian in the vicinity of high-symmetry BZ wave vector through the allowed irreducible representations (IRs) of the little group [32]. Allowed IRs of LDGs are subduced from the corresponding space groups IRs (found on Bilbao Crystallographic Server [33]), and also independently constructed by POL-Sym code [34]. Concerning LDGs with TRS, the dimensions [33, 35] of the allowed IRs (actually co-representations) are 1, 2 or 4, and for generic ones, giving bands degeneracy, this is 1 or 2. Here we focus on the band structures near quadruple points at high-symmetry momenta. Further, we do not consider generically degenerate bands, giving double degenerate Dirac dispersion (precisely, it consists of two double spinfull degenerate cones meeting at one fourfold degenerate point); this automatically excludes centrosymmetric crystals, as Kramers degeneracy in them forbids non-degenerate bands [36]. Among the remaining groups, only twelve are with special points with four-dimensional allowed (co)representation.

Analysis of all allowed IRs R of little groups $G(\mathbf{k}_0)$ of HSPs \mathbf{k}_0 in LDG lacking the inversion symmetry gives the following conditions for quadruple point: \mathbf{k}_0 is time-reversal invariant momentum, R is two-dimensional, either real or complex IR. Therefore, we consider $\hat{H}(\mathbf{k})$ being Hamiltonian of the system \hat{H}_0 (including spin–orbit) in the basis $\{|\Psi_1\rangle, |\Psi_2\rangle, |\theta\Psi_1\rangle, |\theta\Psi_2\rangle\}$, where the spinors $|\Psi_i\rangle = |\Psi_i(\mathbf{k})\rangle$ ($i = 1, 2$ counts two bands touching each other at \mathbf{k}_0 also in the absence of TRS) belong to R at \mathbf{k}_0 and θ is an anti-unitary operator of TRS, for which we used $\theta^2 = -\hat{\sigma}_0$, since spinfull case is considered. Throughout the text $\hat{\sigma}_0$ is two-by-two unit matrix, and $\hat{\sigma}_1, \hat{\sigma}_2, \hat{\sigma}_3$ are Pauli matrices. Denoting the little group elements by $\ell = (h|\mathbf{r}_h + \mathbf{b})$, where h is crystallographic double point group element, while \mathbf{r}_h and \mathbf{b} are fractional and lattice translation, respectively, one gets the conditions imposed by time-reversal and geometrical symmetries on $\hat{H}(\mathbf{k}_0 + \mathbf{q})$ in the vicinity of \mathbf{k}_0 (therefore, the wavevector \mathbf{q} is small):

$$\hat{H}^*(\mathbf{k}_0 + \mathbf{q}) = \hat{T}^\dagger \hat{H}(\mathbf{k}_0 - \mathbf{q}) \hat{T}, \quad (2.1)$$

$$\hat{H}(\mathbf{k}_0 + \mathbf{q}) = \hat{D}^\dagger(\ell) \hat{H}(\mathbf{k}_0 + \mathbf{h}'\mathbf{q}) \hat{D}(\ell). \quad (2.2)$$

Here, $\hat{D} = \text{diag}(\hat{R}, \hat{R}^*)$, and \mathbf{h}' is an operator reduction of vector representation \hat{h} to 2D BZ, while $\hat{T} = -i\hat{\sigma}_2 \otimes \hat{\sigma}_0$ represents the action of θ on the basis of spinors.

To focus on the terms linear in \mathbf{q} , Hamiltonian is expanded in the form $\hat{H}(\mathbf{k}_0 + \mathbf{q}) \approx \sum_{i=1,2} q_i \frac{\partial \hat{H}(\mathbf{k}_0 + \mathbf{q})}{\partial q_i} \big|_{\mathbf{q}=0}$ (energy scale is conveniently shifted such that $\hat{H}(\mathbf{k}_0) = 0$). To incorporate symmetry, the matrix elements of the Hamiltonian gradient are arranged into the four-by-eight matrix \hat{W} , which entries $w_{pq} = (w_{pq}^1 \ w_{pq}^2)$ are pairs $w_{pq}^i = \frac{\partial H_{pq}(\mathbf{k}_0 + \mathbf{q})}{\partial q_i} \big|_{\mathbf{q}=0}$. The form

Table 1. Groups providing dispersions (3.1). Notations for layer (columns 1 and 2) and space groups (columns 4, 5 and 6) are according to [37, 38] respectively. IR notation in the eighth column is as in Bilbao Crystallographic Server [33]. Effective Hamiltonian is indicated in the last column by the nonzero parameters (and their interrelations) of (2.5). For the last four groups $a = c$ while \bar{M}_6 and \bar{M}_7 are conjugated pair of IRs.

Layer double group			Corresponding space double group						
Group		IR	Group		Plane	IR	Dispersion	Nonzero v_{pq}^i	
21	$p2_12_12$	\bar{S}_5	18	$P2_12_12$	D_2^3	$z = 0$	\bar{S}_5	(3.1a)	$v_{13}^1, v_{23}^1, v_{33}^1, v_{11}^2, v_{21}^2, v_{31}^2$
25	$pba2$	\bar{S}_5	32	$Pba2$	C_{2v}^8	$z = 0$	\bar{S}_5	(3.1a)	$v_{13}^1, v_{23}^1, v_{33}^1, v_{11}^2, v_{21}^2, v_{31}^2$
28	$pm2_1b$	\bar{Y}_5, \bar{S}_5	26	$Pmc2_1$	C_{2v}^2	$y = 0$	\bar{Z}_5, \bar{U}_5	(3.1a)	$v_{11}^1, v_{21}^1, v_{31}^1, v_{10}^2, v_{20}^2, v_{30}^2$
29	$pb2_1m$	\bar{Y}_5, \bar{S}_5	26	$Pmc2_1$	C_{2v}^2	$x = 0$	\bar{Z}_5, \bar{T}_5	(3.1b)	$v_{02}^1, v_{10}^2, v_{20}^2, v_{30}^2$
30	$pb2b$	\bar{Y}_5, \bar{S}_5	27	$Pcc2$	C_{2v}^3	$x = 0$	\bar{Z}_5, \bar{T}_5	(3.1a)	$v_{11}^1, v_{21}^1, v_{31}^1, v_{10}^2, v_{20}^2, v_{30}^2$
32	$pm2_1n$	\bar{Y}_5	31	$Pmn2_1$	C_{2v}^7	$y = 0$	\bar{Z}_5	(3.1a)	$v_{13}^1, v_{23}^1, v_{33}^1, v_{10}^2, v_{20}^2, v_{30}^2$
33	$pb2_1a$	\bar{Y}_5	29	$Pca2_1$	C_{2v}^5	$y = 0$	\bar{Z}_5	(3.1b)	$v_{33}^1, v_{11}^2, v_{21}^2, v_{30}^2$
34	$pb2n$	\bar{Y}_5	30	$Pnc2$	C_{2v}^6	$x = 0$	\bar{Z}_5	(3.1a)	$v_{13}^1, v_{23}^1, v_{33}^1, v_{10}^2, v_{20}^2, v_{30}^2$
54	$p42_12$	(\bar{M}_6, \bar{M}_7)	90	$P42_12$	D_4^2	$z = 0$	(\bar{M}_6, \bar{M}_7)	(3.1a)	$\left\{ \begin{array}{l} v_{02}^1 = v_{02}^2 = v_{31}^1 = -v_{31}^2 \\ v_{10}^1 = v_{10}^2 = v_{23}^1 = -v_{23}^2 \\ v_{13}^1 = -v_{13}^2 = -v_{20}^1 = -v_{20}^2 \end{array} \right\}$
56	$p4bm$	(\bar{M}_6, \bar{M}_7)	100	$P4bm$	C_{4v}^2	$z = 0$	(\bar{M}_6, \bar{M}_7)	(3.1a)	
58	$p\bar{4}2_1m$	(\bar{M}_6, \bar{M}_7)	113	$P\bar{4}2_1m$	D_{2d}^3	$z = 0$	(\bar{M}_6, \bar{M}_7)	(3.1a)	
60	$p\bar{4}b2$	(\bar{M}_6, \bar{M}_7)	117	$P\bar{4}b2$	D_{2d}^7	$z = 0$	(\bar{M}_6, \bar{M}_7)	(3.1a)	

$$\hat{W} = \begin{pmatrix} w_{11} & w_{12} & w_{13} & w_{14} \\ w_{12}^* & w_{22} & w_{14} & w_{24} \\ w_{13}^* & w_{14}^* & -w_{11} & -w_{12}^* \\ w_{14}^* & w_{24}^* & -w_{12} & -w_{22} \end{pmatrix} \quad (2.3)$$

follows from the relation (2.1), together with $w_{pq}^i = w_{qp}^{i*}$ corresponding to the requirement that Hamiltonian \hat{H} is a Hermitian operator. Note that the form (2.3) of \hat{W} leads to the traceless Hamiltonian: it excludes the scalar term (which imposes the tilt of the bands). The geometrical symmetries are incorporated by (2.2), which is rewritten [11, 29] as an efficient fixed point condition

$$|\hat{W}\rangle = \hat{D} \otimes \hat{D}^* \otimes \hat{h}' |\hat{W}\rangle, \quad (2.4)$$

on the column vector (32×1) form $|\hat{W}\rangle$ of \hat{W} . The equation (2.4) is solved with help of the group projection operators for all of the twelve noncentrosymmetric groups hosting quadruple points at high symmetry momenta; in this way, the symmetry determines form of \hat{W} . To explicate this, it is more convenient to use another general expansion of the effective low energy Hamiltonian,

$$\hat{H}(\mathbf{q}) = \sum_{p,q=0}^3 \sum_{i=1}^2 q_i v_{pq}^i \hat{\sigma}_p \otimes \hat{\sigma}_q, \quad (2.5)$$

and find the constraints imposed by symmetry on the real coefficients v_{pq}^i (simply interrelated with w_{pq}^i).

3. Results and discussion

3.1. Symmetry adapted Hamiltonians and dispersions

Groups hosting new dispersions are listed in table 1. Besides intrinsic layer group notation (the first part), the space group

of the system obtained by periodic repetition of the layer along axis perpendicular to it (column plane) according to Bilbao Crystallographic Server is also given (second part), where the directions x , y and z are along axes of orthorhombic/tetragonal 3D primitive unit cell. On the other hand, in POLSym approach we used convention that layers are in xy -plane. Orthogonal lattice vectors \mathbf{a}_1 and \mathbf{a}_2 span primitive rectangular/square 2D unit cell, while reciprocal lattice vectors \mathbf{k}_1 and \mathbf{k}_2 satisfy $\mathbf{a}_j \cdot \mathbf{k}_l = 2\pi\delta_{jl}$ and q_1, q_2 are projections of \mathbf{q} along \mathbf{k}_1 and \mathbf{k}_2 . Relevant BZs are in figure 2.

Effective Hamiltonians allowed by symmetry group in the special points of Brillouin's zone are presented in the last column of the table 1: the nonzero real coefficients v_{pq}^i in the expansion (2.5) are specified, together with the constraints among them. The listed forms correspond to the group settings (lattice vectors and coordinate origin) and double valued irreducible co-representations obtained by POLSym code. In fact, this enabled flexibility in the choice of generators (coordinate system and translational periods), which finally results in the form of irreducible co-representations. These are chosen such to get the same form of the effective Hamiltonian whenever it is possible (for different groups). Equivalent (but different) settings (and co-representations) produce different (still equivalent with respect to dispersions) Hamiltonian forms. Clearly, the exact values of the nonzero coefficients v_{pq}^i (listed in the last column of the table 1) are material dependent. The groups' generators and their representative matrices in the allowed co-representations associated to the specified high-symmetry points are in the table 2. It should be remarked that in all the considered cases this point is fixed by the whole gray group, i.e. the little group is the gray (double) group, and the allowed co-representations of the little group are simultaneously the irreducible co-representations of the gray group. The matrices of the relevant co-representations are four-dimensional. In all the cases time-reversal corresponds to the matrix \hat{T} ; all other generators are represented by the block-diagonal

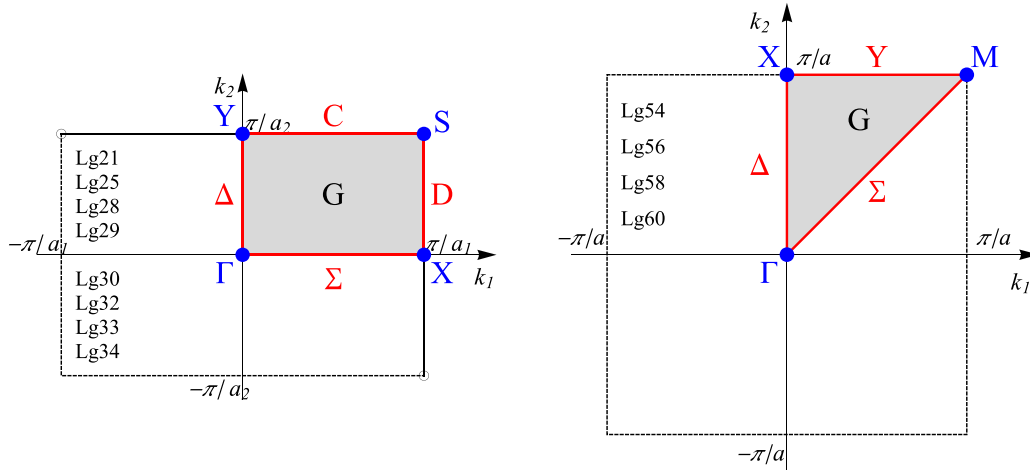


Figure 2. BZs of the groups (listed in table 1) supporting dispersions (3.1). For layer groups 28, 29, 30, 32, 33 and 34 vector k_2 is along (screw) axis of order two.

matrices $\hat{D} = \text{diag}(\hat{R}, \hat{R}^*)$, with mutually conjugated 2×2 blocks. Therefore, only this block, \hat{R} , is given in the table 2.

The described technique leads to two new types of dispersions (figure 1; crossings are taken at $E = 0$). The first one is PF, with four bands (obtained for $u, v = \pm 1$):

$$E_{v,u}(\mathbf{q}) = v \sqrt{aq_1^2 + cq_2^2 + u b |q_1 q_2|}. \quad (3.1a)$$

The expression under the square root is non-negative since a, b and c are positive quantities (functions of v_{pq}^i) such that $b^2 - 4ac < 0$. For quadratic layer groups (54, 56, 58, 60) $c = a$, and above dispersion degenerates to the isotropic one $E_{v,u} = v \sqrt{aq^2 + u b |q_1 q_2|}$. Two groups, 29 and 33, enforce $b^2 - 4ac = 0$, hosting thus FT dispersions (with bands counted by $u, v = \pm 1$):

$$E_{v,u}(\mathbf{q}) = v |f |q_1| + u g |q_2||, \quad (3.1b)$$

with f, g positive quantities, also functions of v_{pq}^i . Note that on the other side, the limit $b \rightarrow 0^+$ gives Dirac dispersion.

3.2. Density of states

Dispersions (3.1), differing from the well-known Dirac, semi-Dirac or quadratic, impose specific physical properties. In this context, one must take into account the range of validity of these forms, describing the realistic band structures only in the vicinity of high-symmetry point. In particular, corresponding density of states (DOS) near $E = 0$ are:

$$\rho_{\text{PF}}^{\text{SOC}} = \frac{2|E|}{\pi \sqrt{4ac - b^2}}, \quad (3.2a)$$

$$\rho_{\text{FT}}^{\text{SOC}} \approx \frac{L}{4\pi^2 \sqrt{f^2 + g^2}}. \quad (3.2b)$$

Unlike to PF, but similarly to 3D nodal semimetals [39], exact calculation of DOS of FT is prevented due to the non-circular iso-energetic lines (figure 1). Thus, the last expression corresponds to realistic situations where the horizontal parts of band crossing lines are of the length L (this is an effective

range of approximation). In non-SOC case calculation of DOS gives doubled results (3.2), since each energy is spin degenerate, which is then decoupled from the orbital one. Non zero DOS of FT near $E = 0$ is in contrast to DOS of Dirac or PF dispersions being proportional to $|E|$, as well as to semi-Dirac which is proportional to $\sqrt{|E|}$. This affects many properties, to mention only charge and spin transport. Further, it can be shown that the electron effective mass, obtained from band curvatures, for all dispersions (3.1) vanishes. Let us emphasize that the higher order terms, neglected in derivation cannot change the obtained band topology (figure 1), though may distort bands slightly.

3.3. Symmetry breaking

Despite the obtained dispersions are essential, i.e. resistant to symmetry preserving perturbation, an interesting additional insight is gained by considering symmetry breaking. Herein, taking into account group-subgroup relations, we discuss the possibilities of robustness or switching between various dispersions at the same BZ-point by lowering the symmetry, e.g. due to strain. It is expected that decreasing the number of symmetry elements leads to relaxing the constraints imposed on Hamiltonians, and consequently increasing (or preserving) the number of independent parameters. In this context, taking into account the number of non-zero parameters v_{pq}^i of (2.5) given in table 1, it is meaningful to consider the transitions from FT to anisotropic PF, as well as from isotropic PF to FT, when the symmetry is lowered. Precisely, the allowed four-band model Hamiltonian diagonalizing in PF dispersion have six real independent parameters, which are reduced to three for quadratic groups; similarly, there are 4 real independent Hamiltonian parameters for FT. Before proceeding, let us take a brief look into the robustness of FT and PF.

Regarding groups 29 and 33 supporting FT dispersion, symmetry reduction in which either nonsymmorphic glide plane or screw axis (but not both) is retained causes that FT at the Y point splits into two non-degenerate conical dispersions. Opposite out-of-plane shifts of the adjacent nuclei positioned

Table 2. Allowed irreducible co-representations: for each group and corresponding HSP, the generators are listed, and the block-diagonal part \hat{R} of double valued co-representation \hat{D} representing these generators (in the same order). Here, $C_{n\hat{n}}$ is rotation for $2\pi/n$ around axis \hat{n} (which is \hat{x} , \hat{y} , \hat{z} , or $\hat{c} = \frac{1}{\sqrt{2}}(\hat{x} + \hat{y})$), $m_{\hat{n}}$ is vertical mirror plane which contains \hat{n} axis, m_h is horizontal mirror plane, and $S_n = C_{n\hat{z}}m_h$.

Group	HSP	Generators		\hat{R}			
21	S	$(C_{2\hat{x}} \frac{1}{2}0)$	$(C_{2\hat{y}} 0\frac{1}{2})$	$\hat{\sigma}_3$	$\hat{\sigma}_1$		
25	S	$(m_{\hat{x}} \frac{1}{2}0)$	$(m_{\hat{y}} 0\frac{1}{2})$	$\hat{\sigma}_3$	$\hat{\sigma}_1$		
28	Y	$(I 10)$	$(C_{2\hat{y}} 0\frac{1}{2})$	$m_{\hat{y}}$	$\hat{\sigma}_0$	$-\hat{\sigma}_3$	$-i\hat{\sigma}_2$
28	S	$(I 10)$	$(C_{2\hat{y}} 0\frac{1}{2})$	$m_{\hat{y}}$	$-\hat{\sigma}_0$	$-\hat{\sigma}_3$	$-i\hat{\sigma}_2$
29	Y	$(I 10)$	$(C_{2\hat{y}} 0\frac{1}{2})$	m_h	$\hat{\sigma}_0$	$-\hat{\sigma}_3$	$-i\hat{\sigma}_2$
29	S	$(I 10)$	$(C_{2\hat{y}} 0\frac{1}{2})$	m_h	$-\hat{\sigma}_0$	$-\hat{\sigma}_3$	$-i\hat{\sigma}_2$
30	Y	$(I 10)$	$(m_{\hat{y}} 0\frac{1}{2})$	$C_{2\hat{y}}$	$\hat{\sigma}_0$	$-\hat{\sigma}_3$	$-i\hat{\sigma}_2$
30	S	$(I 10)$	$(m_{\hat{y}} 0\frac{1}{2})$	$C_{2\hat{y}}$	$-\hat{\sigma}_0$	$-\hat{\sigma}_3$	$-i\hat{\sigma}_2$
32	Y	$(I 10)$	$(m_h \frac{1}{2}\frac{1}{2})$	$m_{\hat{y}}$	$\hat{\sigma}_0$	$-\hat{\sigma}_3$	$-i\hat{\sigma}_2$
33	Y	$(m_h \frac{1}{2}0)$	$(C_{2\hat{y}} 0\frac{1}{2})$		$i\hat{\sigma}_3$	$\hat{\sigma}_1$	
34	Y	$(I 10)$	$(m_h \frac{1}{2}\frac{1}{2})$	$C_{2\hat{y}}$	$\hat{\sigma}_0$	$-\hat{\sigma}_3$	$-i\hat{\sigma}_2$
54	M	$(I 10)$	$(C_{2\hat{c}} \frac{1}{2}\frac{1}{2})$	$C_{4\hat{z}}$	$-\hat{\sigma}_0$	$-i\hat{\sigma}_2$	$e^{-i\frac{3\pi}{4}} \text{diag}(1, i)$
56	M	$(I 10)$	$(m_{\hat{c}} \frac{1}{2}\frac{1}{2})$	$C_{4\hat{z}}$	$-\hat{\sigma}_0$	$-i\hat{\sigma}_2$	$e^{-i\frac{3\pi}{4}} \text{diag}(1, i)$
58	M	$(I 10)$	$(m_{\hat{c}} \frac{1}{2}\frac{1}{2})$	S_4	$-\hat{\sigma}_0$	$-i\hat{\sigma}_2$	$e^{-i\frac{3\pi}{4}} \text{diag}(1, i)$
60	M	$(I 10)$	$(C_{2\hat{c}} \frac{1}{2}\frac{1}{2})$	S_4	$-\hat{\sigma}_0$	$-i\hat{\sigma}_2$	$e^{-i\frac{3\pi}{4}} \text{diag}(1, i)$

in the mirror plane, transforms mirror into a glide plane, while doubling the lattice constant; this in turn halves primitive vector \mathbf{k}_1 of the reciprocal lattice. Group 29 reduces to 33 and the S point in 29 becomes Y point in 33. Consequently, FT in Y and S points in 29 are robust against lowering the symmetry to group 33. Similarly, concerning the PF, any homogeneous stretching along \mathbf{a}_1 or \mathbf{a}_2 axis deforms square primitive cell to rectangular, reducing the symmetries of layer groups 54 and 58 (56 and 60) to the group 21 (25) and causes PF to change from isotropic to anisotropic form, which implies direction-dependent electronic and related properties.

Since PF is a generalized form of FT, one could expect that the parameters of these dispersions can be interrelated by tuning. However, continuous transformation from FT to PF at the same point of the BZ is not possible, since neither of groups supporting FT is a subgroup of any of groups allowing PF, nor vice-versa. The expression (3.2a) for DOS of PF shows that the changing parameters such that PF approaches to FT results in a singularity at zero energy. In the other words, if opposite would hold, arbitrarily small displacements of nuclei, being sufficient to lower the symmetry, would cause a jump of (graphene-like) negligible DOS of PF to a finite and constant DOS of FT, which we found unlikely. At the same time, such obstruction from DOS does not forbid the transition between Dirac (double degenerate cones with four-fold degenerate point) and PF, nor it forbids splitting of FT and PF into two non-degenerate conical dispersions (with double degenerate point).

Following the above arguments, it is expected that transition from Dirac cone to PF may be realized by lowering the symmetry, since Dirac dispersions has less independent parameters than PF. According to [5] Dirac semimetals in time-reversal invariant two-dimensional systems with strong SOC are possible in nonsymmorphic groups with inversion symmetry. E.g. let us consider the layer group 46 ($pmmn$), hosting Dirac cones

at X , Y and S HSPs (the BZ is the same as this one given on the left panel in figure 2). It is expected that the violation of the inversion symmetry leads to Weyl points or node [5]. However, listing all subgroups, it turns out that the two of the subgroups, 32 and 21, actually host PF in the points Y and S , respectively. Indeed, in [46], using spinfull tight-binding model with four sites (with s-orbitals) per unit cell, authors show that at fillings 2, 6, system invariant under double layer group 21 is semimetal, which hosts one fourfold degenerate and four Weyl points. A plethora of such cases, where groups allowing PF from the table 1 are subgroups of symmetry groups of Dirac semimetals, indicates candidates for transitions between centrosymmetric and noncentrosymmetric crystals with protected four-fold band crossing point. Moreover, the existence of such essential fourfold degenerate point simultaneously with double degenerate Weyl points in the same system, makes that the layers from our list represent possible two-dimensional materials suitable for the study of their interplay.

3.4. Material realization

Despite the fabrication of freestanding layers is not always feasible, the above theoretical predictions required material realizations, or at least numerical simulations. To find realistic material with layer groups from table 1 we searched the list [41] of 3D layered materials, synthesis of which has been reported in the literature. In the table 3 we listed potential material candidates with symmetry groups allowing the predicted peculiar dispersions. These are laboratory fabricated 3D crystals with layered structures, which could be easily or potentially exfoliated into layers.

It is interesting to single out our group-theoretical findings indicated that dispersions (3.1) are not preserved when SOC is neglected, except for the LDG 33, which supports FT dispersion also in that case [29]. Inclusion of SOC moves FT from

Table 3. Material candidates: layered systems with symmetry groups hosting the dispersions (3.1). Layer and corresponding space groups are listed for materials given by a formula and materials project ID. Abbreviations EE and PE stand for easily and potentially exfoliable, respectively, according to [41].

	Layer group		Space group	Formula	ID	EE/PE
21	$p2_12_12$	18	$P2_12_12$	As ₂ SO ₆	mp-27230	EE
				MgMoTeO ₆	mp-1210722	EE
25	$pba2$	32	$Pba2$	Au ₂ Se ₂ O ₇	mp-28095	EE
				Re ₂ S ₂ O ₁₃ -I	mp-974650	EE
28	$pm2_1b$	26	$Pmc2_1$	TiP ₅	mp-27411	EE
				KO ₂ H ₄ F	mp-983327	PE
				NaGe ₃ P ₃	mp-1104707	PE
29	$pb2_1m$	26	$Pmc2_1$	WO ₂ Cl ₂	mp-32539	EE
32	$pm2_1n$	31	$Pmn2_1$	CuCOCl	mp-562090	EE
33	$pb2_1a$	29	$Pca2_1$	BiIO ₄	mp-1191266	PE
				KPSe ₆	mp-18625	EE
58	$p\bar{4}2_1m$	113	$P\bar{4}2_1m$	LiReO ₂ F ₄	mp-554108	EE

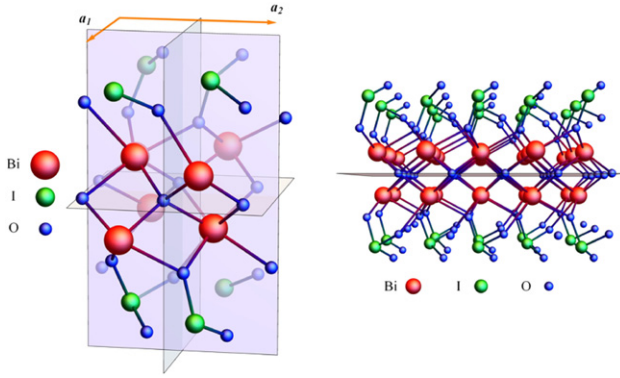


Figure 3. Crystal structure of BiIO₄ mono-layer: elementary cell (left) and a part of layer (right).

BZ corners to the Y -point. The material BiIO₄ belongs to corresponding space group 29 and has layers parallel to the $y = 0$ plane. Consequently, it should exfoliate to layer group 33 so we choose it for further DFT investigations, as an example of achievements of our theory. Since IRs from table 1 are the only extra IRs in these BZ points, the dispersions (3.1) are unavoidable for crystals with symmetry of these groups. On the other hand, the position of Fermi level cannot be determined solely by symmetry arguments, nor it can be guaranteed that no other bands cross or touch the Fermi level.

We determined crystal (figure 3) and band structure (figure 4) of BiIO₄ mono-layer configuration using DFT calculations: full relaxation and bands calculations were performed by QUANTUM ESPRESSO software package [42], full relativistic PAW pseudopotentials [43, 44], with the Perdew–Burke–Ernzerhof exchange–correlation functional [45]. The energy cutoff for electron wavefunction and charge density of 47 Ry and 476 Ry were chosen, respectively. The band structures were found in 500 k -points on selected path, and 2500 k -points for 2D band structure plots in the vicinity of HSPs.

Crystal structure of mono-layer is shown in figure 3. It belongs to rectangular lattice of the group 33, with nearly equal $a_1 = 0.566$ nm and $a_2 = 0.575$ nm. Band structure of BiIO₄

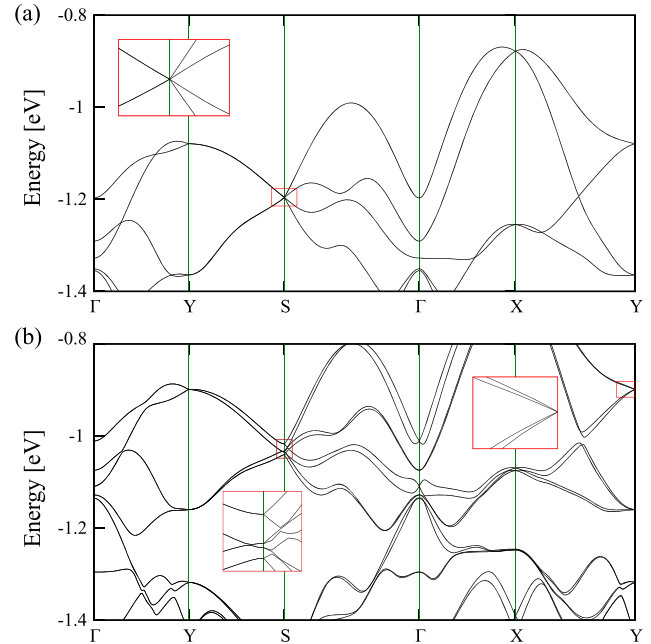


Figure 4. Band structure of BiIO₄ mono-layer without SOC (top) and with SOC (bottom), with insets showing magnified FT and split FT dispersions. The Fermi level is set to zero eV.

mono-layer with and without SOC is shown in figure 4. It turns out that the system is insulating in undoped and ungated regime. The closest to Fermi level FT state is at -0.9 eV. When SOC is neglected energy at the point S is eightfold degenerate (including spin), which gives electron filling of $8n$ that is necessary for insulating systems [40]. With inclusion of SOC the eightfold spinfull degeneracy at S is lifted, but sets of eight non-degenerate bands each, form *cat's cradle* structure along ΓX line, as predicted in reference [46]. This gives again electron filling of $8n$ [46, 47]. Our electron filling of 184, derived from DFT calculations, is indeed divisible by 8. Electron filling for DLG 33 prevents FT to be the only dispersion at the Fermi level, while for remaining groups in table 1 the filling condition necessary for Fermi surface consisting of isolated points is $\nu = 4n + 2$.

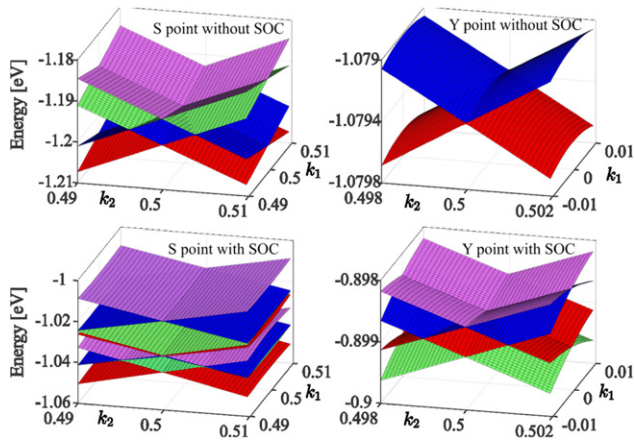


Figure 5. Band structures of BiIO₄ mono-layer without and with SOC near points *S* and *Y*. Inclusion of SOC turns FT dispersion into nodal lines in *S*, and degenerate Dirac line into FT in *Y*.

Behavior of FT states with inclusion of SOC is shown in figure 5. In non-SOC case, two pairs of Dirac lines meet at the point *S* and form the FT states. SOC splits eightfold degenerate band at *S* into four double degenerate ones. Near point *Y*, SOC splits fourfold spinfull degenerate Dirac line into one FT state. Since SOC strength is proportional to the fourth power of the atomic number [48], heavy elements in the material induced observable splitting.

4. Conclusions

Characterized by band crossings (touching) points (lines) at Fermi level from which energies disperse linearly, nodal metals/semimetals take an important role in investigations of various topological properties of crystals. Among them, symmetry-enforced ones represent a class of materials hosting such dispersions in HSPs due to increased degeneracy. In the language of group theory, while the spinless case is described by the ordinary group of geometrical transformations, the spinfull situation, when system is robust on spin-orbit perturbation, needs double groups. Additional inclusion of TRS leads to gray magnetic ordinary or double group. The increased degeneracy of energy is enabled by higher dimensional allowed irreducible (co)representations of the corresponding underlying crystal symmetry.

New fermions in 2D materials revealed by application of full gray double layer group symmetry contribute to the interesting physical phenomena of layered systems: two new types of dispersions beyond Dirac, PF and FT, accompany the fourfold degeneracy of bands in high-symmetry points. Our findings single out list of twelve nonsymmorphic and non-centrosymmetric layer groups that support such unusual linear electronic dispersions. As the method is not based on the topological mechanism (invoking nonsymmorphic symmetry), the result is general, verifying *a posteriori* the necessity of nonsymmorphic elements for the considered dispersions. Providing this list, numerical simulations aimed to find material realizations of the peculiar dispersions are facilitated, which is of a great importance to achieve corresponding physical properties. PF dispersion occurs in ten groups; in particular, there

are single isolated HSP hosting it in the groups $p2_12_12$, $pba2$ (point *S*), $pm2_1n$, $pb2n$ (*Y*), and $p42_12$, $p4bm$, $p42_1m$, $p4b2$ (*M*), while the groups $pm2_1b$ and $pb2b$ have two such points (*Y*, *S*). On the other hand, the FT type of dispersion in the group $pb2_1a$ is hosted in single (*Y*), and in the group $pb2_1m$ in two HSPs (*Y*, *S*).

Particularly interesting are groups $pb2_1a$, supporting FT dispersion both with and without SOC, as well as $pba2$ and $p4bm$, which are also wallpaper groups, preserved even when perpendicular, homogenous electric field is applied (e.g. due to gating). Moreover, coexistence of degenerate point and lines at the same energy in FT dispersion may lead to some new phenomena. FT dispersion has constant contribution to DOS, manifested as a plateau nearby zero energy in FT. This may be important in technological applications, especially when electron and/or spin transport are looked for, like materials for solar cells [49], spintronic etc. On the contrary, PF dispersion, similarly to Dirac ones, contributes by linear DOS with no states on zero energy. It has both isotropic and anisotropic forms which may be continuously transformed into each other by crystal deformations.

Our numerical calculations show that layered BiIO₄ 3D crystal, exfoliates to stable mono-layer having a symmetry group from our list. Band structure of BiIO₄ mono-layer confirms theoretical prediction, but further efforts are necessary in order to place the Fermi level at right energy.

Acknowledgments

Authors VD, AŠ and JP acknowledge funding provided by the Institute of Physics Belgrade, through the Grant by the Ministry of Education, Science and Technological Development of the Republic of Serbia. NL, BN and MD were supported by the Serbian Ministry of Education, Science and Technological Development under Project Number OI171035. DFT calculations were performed using computational resources at Johannes Kepler University, Linz, Austria.

ORCID iDs

V Damjanović <https://orcid.org/0000-0001-7517-6439>
 N Lazić <https://orcid.org/0000-0002-3634-0301>
 A Šolajić <https://orcid.org/0000-0002-0553-0858>
 J Pešić <https://orcid.org/0000-0002-8600-7187>
 B Nikolić <https://orcid.org/0000-0002-7241-3248>
 M Damjanović <https://orcid.org/0000-0003-2806-253X>

References

- [1] Gupta S, Kutana A and Yakobson B I 2018 Dirac cones and nodal line in borophene *J. Phys. Chem. Lett.* **9** 2757–62
- [2] Zhang Y, Kang J, Zheng F, Gao P-F, Zhang S-L and Wang L-W 2019 Borophosphene: a new anisotropic Dirac cone mono-layer with a high Fermi velocity and a unique self-doping feature *J. Phys. Chem. Lett.* **10** 6656–63
- [3] Zhang L Z, Wang Z F, Wang Z M, Du S X, Gao H-J and Liu F 2015 Highly anisotropic Dirac fermions in square graphynes *J. Phys. Chem. Lett.* **6** 2959–62

- [4] Fang C, Gilbert M J, Dai X and Andrei Bernevig B 2012 Multi-Weyl topological semimetals stabilized by point group symmetry *Phys. Rev. Lett.* **108** 266802
- [5] Young S M and Kane C L 2015 Dirac semimetals in two dimensions *Phys. Rev. Lett.* **115** 126803
- [6] van Miert G and Smith C M 2016 Dirac cones beyond the honeycomb lattice: a symmetry-based approach *Phys. Rev. B* **93** 035401
- [7] Wang J 2017 Antiferromagnetic Dirac semimetals in two dimensions *Phys. Rev. B* **95** 115138
- [8] Kim J, Baik S S, Jung S W, Sohn Y, Ryu S H, Choi H J, Yang B-J and Kim K S 2017 Two-dimensional Dirac fermions protected by space-time inversion symmetry in black phosphorus *Phys. Rev. Lett.* **119** 226801
- [9] Young S M and Wieder B J 2017 Filling-enforced magnetic Dirac semimetals in two dimensions *Phys. Rev. Lett.* **118** 186401
- [10] Kawarabayashi T, Aoki H and Hatsugai Y 2019 Topologically protected doubling of tilted Dirac fermions in two dimensions *Phys. Status Solidi B* **256** 1970025
- [11] Mañes J L 2012 Existence of bulk chiral fermions and crystal symmetry *Phys. Rev. B* **85** 155118
- [12] Damljanić V and Gajić R 2016 Existence of Dirac cones in the Brillouin zone of diperiodic atomic crystals according to group theory *J. Phys.: Condens. Matter* **28** 085502
- [13] Damljanić V and Gajić R 2016 Addendum to existence of Dirac cones in the Brillouin zone of diperiodic atomic crystals according to group theory *J. Phys.: Condens. Matter* **28** 439401
- [14] Park S and Yang B-J 2017 Classification of accidental band crossings and emergent semimetals in two-dimensional noncentrosymmetric systems *Phys. Rev. B* **96** 125127
- [15] Wieder B J, Bradlyn B, Wang Z, Cano J, Kim Y, Kim H-S D, Rappe A M, Kane C L and Andrei Bernevig B 2018 Wallpaper fermions and the nonsymmorphic Dirac insulator *Science* **361** 246–51
- [16] Wieder B J, Kim Y, Rappe A M and Kane C L 2016 Double Dirac semimetals in three dimensions *Phys. Rev. Lett.* **116** 186402
- [17] Bradlyn B, Cano J, Wang Z, Vergniory M G, Felser C, Cava R J and Andrei Bernevig B 2016 Beyond Dirac and Weyl fermions: unconventional quasiparticles in conventional crystals *Science* **353** aaf5037
- [18] Zhu Z, Winkler G W, Wu Qian, Ju L and Alexey A 2016 Soluyanov. Triple point topological metals *Phys. Rev. X* **6** 031003
- [19] Wang Z, Alexandradinata A, Cava R J and Andrei Bernevig B 2016 Hourglass fermions *Nature* **532** 189–94
- [20] Lv B Q *et al* 2017 Observation of three-component fermions in the topological semimetal molybdenum phosphide *Nature* **546** 627–31
- [21] Barik R K, Shinde R and Singh A K 2018 Multiple triple-point fermions in Heusler compounds *J. Phys.: Condens. Matter* **30** 375702
- [22] Yang Y *et al* 2019 Topological triply degenerate point with double Fermi arcs *Nat. Phys.* **15** 645–9
- [23] Ma J *et al* 2017 Experimental evidence of hourglass fermion in the candidate nonsymmorphic topological insulator KHgSb *Sci. Adv.* **3** e1602415
- [24] Wang S-S, Liu Y, Yu Z-M, Sheng X-L and Yang S A 2017 Hourglass Dirac chain metal in rhenium dioxide *Nat. Commun.* **8** 1844
- [25] Singh B, Ghosh B, Su C, Lin H, Agarwal A and Bansil A 2018 Topological hourglass Dirac semimetal in the nonpolar phase of Ag_2BiO_3 *Phys. Rev. Lett.* **121** 226401
- [26] Novoselov K S, Geim A K, Morozov S V, Jiang D, Zhang Y, Dubonos S V, Grigorieva I V and Firsov A A 2004 Electric field effect in atomically thin carbon films *Science* **306** 666–9
- [27] Kim J *et al* 2015 Observation of tunable band gap and anisotropic Dirac semimetal state in black phosphorus *Science* **349** 723–6
- [28] Wang Z M 2014 *MoS₂ Materials, Physics and Devices* (Berlin: Springer)
- [29] Damljanić V, Popov I and Gajić R 2017 Fortune teller fermions in two-dimensional materials *Nanoscale* **9** 19337–45
- [30] Kopciuszynski M, Krawiec M, Żurawek L and Zdyb R 2020 Experimental evidence of a new class of massless fermions *Nanoscale Horiz.* **5** 679–82
- [31] Nguyen S D, Yeon J, Kim S-H and Shiv Halasyamani P 2011 $\text{BiO}(\text{IO}_3)$: a new polar iodate that exhibits an Aurivillius-type $(\text{Bi}_2\text{O}_2)^{2+}$ layer and a large SHG response *J. Am. Chem. Soc.* **133** 12422–5
- [32] Cornwell J F 1984 *Group Theory in Physics* (New York: Academic)
- [33] Elcoro L *et al* 2017 Double crystallographic groups and their representations on the Bilbao Crystallographic Server *J. Appl. Crystallogr.* **50** 1457–77
- [34] Damljanić M and Milošević I 2015 Full symmetry implementation in condensed matter and molecular physics—modified group projector technique *Phys. Rep.* **581** 1–43
- [35] Litvin D B and Wike T R 1991 *Character Tables and Compatibility Relations of the Eighty Layer Groups and Seventeen Plane Groups* (New York: Plenum)
- [36] Dresselhaus M S, Dresselhaus G and Jorio A 2008 *Group Theory* (Berlin: Springer)
- [37] Kopsky V and Litvin D B 2002 *International Tables of Crystallography Volume E: Subperiodic Groups* (Dordrecht: Kluwer)
- [38] Hahn T 2005 *International Tables of Crystallography Volume A: Space-Group Symmetry* (Berlin: Springer)
- [39] Burkov A A, Hook M D and Leon B 2011 Topological nodal semimetals *Phys. Rev. B* **84** 235126
- [40] Watanabe H, Po H C, Zaletel M P and Vishwanath A 2016 Filling-enforced gaplessness in band structures of the 230 space groups *Phys. Rev. Lett.* **117** 096404
- [41] Mounet N *et al* 2018 Two-dimensional materials from high-throughput computational exfoliation of experimentally known compounds *Nat. Nanotechnol.* **13** 246–52
- [42] Giannozzi P *et al* 2009 QUANTUM ESPRESSO: a modular and open-source software project for quantum simulations of materials *J. Phys.: Condens. Matter* **21** 395502
- [43] Blöchl P E 1994 Projector augmented-wave method *Phys. Rev. B* **50** 17953–79
- [44] Kresse G and Joubert D 1999 From ultrasoft pseudopotentials to the projector augmented-wave method *Phys. Rev. B* **59** 1758–75
- [45] Perdew J P, Burke K and Ernzerhof M 1996 Generalized gradient approximation made simple *Phys. Rev. Lett.* **77** 3865–8
- [46] Wieder B J and Kane C L 2016 Spin–orbit semimetals in the layer groups *Phys. Rev. B* **94** 155108
- [47] Watanabe H, Po H C, Vishwanath A and Zaletel M 2015 Filling constraints for spin-orbit coupled insulators in symmorphic and nonsymmorphic crystals *Proc. Natl Acad. Sci.* **112** 14551–6
- [48] Yang S A 2016 Dirac and Weyl materials: fundamental aspects and some spintronics applications *SPIN* **06** 1640003
- [49] Boriskina S, Zhou J, Ding Z and Chen G 2018 Efficiency limits of solar energy harvesting via internal photoemission in carbon materials *Photonics* **5** 4

Short-Range Order in VI_3

Sanja Djurdjic Mijin, A. M. Milinda Abeykoon, Andrijana Šolajić, Ana Milosavljević, Jelena Pešić, Yu Liu, Cedimir Petrovic, Zoran V. Popović, and Nenad Lazarević*

Cite This: *Inorg. Chem.* 2020, 59, 16265–16271

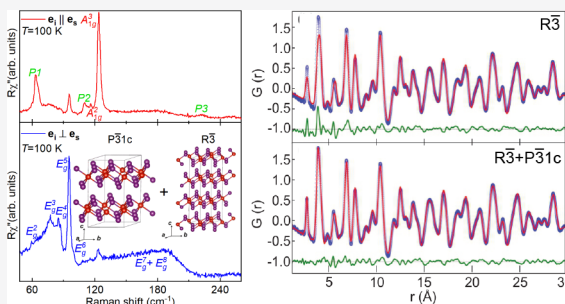
Read Online

ACCESS |

Metrics & More

Article Recommendations

ABSTRACT: We present a detailed investigation of the crystal structure of VI_3 , a two-dimensional van der Waals material of interest for studies of low-dimensional magnetism. As opposed to the average crystal structure that features $R\bar{3}$ symmetry of the unit cell, our Raman scattering and X-ray atomic pair distribution function analysis supported by density functional theory calculations point to the coexistence of short-range ordered $P\bar{3}1c$ and long-range ordered $R\bar{3}$ phases. The highest-intensity peak, A_{1g}^3 , exhibits a moderate asymmetry that might be traced back to the spin–phonon interactions, as in the case of CrI_3 .



INTRODUCTION

A well-known family of transition metal trihalides (TMTs) MX_3 ($X = \text{Cr}, \text{B}, \text{or I}$) have received a great deal of attention due to potential existence of two-dimensional (2D) ferromagnetism,^{1–6} which has been confirmed in CrI_3 .^{7,8} The similar crystal structure and magnetic properties of CrI_3 and VI_3 fostered a belief that the same might be found in the latter. In fact, magnetization measurements revealed the 2D ferromagnetic nature of VI_3 with a Currie temperature (T_c) of around 50 K.^{9,10} Contrary to a layer-dependent ferromagnetism in CrI_3 ,¹¹ the first-principles calculations predict that ferromagnetism in VI_3 persists down to a single layer,⁹ making it a suitable candidate for engineering 2D spintronic devices. Resistivity measurements showed VI_3 is an insulator with an optical band gap of ~ 0.6 eV.^{9,12}

Whereas laboratory X-ray diffraction studies reported three possible high-temperature VI_3 unit cell symmetries,^{9,12–14} high-resolution synchrotron X-ray diffraction confirmed a rhombohedral $R\bar{3}$ space group.¹⁰ A very recently published Raman spectroscopy study indicated that the VI_3 crystal structure can be described within the C_{2h} point group.¹⁵ All results agree on the existence of a phase transition at a temperature of 79 K. However, the subtle¹² structural changes below 79 K are still under debate.

The long-range magnetic order in ultrathin 2D van der Waals (vdW) crystals stems from strong uniaxial anisotropy, in contrast to materials with isotropic exchange interactions where order parameters are forbidden.^{16–18} 2D vdW magnetic materials are of interest both as examples of exotic magnetic order¹⁹ and for potential applications in spintronic technology.^{2,4,20,21}

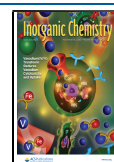
Atomically thin flakes of CrCl_3 have a magnetic transition temperature that is different from that of bulk crystals possibly

due to the different crystal structure of the monolayer and ultrathin crystals when compared to bulk.^{22,23} Similar observations were made on CrI_3 monolayers.^{22,24,25} It has been proposed²³ that the second anomaly in heat capacity in bulk CrCl_3 arises due to regions close to the surface that host a different crystal structure when compared to bulk;^{26,27} however, due to the substantial mass fraction detected in heat capacity measurements, this could also reflect differences between the short-range order and long-range crystallographic order of Bragg planes. The short-range order is determined by the space group that is energetically favorable for a monolayer or a few layers, whereas the long-range crystallographic order is established over large packing lengths.

In this paper, we present an experimental Raman scattering study of the bulk VI_3 high-temperature structure, supported by density functional theory (DFT) calculations and the X-ray atomic pair distribution function (PDF) analysis. The comparison between the Raman experiment and DFT calculations for each of the previously reported space groups suggested that the high-temperature lattice vibrations of bulk VI_3 are consistent with a $P\bar{3}1c$ trigonal structure. Nine ($2A_{1g} + 7E_g$) of 12 observed peaks were assigned on the basis of factor group analysis (FGA) and DFT calculations. The PDF analysis indicated the coexistence of two crystallographic phases at two different interatomic distances, short-range ordered $P\bar{3}1c$ and

Received: July 12, 2020

Published: October 23, 2020



long-range ordered $R\bar{3}$, as two segregated phases and/or as randomly distributed short-range ordered $P\bar{3}1c$ domains in the long-range ordered $R\bar{3}$ lattice. Raman data displayed a moderate asymmetry of the A_{1g}^3 phonon line. This behavior was attributed to the spin–phonon interaction, similar to the case for CrI_3 . The additional peaks in our spectra obey A_g selection rules and can be described in terms of overtones, as well as the A_{2g} silent modes “activated” by the symmetry breaking.

EXPERIMENTAL AND COMPUTATIONAL DETAILS

The preparation of single-crystal VI_3 samples used in this study is presented elsewhere.¹⁰ For the Raman scattering experiment, a Tri Vista 557 spectrometer was used in the backscattering micro-Raman configuration with a 1800/1800/2400 grooves/mm diffraction grating combination. A Coherent Ar^+/Kr^+ ion laser with a 514 nm line was used as an excitation source. Laser beam focusing was achieved through the microscope objective with 50 \times magnification. The direction of the incident (scattered) light coincides with the crystallographic c axis. The sample, cleaved in open air, was held inside a KONTEC CryoVac continuous helium flow cryostat with a 0.5 mm thick window. Raman scattering measurements were performed under high vacuum (10^{-6} mbar). All of the obtained Raman spectra were corrected by the Bose factor. The spectrometer resolution is comparable to the Gaussian width of 1 cm^{-1} .

PDF and wide-angle X-ray scattering measurements were carried out in capillary transmission geometry using a PerkinElmer amorphous silicon area detector placed 206 and 983 mm downstream from the sample, respectively, at beamline 28-ID-1 (PDF) of National Synchrotron Light Source II at Brookhaven National Laboratory. The setup utilized a 74.3 keV ($\lambda = 0.1668\text{ \AA}$) X-ray beam.

Two-dimensional diffraction data were integrated using the Fit2D software package.²⁸ Data reduction was performed to obtain experimental PDFs ($Q_{\text{max}} = 26\text{ \AA}^{-1}$) using the xPDFsuite software package.²⁹ The Rietveld and PDF analyses were carried out using GSAS-II³⁰ and PDFgui³¹ software packages, respectively.

Density functional theory calculations were performed using the Quantum Espresso software package,³² employing the PBE exchange–correlation functional³³ and PAW pseudopotentials.^{34,35} All calculations are spin-polarized. The cutoff for wave functions and the charge density were set to 48 and 650 Ry, respectively. The k -points were sampled using the Monkhorst–Pack scheme, on a $6 \times 6 \times 6$ Γ -centered grid for $R\bar{3}$ and $C2/m$ structures and a $12 \times 12 \times 8$ grid for the $P\bar{3}1c$ structure. Optimization of the lattice parameters and atomic positions in the unit cell was performed until the interatomic forces were $<10^{-6}$ Ry/ \AA . To obtain more accurate lattice parameters, treatment of the van der Waals interactions is included using the Grimme-D2 correction. The correlation effects are treated with the Hubbard U correction (LDA+ U), using a rotationally invariant formulation implemented in QE,³⁶ where $U = 3.68\text{ eV}$. Band structure plots are calculated at 800 k -points on the chosen path over high-symmetry points. Phonon frequencies were calculated with the linear response method, as implemented in the -phono part of Quantum Espresso.

RESULTS AND DISCUSSION

The first reported results for VI_3 , dating from the 1950s,^{37–39} indicated that VI_3 adopts a honeycomb layer-type BiI_3 structure described with space group $R\bar{3}$, which is a structure common in TMTs, also found in the low-temperature phase of CrI_3 .^{6,40}

There have been several proposed unit cell symmetries for VI_3 in the literature: $R\bar{3}$,^{12,13} $C2/m$,¹⁴ and $P\bar{3}1c$.⁹ Schematic representations of the $P\bar{3}1c$, $R\bar{3}$, and $C2/m$ crystal structures are depicted in Figure 1. The corresponding crystallographic unit cell parameters, previously reported, are listed in Table 1.

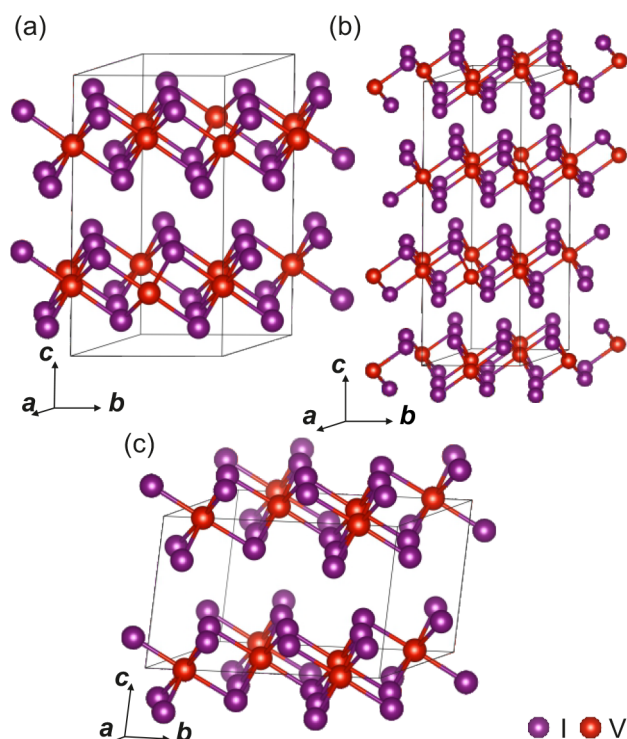


Figure 1. Schematic representation of the high-temperature (a) $P\bar{3}1c$, (b) $R\bar{3}$, and (c) $C2/m$ structures of VI_3 . Black solid lines represent unit cells.

Each of the suggested symmetries implies a different distribution of Raman active modes.

According to FGA, eight ($4A_g + 4E_g$), 11 ($3A_{1g} + 8E_g$), and 12 ($6A_g + 6B_g$) Raman active modes are expected to be observed in the light scattering experiment for $R\bar{3}$, $P\bar{3}1c$, and $C2/m$ crystal structures, respectively. Wyckoff positions, irreducible representations, and corresponding tensors of Raman active modes for each space group are listed in Table 2.

The first step in determining the crystal symmetry from the light scattering experiment is to compare the expected and observed Raman active modes, shown in Figure 2. The red solid line represents the spectrum measured in the parallel polarization configuration, whereas the blue line corresponds to the cross polarization configuration. Five of 12 observed peaks emerge only in parallel, whereas five peaks and a broad peak-like structure can be observed for both polarization configurations. The emergence of the 123.4 cm^{-1} peak in the cross polarization can be understood as a “leakage” of the A_{1g}^3 mode due to a possible finite c axis projection and/or the presence of defects.

Now the peaks that appear only for the parallel polarization configuration can be assigned as either A_{1g} or A_g symmetry modes, assuming the light polarization direction along the main crystal axis of the $C2/m$ structure for the later. On the basis of the FGA for possible symmetry group candidates, the remaining Raman active modes can be either of E_g or B_g symmetry. The selection rules (Table 2) do not allow observation of the B_g symmetry modes for the parallel polarization configuration. Consequently, the peaks that can be observed in both scattering channels were recognized as E_g modes. The absence of B_g modes in the Raman spectra rules out the possibility of the AlCl_3 type of structure (space group $C2/m$). Two possible remaining crystal symmetries ($R\bar{3}$ and

Table 1. Previously Reported Experimental and Calculated Unit Cell Parameters for $P\bar{3}1c$, $R\bar{3}$, and $C2/m$ Structures of VI_3

	$P\bar{3}1c$		$R\bar{3}$		$C2/m$	
	calcd	exp. ⁹	calcd	exp. ¹²	calcd	exp. ¹⁴
<i>a</i> (Å)	6.87	6.89(10)	6.69	6.89(3)	7.01	6.84(3)
<i>b</i> (Å)	6.87	6.89(10)	6.69	6.89(3)	12.14	11.83(6)
<i>c</i> (Å)	13.224	13.289(1)	19.81	19.81(9)	7.01	6.95(4)
α (deg)	90	90	90	90	90	90
β (deg)	90	90	90	90	109.05	108.68
γ (deg)	120	120	120	120	90	90
cell volume (Å ³)	559.62	547.74(10)	767.71	814.09(8)	563.33	533.66(36)

Table 2. Wyckoff Positions of Atoms and Their Contributions to the Γ -Point Phonons for the $R\bar{3}$, $C2/m$, and $P\bar{3}1c$ Structures and the Raman Tensors for the Corresponding Space Groups

space group $P\bar{3}1c$		space group $R\bar{3}$		space group $C2/m$	
atom	irreducible representation	atom	irreducible representation	atom	irreducible representation
V (2a)	$A_{2g} + A_{2u} + E_g + E_u$	V (3a)		V (4g)	$A_g + A_u + 2B_g + 2B_u$
V (2c)	$A_{2g} + A_{2u} + E_g + E_u$	V (6c)	$A_g + A_u + E_g + E_u$	I (4i)	$2A_g + A_u + B_g + 2B_u$
I (12i)	$3A_{1g} + 3A_{1u} + 3A_{2g} + 3A_{2u} + 6E_g + 6E_u$	I (18f)	$3A_g + 3A_u + 3E_g + 3E_u$	I (8j)	$3A_g + 3A_u + 3B_g + 3B_u$

$$A_{1g} = \begin{pmatrix} a & a & b \end{pmatrix}$$

$${}^1E_g = \begin{pmatrix} c & -c & d \\ -c & c & d \\ d & d & d \end{pmatrix} {}^2E_g = \begin{pmatrix} -c & -c & -d \\ -c & c & d \\ d & d & d \end{pmatrix}$$

$$A_g = \begin{pmatrix} a & a & b \end{pmatrix}$$

$${}^1E_g = \begin{pmatrix} c & d & e \\ d & -c & f \\ e & f & e \end{pmatrix} {}^2E_g = \begin{pmatrix} d & -c & -f \\ -c & -d & e \\ -f & e & e \end{pmatrix}$$

$$A_g = \begin{pmatrix} a & d \\ c & b \end{pmatrix}$$

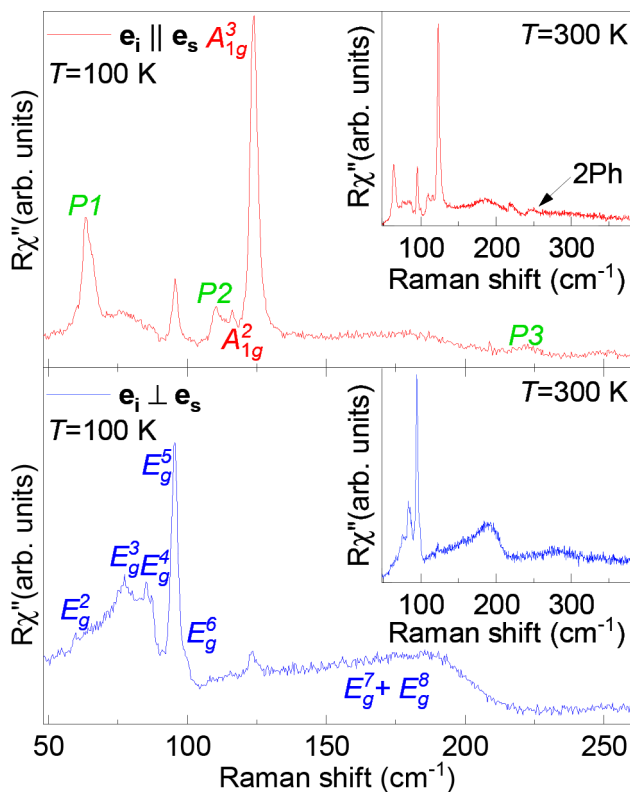
$$B_g = \begin{pmatrix} e & f \\ e & f \end{pmatrix}$$


Figure 2. Raman spectra of the high-temperature VI_3 single-crystal structure measured in parallel (red solid line) and cross (blue solid line) polarization configurations at 100 K. Peaks observed in both spectra were identified as E_g modes, whereas peaks observed only in the red spectrum were assigned as A_{1g} modes. Additional peaks that obey pure A_{1g} symmetry are marked as P1–P3.

$P\bar{3}1c$) are difficult to single out on the basis of the Raman data symmetry analysis alone. To overcome this obstacle, the DFT method was applied for each of the suggested structures.

It was reported in the literature that $P\bar{3}1c$ VI_3 can have two possible electronic states^{9,14,41–43} that both can be obtained using DFT+U calculations by varying the smearing and mixing parameters. This approach resulted in a Mott-insulator state having a lower energy making it the electronic ground state of VI_3 . However, the total energy difference of these two states is small and will not be mentioned further because it is outside of the scope of our analysis. For the sake of completeness, both sets of phonon energies obtained through DFT calculations for these electronic states of the $P\bar{3}1c$ structure are listed in Table 3 together with the results for the $R\bar{3}$ and $C2/m$ space groups as well as the experimental results measured at 100 K.

Now one can see that, even though the Raman mode symmetries for the case of the $R\bar{3}$ crystal structure can describe our Raman spectra, there is a stronger mismatch in calculated and experimentally determined phonon energies when compared to the results obtained for the $P\bar{3}1c$ structure. The deviation is largest for the calculated A_g^1 mode. The closest mode in energy, which obeys the same symmetry rules as the calculated A_g^1 , is a peak at ~ 64.1 cm^{-1} , yielding a deviation of $\sim 30\%$. Also, the calculated energy of the A_g^4 mode could not be identified within our spectrum, with the closest experimental A_g peaks being within 20%. Such deviation in theory and experiment, $>20\%$, indicates that the room-temperature phonon vibrations in VI_3 do not originate predominantly from the BiI_3 structure type either, leaving $P\bar{3}1c$ as the only candidate. This indication is further reinforced by the inability to connect the experimentally observed E_g modes at ~ 77 and ~ 86 cm^{-1} with the $R\bar{3}$ -calculated modes.

Our experimental data (Table 3) are mostly supported by the phonon energies obtained for possible electronic states of

Table 3. Comparison between Calculated Values of Raman Active Phonon Energies for Insulating and Half-Metallic States of the $P\bar{3}1c$ Structure and Experimentally Obtained Values (left)^a and Phonon Symmetries and Calculated Phonon Energies for the $R\bar{3}$ and $C2/m$ Structures of VI_3 ^b

space group $P\bar{3}1c$				space group $R\bar{3}$		space group $C2/m$	
symmetry	calcd (cm ⁻¹)	calcd (cm ⁻¹)	exp. (cm ⁻¹)	symmetry	calcd (cm ⁻¹)	symmetry	calcd (cm ⁻¹)
E_g^1	17.2	15.2	—	E_g^1	45.2	A_g^1	58.1
A_{2g}^1 (silent)	35.0	56.8	—	E_g^2	69.9	B_g^1	60.0
E_g^2	62.2	61.6	59.8	A_g^1	99.3	A_g^2	82.7
A_{2g}^2 (silent)	69.4	72.3	—	E_g^3	99.8	B_g^2	82.9
E_g^3	74.1	75.9	77.2	A_g^2	105.1	A_g^3	85.7
A_{1g}^1	83.3	84.2	—	A_g^3	135.5	B_g^3	88.9
E_g^4	84.9	86.6	86.7	A_g^4	167.9	A_g^4	99.3
E_g^5	91.5	98.4	95.2	E_g^4	176.8	B_g^4	99.3
A_{2g}^3 (silent)	92.2	96.3	—			A_g^5	122.3
E_g^6	97.4	108.3	100.4			B_g^5	149.9
A_{1g}^2	113.2	119.3	116.8			B_g^6	161.0
A_{1g}^3	117.1	123.9	123.4			A_g^6	164.0
A_{2g}^4 (silent)	121.3	147.8	—				
E_g^7	132.2	151.9	c				
E_g^8	149.4	166.9	c				
A_{2g}^5 (silent)	185.9	212.1	—				

^aThe experimental values were determined at 100 K. The experimental uncertainty is 0.3 cm⁻¹. ^bAll calculations were performed at 0 K. ^cSee the text for an explanation.

the $P\bar{3}1c$ trigonal structure with deviations of around 10% and 15%. Nine of 11 Raman modes were singled out and identified, with E_g^1 being not observable in our experimental setup due to its low energy. The A_{1g}^1 mode might be missing due to its low intensity and/or the finite spectrometer resolution. The most striking was the observation of the broad feature at ~ 180 cm⁻¹, persisting up to 300 K in both scattering channels. Whereas its line shape resembles those of the two-magnon type of excitation, we believe that scenario is unlikely for a ferromagnetic material. The energy region where the feature was observed may also suggest the possibility of a two-phonon type of excitation. However, their scattering cross sections are usually small and dominated by overtones, thus mostly observed for the parallel scattering configuration.⁴⁵ For example, such an excitation was observed at ~ 250 cm⁻¹ (Figure 2). Finally, the observed feature also falls into the energy region where, as suggested by the numerical calculations, observation of the E_g^7 and E_g^8 modes is expected. We believe that it is actually a complex structure comprising E_g^7 and E_g^8 Raman modes, significantly broadened by the spin-phonon interaction, that is particularly strong on these phonon branches. The proximity of the two very broad, presumably asymmetric peaks hampers their precise assignment.

Closer inspection of other Raman peaks revealed that some of them also exhibit an asymmetric line shape. To further demonstrate this virtue, we have quantitatively analyzed the highest-intensity peak, A_{1g}^3 , using the symmetric Voigt line shape and convolution of a Fano profile and a Gaussian.^{44–46} The asymmetric line shape (with a Fano parameter of $|q| = 12.3$) gives a slightly better agreement with the experimental data, as depicted in Figure 3. Considering that the observed asymmetry in similar materials was shown to reflect the spin-phonon interaction,^{46,47} we propose it as a possible scenario in VI_3 , as well.

Our findings, based on the inelastic light scattering experiments, at first glance differ from those presented in ref 10. To resolve this discrepancy, we used synchrotron X-ray Rietveld and PDF analysis. Typically, the short-range order

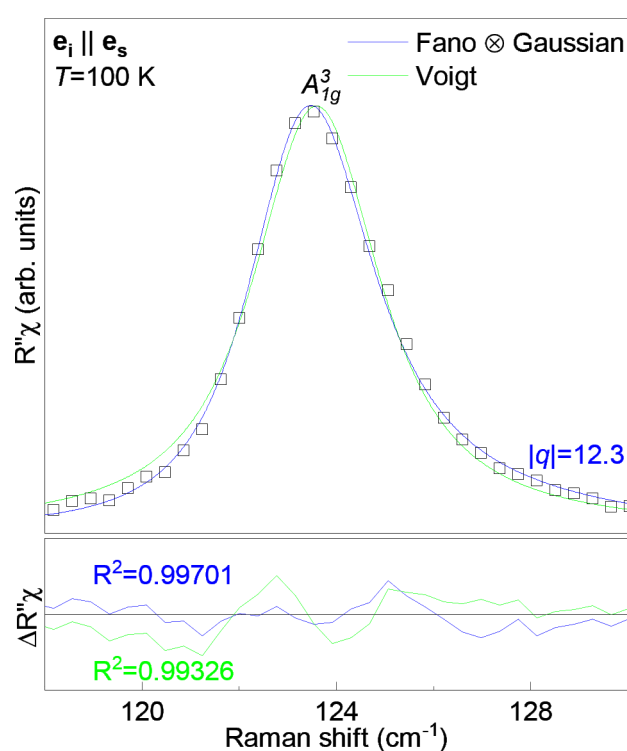


Figure 3. Quantitative analysis of the A_{1g}^3 mode. The blue solid line represents the line shape obtained as a convolution of the Fano line shape and the Gaussian, whereas the green one represents a Voigt profile fitted to experimental data (\square). For details, see refs 44 and 45.

(SRO) contributes to diffuse scattering under the long-range order (LRO) Bragg peaks when they coexist. Because the diffuse scattering is subtracted as part of the background in the Rietveld refinement, this method is more sensitive to the average structure of materials. In contrast, PDF analysis is performed on the sine Fourier transform of the properly corrected diffraction pattern, including both Bragg and diffuse

components. PDF is a real space function that provides a histogram of interatomic distances, which contain information regarding all length scales.^{48–51} The 1–10 and 11–30 Å PDF length scales are more sensitive to SRO and LRO, respectively. For the VI_3 system, the best Rietveld fit was obtained using the $\text{R}\bar{3}$ space group (Figure 4a), in agreement with that previously

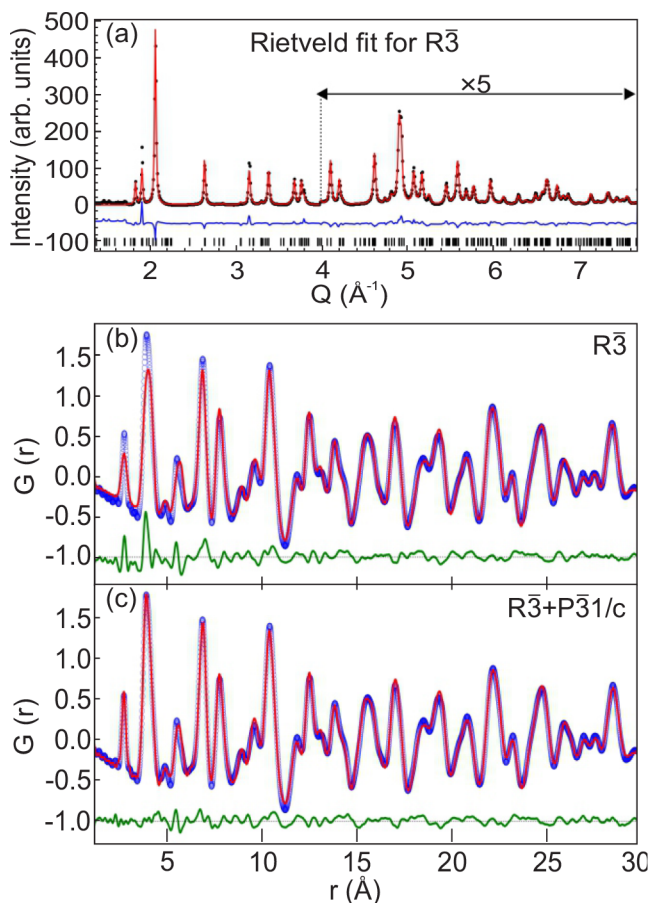


Figure 4. Best structural model fits to diffraction data. (a) Rietveld fit using the $\text{R}\bar{3}$ space group with black vertical bars indicating calculated peak positions. (b) PDF fit using the $\text{R}\bar{3}$ space group. (c) Two-phase PDF fit using $\text{R}\bar{3}$ and $\text{P}\bar{3}1\text{c}$ space groups to fit LRO and SRO, respectively. Black dots (XRD) and blue dots (PDF) represent experimental data, and red solid lines represent the model-based fits. The fit residues are shown at the bottom of each plot.

observed.¹⁰ Not surprisingly, LRO obtained from the Rietveld refinement showed a good agreement on the PDF length scale of 10–30 Å. However, the $\text{R}\bar{3}$ space group gave a poor fit on the length scale of 1.5–15 Å with refined $\delta 1$ to account for correlated motion (Figure 4b). In contrast, $\text{P}\bar{3}1\text{c}$ gave a better fit to SRO, but a poor fit to LRO. The best PDF fits were obtained by refining a weighted two-phase structural model containing ~25 wt % SRO $\text{P}\bar{3}1\text{c}$ and ~75 wt % LRO $\text{R}\bar{3}$ phases. The refined correlation length of the SRO is ~15–20 Å (Figure 4c). These results suggest two possible scenarios: (1) coexistence of two segregated phases, LRO $\text{R}\bar{3}$ and SRO $\text{P}\bar{3}1\text{c}$, and (2) randomly distributed short-range ordered $\text{P}\bar{3}1\text{c}$ domains in the long-range ordered $\text{R}\bar{3}$ lattice. A detailed structural analysis is required to pinpoint scenario 1 and/or 2, which is beyond the scope of this work.

In addition to the peaks already assigned to Γ -point Raman active phonons of the $\text{P}\bar{3}1\text{c}$ crystal structure (Table 2), three

additional peaks at 64.2 cm^{-1} ($\text{P}1$), 110.1 cm^{-1} ($\text{P}2$), and 220.6 cm^{-1} ($\text{P}3$) are observed (see Figure 2). According to the results of DFT, energies of these modes correspond well to those calculated for silent A_{2g}^2 , A_{2g}^3 , and A_{2g}^5 modes. Their observability in Raman data may come from the release of the symmetry selection rules by breaking of the (translation) symmetry as suggested by the PDF in both scenarios.^{52–55} However, as previously discussed, these peaks obey A_{1g} selection rules, indicating the possibility for them to be overtones in nature. In this less likely scenario, the phonon–phonon coupling is enhanced by the spin–phonon interaction and/or by the structural imperfections, thus enhancing the Raman scattering rate for the two-phonon processes.⁴⁵ Hence, the observed Raman modes reflect the symmetry of phonon vibrations related to the SRO.^{56,57} It is interesting to note that, besides a possible short-range crystallography that is different from the average, VI_3 might also feature short-range magnetic order above 79 K.¹⁴

CONCLUSION

In summary, room-temperature phonon vibrations of VI_3 stem from the $\text{P}\bar{3}1\text{c}$ symmetry of the unit cell. The PDF analysis suggested the coexistence of two phases, short-range ordered $\text{P}\bar{3}1\text{c}$ and long-range ordered $\text{R}\bar{3}$, as two segregated phases and/or as randomly distributed short-range ordered $\text{P}\bar{3}1\text{c}$ domains in the long-range ordered $\text{R}\bar{3}$ lattice. Nine of 12 observed peaks in the Raman spectra were assigned in agreement with $\text{P}\bar{3}1\text{c}$ symmetry calculations. Three additional peaks, which obey A_{1g} symmetry rules, could be explained as either overtones or as activated A_{2g} silent modes caused by a symmetry breaking. The asymmetry of one of the A_{1g} phonon modes, together with the anomalous behavior of E_g^7 and E_g^8 , indicates strong spin–phonon coupling, which has already been reported in similar 2D materials.^{46,58}

AUTHOR INFORMATION

Corresponding Author

Nenad Lazarević – Institute of Physics Belgrade, University of Belgrade, 11080 Belgrade, Serbia; orcid.org/0000-0001-6310-9511; Email: nenadl@ipb.ac.rs

Authors

Sanja Djurdjic Mijin – Institute of Physics Belgrade, University of Belgrade, 11080 Belgrade, Serbia

A. M. Milinda Abeykoon – National Synchrotron Light Source II, Brookhaven National Laboratory, Upton, New York 11973, United States

Andrijana Solajic – Institute of Physics Belgrade, University of Belgrade, 11080 Belgrade, Serbia

Ana Milosavljevic – Institute of Physics Belgrade, University of Belgrade, 11080 Belgrade, Serbia

Jelena Pešić – Institute of Physics Belgrade, University of Belgrade, 11080 Belgrade, Serbia

Yu Liu – Condensed Matter Physics and Materials Science Department, Brookhaven National Laboratory, Upton, New York 11973-5000, United States; orcid.org/0000-0001-8886-2876

Cedomir Petrovic – Condensed Matter Physics and Materials Science Department, Brookhaven National Laboratory, Upton, New York 11973-5000, United States; orcid.org/0000-0001-6063-1881

Zoran V. Popović – Institute of Physics Belgrade, University of Belgrade, 11080 Belgrade, Serbia; Serbian Academy of Sciences and Arts, 11000 Belgrade, Serbia

Complete contact information is available at:
<https://pubs.acs.org/10.1021/acs.inorgchem.0c02060>

Notes

The authors declare no competing financial interest.

ACKNOWLEDGMENTS

The authors acknowledge funding provided by the Institute of Physics Belgrade, through a grant from the Ministry of Education, Science and Technological Development of the Republic of Serbia, Project F-134 of the Serbian Academy of Sciences and Arts, and the Science Fund of the Republic of Serbia, PROMIS, 6062656, StrainedFeSC. DFT calculations were performed using computational resources at Johannes Kepler University (Linz, Austria). Materials synthesis was supported by the U.S. DOE-BES, Division of Materials Science and Engineering, under Contract DE-SC0012704 (BNL). This research used beamline 28-ID-1 of National Synchrotron Light Source II, a U.S. DOE Office of Science User Facility operated for the DOE Office of Science by Brookhaven National Laboratory under Contract DE-S.


REFERENCES

- (1) Seyler, K. L.; Zhong, D.; Klein, D. R.; et al. Ligand-field helical luminescence in a 2D ferromagnetic insulator. *Nat. Phys.* **2018**, *14*, 277–281.
- (2) Klein, D. R.; MacNeill, D.; Lado, J. L.; Soriano, D.; Navarro-Moratalla, E.; Watanabe, K.; et al. Probing magnetism in 2D van der Waals crystalline insulators via electron tunneling. *Science* **2018**, *360*, 1218–1222.
- (3) Huang, B.; Clark, G.; Klein, D. R.; MacNeill, D.; Navarro-Moratalla, E.; Seyler, K. L.; et al. Electrical control of 2D magnetism in bilayer CrI₃. *Nat. Nanotechnol.* **2018**, *13*, 544–548.
- (4) Jiang, S.; Li, L.; Wang, Z.; Mak, K. F.; Shan, J. Controlling magnetism in 2D CrI₃ by electrostatic doping. *Nat. Nanotechnol.* **2018**, *13*, 549–553.
- (5) McGuire, M. A.; Clark, G.; KC, S.; Chance, W. M.; Jellison, G. E.; Cooper, V. R.; Xu, X.; Sales, B. C. Magnetic behavior and spin-lattice coupling in cleavable van der Waals layered CrCl₃ crystals. *Phys. Rev. Materials* **2017**, *1*, 014001.
- (6) Djurdjic-Mijin, S. D.; Solajić, A.; Pešić, J.; Šćepanović, M.; Liu, Y.; Baum, A.; et al. Lattice dynamics and phase transition in CrI₃ single crystals. *Phys. Rev. B: Condens. Matter Mater. Phys.* **2018**, *98*, 104307.
- (7) Thiel, L.; Wang, Z.; Tschudin, M.; Rohner, D.; Gutierrez-Lezama, I. G.; Ubrig, N.; et al. Probing magnetism in 2D materials at the nanoscale with single-spin microscopy. *Science* **2019**, *364*, 973–976.
- (8) Lin, G. T.; Luo, X.; Chen, F. C.; Yan, J.; Gao, J. J.; Sun, Y.; et al. Critical behavior of two-dimensional intrinsically ferromagnetic semiconductor CrI₃. *Appl. Phys. Lett.* **2018**, *112*, 072405.
- (9) Son, S.; Coak, M. J.; Lee, N.; Kim, J.; Kim, T. Y.; Hamidov, H.; et al. Bulk properties of the van der Waals hard ferromagnet VI₃. *Phys. Rev. B: Condens. Matter Mater. Phys.* **2019**, *99*, 041402.
- (10) Liu, Y.; Abeykoon, M.; Petrovic, C. Critical behavior and magnetocaloric effect in VI₃. *Phys. Rev. Research* **2020**, *2*, 013013.
- (11) Huang, B.; Clark, G.; Navarro-Moratalla, E.; Klein, D. R.; Cheng, R.; Seyler, K. L.; et al. Layer-dependent ferromagnetism in a van der Waals crystal down to the monolayer limit. *Nature* **2017**, *546*, 270–273.
- (12) Kong, T.; Stolze, K.; Timmons, E. I.; Tao, J.; Ni, D.; Guo, S.; et al. VI₃ – a New Layered Ferromagnetic Semiconductor. *Adv. Mater.* **2019**, *31*, 1808074.
- (13) Doležal, P.; Kratochvílová, M.; Holý, V.; Čermak, P.; Sechovský, V.; Dušek, M.; et al. Crystal structures and phase transitions of the van der Waals ferromagnet VI₃. *Phys. Rev. Materials* **2019**, *3*, 121401.
- (14) Tian, S.; Zhang, J.-F.; Li, C.; Ying, T.; Li, S.; Zhang, X.; et al. Ferromagnetic van der Waals Crystal VI₃. *J. Am. Chem. Soc.* **2019**, *141*, 5326–5333.
- (15) Wang, Y.-M.; Tian, S.-J.; Li, C.-H.; Jin, F.; Ji, J.-T.; Lei, H.-C.; Zhang, Q.-M. Raman scattering study of two-dimensional magnetic van der Waals compound VI₃. *Chin. Phys. B* **2020**, *29*, 056301.
- (16) Lee, I.; Utermohlen, F. G.; Weber, D.; Hwang, K.; Zhang, C.; van Tol, J.; Goldberger, J. E.; Trivedi, N.; Hammel, P. C. Fundamental Spin Interactions Underlying the Magnetic Anisotropy in the Kitaev Ferromagnet CrI₃. *Phys. Rev. Lett.* **2020**, *124*, 017201.
- (17) Xu, C.; Feng, J.; Xiang, H.; Bellaiche, L. Interplay between Kitaev interaction and single ion anisotropy in ferromagnetic CrI₃ and CrGeTe₃ monolayers. *npj Comput. Mater.* **2018**, *4*, 57.
- (18) Mermin, N. D.; Wagner, H. Absence of Ferromagnetism or Antiferromagnetism in One- or Two-Dimensional Isotropic Heisenberg Models. *Phys. Rev. Lett.* **1966**, *17*, 1133–1136.
- (19) Pershoguba, S. S.; Banerjee, S.; Lashley, J. C.; Park, J.; Ågren, H.; Aeppli, G.; Balatsky, A. V. Dirac Magnons in Honeycomb Ferromagnets. *Phys. Rev. X* **2018**, *8*, 011010.
- (20) Liu, J.; Shi, M.; Mo, P.; Lu, J. Electrical-field-induced magnetic Skyrmion ground state in a two-dimensional chromium tri-iodide ferromagnetic monolayer. *AIP Adv.* **2018**, *8*, 055316.
- (21) Jiang, S.; Li, L.; Wang, Z.; Shan, J.; Mak, K. Spin tunnel field-effect transistors based on two-dimensional van der Waals heterostructures. *Nature Electronics* **2019**, *2*, 159.
- (22) Klein, D. R.; MacNeill, D.; Song, Q.; Larson, D. T.; Fang, S.; Xu, M.; Ribeiro, R. A.; Canfield, P. C.; Kaxiras, E.; Comin, R.; Jarillo-Herrero, P. Enhancement of interlayer exchange in an ultrathin two-dimensional magnet. *Nat. Phys.* **2019**, *15*, 1255–1260.
- (23) Wang, Z.; Gibertini, M.; Dumcenco, D.; Taniguchi, T.; Watanabe, K.; Giannini, E.; Morpurgo, A. Determining the phase diagram of atomically thin layered antiferromagnet CrCl₃. *Nat. Nanotechnol.* **2019**, *14*, 1116.
- (24) Ubrig, N.; Wang, Z.; Teyssier, J.; Taniguchi, T.; Watanabe, K.; Giannini, E.; Morpurgo, A. F.; Gibertini, M. Low-temperature monoclinic layer stacking in atomically thin CrI₃ crystals. *2D Mater.* **2020**, *7*, 015007.
- (25) Sun, Z.; et al. Giant nonreciprocal second-harmonic generation from antiferromagnetic bilayer CrI₃. *Nature* **2019**, *572*, 497–501.
- (26) McGuire, M. A.; Clark, G.; KC, S.; Chance, W. M.; Jellison, G. E.; Cooper, V. R.; Xu, X.; Sales, B. C. Magnetic behavior and spin-lattice coupling in cleavable van der Waals layered CrCl₃ crystals. *Phys. Rev. Materials* **2017**, *1*, 014001.
- (27) Kuhlow, B. Magnetic Ordering in CrCl₃ at the Phase Transition. *physica status solidi (a)* **1982**, *72*, 161–168.
- (28) Hammersley, A. P.; Svensson, S. O.; Hanfland, M.; Fitch, A. N.; Hausermann, D. Two-dimensional detector software: From real detector to idealised image or two-theta scan. *High Pressure Res.* **1996**, *14*, 235–248.
- (29) Yang, X.; Juhas, P.; Farrow, C. L.; Billinge, S. J. L. *xPDFsuite: an end-to-end software solution for high throughput pair distribution function transformation, visualization and analysis*; 2014.
- (30) Toby, B. H.; Von Dreele, R. B. GSAS-II: the genesis of a modern open-source all purpose crystallography software package. *J. Appl. Crystallogr.* **2013**, *46*, 544–549.
- (31) Farrow, C. L.; Juhas, P.; Liu, J. W.; Bryndin, D.; Božin, E. S.; Bloch, J.; Proffen, T.; Billinge, S. J. L. PDFfit2 and PDFgui: computer programs for studying nanostructure in crystals. *J. Phys.: Condens. Matter* **2007**, *19*, 335219.
- (32) Giannozzi, P.; et al. QUANTUM ESPRESSO: a modular and open-source software project for quantum simulations of materials. *J. Phys.: Condens. Matter* **2009**, *21*, 395502.
- (33) Perdew, J. P.; Burke, K.; Ernzerhof, M. Generalized Gradient Approximation Made Simple. *Phys. Rev. Lett.* **1996**, *77*, 3865–3868.

- (34) Blöchl, P. E. Projector augmented-wave method. *Phys. Rev. B: Condens. Matter Mater. Phys.* **1994**, *50*, 17953–17979.
- (35) Kresse, G.; Joubert, D. From ultrasoft pseudopotentials to the projector augmented-wave method. *Phys. Rev. B: Condens. Matter Mater. Phys.* **1999**, *59*, 1758–1775.
- (36) Cococcioni, M.; de Gironcoli, S. Linear response approach to the calculation of the effective interaction parameters in the LDA + U method. *Phys. Rev. B: Condens. Matter Mater. Phys.* **2005**, *71*, 035105.
- (37) Juza, D.; Giegling, D.; Schäfer, H. Über die Vanadiniodide VJ₂ und VJ₃. *Z. Anorg. Allg. Chem.* **1969**, *366*, 121–129.
- (38) Berry, K. O.; Smardzewski, R. R.; McCarley, R. E. Vaporization reactions of vanadium iodides and evidence for gaseous vanadium-(IV) iodide. *Inorg. Chem.* **1969**, *8*, 1994–1997.
- (39) Klemm, W.; Krose, E. Die Kristallstrukturen von ScCl₃, TiCl₃ und VCl₃. *Z. Anorg. Chem.* **1947**, *253*, 218–225.
- (40) Liu, Y.; Petrovic, C. Three-dimensional magnetic critical behavior in CrI₃. *Phys. Rev. B: Condens. Matter Mater. Phys.* **2018**, *97*, 014420.
- (41) He, J.; Ma, S.; Lyu, P.; Nachtigall, P. Unusual Dirac half-metallicity with intrinsic ferromagnetism in vanadium trihalide monolayers. *J. Mater. Chem. C* **2016**, *4*, 2518–2526.
- (42) Wang, Y.-P.; Long, M.-Q. Electronic and magnetic properties of van der Waals ferromagnetic semiconductor VI₃. *Phys. Rev. B: Condens. Matter Mater. Phys.* **2020**, *101*, 024411.
- (43) Li, Y.; Liu, Y.; Wang, C.; Wang, J.; Xu, Y.; Duan, W. Electrically tunable valleytronics in quantum anomalous Hall insulating transition metal trihalides. *Phys. Rev. B: Condens. Matter Mater. Phys.* **2018**, *98*, 201407.
- (44) Lazarević, N.; Popović, Z. V.; Hu, R.; Petrovic, C. Evidence for electron-phonon interaction in Fe_{1-x}M_xSb₂ (M = Co and Cr 0 ≤ x ≤ 0.5) single crystals. *Phys. Rev. B: Condens. Matter Mater. Phys.* **2010**, *81*, 144302.
- (45) Baum, A.; Milosavljević, A.; Lazarević, N.; Radonjić, M. M.; Nikolić, B.; Mitschek, M.; Maranloo, Z. I.; Šćepanović, M.; Grujić-Brojčin, M.; Stojilović, N.; Opel, M.; Wang, A.; Petrovic, C.; Popović, Z. V.; Hackl, R. Phonon anomalies in FeS. *Phys. Rev. B: Condens. Matter Mater. Phys.* **2018**, *97*, 054306.
- (46) Milosavljević, A.; Solajic, A.; Pešić, J.; Liu, Y.; Petrovic, C.; Lazarević, N.; Popović, Z. V. Evidence of spin-phonon coupling in CrSiTe₃. *Phys. Rev. B: Condens. Matter Mater. Phys.* **2018**, *98*, 104306.
- (47) McCarty, K. F.; Radousky, H. B.; Hinks, D. G.; Zheng, Y.; Mitchell, A. W.; Folkerts, T. J.; Shelton, R. N. Electron-phonon coupling in superconducting Ba_{0.6}K_{0.4}BiO₃: A Raman scattering study. *Phys. Rev. B: Condens. Matter Mater. Phys.* **1989**, *40*, 2662–2665.
- (48) Proffen, T.; Page, K. L.; McLain, S. E.; Clausen, B.; Darling, T. W.; TenCate, J. A.; Lee, S.-Y.; Ustundag, E. Atomic pair distribution function analysis of materials containing crystalline and amorphous phases. *Z. Kristallogr.* **2005**, *220*, 1002–1008.
- (49) Bordet, P. Application of the pair distribution function analysis for the study of cultural heritage materials. *C. R. Phys.* **2018**, *19*, 561–574.
- (50) Bozin, E. S.; Yin, W. G.; Koch, R. J.; Abeykoon, M.; Hor, Y. S.; Zheng, H.; Lei, H. C.; Petrovic, C.; Mitchell, J. F.; Billinge, S. J. L. Local orbital degeneracy lifting as a precursor to an orbital-selective Peierls transition. *Nat. Commun.* **2019**, *10*, 3638.
- (51) Egami, T.; Billinge, S. J. L. *Underneath the Bragg Peaks: Structural Analysis of Complex Materials*; 2003; p 16.
- (52) Jin, F.; Lazarević, N.; Liu, C.; Ji, J.; Wang, Y.; He, S.; Lei, H.; Petrovic, C.; Yu, R.; Popović, Z. V.; Zhang, Q. Phonon anomalies and magnetic excitations in BaFe₂Se₂O. *Phys. Rev. B: Condens. Matter Mater. Phys.* **2019**, *99*, 144419.
- (53) Moskovits, M.; Dilella, D. Surface-enhanced Raman spectroscopy of benzene and benzene-d₆ adsorbed on silver. *J. Chem. Phys.* **1980**, *73*, 6068–6075.
- (54) Dubroka, A.; Humlíček, J.; Abrashev, M. V.; Popović, Z. V.; Sapiña, F.; Cantarero, A. Raman and infrared studies of La_{1-y}Sr_yMn_{1-x}M_xO₃ (M = Cr, Co, Cu, Zn, Sc or Ga): Oxygen disorder and local vibrational modes. *Phys. Rev. B: Condens. Matter Mater. Phys.* **2006**, *73*, 224401.
- (55) Souza Filho, A. G.; Faria, J. L. B.; Guedes, I.; Sasaki, J. M.; Freire, P. T. C.; Freire, V. N.; Mendes Filho, J.; Xavier, M. M.; Cabral, F. A. O.; de Araújo, J. H.; da Costa, J. A. P. Evidence of magnetic polaronic states in La_{0.70}Sr_{0.30}Mn_{1-x}Fe_xO₃ manganites. *Phys. Rev. B: Condens. Matter Mater. Phys.* **2003**, *67*, 052405.
- (56) Lekgoathi, M.; Kock, L. Effect of short and long range order on crystal structure interpretation: Raman and powder X-ray diffraction of LiPF₆. *Spectrochim. Acta, Part A* **2016**, *153*, 651–654.
- (57) Wolverton, C.; Zunger, A.; Lu, Z.-W. Long-versus short-range order in Ni₃V and Pd₃V alloys. *Phys. Rev. B: Condens. Matter Mater. Phys.* **1994**, *49*, 16058.
- (58) Webster, L.; Liang, L.; Yan, J.-A. Distinct spin-lattice and spin-phonon interactions in monolayer magnetic CrI₃. *Phys. Chem. Chem. Phys.* **2018**, *20*, 23546–23555.

RESEARCH ARTICLE

Vacancies and spin–phonon coupling in $\text{CrSi}_{0.8}\text{Ge}_{0.1}\text{Te}_3$

Ana Milosavljević¹  | Andrijana Šolajić¹ | Bojana Višić¹ | Marko Opačić¹ | Jelena Pešić¹ | Yu Liu² | Cedomir Petrović² | Zoran V. Popović^{1,3} | Nenad Lazarević¹

¹Institute of Physics Belgrade, University of Belgrade, Pregrevica 118, Belgrade, 11080, Serbia

²Condensed Matter Physics and Materials Science Department, Brookhaven National Laboratory, Upton, New York, 11973-5000, USA

³Serbian Academy of Sciences and Arts, Knez Mihailova 35, Belgrade, 11000, Serbia

Correspondence

Ana Milosavljević, Institute of Physics Belgrade, University of Belgrade, Pregrevica 118, 11080 Belgrade, Serbia.
Email: ana.milosavljevic@ipb.ac.rs

Funding information

Serbian Academy of Sciences and Arts, Grant/Award Number: F-134; Slovenian Research Agency, Grant/Award Number: P1-0099; Ministry of Education, Science and Technological Development of the Republic of Serbia U.S. DOE-BES, Division of Materials Science and Engineering, Grant/Award Number: DE-SC0012704

Abstract

We report temperature-dependent Raman scattering and magnetization studies of van der Waals ferromagnetic compound $\text{CrSi}_{0.8}\text{Ge}_{0.1}\text{Te}_3$. Magnetic susceptibility measurements revealed dominant ferromagnetic interactions below T_C which shift to the lower values due to the presence of vacancies. A Raman active mode, additional to the ones predicted by symmetry in the parent compounds, has been observed. This A_g symmetry mode most likely emerges as a consequence of the atomic vacancies on Si/Ge site. Presence of the strong spin–phonon coupling at temperature around 210 K is indicated by deviations from conventional phonon self-energy temperature dependence of all analysed modes.

KEYWORDS

magnetism, phonons, raman spectroscopy, van der Waals materials

1 | INTRODUCTION

Considerable progress has been made in the field of material science through developing new materials and revealing their properties in the last decade. Namely, in the recent years, large family of van der Waals materials with inherent magnetism became the focus of experimental and theoretical research, because they seem suitable for numerous technical applications.^[1–7] The family includes $\text{Fe}_{3-x}\text{GeTe}_2$ metallic materials with high magnetic transition temperature,^[8–10] semiconductors CrXTe_3 ($X = \text{Si, Ge, Sn}$) and CrX_3 ($X = \text{Cl, Br, I}$) monolayers^[2,11–13] and heterostructures.^[14]

CrSiTe_3 and CrGeTe_3 are ferromagnetic (FM) semiconductors with band gap of 0.4 and 0.7 eV and Curie temperatures (T_C) of 32 and 61 K, respectively.^[15–18] Twinning of CrSiTe_3 single crystals along c -axes was revealed by X-ray diffraction experiment as well as Cr^{3+} ions magnetic order.^[15] Recently, through high-resolution angle-resolved photoemission spectroscopy (ARPES), it was possible to identify full electronic structure near the Fermi level. Due to spin–orbit coupling, CrSiTe_3 is a Mott-type FM insulator.^[19] Electronic structure of CrGeTe_3 single crystals was also investigated by ARPES.^[20] It was shown that the low-lying valence bands are centred around the Γ point and are mainly formed from Te 5p orbitals.

Raman scattering studies of CrSiTe_3 reveal strong spin-lattice coupling in the paramagnetic phase^[15,21] as a consequence of a short-range magnetic order in this compound. In addition to renormalization of energies and linewidths of observed Raman active modes, coupling of doubly degenerate E_g mode with magnetic continuum was found.^[21] The coupling results in an asymmetric phonon line shape up to 180 K. Besides the splitting of two low-energy E_g modes in the magnetic phase of CrGeTe_3 and unconventional behaviour of phonon properties around transition temperature, experimental results indicate spin-phonon coupling effect with magnetic quasi-elastic scattering.^[22] Pressure-dependent Raman scattering study of CrGeTe_3 showed a decrease in bond length, the deviation of Cr-Te-Cr angle, and reduction of phase transition temperature.^[23]

Change of the carrier concentration plays an important role in the physics of semiconducting materials as it can lead to surprising physical properties. Very small variations in dopant concentrations can lead to structural modifications and considerable changes in magnetic transition temperature. Here, we report a Raman scattering and magnetization studies of $\text{CrSi}_{0.8}\text{Ge}_{0.1}\text{Te}_3$. Our scanning electron microscopy (SEM) measurements reveal 10% of Ge atoms concentration and 10% of vacancies. Vacancies induced a decrease in T_C was detected within magnetic susceptibility measurements. In the Raman scattering results, we identified three A_g and four E_g symmetry modes. Additional peak of the A_g symmetry is also observed in our spectra. This mode may be traced to vacancies and possible inhomogeneous distribution of Ge atoms substitution on Si atomic site at nano-scale. Energies of modes predicted by symmetry analysis are found between the experimental values of parent compounds CrSiTe_3 and CrGeTe_3 , reported previously in Milosavljević et al.^[21] The presence of the strong spin-phonon interaction at temperature around 210 K is indicated in small deviations from conventional temperature-dependent behaviour of the observed modes energies and linewidths, including additional one.

2 | EXPERIMENT AND NUMERICAL METHOD

$\text{CrSi}_{0.8}\text{Ge}_{0.1}\text{Te}_3$ single crystals were grown as described previously.^[24] Magnetic properties were measured in a Quantum Design MPMS-XL5 system.

SEM measurements were performed using FEI HeliosNanolab 650. This microscope is equipped with an Oxford Instruments energy dispersive spectroscopy (EDS) system with an X-max SSD detector operating at 20 kV. Measurements were performed on as-cleaved samples

deposited on a graphite tape. The elemental composition EDS mapping was obtained on crystals that appeared to be uniform for several tens of microns. The maps show the presence of Cr, Ge, Te and Si.

For Raman scattering experiment, Tri Vista 557 spectrometer was used in the subtractive backscattering micro-Raman configuration. The combination of gratings was 1800/1800/2400 grooves/mm and the entrance slit of 80 μm . Solid state laser with 532-nm line was used as an excitation source. In our scattering configuration, plane of incidence is ab -plane, where $|a|=|b|$ ($\angle(a,b)=120^\circ$), with incident (scattered) light propagation direction along c -axes. Samples were cleaved in the air before being placed in vacuum. All measurements were performed in high vacuum (10^{-6} mbar) using a KONTI CryoVac continuous Helium flow cryostat with 0.5-mm thick window. Laser beam focusing was achieved using microscope objective with $\times 50$ magnification. All spectra were corrected for Bose factor.

Spin-polarized density functional theory calculations were performed in Quantum Espresso software package,^[25] based on plane waves and pseudopotentials, using Perdew-Burke-Ernzerhof (PBE) exchange-correlation functional^[26] and projector augmented wave (PAW) pseudopotentials.^[27,28] The cutoff for wavefunctions and the charge density of 85 and 425 Ry were chosen, respectively. The k -point were sampled using the Monkhorst-Pack scheme, on $8 \times 8 \times 8$ Γ centred grid used for both structures. Optimization of the lattice parameters and atomic positions in unit cell was performed until the interatomic forces were minimized down to 10^{-6} Ry/ \AA . Treatment of the van der Waals interactions is included using the Grimme-D2 correction, in order to obtain the lattice parameters more accurately. Phonon wave numbers were calculated within the linear response method, as implemented in PHonon part of Quantum Espresso.

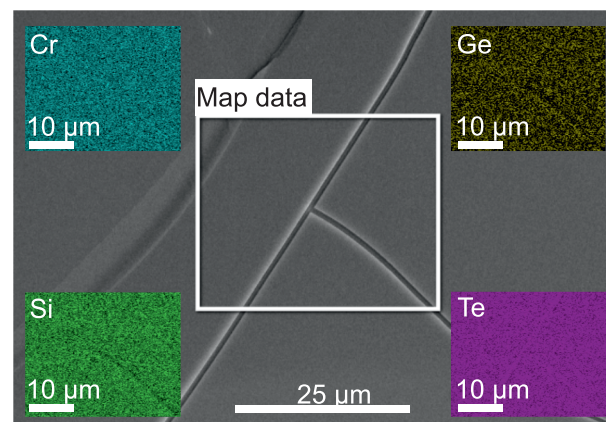


FIGURE 1 Energy dispersive spectroscopy (EDS) mapping on a $\text{CrSi}_{0.8}\text{Ge}_{0.1}\text{Te}_3$ single crystal [Colour figure can be viewed at wileyonlinelibrary.com]

3 | RESULTS AND DISCUSSION

In order to investigate uniformity and elemental composition of $\text{CrSi}_{0.8}\text{Ge}_{0.1}\text{Te}_3$ sample, SEM measurements were performed on as-cleaved crystals. EDS mapping presented in Figure 1 shows that the ratio of Cr:Si:Ge:Te (averaged over 10 measurements) is 1:0.8:0.1:3. This result reveals the presence of 10% Ge atomic vacancies in the sample.

Figure 2a,b presents the temperature dependence of zero-field cooling (ZFC) magnetic susceptibility $\chi(T) = M(T)/H$ measured in 1-kOe magnetic field applied parallel to a (a) and c (b) crystallographic axes. Curie–Weiss law $\chi = \frac{C}{T - \theta}$ fit at high temperatures yields Weiss temperatures $\theta_a = 61(2)$ K, $\theta_c = 70(2)$ K and high temperature paramagnetic moments $\mu_{\text{eff},a} = 4.14(2)\mu_B$ and $\mu_{\text{eff},c} = 3.91(2)\mu_B$ for $\text{CrSi}_{0.8}\text{Ge}_{0.1}\text{Te}_3$, consistent with dominant FM interactions below T_c and in line with the observed FM T_c and magnetic hysteresis loops.^[13,24] The approximate T_c value can be determined from the minima of the $d\chi/dT$ curves insets in Figure 2(a,b). It should be noted

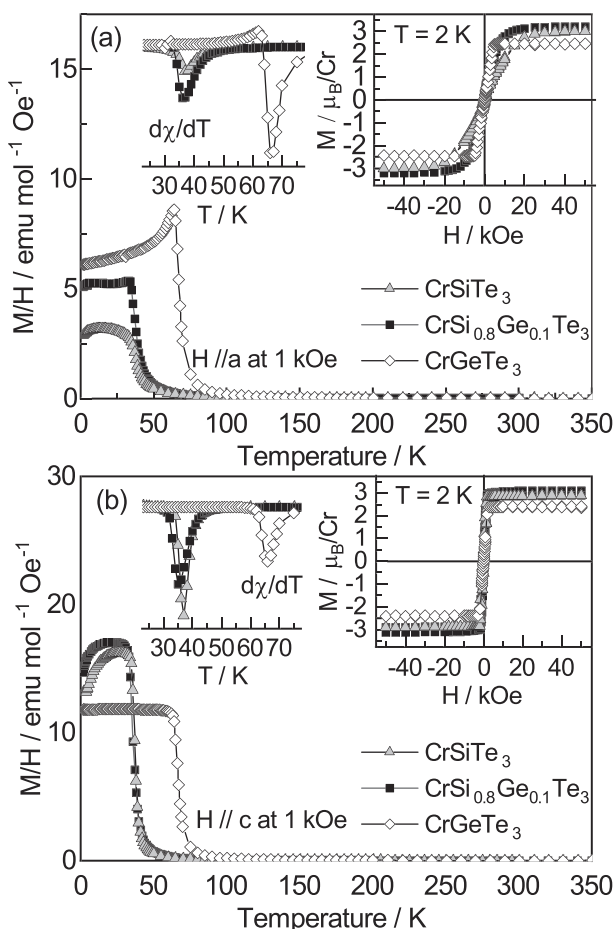


FIGURE 2 Temperature dependence of zero-field cooling (ZFC) $\chi = M/H$ for CrSiTe_3 , $\text{CrSi}_{0.8}\text{Ge}_{0.1}\text{Te}_3$ and CrGeTe_3 in 1-kOe magnetic field applied in-plane (a) and along the c -axis (b). Insets show transition temperatures of ferromagnetic orders ($d\chi/dT$) and magnetic hysteresis loops taken at 2 K

that, instead of monotonous rise, there is a weak but discernible shift to lower temperature in $d\chi/dT$ in $\text{CrSi}_{0.8}\text{Ge}_{0.1}\text{Te}_3$ when compared with CrSiTe_3 . This small reduction in FM transition temperature is likely induced by the presence of vacancies, as suggested by the EDS data. The presence of vacancies in this class of materials usually disarrange magnetic exchange due to disorder increment, which leads to the reduction of T_c .^[29]

Isostructural parent compounds CrSiTe_3 and CrGeTe_3 crystallize in the rhombohedral crystal structure, described with space group $R\bar{3}$ (C_{3i}^2).^[30] According to factor group analysis, five A_g and five double degenerate E_g symmetry modes are expected to be observed in the light scattering experiment. Detailed symmetry analysis, phonon mode distribution and selection rules for parent compounds (CrSiTe_3 and CrGeTe_3) can be found in Milosavljević et al.^[21] In our scattering configuration, the plane of incidence is ab plane, where $|a| = |b|$ ($\angle(a,b) = 120^\circ$) (inset in Figure 3), and the direction of incident (scattered) light propagation is along c -axes. According to the selection rules for this scattering configuration,^[21] all Raman active modes may be observed, having in mind that A_g symmetry modes can be detected only in parallel polarization configuration. The E_g symmetry modes are expected to appear in both the parallel and cross polarization configurations. Raman spectra of $\text{CrSi}_{0.8}\text{Ge}_{0.1}\text{Te}_3$, obtained by continuous change of the angle between polarization vectors of incident and

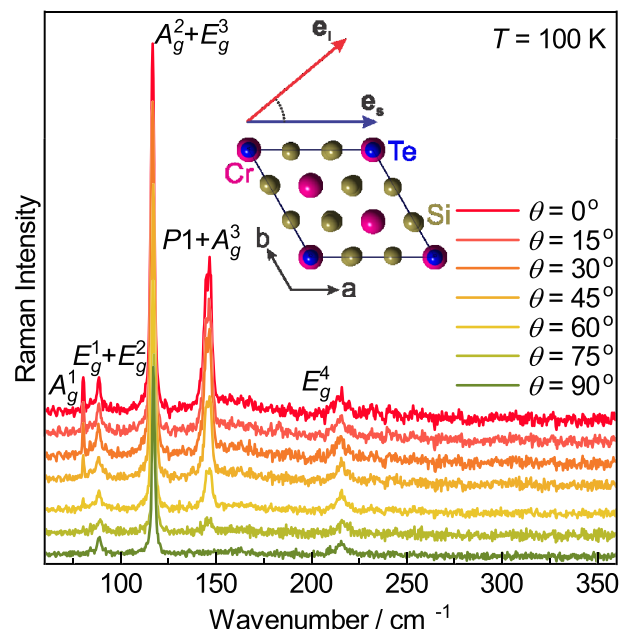


FIGURE 3 Raman spectra of $\text{CrSi}_{0.8}\text{Ge}_{0.1}\text{Te}_3$ single crystal, measured at 100 K, as a function of angle θ , between incident and scattered light polarization. Inset: schematic representation of the incident and scattered light polarization with respect to the crystal orientation [Colour figure can be viewed at wileyonlinelibrary.com]

scattered light, $\theta = \angle(\mathbf{e}_i, \mathbf{e}_s)$, ($0^\circ \leq \theta \leq 90^\circ$) at 100 K, are shown in Figure 3. It can be seen that by changing this angle, starting from $\theta = 0^\circ$, the intensities of the peaks at energies 80.2, 116.4 and 145.5 cm^{-1} continuously decrease and completely vanish for polarization angle of 90° . Therefore, these excitations obey pure A_g symmetry. On the other hand, the peaks at energies of 84.5, 88.3, 117.2 and 215.0 cm^{-1} are not influenced by change of polarization angle, so they can be identified as E_g symmetry modes.

Here, one should note that the feature observed at around 117 cm^{-1} in both scattering configurations is actually a two-peak structure comprising of 116.4 cm^{-1} A_g and 117.2 cm^{-1} E_g symmetry modes. Detailed analysis of the structure for two scattering configurations is presented in Figure A1 of Appendix. Furthermore, closer inspection of the data revealed that peak at energy of 145.5 cm^{-1} , which obeys pure A_g symmetry, is also composed of two modes, P1 (144.6 cm^{-1}) and A_g^3 (146.7 cm^{-1}), as shown in Figure A2 of Appendix.

Calculated optical phonon wavenumbers of the parent compounds, CrSiTe_3 and CrGeTe_3 , together with their experimental Raman active values as well as Raman mode energies of $\text{CrSi}_{0.8}\text{Ge}_{0.1}\text{Te}_3$, are compiled in Table 1. As expected, experimental values of $\text{CrSi}_{0.8}\text{Ge}_{0.1}\text{Te}_3$ Raman active modes are found between the values of the observed modes in parent compounds.^[21] Figure 4a shows compositional evolution of the peaks with highest

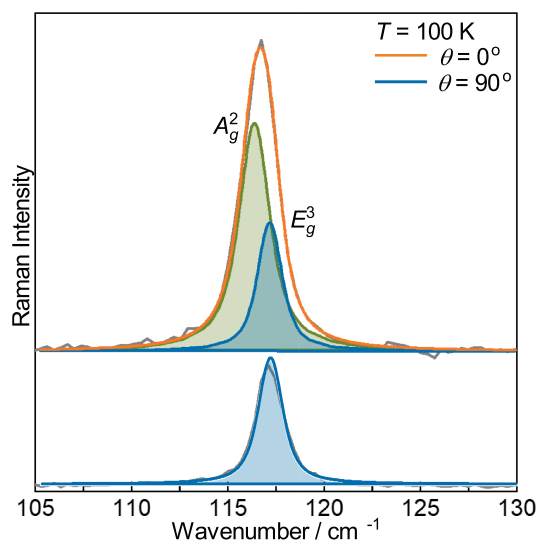


FIGURE A1 Decomposition of unresolved A_g^2 and E_g^3 symmetry modes obtained by simultaneous modelling in parallel and cross polarization configuration. Grey line represents the measured data, Voigt line of A_g^2 mode is shown by green, and blue lines represent the E_g^3 symmetry mode in parallel (upper panel) and cross (lower panel) polarization. The orange line is the superposition of these two lines [Colour figure can be viewed at wileyonlinelibrary.com]

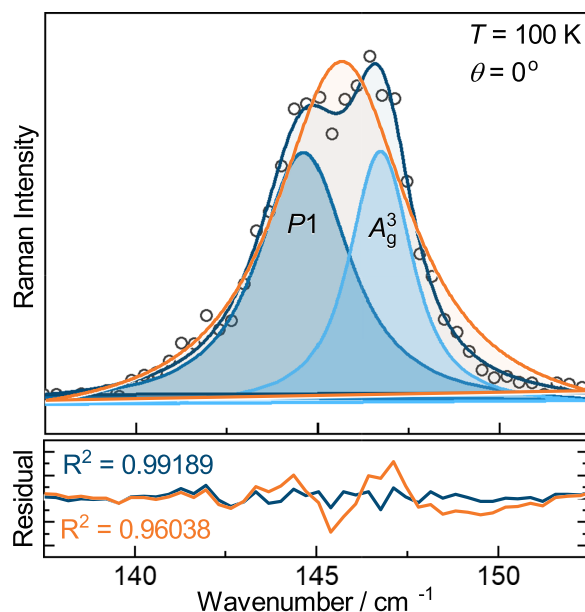


FIGURE A2 Decomposition of phonon mode in parallel scattering configuration on two A_g symmetry modes. Open circles represent the measured data and the blue one sum of two Voigt profile line shapes. Data modelled with one Voigt profile line shape (orange line) deviates significantly from measured data [Colour figure can be viewed at wileyonlinelibrary.com]

intensity, assigned as E_g^3 and A_g^3 symmetry modes in parent compounds. The E_g^3 mode energy changes almost linearly (Figure 4b), as a consequence of change in lattice parameters and “change of mass” effect. The observed energy shift is followed by doubling of the linewidth, dominantly induced by the significant crystalline disorder. The similar type of behaviour, with somewhat larger increase in the linewidth, was also observed for the A_g^3 symmetry mode. The most striking feature was the additional A_g symmetry mode (denoted as P1, see Figure A2 of the Appendix), observed in the doped sample. Generally, both the substitutional defects and vacancies may have similar impact on the Raman modes energy and linewidth. Here, the appearance of P1 peak can be understood as a consequence of the presence of vacancies on Si/Ge atomic site and their inharmonic distribution at nano-scale. The mode “splitting” is detected only for the A_g^3 but not for other observed modes, due to the fact that different nature of these vibrations results in different values of energy shifts. In the case of other modes, the difference between the shifts for corresponding domains is smaller than the spectral resolution of the instrument ($\sim 1.8 \text{ cm}^{-1}$), and therefore, the separate modes can not be resolved.

Figure 5 shows $\text{CrSi}_{0.8}\text{Ge}_{0.1}\text{Te}_3$ Raman scattering spectra measured at various temperatures. For clarity, spectra obtained for cross polarization configuration are

TABLE 1 Phonon symmetry, calculated ($T = 0$ K) and experimental ($T = 100$ K) Raman active phonon wavenumbers of parent compounds CrSiTe_3 and CrGeTe_3 .^[21] Experimental values for Raman active phonons of $\text{CrSi}_{0.8}\text{Ge}_{0.1}\text{Te}_3$ at 100 K are shown in the last column

Raman active modes					
Symmetry	Calculations		Experiment		
	CrSiTe_3	CrGeTe_3	CrSiTe_3	CrGeTe_3	$\text{CrSi}_{0.8}\text{Ge}_{0.1}\text{Te}_3$
A_g^1	88.2	84.2	—	—	80.2
E_g^1	93.5	82.0	88.9	83.5	84.5
E_g^2	96.9	90.8	—	—	88.3
E_g^3	118.3	114.2	118.2	112.2	117.2
A_g^2	122.0	105.9	—	—	116.4
A_g^3	148.0	134.8	147.4	137.9	146.7
A_g^4	208.7	200.3	—	—	—
E_g^4	219.5	209.6	217.2	217.5	215.0
E_g^5	357.4	229.8	—	—	—
A_g^5	508.9	290.7	—	296.6	—

Note: All values are given in cm^{-1} .

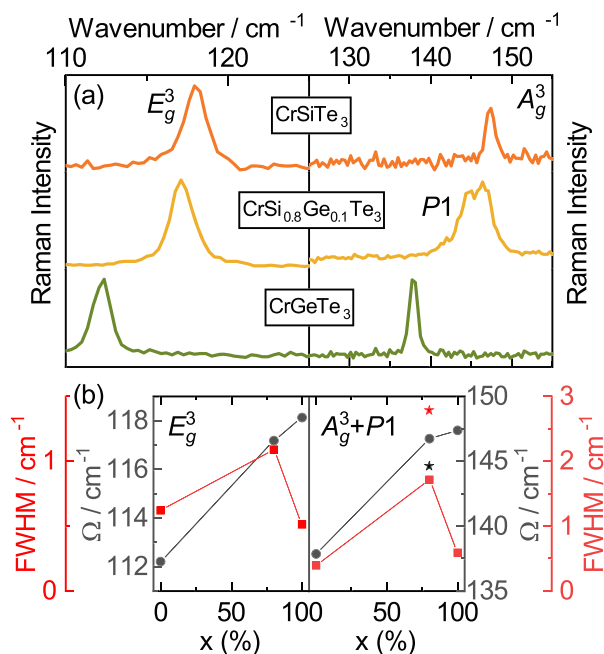


FIGURE 4 (a) Raman scattering spectra of E_g^3 and A_g^3 phonon modes of CrSiTe_3 (orange line), $\text{CrSi}_{0.8}\text{Ge}_{0.1}\text{Te}_3$ (yellow line) and CrGeTe_3 (green line) at $T = 100$ K measured in cross (left panel) and parallel (right panel) scattering configuration, respectively. (b) Energy (grey line) and linewidth (red line) of these two modes with respect to the percentage of Si atoms concentration. Energy and linewidth of $P1$ mode are marked with black and red star, respectively [Colour figure can be viewed at wileyonlinelibrary.com]

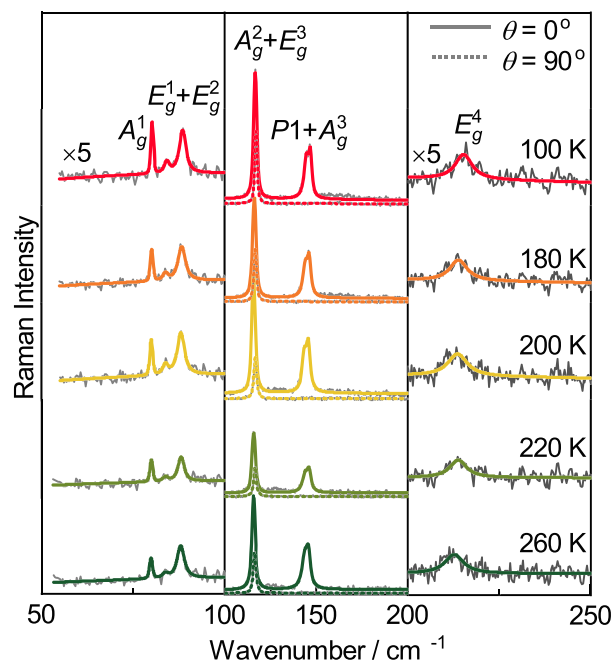


FIGURE 5 Raman spectra of $\text{CrSi}_{0.8}\text{Ge}_{0.1}\text{Te}_3$ single crystal measured at various temperatures. The spectra were analysed by using multiple Voigt peak functions and a single $\chi''_{\text{cont}} = a\Gamma\omega/(\Gamma^2 + \omega^2) + b\omega$ function, for parallel ($\theta = 0^\circ$, solid coloured lines) and cross ($\theta = 90^\circ$, dashed coloured lines) scattering configuration. For clarity, higher and lower energy ranges (left and right panel) are multiplied by the factor of five [Colour figure can be viewed at wileyonlinelibrary.com]

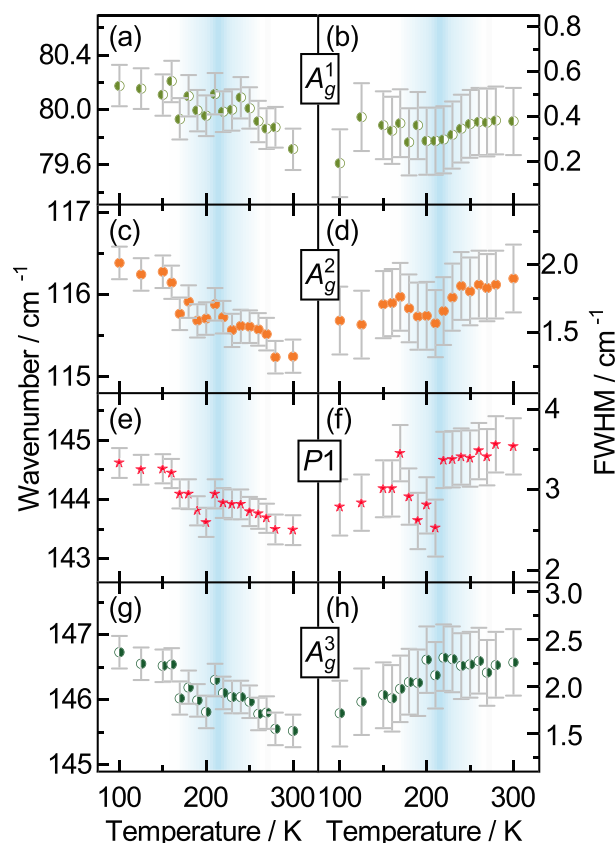


FIGURE 6 Energy and linewidth temperature dependence of A_g^1 (a,b), A_g^2 (c,d), $P1$ (e,f) and A_g^3 (g,h) Raman modes [Colour figure can be viewed at wileyonlinelibrary.com]

only shown for the mid-energy range. Temperature dependence of energies and linewidths of all the observed A_g symmetry modes, including $P1$, are presented in Figure 6. By heating the sample from 100 K to approximately 210 K, monotonous decrease in energy of all the A_g symmetry modes is present, dominantly driven by thermal expansion.^[31] In the temperature region around 210 K, these modes' energy exhibit small deviation, followed by a continuous decrease up to room temperature. In the same temperature region, deviation from expected anharmonic type of behaviour is observed for all the A_g symmetry modes linewidth. This effect is more pronounced for higher energy modes where the anharmonicity is expected to be higher. Similar response of analysed E_g symmetry modes is present and shown in Figure 7.

Concerning previously reported strong spin-phonon coupling in CrSiTe_3 ,^[15,21] which persists up to 180 K, we believe that this unconventional behaviour of energies and linewidths can be attributed to the coupling of the phonon modes to the spin system.^[32] Due to the doping and presence of vacancies, strong magnetic correlations in $\text{CrSi}_{0.8}\text{Ge}_{0.1}\text{Te}_3$ are sustained up to 210 K.

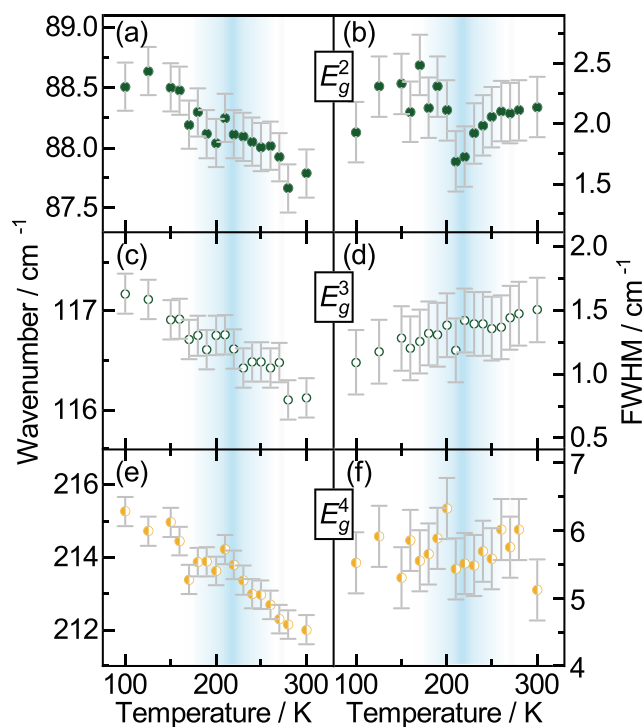


FIGURE 7 Energy and linewidth temperature dependence of E_g^2 (a,b), E_g^3 (c,d) and E_g^4 (e,f) symmetry modes [Colour figure can be viewed at wileyonlinelibrary.com]

4 | CONCLUSIONS

In summary, we presented temperature-dependent Raman scattering and magnetization studies of doped van der Waals ferromagnet $\text{CrSi}_{0.8}\text{Ge}_{0.1}\text{Te}_3$. SEM measurements revealed the presence of 10% vacancies on Si/Ge atomic site. As a consequence, magnetization measurements detected small but clear decrease in T_C . Seven out of 10 Raman active modes have been assigned in our Raman spectra. Temperature dependence of all the observed modes shows the persistence of magnetic correlations up to 210 K. In addition, the results revealed the appearance of the peak that obey pure A_g symmetry, which is attributed to the possible inhomogeneous distribution of Ge atoms and vacancies at nano-scale. This study provides an insight into the impact of doping and presence of vacancies on magnetic and lattice properties in this class of materials.

ACKNOWLEDGEMENTS

This work was supported by the Ministry of Education, Science and Technological Development of the Republic of Serbia and project no F-134 of the Serbian Academy of Sciences and Arts. DFT calculations were performed using computational resources at Johannes Kepler University, Linz, Austria. Electron microscopy was performed at Jozef Stefan Institute, Ljubljana, Slovenia,

under Slovenian Research Agency contract P1-0099 (B. V.). Work at BNL (crystal synthesis and magnetic characterization) was supported by the U.S. DOE-BES, Division of Materials Science and Engineering, under Contract No. DE-SC0012704.

ORCID

Ana Milosavljević  <https://orcid.org/0000-0002-8654-0475>

REFERENCES

- [1] F. Hellman, A. Hoffmann, Y. Tserkovnyak, G. S. Beach, E. E. Fullerton, C. Leighton, A. H. MacDonald, D. C. Ralph, D. A. Arena, H. A. Dürr, P. Fischer, *Rev. Mod. Phys.* **2017**, 89, 025006.
- [2] N. Sivadas, M. W. Daniels, R. H. Swendsen, S. Okamoto, D. Xiao, *Phys. Rev. B* **2015**, 91, 235425.
- [3] K. S. Novoselov, A. K. Geim, S. V. Morozov, D. Jiang, Y. Zhang, S. V. Dubonos, I. V. Grigorieva, A. A. Firsov, *Science* **2004**, 306(5696), 666.
- [4] Q. H. Wang, K. Kalantar-Zadeh, A. Kis, J. N. Coleman, M. S. Strano, *Nat. Nanotechnol.* **2012**, 7, 699.
- [5] G. Cheng, L. Lin, L. Zhenglu, J. Huiwen, S. Alex, X. Yang, C. Ting, B. Wei, W. Chenzhe, W. Yuan, Z. Q. Qiu, R. J. Cava, G. L. Steven, X. Jing, Z. Xiang, *Nature* **2017**, 546, 265.
- [6] B. Huang Bevin, G. Clark, E. Navarro-Moratalla, D. R. Klein, R. Cheng, K. L. Seyler, D. Zhong, E. Schmidgall, M. A. McGuire, D. H. Cobden, W. Yao, *Nature* **2017**, 546, 270.
- [7] K. S. Burch, D. Mandrus, J.-G. Park, *Nature* **2018**, 563(7729), 47.
- [8] J.-X. Zhu, M. Janoschek, D. Chaves, S. J. C. Cezar, T. Durakiewicz, F. Ronning, Y. Sassa, M. Mansson, B. L. Scott, N. Wakeham, E. D. Bauer, J. D. Thompson, *Phys. Rev. B* **2016**, 93, 144404.
- [9] B. Chen, J. H. Yang, H. D. Wang, M. Imai, H. Ohta, C. Michioka, K. Yoshimura, M. H. Fang, *J. Phys. Soc. Japan* **2013**, 82(12), 124711.
- [10] A. Milosavljević, A. Šolajić, S. Djurdjic-Mijin, J. Pešić, B. Višić, Y. Liu, C. Petrovic, N. Lazarević, Z. V. Popović, *Phys. Rev. B* **2019**, 99, 214304.
- [11] M. A. McGuire, H. Dixit, V. R. Cooper, B. C. Sales, *Chem. Mat.* **2015**, 27(2), 612.
- [12] H. L. Zhuang, Y. Xie, P. R. C. Kent, P. Ganesh, *Phys. Rev. B* **2015**, 92, 035407.
- [13] G. T. Lin, H. L. Zhuang, X. Luo, B. J. Liu, F. C. Chen, J. Yan, Y. Sun, J. Zhou, W. J. Lu, P. Tong, Z. G. Sheng, *Phys. Rev. B* **2017**, 95, 245212.
- [14] M. Gibertini, M. Koperski, A. F. Morpurgo, K. S. Novoselov, *Nat. Nanotech.* **2019**, 14(5), 408.
- [15] L. D. Casto, A. J. Clune, M. O. Yokosuk, J. L. Musfeldt, T. J. Williams, H. L. Zhuang, M.-W. Lin, K. Xiao, R. G. Hennig, B. C. Sales, J.-Q. Yan, D. Mandrus, *APL Mat.* **2015**, 3(4), 041515.
- [16] X. Zhang, Y. Zhao, Q. Song, S. Jia, J. Shi, W. Han, *Jpn. J. Appl. Phys.* **2016**, 55(3), 033001.
- [17] B. Siberchicot, S. Jobic, V. Carteaux, P. Gressier, G. Ouvrard, *Phys. J. Chem.* **1996**, 100(14), 5863.
- [18] V. Carteaux, F. Moussa, M. Spiessner, *EPL* **1995**, 29(3), 251.
- [19] J. Zhang, X. Cai, W. Xia, A. Liang, J. Huang, C. Wang, L. Yang, H. Yuan, Y. Chen, S. Zhang, Y. Guo, *Phys. Rev. Lett.* **2019**, 123, 047203.
- [20] Y. F. Li, W. Wang, W. Guo, C. Y. Gu, H. Y. Sun, L. He, J. Zhou, Z. B. Gu, Y. F. Nie, X. Q. Pan, *Phys. Rev. B* **2018**, 98, 125127.
- [21] A. Milosavljević, A. Šolajić, J. Pešić, Y. Liu, C. Petrovic, N. Lazarević, Z. V. Popović, *Phys. Rev. B* **2018**, 98, 104306.
- [22] Y. Tian, M. J. Gray, H. Ji, R. J. Cava, K. S. Burch, *2D Mater.* **2016**, 3(2), 025035.
- [23] Y. Sun, R. C. Xiao, G. T. Lin, R. R. Zhang, L. S. Ling, Z. W. Ma, X. Luo, W. J. Lu, Y. P. Sun, Z. G. Sheng, *Appl. Phys. Lett.* **2018**, 112(7), 072409.
- [24] Y. Liu, C. Petrovic, *Phys. Rev. Mater.* **2019**, 3, 014001.
- [25] P. Giannozzi, S. Baroni, N. Bonini, M. Calandra, R. Car, C. Cavazzoni, D. Ceresoli, G. L. Chiarotti, M. Cococcioni, I. Dabo, A. Dal Corso, *J. Phys. Condens. Matter* **2009**, 21(39), 395502.
- [26] J. P. Perdew, K. Burke, M. Ernzerhof, *Phys. Rev. Lett.* **1996**, 77, 3865.
- [27] P. E. Blöchl, *Phys. Rev. B* **1994**, 50, 17953.
- [28] G. Kresse, D. Joubert, *Phys. Rev. B* **1999**, 59, 1758.
- [29] F. A. May, S. Calder, C. Cantoni, H. Cao, M. A. McGuire, *Phys. Rev. B* **2016**, 93, 014411.
- [30] R. E. Marsh, *J. Solid State Chem.* **1988**, 77(1), 190.
- [31] M. Opačić, N. Lazarević, M. Šćepanović, H. Ryu, H. Lei, C. Petrovic, Z. V. Popović, *J. Phys. Condens. Matter.*, 48(27), 485701.
- [32] F. Feng, N. Lazarević, C. Liu, J. Ji, Y. Wang, S. He, H. Lei, C. Petrovic, R. Yu, Z. V. Popović, Q. Zhang, *Phys. Rev. B* **2019**, 99, 144419.

How to cite this article: Milosavljević A, Šolajić A, Višić B, et al. Vacancies and spin-phonon coupling in CrSi_{0.8}Ge_{0.1}Te₃. *J Raman Spectrosc.* 2020;51:2153–2160. <https://doi.org/10.1002/jrs.5962>

APPENDIX: A DECOMPOSITION OF UNRESOLVED MODES

Analysing the spectra of CrSi_{0.8}Ge_{0.1}Te₃ single crystal, in different polarization configurations (Figure 3), in the energy range around 117 cm⁻¹, becomes clear that lower energy part completely disappears in cross polarization configuration, whereas higher energy part persists. Enlarged part of this energy region is shown in Figure A1, in parallel and cross polarization configuration at temperature of 100 K. After simultaneous modelling of these spectra becomes clear that they consist of the A_g² and E_g³ modes, at energies 116.4 and 117.2 cm⁻¹, respectively. This is completely supported with theoretical calculations presented in Table 1.

On the other hand, existence of P_1 is not predicted by theoretical calculations, as Raman active peak. Only closer inspection and detailed analysis, presented in

Figure A2, shows that much better agreement with experimental results gives modelling as a superposition of two Voigt lines.



Optical and mechanical properties and electron–phonon interaction in graphene doped with metal atoms

Andrijana Šolajić¹ · Jelena Pešić¹ · Radoš Gajić¹

Received: 31 October 2019 / Accepted: 5 March 2020 / Published online: 14 March 2020
© Springer Science+Business Media, LLC, part of Springer Nature 2020

Abstract

Graphene, the first experimentally realized 2D material with outstanding mechanical and electrical properties as well as an excellent optical transparency, is predicted to have many applications in various scientific fields. Furthermore, there are numerous ways for modifications of pure graphene that allow precise tuning of its properties or observation of some new effects, including the applied strain, various types of controlled defects, exposure to electrical or magnetic field, or doping. It is known that graphene with alkali metal atoms adsorbed on its surface becomes superconducting due to enhanced electron–phonon coupling. The question remains what happens with optical and mechanical properties of such structures, can we preserve or enhance these superb properties while making graphene superconducting at the same time. Here we investigate structures based on graphene doped with several metal atoms—Sr, and some transition metal atoms such as Y and Sc. Using the density functional theory, we analyze the optical and elastic properties of those structures, discussing the influence of adsorbed atoms on these properties and calculate the electron–phonon coupling related properties.

Keywords Graphene · DFT · Superconductivity · Electron–phonon interaction · Optical properties · 2D materials

1 Introduction

Since the experimental discovery in 2004, graphene has been attracting enormous attention, not only as the first experimentally realised 2D material as the large scale samples, but mostly for its many unique properties. With this wide spectra of effects, graphene was also predicted to be suitable for various applications (Ferrari 2015; Blake et al. 2008; Todorović et al. 2015; Bonaccorso et al. 2015; Sassi et al. 2017; Liu et al. 2014). Monolayer graphene

This article is part of the Topical Collection on Advanced Photonics Meets Machine Learning.

Guest edited by Goran Gligoric, Jelena Radovanovic and Aleksandra Maluckov.

✉ Andrijana Šolajić
solajic@ipb.ac.rs

¹ Institute of Physics Belgrade, University of Belgrade, Pregrevica 118, Belgrade 11080, Serbia

formed on various metal surfaces was also extensively researched (Wintterlin and Bocquet 2009; Aizawa et al. 1990a, b; Taleb and Farías 2016) along with intercalation of these supported graphene systems (Gall et al. 1997; Shikin et al. 1998; Farías et al. 1999). Up to today, a couple of thousands papers about graphene are published and it is very well-known today how special graphene is and how its characteristics can be tailored to be suitable for even more suitable use. But in the long list of graphene's remarkable properties (Katsnelson et al. 2006; Gusynin and Sharapov 2005; Castro Neto et al. 2006; Lee et al. 2008), there is one notable effect missing, the superconductivity, which is absent in pristine graphene. Among many attempts to make graphene superconducting, a successful idea came from the so-called Graphite intercalation compounds (GICs). GICs are composed from graphite layers, with metallic atoms nested between. They were extensively studied since the 1960s, but with discovery of the superconductivity in some of the GICs (CaC_6 with $T_c = 11.5\text{K}$ and YbC_6 with $T_c = 6.5\text{K}$), an interest in those structures has raised again. The origin of superconductivity in GICs was debated for a long time, but most suggested was that the pairing mediated by electron–phonon interactions as the mechanism (Mazin 2005; Calandra and Mauri 2005), which was later confirmed by experimental data. As it can be observed, in all superconducting GICs there is an intercalant Fermi surface at the Fermi level, and those electrons are strongly coupled to the phonons. As reported in several studies, similar effects are present when going down to the thinnest limit, case of monolayer graphene doped with alkali adatoms in a similar manner to GICs. The electron–phonon coupling constant, λ ,

$$\lambda = \frac{N(0)D^2}{M\omega_{ph}^2}, \quad (1)$$

is proportional to the density of states at the Fermi level and the deformational potential D , and inversely proportional to effective atomic mass M and the frequency of the phonon involved ω_{ph} . As the DOS on the Fermi level in graphene is zero and slowly growing in its vicinity, the superconductivity in pristine graphene can not be observed, similar to pristine bulk graphite. However, the situation is changed upon doping with metallic adatoms, similar as in GICs. In the presence of adatoms, new electronic band is formed, the number of carriers is enlarged and, if the interlayer band occurs at the Fermi level, the electron–phonon coupling λ is enhanced and the coupling to carbon out-of-plane vibrations is promoted. Besides DOS, electron–phonon coupling constant also depends on the deformation potential D , which is inversely related to the distance between the graphene and adatoms. Hence for occurrence of the superconductivity it is favourable for adatoms to be closer to the graphene plane. On the other hand, it was shown that too small distance would result in a complete charge transfer between the graphene and the adatoms, so the interlayer band would be completely empty, as is the case with the bulk LiC_6 where the strong confinement along the z axis leads to interlayer band to be completely unoccupied and the superconductivity is suppressed. In contrary, in the LiC_6 monolayer, the quantum confinement is removed, resulting in partially occupied interlayer band and superconductivity with T_c up to 8K.

Motivated by these results, we wanted to explore graphene doped with Sr atoms and also with some transition metal atoms such as Sc and Y. Besides the electron–phonon properties crucial for the superconductivity, we were interested to investigate mechanical and optical properties also in order to study effects of added adatoms, questioning can we obtain superconducting material and preserve this superb graphene's properties, which would be of great significance for many applications. Using the density functional theory, we analyse the electron–phonon interaction properties and predict the critical temperature in the framework of the

electron–phonon coupling theory. We analyse the mechanical and optical properties of these structures and discuss the influence of adatoms on these properties.

2 Computational details

All calculations were performed in the Quantum Espresso software package (Giannozzi et al. 2009), in the LDA approximation, which is proven to be suitable for graphene systems and often is used. We used norm-conserving pseudopotentials, with the energy cutoff for wavefunctions of 120 Ry, obtained with respect to the convergence test. The unit cell for all doped graphene structures is modelled as $\sqrt{3} \times \sqrt{3}R30^\circ$ supercell of graphene unit cell, with adatoms positioned above the centres of carbon hexagons, the so-called H-site, as it is the most favourable site for all three atoms, according to the DFT study (Nakada and Ishii 2011). In order to avoid the interactions due to periodicity and to simulate a 2D system, the hexagonal c parameter was set to be sufficiently large, more than $c = 10 \text{ \AA}$. Prior to any further calculations, the structures were relaxed to their minimum energy configuration, using the BFGS algorithm. The dielectric function was calculated within the framework of the random-phase approximation (RPA), as implemented in epsilon.x code of QE, on the uniform k -point grid composed of 4096 k -points. The second-order elastic constants were calculated using the ElaStic code. First, the strain type and strength is chosen, and for each deformation, total energies are calculated. From the second derivatives of energy curves, elastic constants are calculated. Here we used amplitudes of 7% positive and negative Lagrangian strain.

The grid for electron–phonon coupling was used up to $48 \times 48 \times 1$ electronic k -mesh and $12 \times 12 \times 1$ phonon-momentum mesh using the Monkhorst pack. The electron–phonon coupling parameter λ and the critical temperature T_c are obtained with the isotropic Eliashberg theory. The Eliashberg function is defined as

$$\alpha^2 F(\omega) = \frac{1}{N(0)N_k N_q} \sum_{n\mathbf{k}, m\mathbf{q}, \nu} |g_{n\mathbf{k}, m\mathbf{k}+\mathbf{q}}^\nu|^2 \times \delta(\epsilon_{n\mathbf{k}}) \delta(\epsilon_{m\mathbf{k}+\mathbf{q}}) \delta(\omega - \omega_q^\nu) \quad (2)$$

where $N(0)$ is total density of states per spin, N_k and N_q are the total numbers of k and q points. $g_{n\mathbf{k}, m\mathbf{k}+\mathbf{q}}^\nu$ is the electron–phonon matrix element, and electron eigenvalues and the band indexes are labelled with n and m , the wavevectors \mathbf{k} and $\mathbf{k} + \mathbf{q}$, the phonon frequencies with the mode number ν and the wavevector \mathbf{q} . From previous equation, the electron–phonon coupling coefficient is given as

$$\lambda(\omega) = 2 \int_0^\omega \frac{\alpha^2 F(\omega')}{\omega'} d\omega' \quad (3)$$

The total electron phonon coupling is obtained for $\omega \rightarrow \infty$. The superconducting critical temperature is estimated using the Allen–Dynes formula,

$$T_c = \frac{\omega_{\log}}{1.2} \exp \left[\frac{-1.04(1 + \lambda)}{\lambda(1 - 0.62\mu^*) - \mu^*} \right] \quad (4)$$

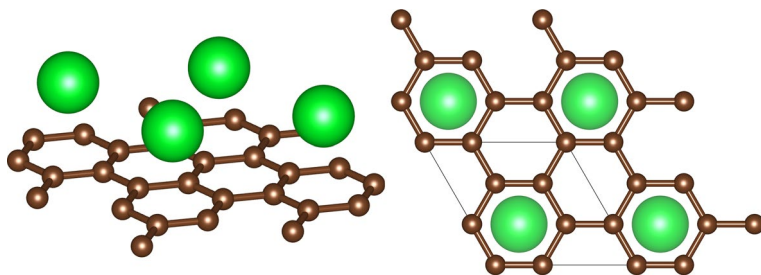


Fig. 1 The structure of graphene with atoms adsorbed on H-site. On the right, top view of structure is shown, with unit cell marked with black line

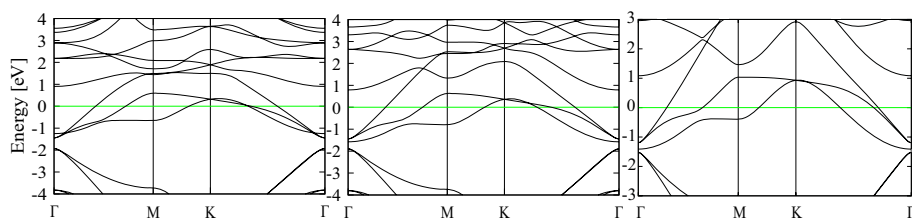


Fig. 2 Electronic structure of ScC_6 , YC_6 and SrC_6 along Γ -M-K- Γ direction. Fermi level is centered on 0 eV

where μ^* is the screened Coulomb pseudopotential and

$$\omega_{\log} = \exp \left[\frac{2}{\lambda} \int \frac{d\omega}{\omega} \alpha^2 F(\omega) \log \omega \right] \quad (5)$$

is the phonon frequencies logarithmic average.

3 Results and Discussion

The atomic structure of SrC_6 monolayer is consisted of graphene sheet covered with Sr adatoms positioned in the H-site, as shown in Fig. 1. Upon relaxing the systems, obtained distance between the graphene sheet and the adatom are $h = 2.22 \text{ \AA}$ for SrC_6 , $h = 2.04 \text{ \AA}$ for YC_6 , and $h = 1.76 \text{ \AA}$ for ScC_6 . Comparing to, for example the bulk SrC_6 compound, where this distance is 2.475 \AA , Sr atoms are closer to the graphene plane, more nested in the centres of carbon hexagons.

The electronic structure of SrC_6 monolayer is discussed in details in our previous work (Šolajić et al. 2018). We have shown the interlayer band that is forming due to the presence of Sr atoms, positioned near the Fermi level, partially occupied. Carbon π^* bands are strongly hybridized with new adatom-derived bands and also the DOS on Fermi level is significantly raised. Very similar are monolayers of ScC_6 and YC_6 , without almost any qualitative difference or significant difference in position of the Fermi level. Electronic structure of all three systems are shown in Fig. 2.

Motivated with those results, we proceeded to calculate the phonon dispersion and electron phonon coupling. In Fig. 3 the phonon dispersion of SrC_6 and phonon density of states for all structures are shown. The adatom contribution to phonon modes is marked

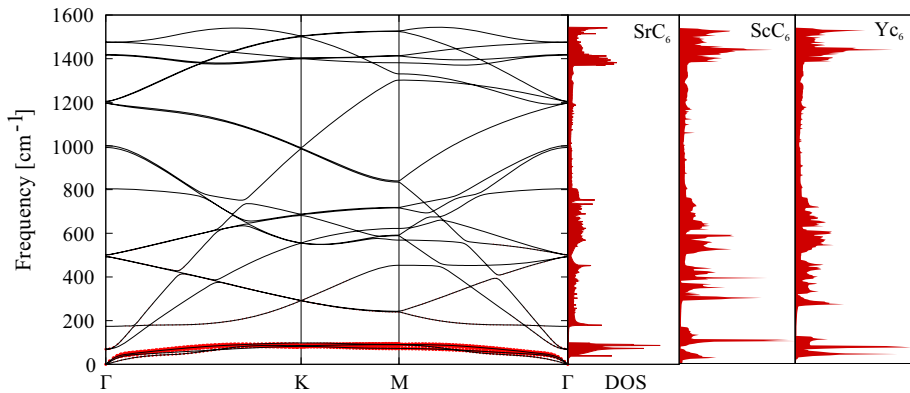


Fig. 3 Phonon dispersion for SrC_6 -mono and phonon density of states for all three structures

with red circles. The phonon dispersions do not show any negative modes and they suggest that systems are dynamically stable. Similar to other metal doped graphene structures, we can observe three distinguished regions. Lowest region belongs to adatom modes, in the middle region are positioned carbon out-of-plane modes, and highest modes are C–C stretching modes. Since the phonon dispersions show minor differences for all three structures, presented is only SrC_6 . First two modes with lowest energies (degenerated one at $\approx 70 \text{ cm}^{-1}$ and one at $\approx 175 \text{ cm}^{-1}$) are related to pristine graphene's acoustic modes. That can be also seen in Fig 4. of our previous study (Šolajić et al. 2018), for the lowest mode at 70 cm^{-1} , the in plane displacements of carbon atoms are like TA and LA modes, with the adatom oscillating in opposite direction, and analogue case for the mode at 175 cm^{-1} , related to ZA graphene mode. This splitting of ZA-like mode from the lower two is similar to the case where graphene layer is formed on metal substrates, and the gap at the Γ point is introduced due to interaction of graphene with substrate [The shift of ZA mode is seen at 48 cm^{-1} in graphene on Cu(111) substrate (Taleb and Fariás 2016) and at 282 cm^{-1} for graphene on transition-metal carbides TaC(111), HfC(111) and TiC(111) (Aizawa et al. 1990b)]. We can consider that the splitting of the ZA-like mode can be described in a similar way, representing the interaction between the graphene and adsorbed metal atoms. The formed gap depends on the strength of the graphene-substrate coupling and as given in the following models. For free-standing pristine graphene, the dispersion of the acoustic ZA mode in the vicinity of the Γ point is given by Taleb et al. (2015):

$$\omega_{\text{ZA}}^{\text{free}}(\mathbf{q}) = \sqrt{\frac{\kappa}{\rho_{2D}}} \mathbf{q}^2, \quad (6)$$

where $\rho_{2D} = 7.6 \times 10^{-8} \text{ g/cm}^2$ is the two-dimensional mass density of graphene. Coupling to the substrate introduces a gap at a frequency ω_0 at the Γ point and the dispersion relation is given by Amorim and Guinea (2013)

$$\omega_{\text{ZA}}^{\text{free}}(\mathbf{q}) = \sqrt{\frac{\kappa}{\rho_{2D}}} \mathbf{q}^4 + \omega_0^2, \quad (7)$$

where $\omega_0 = \sqrt{g/\rho_{2D}}$ and g is the coupling strength between graphene and substrate. Following this model, we can approximate the similar interaction of graphene with adsorbed

metal layer and determine the $g = 0.739 \times 10^{19} \text{ N/m}^3$. This value is significantly smaller than for graphene on various substrates [from $g = 5.7 \times 10^{19} \text{ N/m}^3$ for graphene on Cu (Taleb et al. 2015), to the order of 2×10^{21} for the (111) surface of transition metal carbides (Amorim and Guinea 2013)], as somewhat expecting given that the graphene is covered with not so dense placed Sr metal atoms and not suspended on a real surface.

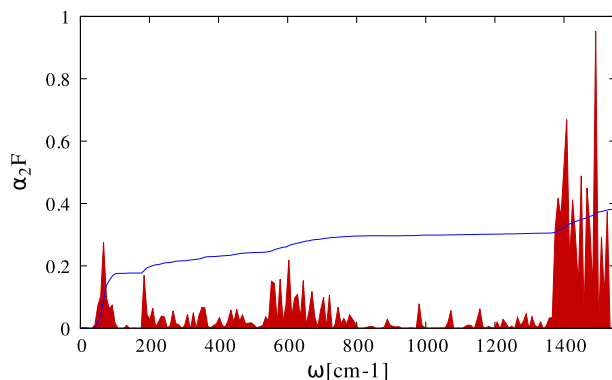
The right side of Fig. 3 shows the phonon DOS for doped graphene structures. For all three structures, the phonon DOS is largest in the adatom region, as well in carbon in-plane modes area. As it can be seen in Eliashberg function, presented in Fig. 4, those modes also have significant contribution in electron–phonon coupling. The choice of adatom does not affect the phonon density of states and, in every of three systems, largest peaks are in low energy region and the highest ones with some minor difference in positions of peaks.

In the Eliashberg function calculated for SrC_6 monolayer, shown in Fig. 4, three distinguished peaks are present as expected, one from the lowest adatom-related modes, one wide and narrow in the middle-energy region, and the highest peak at $1400\text{--}1500 \text{ cm}^{-1}$ related to the carbon in-plane modes. Although the C–C stretching modes are strongly coupled with electronic states at Fermi level, the λ parameter is enhanced most in the low energy region related to adatoms (≈ 0.18), given that it depends on the phonon energy inversely, so the low-energy modes have largest contribution to electron–phonon coupling constant. Comparing this to bulk SrC_6 compound (Calandra and Mauri 2006), we can observe slightly softened Sr_z phonon mode, giving a larger peak in Eliashberg function. However, in the middle region, the contribution of carbon out-of-plane modes is significantly smaller and the contribution to electron–phonon coupling is drastically lowered than in bulk. Very similar case is reported with CaC_6 (Calandra and Mauri 2006; Profeta et al. 2012) where the carbon out-of-plane vibrations are similar in bulk and the monolayer case but overall contribution to λ is decreased in the monolayer. This is also an opposite to the LiC_6 where the removal of confinement gives a rise to the λ .

Overall electron–phonon coupling constant in SrC_6 -monolayer is $\lambda = 0.38$, with $\omega_{\log} = 280.9 \text{ cm}^{-1}$. The superconducting transition temperature, estimated using the Allen–Dynes formula with $\mu^* = 0.112$ is $T_c = 0.9 \text{ K}$, lower than in its bulk counterpart (3K). Both other structures have very similar electronic and phonon structure and enhanced electron–phonon coupling is expected, with critical temperatures in similar range. Further calculations of electron–phonon coupling parameter are needed to be confirmed.

Interested to see what happens with mechanical properties that are superb in graphene, we calculated the elastic constants of our doped structures and compare them

Fig. 4 Eliashberg function with integrated electron–phonon coupling parameter for SrC_6 -mono



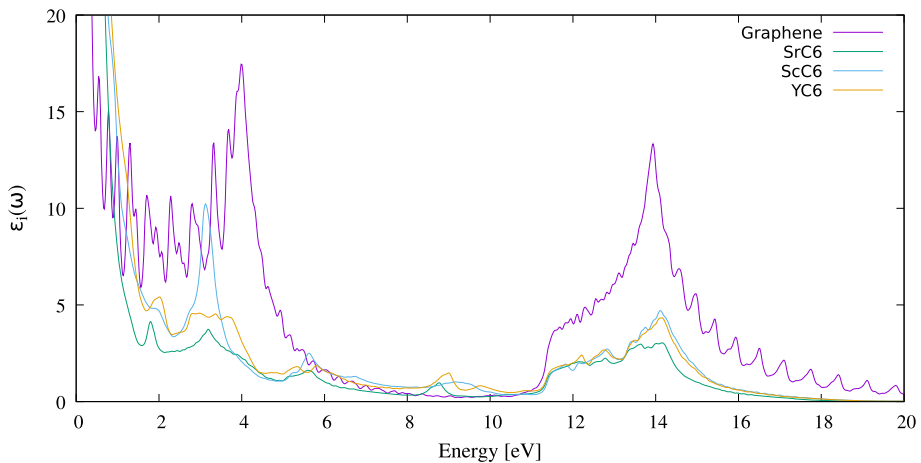


Fig. 5 Eliashberg function with integrated electron–phonon coupling parameter for SrC6-mono

with pristine graphene, which are shown in Table 1. 2D hexagonal, square and rectangular lattices have 4 non-zero second-order elastic constants, c_{11} , c_{12} , c_{22} and c_{66} , where due to symmetry, in case of hexagonal lattice, only two elastic constants are independent because $c_{11} = c_{22}$ and $c_{66} = \frac{1}{2}(c_{11} - c_{22})$. In this case, the Young modulus and Poisson's ratio are defined according to Wei and Peng (2014) as $Y = \frac{c_{11}^2 - c_{12}^2}{c_{11}}$ and $\nu = \frac{c_{21}}{c_{11}}$. Obtained results for elastic properties of pristine graphene are overall in good agreement with previous experimental and theoretical studies. Calculated elastic constants c_{11} and c_{12} are both larger than in literature (estimated to be around 350 and 60 N/m, respectively), so the Young Modulus is also larger (experimentally measured to 342 N/m in Politano et al. 2012 and 340 N/m in Lee et al. 2008). The Poisson's ratio is however accurately obtained to 0.19, presumably due to both c_{11} and c_{12} similarly overestimated. Pristine graphene has extraordinary large values of elastic constants and also can be stretched up to roundly 20%. It is clearly observable that upon doping, elastic constants drop to almost half of the pristine graphene ones, as it is somewhat expected due to added adatoms on top of graphene surface. Still, that leaves these parameters very high in comparison to many other similar 2D materials. Moreover, parameters such as Young modulus remains exceptionally good. The elastic constants and Young modulus of doped graphene structures are in range of hBN and slightly larger than SiC (Andrew et al. 2012; Zhang et al. 2017), and still much larger than many other 2D structures, such as MgB₂ (Pešić et al. 2019) or silicene (Zhang et al. 2017). This possibility to

Table 1 The calculated elastic constants, Young's modulus Y , Poisson's ratio ν and the shear modulus G , for pristine graphene, ScC₆, YC₆ and SrC₆ monolayers

	c_{11}	c_{12}	c_{66}	Y	ν	G
Graphene	462.3	79.6	191.4	448.6	0.19	94.67
ScC ₆	244.8	37.2	103.8	239.2	0.15	103.83
SrC ₆	205.9	33.3	86.3	200.5	0.16	86.26
YC ₆	239.7	38.2	100.8	233.6	0.16	100.77

All parameters are given in units of N/m, except the Poisson's ratio which is dimensionless

strain graphene can be also exploited for tuning superconducting properties, as previously was shown that certain types of strain can enhance the superconducting critical temperature significantly. Pešić et al. (2014).

Calculated imaginary part of dielectric function for our doped structures and pristine graphene, for the electric field vector perpendicular to the c axis, is shown in Fig. 5. Dielectric function of pristine graphene is discussed before (Marinopoulos et al. 2004) and we will not discuss it in details. Our calculations are in agreement with previous theoretical as well experimental studies, showing clear peaks at 4 eV and 14 eV, originating from $\pi \rightarrow \pi^*$ and $\sigma \rightarrow \sigma^*$ interband transitions. The singularity at zero frequency is present and shows metalicity of the system. Upon doping, two small differences can be observed. First, the first peak which is in pristine graphene at 4 eV is shifted to around 3 eV and it is lower intensity in all structures. The second peak at 14 eV does not change position in energy, but drops to much lower intensity in all three structures. These lower intensities and changes in positions of the peaks can be related to Fermi level shift and an adatom influence on π^* bands. Varying the type of dopants however does not make any significant changes in position or intensity of these peaks, except in case of ScC_6 monolayer where intensity of first peak is slightly smaller than in pristine graphene. Moreover, none of the changes in dielectric function induced by adatoms is crucial for the quality of the optical properties and they remain superb as in pristine graphene.

4 Conclusions

In this work we investigated the electron–phonon coupling and possibility of superconductivity in graphene doped with Sr, Y and Sc adatoms, as well their mechanical and optical properties. The bulk SrC_6 which is superconducting with $T_c = 3\text{K}$, was studied theoretically as well experimentally. Moreover, previously studied electronic properties predict the monolayer as good candidate for occurrence of superconductivity. Here we expanded our research by doping with transition metals such as Sc and Y. The phonon dispersion of systems show they are dynamically stable, with no negative frequencies present. Using the isotropic Eliashberg theory, we calculated the total electron–phonon coupling parameter of SrC_6 monolayer, $\lambda = 0.38$. As in bulk SrC_6 compound, superconductivity is occurring, but with lower T_c , which is estimated as $T_c = 0.9\text{K}$ using the Allen–Dynes formula with $\mu^* = 0.112$. Other two discussed structures have similar electronic structure and density of states, as well the phonon dispersion too and have potential to have superconducting properties with similar critical temperatures, and need further investigation. Our calculations of elastic constants and mechanical properties show that upon doping graphene, elastic constants and other parameters like Young modulus, drop by half of pristine graphene’s, which is still extraordinary good in comparison to many similar structures. Calculated imaginary parts of dielectric constants show no significant changes other than lower intensities of the peaks and slightly shifting in energy. This makes those structures an excellent candidates for potential applications.

Acknowledgements The authors acknowledge funding provided by the Institute of Physics Belgrade, through the grant by the Ministry of Education, Science, and Technological Development of the Republic of Serbia. DFT calculations were performed using computational resources at Johannes Kepler University, Linz, Austria.

References




- Aizawa, T., Souda, R., Otani, S., Ishizawa, Y., Oshima, C.: Anomalous bond of monolayer graphite on transition-metal carbide surfaces. *Phys. Rev. Lett.* **64**, 768–771 (1990a). <https://doi.org/10.1103/PhysRevLett.64.768>
- Aizawa, T., Souda, R., Otani, S., Ishizawa, Y., Oshima, C.: Bond softening in monolayer graphite formed on transition-metal carbide surfaces. *Phys. Rev. B* **42**, 11469–11478 (1990b). <https://doi.org/10.1103/PhysRevB.42.11469>
- Amorim, B., Guinea, F.: Flexural mode of graphene on a substrate. *Phys. Rev. B* **88**(11), 115418–115425 (2013)
- Andrew, R.C., Mapasha, R.E., Ukpong, A.M., Chetty, N.: Mechanical properties of graphene and boron–itrene. *Phys. Rev. B* **85**, 125428–125437 (2012). <https://doi.org/10.1103/PhysRevB.85.125428>
- Blake, P., Brimicombe, P.D., Nair, R.R., Booth, T.J., Jiang, D., Schedin, F., Ponomarenko, L.A., Morozov, S.V., Gleeson, H.F., Hill, E.W., Geim, A.K., Novoselov, K.S.: Graphene-based liquid crystal device. *Nano Lett.* **8**(6), 1704–1708 (2008). <https://doi.org/10.1021/nl080649i>
- Bonaccorso, F., Colombo, L., Yu, G., Stoller, M., Tozzini, V., Ferrari, A.C., Ruoff, R.S., Pellegrini, V.: Graphene, related two-dimensional crystals, and hybrid systems for energy conversion and storage. *Science* (2015). <https://doi.org/10.1126/science.1246501>
- Calandra, M., Mauri, F.: Theoretical explanation of superconductivity in c_6 Ca. *Phys. Rev. Lett.* **95**, 237002–237006 (2005). <https://doi.org/10.1103/PhysRevLett.95.237002>
- Calandra, M., Mauri, F.: Possibility of superconductivity in graphite intercalated with alkaline earths investigated with density functional theory. *Phys. Rev. B* **74**, 094507–094515 (2006). <https://doi.org/10.1103/PhysRevB.74.094507>
- Castro Neto, A.H., Guinea, F., Peres, N.M.R.: Edge and surface states in the quantum hall effect in graphene. *Phys. Rev. B* **73**, 205408–205416 (2006). <https://doi.org/10.1103/PhysRevB.73.205408>
- Fariás, D., Shikin, A.M., Rieder, K.H., Dedkov, Y.S.: Synthesis of a weakly bonded graphite monolayer on ni(111) by intercalation of silver. *J. Phys. Condens. Matter* **11**(43), 8453–8458 (1999). <https://doi.org/10.1088/0953-8984/11/43/308>
- Ferrari, A.C., et al.: Science and technology roadmap for graphene, related two-dimensional crystals, and hybrid systems. *Nanoscale* **7**, 4598–4810 (2015). <https://doi.org/10.1039/C4NR01600A>
- Gall, N.R., Rut'kov, E.V., Tontegode, A.Y.: Two dimensional graphite films on metals and their intercalation. *Int. J. Mod. Phys. B* **11**(16), 1865–1911 (1997). <https://doi.org/10.1142/S0217979297000976>
- Giannozzi, P., et al.: Quantum espresso: a modular and open-source software project for quantum simulations of materials. *J. Phys. Condens. Matter* **21**(39), 395502–395521 (2009)
- Gusynin, V.P., Sharapov, S.G.: Unconventional integer quantum hall effect in graphene. *Phys. Rev. Lett.* **95**, 146801–146805 (2005). <https://doi.org/10.1103/PhysRevLett.95.146801>
- Katsnelson, M., Novoselov, K., Geim, A.: Chiral tunnelling and the klein paradox in graphene. *Nat. Phys.* **2**(9), 620–625 (2006). <https://doi.org/10.1038/nphys384>
- Lee, C., Wei, X., Kysar, J.W., Hone, J.: Measurement of the elastic properties and intrinsic strength of monolayer graphene. *Science* **321**(5887), 385–388 (2008). <https://doi.org/10.1126/science.1157996>
- Liu, C.H., Chang, Y.C., Norris, T.B., Zhong, Z.: Graphene photodetectors with ultra-broadband and high responsivity at room temperature. *Nat. Nanotechnol.* **9**(4), 273–278 (2014)
- Marinopoulos, A.G., Reining, L., Rubio, A., Olevano, V.: Ab initio study of the optical absorption and wave-vector-dependent dielectric response of graphite. *Phys. Rev. B* **69**, 245419–245431 (2004). <https://doi.org/10.1103/PhysRevB.69.245419>
- Mazin, I.I.: Intercalant-driven superconductivity in YbC_6 and CaC_6 . *Phys. Rev. Lett.* **95**, 227001–227005 (2005). <https://doi.org/10.1103/PhysRevLett.95.227001>
- Nakada, K., Ishii, A.: DFT calculation for adatom adsorption on graphene. In: Gong, J.R. (ed.) *Graphene Simulation*. InTech, Rijeka, Croatia (2011)
- Pešić, J., Gajić, R., Hingerl, K., Belić, M.: Strain-enhanced superconductivity in li-doped graphene. *Europhys. Lett.: EPL* **108**(6), 67005–67011 (2014)
- Pešić, J., Popov, I., Šolajić, A., Damjanović, V., Hingerl, K., Belić, M., Gajić, R.: Ab initio study of the electronic, vibrational, and mechanical properties of the magnesium diboride monolayer. *Condens. Matter* (2019). <https://doi.org/10.3390/condmat4020037>
- Politano, A., Marino, A.R., Campi, D., Fariás, D., Miranda, R., Chiarello, G.: Elastic properties of a macroscopic graphene sample from phonon dispersion measurements. *Carbon* **50**(13), 4903–4910 (2012). <https://doi.org/10.1016/j.carbon.2012.06.019>
- Profeta, G., Calandra, M., Mauri, F.: Phonon-mediated superconductivity in graphene by lithium deposition. *Nat. Phys.* **8**(2), 131–134 (2012)

- Sassi, U., Parret, R., Nanot, S., Bruna, M., Borini, S., De Fazio, D., Zhao, Z., Lidorikis, E., Koppens, F., Ferrari, A., et al.: Graphene-based mid-infrared room-temperature pyroelectric bolometers with ultra-high temperature coefficient of resistance. *Nat. Commun.* **8**, 14311–14321 (2017)
- Shikin, A.M., Fariás, D., Rieder, K.H.: Phonon stiffening induced by copper intercalation in monolayer graphite on ni(111). *Europhys. Lett.: EPL* **44**(1), 44–49 (1998). <https://doi.org/10.1209/epl/1998-00432-x>
- Šolajić, A., Pešić, J., Gajić, R.: Ab-initio calculations of electronic and vibrational properties of sr and yb intercalated graphene. *Opt. Quantum Electron.* **50**(7), 276–286 (2018). <https://doi.org/10.1007/s11082-018-1541-x>
- Taleb, A.A., Fariás, D.: Phonon dynamics of graphene on metals. *J. Phys. Condens. Matter* **28**(10), 103005–103024 (2016). <https://doi.org/10.1088/0953-8984/28/10/103005>
- Taleb, A.A., Yu, H.K., Anemone, G., Fariás, D., Wodtke, A.M.: Helium diffraction and acoustic phonons of graphene grown on copper foil. *Carbon* **95**, 731–737 (2015). <https://doi.org/10.1016/j.carbon.2015.08.110>
- Todorović, D., Matković, A., Milićević, M., Jovanović, D., Gajić, R., Salom, I., Spasenović, M.: Multilayer graphene condenser microphone. *2D Mater.* **2**(4), 045013–045019 (2015)
- Wei, Q., Peng, X.: Superior mechanical flexibility of phosphorene and few-layer black phosphorus. *Appl. Phys. Lett.* **104**(25), 251915–251920 (2014). <https://doi.org/10.1063/1.4885215>
- Winterlin, J., Bocquet, M.L.: Graphene on metal surfaces. *Surface Science* **603**(10), 1841–1852 (2009). <https://doi.org/10.1016/j.susc.2008.08.037>. (Special Issue of Surface Science dedicated to Prof. Dr. Dr. h.c. mult. Gerhard Ertl, Nobel-Laureate in Chemistry 2007)
- Zhang, Z., Yang, Y., Penev, E.S., Yakobson, B.I.: Elasticity, flexibility, and ideal strength of borophenes. *Adv. Funct. Mater.* **27**(9), 1605059–1605066 (2017). <https://doi.org/10.1002/adfm.201605059>

Publisher's Note Springer Nature remains neutral with regard to jurisdictional claims in published maps and institutional affiliations.

Article

Ab Initio Study of the Electronic, Vibrational, and Mechanical Properties of the Magnesium Diboride Monolayer

Jelena Pešić ^{1,*} , Igor Popov ^{1,2} , Andrijana Šolajić ¹, Vladimir Damljanović ¹ , Kurt Hingerl ³, Milivoj Belić ⁴ and Radoš Gajić ¹

¹ Laboratory for graphene, other 2D materials and ordered nanostructures, Center for Solid State Physics and New Materials, Institute of Physics Belgrade, University of Belgrade, 11080 Belgrade, Serbia; popov@ipb.ac.rs (I.P.); solajic@ipb.ac.rs (A.Š.); damlja@ipb.ac.rs (V.D.); rgajic@ipb.ac.rs (R.G.)

² Institute for Multidisciplinary Research, University of Belgrade, Kneza Višeslava 1, 11030 Belgrade, Serbia

³ Center for Surface and Nanoanalytics, Johannes Kepler University, 4040 Linz, Austria; Kurt.Hingerl@jku.at

⁴ Science Program, Texas A&M University at Qatar, Doha P.O. Box 23874, Qatar; milivoj.belic@qatar.tamu.edu

* Correspondence: yelena@ipb.ac.rs

Received: 15 March 2019; Accepted: 1 April 2019; Published: 2 April 2019



Abstract: Magnesium diboride gained significant interest in the materials science community after the discovery of its superconductivity, with an unusually high critical temperature of 39 K. Many aspects of the electronic properties and superconductivity of bulk MgB_2 and thin sheets of MgB_2 have been determined; however, a single layer of MgB_2 has not yet been fully theoretically investigated. Here, we present a detailed study of the structural, electronic, vibrational, and elastic properties of monolayer MgB_2 , based on ab initio methods. First-principles calculations reveal the importance of reduction of dimensionality on the properties of MgB_2 and thoroughly describe the properties of this novel 2D material. The presence of a negative Poisson ratio, higher density of states at the Fermi level, and a good dynamic stability under strain make the MgB_2 monolayer a prominent material, both for fundamental research and application studies.

Keywords: magnesium diboride; 2D materials; density functional theory

PACS: 71.15.Mb; 74.70.Ad

1. Introduction

Magnesium diboride was first synthesized and had its structure confirmed in 1953 [1]. An interest in its properties has grown ever since 2001, when it was discovered that MgB_2 exhibits the highest superconducting transition temperature T_c of all metallic superconductors. It is an inter-metallic s-wave compound superconductor with a quasi-two dimensional character [2] and a critical temperature of superconductive transition at $T_c = 39$ K. The experimental confirmation of the isotope effect [3] in MgB_2 indicated that it is a phonon-mediated BCS superconductor. A better definition would describe MgB_2 as self-doped semimetal with a crucial σ -bonding band that is nearly filled [4]. The basic aspects of the electronic structure and pairing is in a rather strong coupling of high frequency boron–boron stretch modes to the bonding electronic boron–boron states at the Fermi surface. The phonon-mediated mechanism with different coupling strengths between a particular phonon mode and selected electronic bands, boron σ - and π -bands [5–13], results in the presence of two superconducting gaps at the Fermi level. MgB_2 has already been fabricated in bulk, as single crystals, and as a thin film, and shows potential for practical applications.

The discovery of graphene in 2004 [14] sparked an interest in 2D materials and their properties. A variety of new properties, which distinguished graphene from graphite [14–22], inspired a search for other low-dimensional limits of layered materials and possibilities they offered. Interest in a low-dimensional limit of MgB_2 has arisen in past years, showing that it is superconductive even in a monolayer [23,24].

MgB_2 has a distinct layer structure, where boron atoms form a honeycomb layer and magnesium atoms are located above the center of the hexagons, between every boron plane. The boron layers alternate with a triangular lattice of magnesium layers. There is a noticeable structural similarity of MgB_2 to graphite-intercalated compounds (GICs), some of which also exhibit superconductivity [25–29]. Both monolayer and two-layer graphene, decorated/intercalated with atoms of alkali and alkaline earth metals, exhibit superconductivity and have been thoroughly studied using ab initio methods and isotropic and anisotropic Eliashberg theory [30–32].

Furthermore, a similarity in the electronic structure between GICs and MgB_2 exists. The peculiar and unique property of MgB_2 is a consequence of the incomplete filling of two σ bands corresponding to strongly covalent sp^2 -hybrid bonding within the graphite-like boron layers [33].

Here, we present a comprehensive study of the electronic, vibrational, and mechanical properties of MgB_2 using ab initio methods, in order to provide its detail description.

2. Computational Details

MgB_2 has a hexagonal unit cell and consists of graphite-like B_2 layers stacked with the Mg atoms in between, as shown in Figure 1. The first-principles calculations were performed within the density functional theory (DFT) formalism, using a general gradient approximation (GGA) to calculate the electronic structure. For all electronic and phonon structure, the Quantum Espresso software package [34] was used with ultra-soft pseudopotentials and a plane-wave cutoff energy of 30 Ry. All calculated structures are relaxed to their minimum energy configuration, following the internal force on atoms and stress tensor of the unit cell. We used the Monkhorst-Pack $48 \times 48 \times 48$ and $40 \times 40 \times 1$ k-meshes, for the calculations of the electronic structure of the MgB_2 bulk and MgB_2 monolayer, respectively. The phonon frequencies are calculated using Density Functional Perturbation Theory (DPFT) on the $12 \times 12 \times 12$ and $20 \times 20 \times 1$ phonon wave vector mesh for the bulk and monolayer structures, respectively. In two-dimensional systems, the van der Waals (vdW) interaction was found to play an important role on the electronic structure [35]; however, as this is study on monolayer MgB_2 , we do not treat vdW interactions, especially since, in this case, the effects are minor and including them would add additional computational costs but would not yield more accurate results.

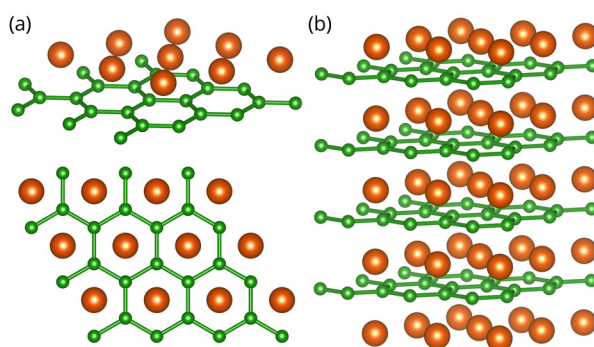


Figure 1. Crystal structure of the MgB_2 monolayer (a) and bulk MgB_2 (b), with a hexagonal unit cell. Green (orange) spheres represent Boron (Magnesium) atoms. Color online.

The crystal structure of MgB_2 and the MgB_2 monolayer are presented in Figure 1. The lattice parameters for the bulk MgB_2 are in agreement with the experimental results, $a = 3.083 \text{ \AA}$ and

$c/a = 1.142$ [9]. In order to avoid an interlayer interaction due to the periodicity and to simulate a 2D material, an artificial vacuum layer was set to be 25 Å. When the monolayer is modelled, the structure is geometrically optimized, allowing the atoms to reach a minimum potential energy state. The bond length between neighbouring atoms remained to be 1.78 Å, but the distance from the boron layer to the Mg atoms changed from $h = 1.76$ Å to $h = 1.60$ Å.

For the molecular dynamics (MD) study, the Siesta code was utilized [36]. The super-cell is built by repeating the unit cell three times in both in-plane directions, whereas the lattice vector in the perpendicular direction is 15 Å, providing a large enough vacuum space between the 2D material and its periodic replica in order to avoid their mutual interaction. The lattice parameters and the geometry of the unit cell are initially optimized using the conjugate gradient method. The Perdew-Burke-Ernzerhof form of the exchange-correlation functional [37], the double-zeta polarized basis set, and the Troulier-Martins pseudopotentials [38] were used in all MD calculations.

The second-order elastic constants were calculated using the ElaStic software package [39]. First, the direction is projected from the strain tensor and total energies for each deformation are calculated. Elastic constants are then calculated using the second derivatives of the energy curves, dependent on the parameter η . In our calculations, the maximum positive and negative amplitudes of 5% Lagrangian strain were applied, with a step of 0.1%.

For the 2D square, rectangular, or hexagonal lattices, the non-zero second-order elastic constants, in Voigt notation, are c_{11} , c_{22} , c_{12} , and c_{66} . Due to symmetry, in hexagonal structures $c_{11} = c_{22}$ and $c_{66} = \frac{1}{2}(c_{11} - c_{12})$; so, we have 2 independent elastic constants. The layer modulus, which represents the resistance of a 2D material to stretching, is given as

$$\gamma = \frac{1}{4}(c_{11} + c_{22} + 2c_{12}).$$

The 2D Young modulus Y for strains in the (10) and (01) directions, Poisson's ratio ν and the shear modulus G are obtained from the following relations,

$$Y = \frac{c_{11}^2 - c_{12}^2}{c_{11}}, \quad \nu = \frac{c_{12}}{c_{22}}, \quad G = c_{66}.$$

Units for elastic constants and those parameters are N/m.

3. Results and Discussion

In order to determine the stability of a single layer of MgB_2 , we perform MD simulations based on DFT and the super-cell approach. Besides the system with optimized (pristine) lattice parameters, we also consider a biaxially stretched system (up to 3% of tensile strain) and biaxially compressed system (up to 5% of compressive strain). The MD simulations are conducted in the range of temperatures between 50–300 K, with a step of 50 K, using the Nosé–Hoover thermostat [40].

Figure 2a shows the average distance between Mg and B atomic layers, as evolved over a time of 1 ps. Throughout the simulation time, there is no further evolution of the z-coordinate and the Mg atom shows only oscillatory movement around the equilibrium positions (as is shown in Figure 2). Importantly, the separation indicates that the Mg atoms do not leave the surface of the MgB_2 crystal. The plane in which the Mg atoms reside shifts away from the plane of the B atoms on average by 0.09 Å in a compressed crystal, while the distance between the planes decreases on average by 0.42 Å in the stretched system. This (relatively larger) shift in the latter case can be understood by analysing the details of the MgB_2 atomic structure. When the crystal is biaxially stretched, its Mg–B bond lengths increase, which is partially compensated by the nesting of the Mg atoms in the hollow sites closer to the B sublattice. Despite these atomic shifts, the MD simulations show the structural stability of the system. The stability from the MD simulations can be further quantitatively derived from the global Lindemann index, the dependence of which on temperature is shown in Figure 2b. It is calculated

for the pristine crystal, with a compressive strain of 5% and a tensile strain of 3%, from the local Lindemann indices, given by the formula

$$q_i = \frac{1}{N-1} \sum_{j \neq i} \frac{\sqrt{\langle r_{ij}^2 \rangle - \langle r_{ij} \rangle^2}}{\langle r_{ij} \rangle},$$

by averaging over all atoms. Here q_i is the local Lindemann index of atom i , N is number of atoms, r_{ij} is a separation between atoms i and j , and the angle brackets denote averaging over time (i.e., MD steps) [41]. The linear behaviour of the Lindemann indices indicate that systems are stable, at least up to room temperature.

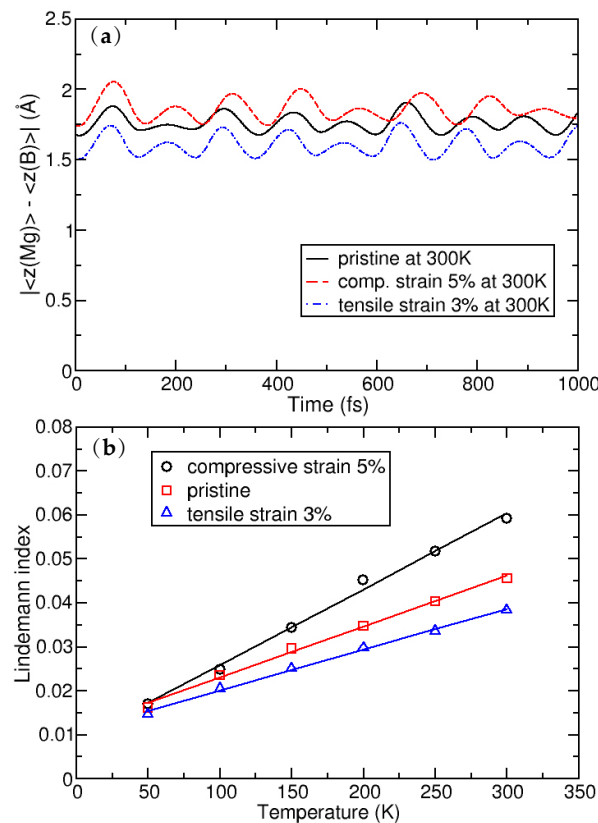


Figure 2. (a): Average distance between the Mg and B atomic layers; and (b): the dependence of the global Lindemann index as a function of temperature.

The calculated second-order elastic constants and other structural parameters for monolayer MgB_2 are given in Table 1. All elastic constants related to the bulk material (those that have 3, 4, or 5 in their subscripts), are calculated close to zero, as is expected for the monolayer. Compared to similar 2D materials, the layer modulus of MgB_2 of 30.18 N/m is relatively small (in the range of Silicene and Germanene), roughly five times smaller than that of graphene or h-BN, for example [42,43]. Similar results are obtained for the Young modulus. Compared to borophene (two-dimensional boron sheets with rectangular structures) [44], which is a hard and brittle 2D material that exhibits an extremely large Young's modulus of 398 N/m along the a direction [45], the MgB_2 monolayer has a significantly smaller value of 63.29 N/m. The most interesting observation in the elastic properties of the MgB_2 monolayer is that the c_{12} constant is negative, which gives a negative Poisson ratio in the a and b directions, too—although, with a very small negative value of -0.05 . However, compared to 2D borophene, which has an out-of-plane negative Poisson's ratio (that effectively holds the strong boron bonds lying along the a direction and makes the boron sheet show superior mechanical flexibility along

the b direction [46]), we obtain similar values [45]. For comparison, graphene has a Young modulus of 352.2 N/m and a Poisson ratio of 0.185 [42]. After confirming its stability and determining the elastic properties of the MgB_2 monolayer, we study its electronic properties. In Figure 3, the electronic structures of bulk MgB_2 and the MgB_2 monolayer are presented. The band structures for the bulk along the high-symmetry points Γ -K-M- Γ -A-L, and for the monolayer along Γ -K-M- Γ were calculated. The Fermi level is set to zero. The band structure of the bulk is in full agreement with previous studies [10,47–49]. The two bands crossing the Fermi level play a crucial role in the electronic properties of MgB_2 . The density of the states around E_f are predominantly related to the B atoms and their p -orbitals, whereas the Mg atom contribution is negligible in this region. Previous studies described Mg as fully ionized and showed that the electrons donated to the system are not localized on the anion but, rather, are distributed over the whole crystal [6]. A similarity to graphite can be observed, with three σ bands, corresponding to the in-plane sp_xp_y (sp^2) hybridization in the boron layer and two π -bands of boron p_z orbitals [33]. Boron $p_{x(y)}$ and p_z orbitals contribute as σ and π states. Analysing projected DOS, one concludes that the σ states are considerably involved in the total density of states at the Fermi level, while the π states have only a partial contribution. It is worth emphasizing that the bulk bands of this material at the K-point above the Fermi level present a formation similar to the Dirac cones in graphene.

In the monolayer, there is an increase in the total density of states at the Fermi level from $N(E_f)_{\text{bulk}} = 0.72$ states/eV to $N(E_f)_{\text{mono}} = 0.97$ states/eV. In the same manner as in the bulk, the monolayer Mg atoms negligibly contribute to the density of states at the Fermi level, and the main contribution comes from the B p -orbitals. The characteristic Dirac cone-like structure is still present and closer to the Fermi level. Dg77, as the symmetry group of the MgB_2 monolayer, hosts a Dirac-like dispersion in the vicinity of the K-point in the hexagonal Brillouin zone, if the orbital wave functions belong to the 2D representation E of the C_{3v} point group of the wave vector [50,51]. In the tight-binding case, the p_x and p_y orbitals of two boron ions give rise to one E-representation (and to two one-dimensional representations), while the s-orbitals form a basis for one E-representation and p_z -orbitals form a basis for one E-representation as well. This explains the presence of the Dirac cones at the K-point in the band structure of the MgB_2 monolayer (as shown in Figure 3b).

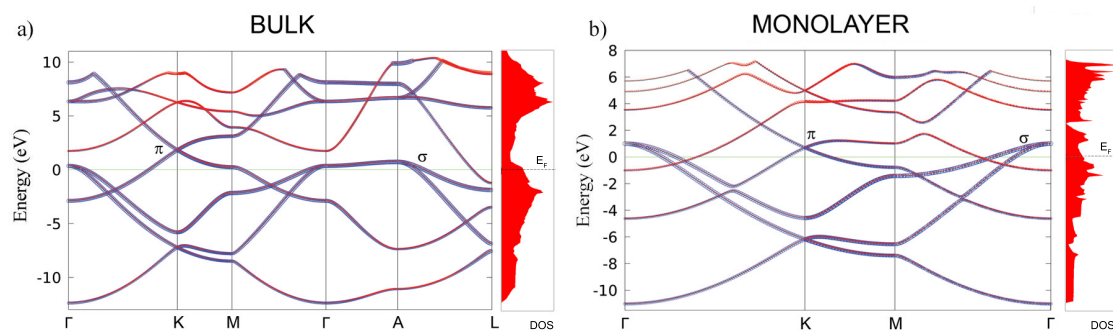


Figure 3. The electronic band structure and total density of states in bulk MgB_2 (a) and the MgB_2 monolayer (b). The blue and red colors represent the B and Mg atoms contributions to the electronic dispersion, respectively.

Table 1. The calculated elastic stiffness constants, layer modulus γ , Young’s modulus Y , Poisson’s ratio ν , and shear modulus G for the MgB_2 monolayer. All parameters are in units of N/m.

c_{11}	c_{12}	c_{66}	γ	Y	ν	G
63.4	−3.1	33.3	30.18	63.29	−0.05	33.3

Figure 4 shows the phonon dispersions for both the bulk and monolayer. For the bulk (in Figure 4a), there are four optical modes at the Γ point. Due to the light atomic mass of the B

atoms and the strong B–B coupling, the two high-frequency modes almost have a pure boron character. The in-plane stretching mode E_{2g} and the out-of-plane mode (where the atoms move in opposite directions B_{1g}) are the boron atom modes. E_{2g} is a doubly-degenerate Raman active mode and experimental studies [6,9] showed that this mode is very sensitive to structural changes and it has a strong electron-phonon coupling. The low-frequency modes (A_{2u}) and double degenerate (E_{1u}) are infrared active and they do not involve changes on in-plane bonds. In Figure 4b, the phonon dispersion of the MgB_2 monolayer is presented. In the phonon spectrum there are no imaginary frequencies, which confirms, once again, the dynamical stability of the system (also demonstrated earlier by the MD calculations).

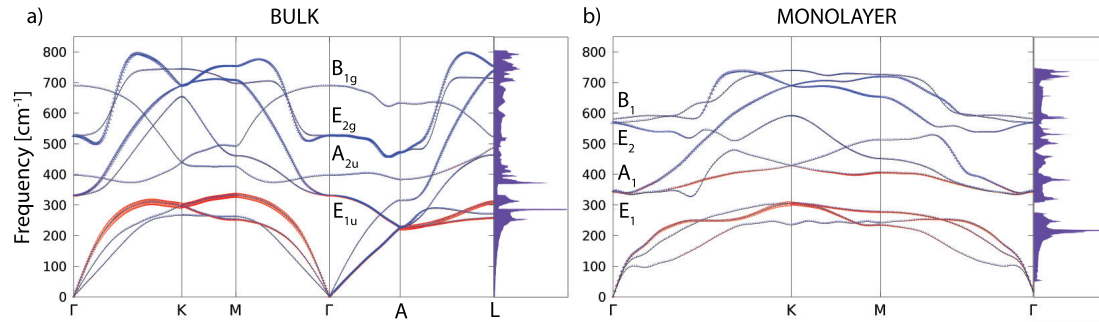


Figure 4. The phonon dispersion and the phonon density of states for the MgB_2 bulk (a) and monolayer (b). The blue and red colours represent the B and Mg atom contributions in the phonon dispersion, respectively.

At the Γ point, there are three acoustic and six optical modes (from which two pairs are doubly degenerate). The optical modes A_1 , B_1 , E_1 , and E_2 are related to the optical modes of the parent material. Two significant differences between the bulk and monolayer spectrum can be observed: The E_1 and A_1 mode become energy degenerate in the monolayer, resulting in either a slight softening (hardening) of the modes which leads to nearly equal frequencies, which opens a gap in the phonon density of states (DOS) between the acoustic and optical modes. A more significant effect concerns the softening of the B_1 mode and hardening of the E_2 mode. As in the bulk E_{2g} mode, the monolayer E_2 mode is strongly coupled to electrons, causing the superconductivity in the monolayer in a similar fashion as in the bulk. In Figure 5, the vibrational frequencies and normal coordinates for the MgB_2 monolayer are presented. The symmetry group is C_{6v} , and the acoustic modes are A_1 and E_1 . The optical modes at the Γ point are A_1 , B_1 , E_1 , and E_2 , where the infrared-active ones are A_1 and E_1 . The Raman-active modes are A_1 , E_1 , and E_2 , and B_1 is silent. In Table 2, the Raman tensor for the MgB_2 monolayer is presented [52]. Similar to graphene, the phonon eigenvectors and the normal coordinates at the Γ -point are determined by symmetry rules and, therefore, are a model independent.

Table 2. Raman tensor of the MgB_2 monolayer.

Raman Tensors					
MgB_2-mono	A_1	E_1	E_2		
$Dg77 = TC_{6v}$	$\begin{pmatrix} a & 0 & 0 \\ 0 & a & 0 \\ 0 & 0 & b \end{pmatrix}$	$\begin{pmatrix} 0 & 0 & c \\ 0 & 0 & 0 \\ c & 0 & 0 \end{pmatrix}$	$\begin{pmatrix} 0 & 0 & 0 \\ 0 & 0 & c \\ 0 & c & 0 \end{pmatrix}$	$\begin{pmatrix} d & 0 & 0 \\ 0 & -d & 0 \\ 0 & 0 & 0 \end{pmatrix}$	$\begin{pmatrix} 0 & -d & 0 \\ -d & 0 & 0 \\ 0 & 0 & 0 \end{pmatrix}$
$O_z \parallel C_6$					
$O_x \parallel \sigma_v$					

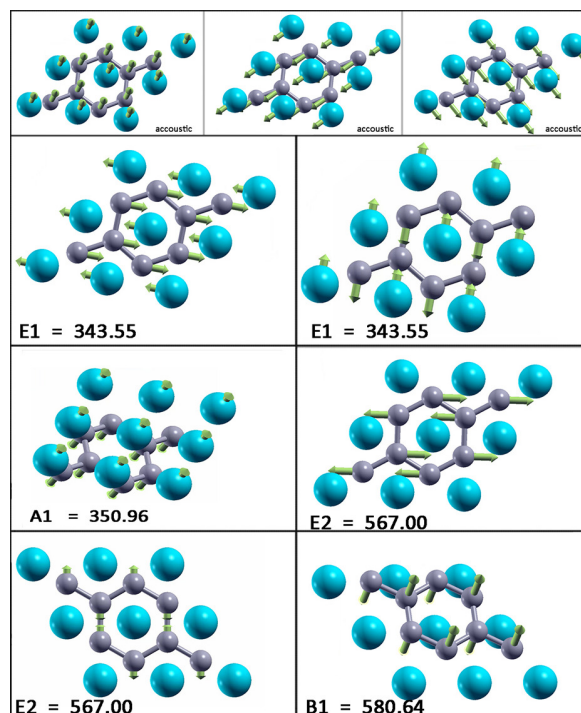


Figure 5. Vibrational frequencies (in wavenumbers) and the vibration normal coordinates at Γ for the MgB_2 monolayer.

4. Conclusions

The electronic band structure, density of states, phonon dispersion, and elastic constants have been calculated for the MgB_2 monolayer and compared to the bulk material, using first-principles calculations within the DFT framework. We demonstrated an increase of electronic density of states at the Fermi level in the monolayer (compared to the bulk) and determined its stability under various strains. These two features are crucial for the enhancement of electron–phonon coupling and they enable significant mechanical modification that increases the critical superconducting temperature. Establishing stability and offering insight into this novel 2D material, we focus on the effects of ultimate lowering of the dimensionality. The question of reduction of dimensionality to its limit, a truly atomic-scale 2D system, and the consequences of this [53–61] are highly relevant, not only to fundamental science but also to applications in nanotechnology.

Author Contributions: Conceptualization, J.P. and R.G.; Validation, K.H., M.B., R.G.; Investigation, J.P., I.P., A.Š. and V.D.; Writing—Original Draft Preparation, J.P., I.P., A.Š. and V.D.; Writing—Review & Editing, J.P.; Supervision, R.G.; Funding Acquisition, K.H., M.B. and R.G.

Funding: This research is supported by Serbian Ministry of Education, Science and Technological Development under projects OI 171005, III 45018, and III 45016 and by the Qatar National Research Fund, cycle 11, under grant number NPRP 11S-1126-170033. K.H. acknowledges the support of the European Commission under the H2020 grant TWINFUSYON.GA692034.

Acknowledgments: The DFT calculations were performed using the computational resources at Johannes Kepler University, Linz, Austria. This work was supported by the Serbian Ministry of Education, Science and Technological Development under projects OI 171005, III 45018, and III 45016.

Conflicts of Interest: The authors declare no conflict of interest.

References

1. Jones, M.E.; Marsh R.E. The preparation and structure of magnesium boride, MgB_2 . *J. Am. Chem. Soc.* **1953**, *76*, 5. [[CrossRef](#)]
2. Nagamatsu, J.; Nakagawa, N.; Muranaka, T.; Zenitani, Y.; Akimitsu, J. Superconductivity at 39 K in magnesium diboride. *Nature* **2001**, *410*, 63. [[CrossRef](#)] [[PubMed](#)]
3. Bud'ko, S.L.; Lapertot, G.; Petrovic, C.; Cunningham, C.E.; Anderson, N.; Canfield, P.C. Boron Isotope Effect in Superconducting MgB_2 . *Phys. Rev. Lett.* **2001**, *86*, 1877. [[CrossRef](#)] [[PubMed](#)]
4. Pickett, W. Superconductivity: 2D Physics, Unknown Mechanisms, Current Puzzles. *Emerg. Phenom. Correl. Matter Lect. Notes Autumn School Corr. Electron.* **2013**, *2013*, 45.
5. Choi, H.J.; Roundy, D.; Sun, H.; Cohen, M.L.; Steven Louie, G. The origin of the anomalous superconducting properties of MgB_2 . *Nature* **2002**, *418*, 758. [[CrossRef](#)]
6. Kortus, J.; Mazin, I.I.; Belaachenko, K.D.; Antropov, V.P.; Boyer, L.L. Superconductivity of Metallic Boron in MgB_2 . *Phys. Rev. Lett.* **2001**, *86*, 4656. [[CrossRef](#)]
7. An, J.M.; Pickett, W.E. Superconductivity of MgB_2 : Covalent Bonds Driven Metallic. *Phys. Rev. Lett.* **2001**, *86*, 4366. [[CrossRef](#)] [[PubMed](#)]
8. Liu, A.Y.; Mazin, I.I.; Kortus, J. Beyond Eliashberg Superconductivity in MgB_2 : Anharmonicity, Two-Phonon Scattering, and Multiple Gaps. *Phys. Rev. Lett.* **2001**, *87*, 087005. [[CrossRef](#)] [[PubMed](#)]
9. Kong, Y.; Dolgov, O.V.; Jepsen, O.; Andersen, O.K. Electron-phonon interaction in the normal and superconducting states of MgB_2 . *Phys. Rev. B* **2001**, *64*, 020501. [[CrossRef](#)]
10. Bohnen, K.-P.; Heid, R.; Renker, B. Phonon Dispersion and Electron-Phonon Coupling in MgB_2 and AlB_2 . *Phys. Rev. Lett.* **2001**, *86*, 5771. [[CrossRef](#)] [[PubMed](#)]
11. Kunc, K.; Loa, I.; Syassen, K.; Kremer, R.K.; Ahn, K. MgB_2 under pressure: phonon calculations, Raman spectroscopy, and optical reflectance. *J. Phys. Condens. Matter* **2001**, *13*, 9945. [[CrossRef](#)]
12. Choi, H.J.; Roundy, D.; Sun, H.; Cohen, M.L.; Louie, S.G. First-principles calculation of the superconducting transition in MgB_2 within the anisotropic Eliashberg formalism. *Phys. Rev. B* **2002**, *66*, 020513. [[CrossRef](#)]
13. Canfield, P.C.; Crabtree, G.W. Magnesium Diboride: Better Late than Never. *Phys. Today* **2003**, *56*, 34. [[CrossRef](#)]
14. Novoselov, K.S.; Geim, A.K.; Morozov, S.V.; Jiang, D.; Zhang, Y.; Dubonos, S.V.; Grigorieva, I.V.; Firsov, A.A. Electric Field Effect in Atomically Thin Carbon Films. *Science* **2004**, *306*, 666–669. [[CrossRef](#)]
15. Katsnelson, M.I.; Novoselov, K.S.; Geim, A.K. Chiral tunnelling and the Klein paradox in graphene. *Nat. Phys.* **2006**, *2*, 620–625. [[CrossRef](#)]
16. Katsnelson, M.I. Zitterbewegung, chirality, and minimal conductivity in graphene. *Eur. Phys. J. B* **2006**, *51*, 157–160. [[CrossRef](#)]
17. Rusin, T.M.; Zawadzki, W. Zitterbewegung of electrons in graphene in a magnetic field. *Phys. Rev. B* **2008**, *78*, 125419. [[CrossRef](#)]
18. Pisana, S.; Lazzeri, M.; Casiraghi, C.; Novoselov, K.S.; Geim, A.K.; Ferrari, A.C.; Mauri, F. Breakdown of the adiabatic Born-Oppenheimer approximation in graphene. *Nat. Mater.* **2007**, *6*, 198–201. [[CrossRef](#)] [[PubMed](#)]
19. Piscanec, S.; Lazzeri, M.; Mauri, F.; Ferrari, A.C.; Robertson, J. Kohn Anomalies and Electron-Phonon Interactions in Graphite. *Phys. Rev. Lett.* **2004**, *93*, 85503. [[CrossRef](#)]
20. Novoselov, K.S.; Jiang, Z.; Zhang, Y.; Morozov, S.V.; Stormer, H.L.; Zeitler, U.; Maan, J.C.; Boebinger, G.S.; Kim, P.; Geim, A.K. Room-temperature quantum Hall effect in graphene. *Science* **2007**, *315*, 1379. [[CrossRef](#)]
21. Zhou, S.Y.; Gweon, G.-H.; Fedorov, A.V.; First, P.N.; de Heer, W.A.; Lee, D.-H.; Guinea, F.; Castro Neto, A.H.; Lanzara, A.; et al. Substrate-induced bandgap opening in epitaxial graphene. *Nat. Mater.* **2007**, *6*, 770–775. [[CrossRef](#)]
22. Zhang, Y.; Tan, Y.; Stormer, H.L.; Kim, P. Experimental observation of the quantum Hall effect and Berry's phase in graphene. *Nature* **2005**, *438*, 201–204. [[CrossRef](#)]
23. Bekaert, J.; Aperi, A.; Partoens, B. Oppeneer, P.M.; Milošević, M.V. Evolution of multigap superconductivity in the atomically thin limit: Strain-enhanced three-gap superconductivity in monolayer MgB_2 . *Phys. Rev. B* **2017**, *96*, 094510.
24. Morshedloo, T.; Roknabadi, M.R.; Behdani, M. First-principles study of the superconductivity in MgB_2 bulk and in its bilayer thin film based on electron–phonon coupling. *Physica C* **2015**, *509*. [[CrossRef](#)]

25. Calandra, M.; Profeta, G.; Mauri, F. Superconductivity in metal-coated graphene. *Phys. Status Solidi (b)* **2012**, *249*, 2544. [[CrossRef](#)]
26. Ludbrook, B.M.; Levy, G.; Nigge, P.; Zonno, M.; Schneider, M.; Dvorak, D.J.; Veenstra, C.N.; Zhdanovich, S.; Wong, D.; Dosanjh, P.; et al. Evidence for superconductivity in Li-decorated monolayer graphene. *Proc. Natl. Acad. Sci. USA* **2015**, *112*, 11795. [[CrossRef](#)] [[PubMed](#)]
27. Profeta, G.; Calandra, M.; Mauri, F. Phonon-mediated superconductivity in graphene by lithium deposition. *Nat. Phys.* **2012**, *8*, 131–134. [[CrossRef](#)]
28. Pešić, J.; Gajić, R.; Hingerl, K.; Belić, M. Strain-enhanced superconductivity in Li-doped graphene. *Europhys. Lett.* **2014**, *108*, 67005. [[CrossRef](#)]
29. Szczesniak, D.; Durajski, A.P.; Szczesniak, R. Influence of lithium doping on the thermodynamic properties of graphene based superconductors. *J. Phys-Condens. Mat.* **2014**, *26*, 255701. [[CrossRef](#)]
30. Durajski, A.; Skoczylas, K.; Szczesniak, R. Superconductivity in bilayer graphene intercalated with alkali and alkaline earth metals. *Phys. Chem. Chem. Phys.* **2019**, *21*, 5925. [[CrossRef](#)] [[PubMed](#)]
31. Zheng, J.-J.; Margine, E.R. First-principles calculations of the superconducting properties in Li-decorated monolayer graphene within the anisotropic Migdal-Eliashberg formalism. *Phys. Rev. B* **2016**, *94*, 064509. [[CrossRef](#)]
32. Margine, E.R.; Lambert, H.; Giustino, F. Electron-phonon interaction and pairing mechanism in superconducting Ca-intercalated bilayer graphene. *Sci. Rep.* **2016**, *6*, 21414. [[CrossRef](#)]
33. Mazin, I.I.; Antropov, V.P. Electronic structure, electron–phonon coupling, and multiband effects in MgB₂. *Phys. C Supercond.* **2003**, *385*, 49–65. [[CrossRef](#)]
34. Giannozzi, P.; Andreussi, O.; Brumme, T.; Bunau, O.; Buongiorno, N.M.; Calandra, M.; Car, R.; Cavazzoni, C.; Ceresoli, D.; Cococcioni, M. et al. Quantum espresso: A modular and open-source software project for quantum simulations of materials. *J. Phys. Condensed Matter* **2009**, *21*, 395502. [[CrossRef](#)] [[PubMed](#)]
35. Lu, N.; Guo, H.; Zhuo, Z.; Wang, L.; Wu, X.; Zeng, X.C. Twisted MX₂/MoS₂ heterobilayers: effect of van der Waals interaction on the electronic structure. *Nanoscale* **2017**, *9*, 19131–19138. [[CrossRef](#)] [[PubMed](#)]
36. Soler, J.M.; Artacho, E.; Gale, J.D.; García, A.; Junquera, J.; Ordejón, P.; Sánchez-Portal, D. The SIESTA method for ab initio order-N materials simulation. *J. Phys. Condens. Matter.* **2002**, *14*, 2745. [[CrossRef](#)]
37. Perdew, J.P.; Burke, K.; Ernzerhof, M. Generalized Gradient Approximation Made Simple. *Phys. Rev. Lett.* **1996**, *77*, 3865–3868. [[CrossRef](#)]
38. Troullier, N.; Martins, J.L. Efficient pseudopotentials for plane-wave calculations. *Phys. Rev. B* **1991**, *43*, 1993–2006. [[CrossRef](#)]
39. Golezorkhtabar, R.; Pavone, P.; Spitaler, J.; Puschnig, P.; Draxl, C. ElaStic: A tool for calculating second-order elastic constants from first principles. *Comput. Phys. Commun.* **2013**, *184*, 1861–1873. [[CrossRef](#)]
40. Nosé, S. A unified formulation of the constant temperature molecular dynamics methods. *J. Chem. Phys.* **1984**, *81*, 511. [[CrossRef](#)]
41. Lindemann, F.A. The calculation of molecular vibration frequencies. *Phys. Z.* **1910**, *11*, 609.
42. Andrew, R.C.; Mapasha, R.E.; Ukpog, A.M.; Chetty, N. Mechanical properties of graphene and boronitrene. *Phys. Rev. B* **2012**, *85*, 125428. [[CrossRef](#)]
43. Zhang, Z.; Yang, Y.; Penev, E.S.; Yakobson, B.I. Elasticity, Flexibility, and Ideal Strength of Borophenes. *Adv. Func. Mater.* **2017**, *27*, 1605059. [[CrossRef](#)]
44. Zhong, H.; Huang, K.; Yu, G.; Yuan, S. Electronic and mechanical properties of few-layer borophene. *Phys. Rev. B* **2018**, *98*, 054104. [[CrossRef](#)]
45. Mannix, A.J.; Zhou, X.F.; Kiraly, B.; Wood, J.D.; Alducin, D.; Myers, B.D.; Liu, X.; Fisher, B.L.; Santiago, U.; Guest, J.R.; et al. Synthesis of borophenes: Anisotropic, two-dimensional boron polymorphs. *Science* **2015**, *350*, 1513–1516. [[CrossRef](#)]
46. Wang, H.; Li, Q.; Gao, Y.; Miao, F.; Zhou, X.-F.; Wan, X.G. Strain effects on borophene: Ideal strength, negative Poisson’s ratio and phonon instability. *New J. Phys.* **2016**, *18*, 073016. [[CrossRef](#)]
47. De la Pena-Seaman, O.; de Cross, R.; Heid, R.; Bohnen, K.-P. Effects of Al and C doping on the electronic structure and phonon renormalization in MgB₂. *Phys. Rev. B* **2009**, *79*, 134523. [[CrossRef](#)]
48. Ponce, S.; Margine, E.R.; Verdi, C.; Giustino, F. EPW: Electron-phonon coupling, transport and superconducting properties using maximally localized Wannier functions. *Comp. Phys. Commun.* **2016**, *209*, 116–133. [[CrossRef](#)]

49. Margine, E.R.; Giustino, F. Anisotropic Migdal-Eliashberg theory using Wannier functions. *Phys. Rev. B* **2013**, *87*, 024505. [[CrossRef](#)]
50. Damljanovic, V.; Gajic, R. Existence of Dirac cones in the Brillouin zone of diperiodic atomic crystals according to group theory. *J. Phys. Condens. Matter* **2016**, *28*, 085502. [[CrossRef](#)]
51. Damljanovic, V.; Gajic, R. Addendum to 'Existence of Dirac cones in the Brillouin zone of diperiodic atomic crystals according to group theory'. *J. Phys. Condens. Matter* **2016**, *28*, 439401. [[CrossRef](#)]
52. Poulet, H.; Mathieu, J.P. *Vibration Spectra and Symmetry of Crystals*; Gordon and Breach: New York, NY, USA, 1976.
53. Szalowski, K. Critical temperature of MgB₂ ultrathin superconducting films: BCS model calculations in the tight-binding approximation. *Phys. Rev. B* **2006**, *74*, 094501. [[CrossRef](#)]
54. Zhang, C.; Wang, Y.; Wang, D.; Zhang, Y.; Liu, Z.-H.; Feng, Q.-R.; Gan, Z.-Z. Suppression of superconductivity in epitaxial MgB₂ ultrathin films. *J. Appl. Phys.* **2013**, *114*, 023903. [[CrossRef](#)]
55. Ao, B.; Zhang, Z.; Tang, T.; Zhao, Y. Potential enhancement of superconductivity in MgB₂ nanosheets: First-principles calculations. *Chem. Phys. Lett.* **2014**, *591*, 185–188. [[CrossRef](#)]
56. Romero-Bermudez, A.; Garcia-Garcia, A.M. Shape resonances and shell effects in thin-film multiband superconductors. *Phys. Rev. B* **2014**, *89*, 024510. [[CrossRef](#)]
57. Romero-Bermudez, A.; Garcia-Garcia, A.M. Size effects in superconducting thin films coupled to a substrate. *Phys. Rev. B* **2014**, *89*, 064508. [[CrossRef](#)]
58. Acharya, N.; Wolak, M.A.; Cunnane, D.P.; Karasik, B.S.; Xi, X.X. MgB₂ ultrathin films fabricated by hybrid physical chemical vapor deposition and ion milling. *APL Mater.* **2016**, *4*, 086114. [[CrossRef](#)]
59. Valentinis, D.; van der Marel, D.; Berthod, C. Rise and fall of shape resonances in thin films of BCS superconductors. *Phys. Rev. B* **2016**, *94*, 054516. [[CrossRef](#)]
60. Narlikar, A.V. Small Superconductors: Introduction. In *The Oxford Handbook of Small Superconductors*, 1st ed.; Narlikar, A.V., Ed.; Oxford University Press: Oxford, UK, 2017.
61. Gariglio, S.; Scheurer, M.; Schmalian, J.; Monteiro, A.M.R.V.L.; Goswami, S.; Caviglia, A. Surface and Interface Superconductivity. In *The Oxford Handbook of Small Superconductors*, 1st ed.; Narlikar, A.V., Ed.; Oxford University Press: Oxford, UK, 2017.



© 2019 by the authors. Licensee MDPI, Basel, Switzerland. This article is an open access article distributed under the terms and conditions of the Creative Commons Attribution (CC BY) license (<http://creativecommons.org/licenses/by/4.0/>).

Lattice dynamics and phase transitions in $\text{Fe}_{3-x}\text{GeTe}_2$

A. Milosavljević,¹ A. Šolajić,¹ S. Djurdjić-Mijin,¹ J. Pešić,¹ B. Višić,¹ Yu Liu (刘育),² C. Petrovic,²
N. Lazarević,¹ and Z. V. Popović^{1,3}

¹*Center for Solid State Physics and New Materials, Institute of Physics Belgrade,*

University of Belgrade, Pregrevica 118, 11080 Belgrade, Serbia

²*Condensed Matter Physics and Materials Science Department, Brookhaven National Laboratory, Upton, New York 11973-5000, USA*

³*Serbian Academy of Sciences and Arts, Knez Mihailova 35, 11000 Belgrade, Serbia*



(Received 23 April 2019; published 17 June 2019)

We present Raman spectroscopy measurements of the van der Waals bonded ferromagnet $\text{Fe}_{3-x}\text{GeTe}_2$, together with lattice dynamics. Four out of eight Raman active modes are observed and assigned, in agreement with numerical calculations. The energies and linewidths of the observed modes display an unconventional temperature dependence at about 150 and 220 K, followed by the nonmonotonic evolution of the Raman continuum. Whereas the former can be related to the magnetic phase transition, the origin of the latter anomaly remains an open question.

DOI: [10.1103/PhysRevB.99.214304](https://doi.org/10.1103/PhysRevB.99.214304)

I. INTRODUCTION

A novel class of magnetism hosting van der Waals bonded materials has recently become of great interest, since the materials are suitable candidates for numbers of technical applications [1–5]. Whereas CrXTe_3 ($X = \text{Si, Ge, Sn}$) and CrX_3 ($X = \text{Cl, Br, I}$) classes maintain low phase transition temperatures [1,6–9] even in a monolayer regime [10], $\text{Fe}_{3-x}\text{GeTe}_2$ has a high bulk transition temperature, between 220 and 230 K [11,12], making it a promising applicant.

The $\text{Fe}_{3-x}\text{GeTe}_2$ crystal structure consists of Fe_{3-x}Ge sublayers stacked between two sheets of Te atoms, and a van der Waals gap between neighboring Te layers [13,14]. Although the structure contains two different types of Fe atoms, it is revealed that vacancies take place only in the Fe2 sites [13,15].

Neutron diffraction, thermodynamic and transport measurements, and Mössbauer spectroscopy were used to analyze the magnetic and functional properties of $\text{Fe}_{3-x}\text{GeTe}_2$, with an Fe atom deficiency of $x \approx 0.1$ and $T_C = 225$ K. It is revealed that at a temperature of 1.5 K, magnetic moments of $1.95(5)\mu_B$ and $1.56(4)\mu_B$ are directed along the easy magnetic c axes [16]. In chemical vapor transport (CVT) grown Fe_3GeTe_2 single crystals, besides the ferromagnetic (FM)-paramagnetic (PM) transition at a temperature of 214 K, FM layers order antiferromagnetically at 152 K [17]. Close to a ferromagnetic transition temperature of 230 K, a possible Kondo lattice behavior, i.e., coupling of traveling electrons and periodically localized spins, is indicated at $T_K = 190 \pm 20$ K, which is in good agreement with theoretical predictions of 222 K [18].

Lattice parameters, as well as the magnetic transition temperature, vary with Fe ion concentration. Lattice parameters a and c follow the opposite trend, whereas the Curie temperature T_C decreases with an increase of Fe ion concentration [15]. For flux-grown crystals, the critical behavior was investigated by bulk dc magnetization around the ferromagnetic phase transition temperature of 152 K [13]. The anomalous Hall effect was also studied, where a significant amount of defects produces bad metallic behavior [19].

Theoretical calculations predict a dynamical stability of Fe_3GeTe_2 single-layer, uniaxial magnetocrystalline anisotropy that originates from spin-orbit coupling [20]. Recently, anomalous Hall effect measurements on single-crystalline metallic Fe_3GeTe_2 nanoflakes with different thicknesses are reported, with a T_C near 200 K and strong perpendicular magnetic anisotropy [21].

We report $\text{Fe}_{3-x}\text{GeTe}_2$ single-crystal lattice dynamic calculations, together with Raman spectroscopy measurements. Four out of eight Raman active modes were observed and assigned. Phonon energies are in a good agreement with theoretical predictions. Analyzed phonon energies and linewidths reveal fingerprint of a ferromagnetic phase transition at a temperature around 150 K. Moreover, discontinuities in the phonon properties are found at temperatures around 220 K. Consistently, in the same temperature range, the Raman continuum displays nonmonotonic behavior.

II. EXPERIMENT AND NUMERICAL METHOD

$\text{Fe}_{3-x}\text{GeTe}_2$ single crystals were grown by the self-flux method as previously described [13]. Samples for scanning electron microscopy (SEM) were cleaved and deposited on graphite tape. Energy dispersive spectroscopy (EDS) maps were collected using a FEI Helios NanoLab 650 instrument equipped with an Oxford Instruments EDS system, equipped with an X-max SSD detector operating at 20 kV. The surface of the as-cleaved $\text{Fe}_{3-x}\text{GeTe}_2$ crystal appears to be uniform for several tens of microns in both directions, as shown in Fig. 4 of Appendix A. Additionally, the elemental composition maps of Fe, Ge, and Te show a distinctive homogeneity of all the three elements (Fig. 5 of Appendix A).

For Raman scattering experiments, a Tri Vista 557 spectrometer was used in the backscattering micro-Raman configuration. As an excitation source, a solid state laser with a 532 nm line was used. In our scattering configuration, the plane of incidence is the ab plane, where $|a| = |b|$ ($\angle(a, b) = 120^\circ$), with the incident (scattered) light propagation direction

TABLE I. Top panel: The type of atoms, Wyckoff positions, each site's contribution to the phonons in the Γ point, and corresponding Raman tensors for the $P6_3/mmc$ space group of $\text{Fe}_{3-x}\text{GeTe}_2$. Bottom panel: Phonon symmetry, calculated optical Raman active phonon frequencies (in cm^{-1}) for the magnetic (M) phase, and experimental values for Raman active phonons at 80 K.

Space group $P6_3/mmc$ (No. 194)			
Fe1 (4e)			$A_{1g} + E_{1g} + E_{2g} + A_{2u} + E_{1u}$
Fe2 (2c)			$E_{2g} + A_{2u} + E_{1u}$
Ge (2d)			$E_{2g} + A_{2u} + E_{1u}$
Te (2c)			$A_{1g} + E_{1g} + E_{2g} + A_{2u} + E_{1u}$
Raman tensors			
$A_{1g} = \begin{pmatrix} a & 0 & 0 \\ 0 & a & 0 \\ 0 & 0 & b \end{pmatrix}$	$E_{1g} = \begin{pmatrix} 0 & 0 & -c \\ 0 & 0 & c \\ -c & c & 0 \end{pmatrix}$	$E_{2g} = \begin{pmatrix} d & -d & 0 \\ -d & -d & 0 \\ 0 & 0 & 0 \end{pmatrix}$	
Raman active modes			
Symmetry	Calculations (M)	Experiment (M)	
E_{2g}^1	50.2		
E_{1g}^1	70.3		
E_{2g}^2	122.2	89.2	
A_{1g}^1	137.2	121.1	
E_{1g}^2	209.5		
E_{2g}^3	228.6	214.8	
A_{1g}^2	233.4	239.6	
E_{2g}^4	334.3		

along the c axes. Samples were cleaved in the air, right before being placed in the vacuum. All the measurements were performed in the high vacuum (10^{-6} mbar) using a KONTE CryoVac continuous helium flow cryostat with a 0.5 mm thick window. To achieve laser beam focusing, a microscope objective with $\times 50$ magnification was used. A Bose factor correction of all spectra was performed. More details can be found in Appendix C.

Density functional theory (DFT) calculations were performed with the QUANTUM ESPRESSO (QE) software package [22]. We used the projector augmented-wave (PAW) pseudopotentials [23,24] with the Perdew-Burke-Ernzerhof (PBE) exchange-correlation functional [25]. The electron wave function and charge density cutoffs of 64 and 782 Ry were chosen, respectively. The k points were sampled using the Monkhorst-Pack scheme, with an $8 \times 8 \times 4$ Γ -centered grid. Both magnetic and nonmagnetic calculations were performed, using the experimentally obtained lattice parameters and the calculated values obtained by relaxing the theoretically proposed structure. In order to obtain the lattice parameters accurately, a treatment of the van der Waals interactions is introduced. The van der Waals interaction was included in all calculations using the Grimme-D2 correction [26]. Phonon frequencies in the Γ point are calculated within the linear response method implemented in QE.

III. RESULTS AND DISCUSSION

$\text{Fe}_{3-x}\text{GeTe}_2$ crystallizes in a hexagonal crystal structure, described with the $P6_3/mmc$ (D_{6h}^4) space group. The atom type, site symmetry, each site's contribution to the phonons

in the Γ point, and corresponding Raman tensors for the $P6_3/mmc$ space group are presented in Table I.

Calculated displacement patterns of Raman active modes, which can be observed in our scattering configuration, are presented in Fig. 1(a). Since the Raman tensor of the E_{1g} mode contains only the z component (Table I), by selection rules, it cannot be detected when measuring from the ab plane in the backscattering configuration. Whereas A_{1g} modes include vibrations of Fe and Te ions along the c axis, E_{2g} modes include in-plane vibrations of all four atoms. The Raman spectra of $\text{Fe}_{3-x}\text{GeTe}_2$ in the magnetic phase (M), at 80 K, and nonmagnetic phase (NM), at 280 K, in a parallel scattering configuration ($\mathbf{e}_i \parallel \mathbf{e}_s$), are presented in Fig. 1 (b). As it can be seen, four peaks at 89.2, 121.1, 214.8, and 239.6 cm^{-1} can be clearly observed at 80 K. According to numerical calculations (see Table I), peaks at 89.2 and 239.6 cm^{-1} correspond to two out of four E_{2g} modes, whereas peaks at 121.1 and 239.6 cm^{-1} can be assigned as two A_{1g} symmetry modes. One should note that numerical calculations performed by using experimentally obtained lattice parameters in the magnetic phase yield a better agreement with experimental values. This is not surprising since the calculations are performed for the stoichiometric compound as opposed to the nonstoichiometry of the sample. Furthermore, it is known that lattice parameters strongly depend on the Fe atom deficiency [15]. All calculated Raman and infrared phonon frequencies, for the magnetic and nonmagnetic phase of $\text{Fe}_{3-x}\text{GeTe}_2$, using relaxed and experimental lattice parameters, together with experimentally observed Raman active modes, are summarized in Table II of Appendix D.

After assigning all observed modes we focused on their temperature evolution. Having in mind finite instrumental

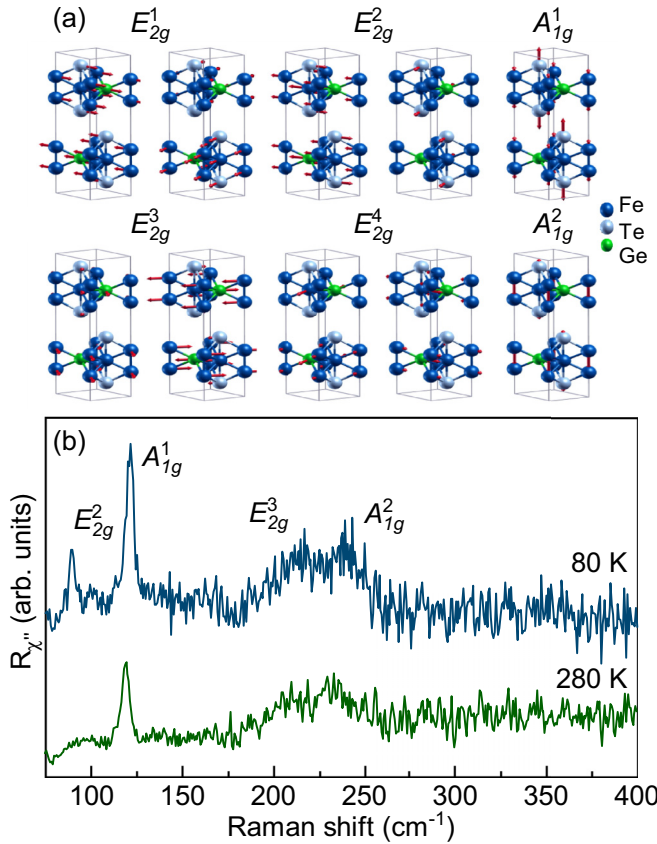


FIG. 1. (a) Displacement patterns of A_{1g} and E_{2g} symmetry modes. (b) Raman spectra of Fe_{3-x}GeTe₂ single crystal measured at different temperatures in a parallel polarization configuration.

broadening, the Voigt line shape was used for the data analysis [27,28]. The modeling procedure is described in detail in Appendix B and presented in Fig. 6. Figure 2 shows the temperature evolution of the energy and linewidth of the A_{1g}^1 , E_{2g}^3 , and A_{1g}^2 modes between 80 and 300 K. Upon heating the sample, both the energy and linewidth of A_{1g}^1 and A_{1g}^2 symmetry modes exhibit a small but sudden discontinuity at about 150 K [Figs. 2(a) and 2(e)]. An apparent discontinuity in energy of all analyzed Raman modes is again present at temperatures around 220 K. In the same temperature range the linewidths of these Raman modes show a clear deviation from the standard anharmonic behavior [27–31].

Apart from the anomalies in the phonon spectra, a closer inspection of the temperature-dependent Raman spectra measured in the parallel polarization configuration reveals a pronounced evolution of the Raman continuum [Fig. 3(a)]. For the analysis we have used a simple model including a damped Lorentzian and linear term, $\chi''_{\text{cont}} \propto a\Gamma\omega/(\omega^2 + \Gamma^2) + b\omega$ [32], where a , b , and Γ are temperature-dependent parameters. Figure 3(b) summarizes the results of the analysis with the linear term omitted (most likely originating from a luminescence). At approximately the same temperatures, where phonon properties exhibit discontinuities, the continuum temperature dependence manifests nonmonotonic behavior. The maximum positions of the curve were obtained by integrating

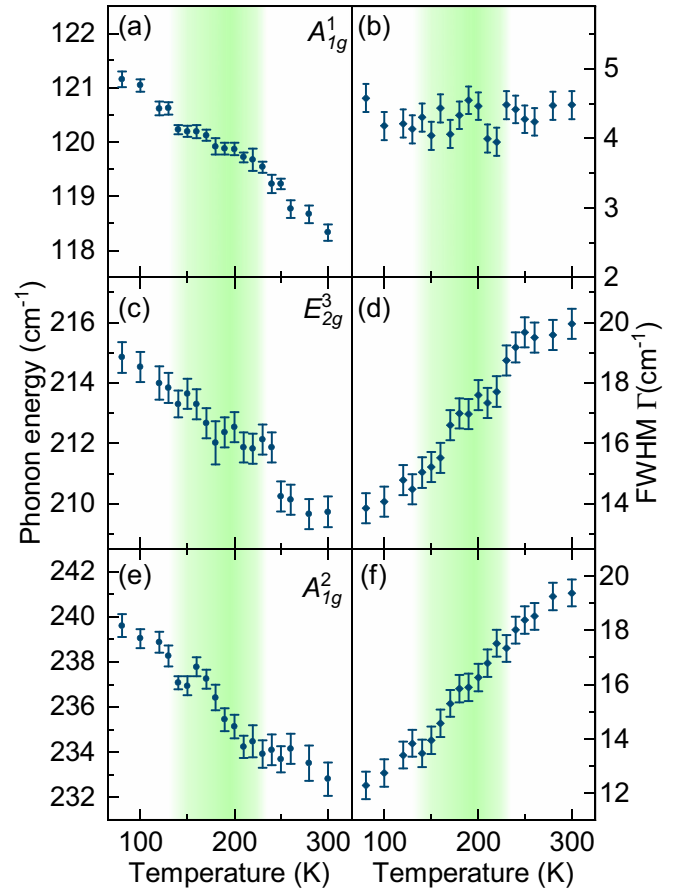


FIG. 2. Energy and linewidth temperature dependence of A_{1g}^1 [(a) and (b)], E_{2g}^3 [(c) and (d)], and A_{1g}^2 [(e) and (f)] phonon modes in Fe_{3-x}GeTe₂.

those shown in Fig. 3(b). The inset of Fig. 3(b) shows the temperature evolution of their displacements. This analysis confirms the presence of discontinuities in the electronic continuum at temperatures around 150 and 220 K, which leaves a trace in the phonon behavior around these temperatures (Fig. 2). While we do not have evidence for the Kondo effect in the Fe_{3-x}GeTe₂ crystals we measured, a modification of the electronic background at FM ordering due to localization or the Kondo effect cannot be excluded.

The temperature evolutions of the phonon self-energies and the continuum observed in the Raman spectra of Fe_{3-x}GeTe₂ suggest the presence of phase transition(s). Magnetization measurements of the samples were performed as described in Ref. [13], revealing a FM-PM transition at 150 K. Thus, the discontinuity in the observed phonon properties around this temperature can be traced back to the weak to moderate spin-phonon coupling. The question remains open regarding the anomaly observed at about 220 K. As previously reported, the Curie temperature of the Fe_{3-x}GeTe₂ single crystals grown by the CVT method is between 220 and 230 K [11,12,14], varying with the vacancy concentration, i.e., a decrease in the vacancy content will result an increment of T_C [15]. On the other hand, the Fe_{3-x}GeTe₂ crystals grown by the self-flux method usually have a lower Curie temperature, since the

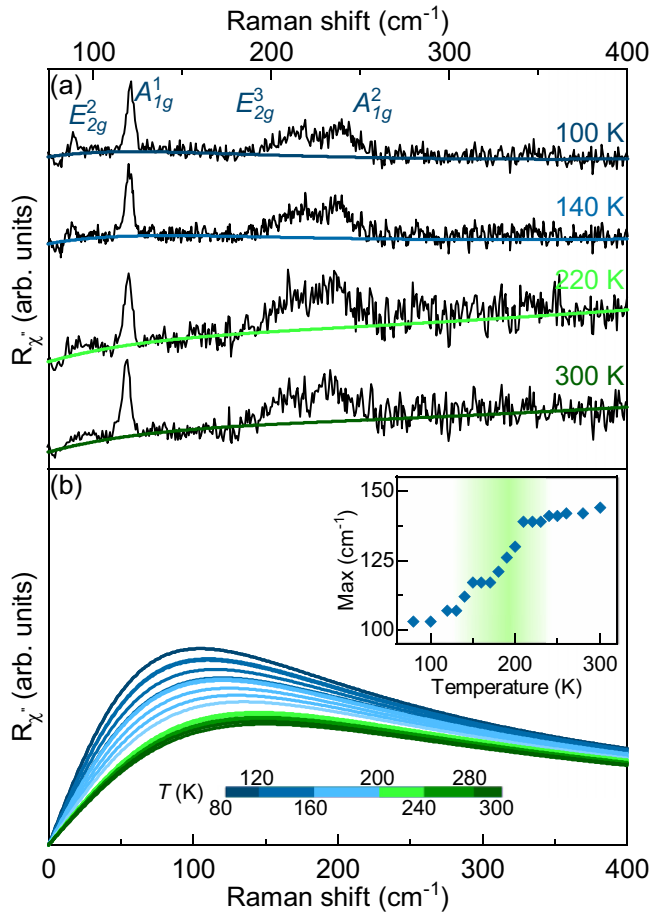


FIG. 3. (a) Raman spectra of $\text{Fe}_{3-x}\text{GeTe}_2$ at four temperatures measured in a parallel polarization configuration. Solid lines represent the theoretical fit to the experimental data. (b) Temperature evolution of the electronic continuum after omitting the linear term. Inset: Displacement of the maximum of fitted curves.

vacancy content is higher [13,15]. Crystals used in the Raman scattering experiment presented here were grown by the self-flux method with a Fe vacancy content of $x \approx 0.36$ [13]. This is in good agreement with our EDS results of $x = 0.4 \pm 0.1$, giving rise to the FM-PM transition at 150 K. Nevertheless,

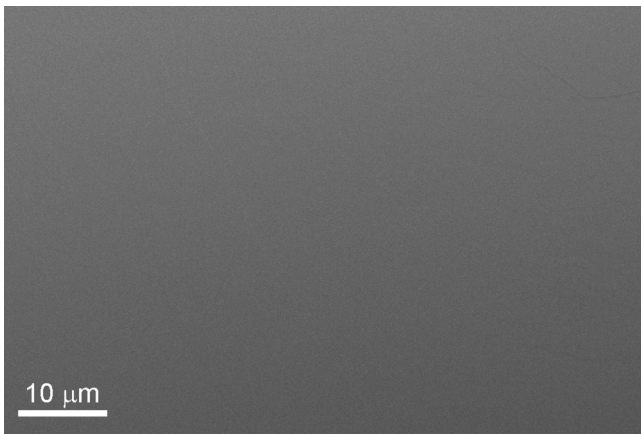


FIG. 4. SEM image of a $\text{Fe}_{3-x}\text{GeTe}_2$ single crystal.

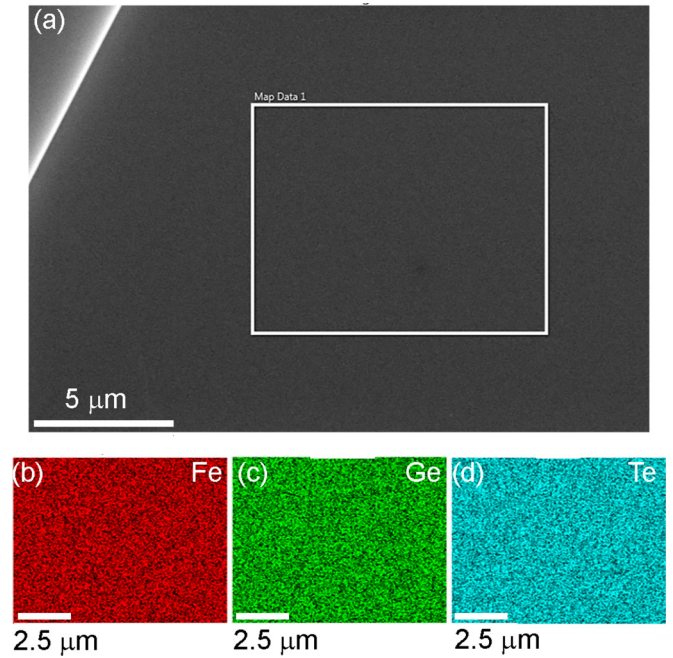


FIG. 5. EDS mapping on a $\text{Fe}_{3-x}\text{GeTe}_2$ single crystal. (a) Secondary electron image of the crystal with the mapping performed within the rectangle. (b)–(d) Associated EDS maps for Fe, Ge, and Te, respectively.

an inhomogeneous distribution of vacancies may result the formation of vacancy depleted “islands” which in turn would result in an anomaly at 220 K similar to the one observed in our Raman data. However, the EDS data (see Fig. 5) do not support this possibility. At this point we can only speculate that while the long-range order temperature is shifted to a lower temperature by the introduction of vacancies, short-range correlations may develop at 220 K.

IV. CONCLUSION

We have studied the lattice dynamics of flux-grown $\text{Fe}_{3-x}\text{GeTe}_2$ single crystals by means of Raman spectroscopy and DFT. Four out of eight Raman active modes, two A_{1g} and two E_{2g} , have been observed and assigned. DFT calculations are in good agreement with experimental results. The temperature dependence of the A_{1g}^1 , E_{2g}^3 , and A_{1g}^2 mode properties reveals a clear fingerprint of spin-phonon coupling, at a temperature of around 150 K. Furthermore, the anomalous behavior in the energies and linewidths of the observed phonon modes is present in the Raman spectra at temperatures around 220 K with the discontinuity also present in the electronic continuum. Its origin still remains an open question, and requires further analysis.

ACKNOWLEDGMENTS

The work was supported by the Serbian Ministry of Education, Science and Technological Development under Projects No. III45018 and No. OI171005. DFT calculations were performed using computational resources at Johannes Kepler University, Linz, Austria. Materials synthesis was supported

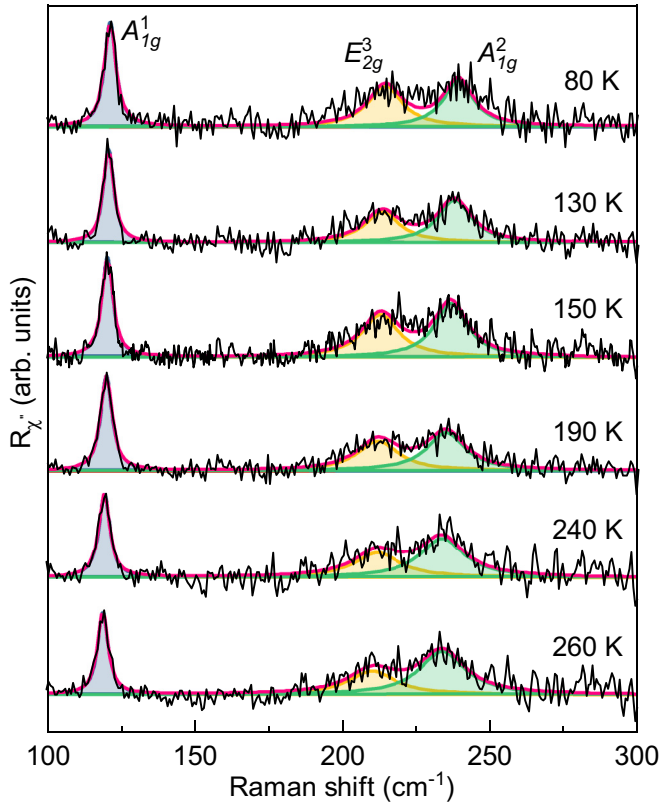


FIG. 6. Modeled Raman spectra of $\text{Fe}_{3-x}\text{GeTe}_2$ single crystal, after subtracting continuum contributions, obtained at various temperatures. For experimental data modeling, the Voigt line shape was used.

by the US Department of Energy, Office of Basic Energy Sciences as part of the Computation Material Science Program (Y.L. and C.P.). Electron microscopy was performed at Jozef Stefan Institute, Ljubljana, Slovenia under Slovenian Research Agency Contract No. P1-0099 (B.V.). This work has received funding from the European Union's Horizon 2020 research and innovation program under the Marie Skłodowska-Curie Grant Agreement No. 645658 (DAFNEOX Project).

APPENDIX A: ELECTRON MICROSCOPY

In order to examine the uniformity of $\text{Fe}_{3-x}\text{GeTe}_2$, Scanning electron microscopy (SEM) was performed on as-cleaved crystals. It can be seen from Fig. 4 that the crystals maintain uniformity for several tens of microns. Furthermore, the elemental composition was obtained using EDS mapping, as shown in Fig. 5. The atomic percentage, averaged over ten measurements, is 47%, 17%, and 36% ($\pm 2\%$) for Fe, Ge, and Te, respectively, with the vacancy content $x = 0.4 \pm 0.1$. The maps associated with the selected elements appear homogeneous, as they are all present uniformly with no apparent islands or vacancies.

APPENDIX B: DATA MODELING

In order to obtain the temperature dependence of the energies and linewidths of the observed $\text{Fe}_{3-x}\text{GeTe}_2$ phonon modes, the Raman continuum, shown in colored lines in

TABLE II. Top panel: Comparison of calculated energies of Raman active phonons using relaxed (R) and experimental [non-relaxed (NR)] lattice parameters for the magnetic (M) and nonmagnetic phase (NM), given in cm^{-1} . Obtained experimental values in the magnetic phase at a temperature of 80 K are given in the last column. Bottom panel: Comparison of calculated energies of infrared optical phonons of $\text{Fe}_{3-x}\text{GeTe}_2$.

Raman active modes					
Calculations					Experiment (M)
Sym.	NM-R	M-R	NM-NR	M-NR	
E_{2g}^1	28.4	49.6	33.9	50.2	
E_{1g}^1	79.2	70.2	71.7	70.3	
E_{2g}^2	115.5	121.0	100.0	122.2	89.2
A_{1g}^1	151.7	139.2	131.7	137.2	121.1
E_{1g}^2	225.5	206.0	194.3	209.5	
E_{2g}^3	238.0	232.6	204.9	228.6	214.8
A_{1g}^2	272.0	262.6	235.7	233.4	239.6
E_{2g}^4	362.0	337.6	315.4	334.7	
Infrared active modes					
A_{2u}^1	70.7	96.6	73.5	92.7	
E_{1u}^1	112.5	121.2	89.4	121.6	
A_{2u}^2	206.0	162.5	183.1	153.7	
E_{1u}^2	226.4	233.6	192.1	231.3	
A_{2u}^3	271.8	248.6	240.8	241.0	
E_{1u}^3	361.1	336.6	314.7	334.7	

Fig. 3(a), was subtracted for simplicity from the raw Raman susceptibility data (black line). The spectra obtained after the subtraction procedure are presented in Fig. 6 (black line) for various temperatures. Because of the finite resolution of the spectrometer and the fact that line shapes of all the observed phonons are symmetric, the Voigt line shape ($\Gamma_G = 0.8 \text{ cm}^{-1}$) was used for data modeling. Blue, yellow, and green lines in Fig. 6 represent fitting curves for A_{1g}^1 , E_{2g}^3 , and A_{1g}^2 phonon modes, respectively, whereas the overall spectral shape is shown in the red line.

APPENDIX C: EXPERIMENTAL DETAILS

Before being placed in a vacuum and being cleaved, the sample was glued to a copper plate with GE varnish in order to achieve good thermal conductivity and prevent strain effects. Silver paste, as a material with high thermal conductivity, was used to attach the copper plate with the sample to the cryostat. The laser beam spot, focused through an Olympus long-range objective of $\times 50$ magnification, was approximately $6 \mu\text{m}$ in size, with a power less than 1 mW at the sample surface. A TriVista 557 triple spectrometer was used in the subtractive mode, with a diffraction grating combination of 1800/1800/2400 grooves/mm and the entrance and second intermediate slit set to $80 \mu\text{m}$, in order to enhance stray light rejection and attain good resolution.

APPENDIX D: CALCULATIONS

In Table II the results of DFT calculations are presented for magnetic (M) and nonmagnetic (NM) relaxed and experimental lattice parameters. For comparison, the

experimental results are shown in the last column. Since the lattice parameters strongly depend on the Fe atom deficiency, the best agreement with experimental results gives the magnetic nonrelaxed solution.

- [1] N. Sivadas, M. W. Daniels, R. H. Swendsen, S. Okamoto, and D. Xiao, Magnetic ground state of semiconducting transition-metal trichalcogenide monolayers, *Phys. Rev. B* **91**, 235425 (2015).
- [2] K. S. Novoselov, A. K. Geim, S. V. Morozov, D. Jiang, Y. Zhang, S. V. Dubonos, I. V. Grigorieva, and A. A. Firsov, Electric field effect in atomically thin carbon films, *Science* **306**, 666 (2004).
- [3] Q. H. Wang, K. Kalantar-Zadeh, A. Kis, J. N. Coleman, and M. S. Strano, Electronics and optoelectronics of two-dimensional transition metal dichalcogenides, *Nat. Nanotechnol.* **7**, 699 (2012).
- [4] C. Gong, L. Li, Z. Li, H. Ji, A. Stern, Y. Xia, T. Cao, W. Bao, C. Wang, Y. Wang, Z. Q. Qiu, R. J. Cava, S. G. Louie, J. Xia, and X. Zhang, Discovery of intrinsic ferromagnetism in two-dimensional van der Waals crystals, *Nature (London)* **546**, 265 (2017).
- [5] B. Huang, G. Clark, E. Navarro-Moratalla, D. R. Klein, R. Cheng, K. L. Seyler, D. Zhong, E. Schmidgall, M. A. McGuire, D. H. Cobden, W. Yao, D. Xiao, P. Jarillo-Herrero, and X. Xu, Layer-dependent ferromagnetism in a van der Waals crystal down to the monolayer limit, *Nature (London)* **546**, 270 (2017).
- [6] M. A. McGuire, H. Dixit, V. R. Cooper, and B. C. Sales, Coupling of crystal structure and magnetism in the layered, ferromagnetic insulator CrI_3 , *Chem. Mater.* **27**, 612 (2015).
- [7] H. L. Zhuang, Y. Xie, P. R. C. Kent, and P. Ganesh, Computational discovery of ferromagnetic semiconducting single-layer CrSnTe_3 , *Phys. Rev. B* **92**, 035407 (2015).
- [8] G. T. Lin, H. L. Zhuang, X. Luo, B. J. Liu, F. C. Chen, J. Yan, Y. Sun, J. Zhou, W. J. Lu, P. Tong, Z. G. Sheng, Z. Qu, W. H. Song, X. B. Zhu, and Y. P. Sun, Tricritical behavior of the two-dimensional intrinsically ferromagnetic semiconductor CrGeTe_3 , *Phys. Rev. B* **95**, 245212 (2017).
- [9] L. D. Casto, A. J. Clune, M. O. Yokosuk, J. L. Musfeldt, T. J. Williams, H. L. Zhuang, M.-W. Lin, K. Xiao, R. G. Hennig, B. C. Sales, J.-Q. Yan, and D. Mandrus, Strong spin-lattice coupling in CrSiTe_3 , *APL Mater.* **3**, 041515 (2015).
- [10] M.-W. Lin, H. L. Zhuang, J. Yan, T. Z. Ward, A. A. Puretzy, C. M. Rouleau, Z. Gai, L. Liang, V. Meunier, B. G. Sumpter, P. Ganesh, P. R. C. Kent, D. B. Geohegan, D. G. Mandrus, and K. Xiao, Ultrathin nanosheets of CrSiTe_3 : A semiconducting two-dimensional ferromagnetic material, *J. Mater. Chem. C* **4**, 315 (2016).
- [11] J.-X. Zhu, M. Janoschek, D. S. Chaves, J. C. Cezar, T. Durakiewicz, F. Ronning, Y. Sassa, M. Mansson, B. L. Scott, N. Wakeham, E. D. Bauer, and J. D. Thompson, Electronic correlation and magnetism in the ferromagnetic metal Fe_3GeTe_2 , *Phys. Rev. B* **93**, 144404 (2016).
- [12] B. Chen, J. H. Yang, H. D. Wang, M. Imai, H. Ohta, C. Michioka, K. Yoshimura, and M. H. Fang, Magnetic properties of layered itinerant electron ferromagnet Fe_3GeTe_2 , *J. Phys. Soc. Jpn.* **82**, 124711 (2013).
- [13] Y. Liu, V. N. Ivanovski, and C. Petrovic, Critical behavior of the van der Waals bonded ferromagnet $\text{Fe}_{3-x}\text{GeTe}_2$, *Phys. Rev. B* **96**, 144429 (2017).
- [14] H.-J. Deiseroth, K. Aleksandrov, C. Reiner, L. Kienle, and R. K. Kremer, Fe_3GeTe_2 and Ni_3GeTe_2 - Two new layered transition-metal compounds: Crystal structures, HRTEM investigations, and magnetic and electrical properties, *Eur. J. Inorg. Chem.* **2006**, 1561 (2006).
- [15] A. F. May, S. Calder, C. Cantoni, H. Cao, and M. A. McGuire, Magnetic structure and phase stability of the van der Waals bonded ferromagnet $\text{Fe}_{3-x}\text{GeTe}_2$, *Phys. Rev. B* **93**, 014411 (2016).
- [16] V. Yu. Verchenko, A. A. Tsirlin, A. V. Sobolev, I. A. Presniakov, and A. V. Shevelkov, Ferromagnetic order, strong magnetocrystalline anisotropy, and magnetocaloric effect in the layered telluride $\text{Fe}_{3-\delta}\text{GeTe}_2$, *Inorg. Chem.* **54**, 8598 (2015).
- [17] J. Yi, H. Zhuang, Q. Zou, Z. Wu, G. Cao, S. Tang, S. A. Calder, P. R. C. Kent, D. Mandrus, and Z. Gai, Competing antiferromagnetism in a quasi-2D itinerant ferromagnet: Fe_3GeTe_2 , *2D Mater.* **4**, 011005 (2016).
- [18] Y. Zhang, H. Lu, X. Zhu, S. Tan, W. Feng, Q. Liu, W. Zhang, Q. Chen, Y. Liu, X. Luo, D. Xie, L. Luo, Z. Zhang, and X. Lai, Emergence of Kondo lattice behavior in a van der Waals itinerant ferromagnet, Fe_3GeTe_2 , *Sci. Adv.* **4**, eaao6791 (2018).
- [19] Y. Liu, E. Stavitski, K. Attenkofer, and C. Petrovic, Anomalous Hall effect in the van der Waals bonded ferromagnet $\text{Fe}_{3-x}\text{GeTe}_2$, *Phys. Rev. B* **97**, 165415 (2018).
- [20] H. L. Zhuang, P. R. C. Kent, and R. G. Hennig, Strong anisotropy and magnetostriction in the two-dimensional Stoner ferromagnet Fe_3GeTe_2 , *Phys. Rev. B* **93**, 134407 (2016).
- [21] C. Tan, J. Lee, S.-G. Jung, T. Park, S. Albarakati, J. Partridge, M. R. Field, D. G. McCulloch, L. Wang, and C. Lee, Hard magnetic properties in nanoflake van der Waals Fe_3GeTe_2 , *Nat. Commun.* **9**, 1554 (2018).
- [22] P. Giannozzi *et al.*, QUANTUM ESPRESSO: A modular and open-source software project for quantum simulations of materials, *J. Phys.: Condens. Matter* **21**, 395502 (2009).
- [23] P. E. Blöchl, Projector augmented-wave method, *Phys. Rev. B* **50**, 17953 (1994).
- [24] G. Kresse and D. Joubert, From ultrasoft pseudopotentials to the projector augmented-wave method, *Phys. Rev. B* **59**, 1758 (1999).
- [25] J. P. Perdew, K. Burke, and M. Ernzerhof, Generalized Gradient Approximation Made Simple, *Phys. Rev. Lett.* **77**, 3865 (1996).
- [26] S. Grimme, Semiempirical GGA-type density functional constructed with a long-range dispersion correction, *J. Comput. Chem.* **27**, 1787 (2006).
- [27] A. Milosavljević, A. Šolajić, J. Pešić, Y. Liu, C. Petrovic, N. Lazarević, and Z. V. Popović, Evidence of spin-phonon coupling in CrSiTe_3 , *Phys. Rev. B* **98**, 104306 (2018).
- [28] A. Baum, A. Milosavljević, N. Lazarević, M. M. Radonjić, B. Nikolić, M. Mitschek, Z. I. Maranloo, M. Šćepanović, M. Grujić-Brožćin, N. Stojilović, M. Opel, A. Wang,

- C. Petrovic, Z. V. Popović, and R. Hackl, Phonon anomalies in FeS, *Phys. Rev. B* **97**, 054306 (2018).
- [29] M. Opačić, N. Lazarević, M. M. Radonjić, M. Šćepanović, H. Ryu, A. Wang, D. Tanasković, C. Petrovic, and Z. V. Popović, Raman spectroscopy of $K_xK_{2-y}Se_2$ single crystals near the ferromagnet–paramagnet transition, *J. Phys.: Condens. Matter* **28**, 485401 (2016).
- [30] Z. V. Popović, N. Lazarević, S. Bogdanović, M. M. Radonjić, D. Tanasković, R. Hu, H. Lei, and C. Petrovic, Signatures of the spin-phonon coupling in $Fe_{1+y}Te_{1-x}Se_x$ alloys, *Solid State Commun.* **193**, 51 (2014).
- [31] Z. V. Popović, M. Šćepanović, N. Lazarević, M. Opačić, M. M. Radonjić, D. Tanasković, H. Lei, and C. Petrovic, Lattice dynamics of $BaFe_2X_3$ ($X = S, Se$) compounds, *Phys. Rev. B* **91**, 064303 (2015).
- [32] T. P. Devereaux and R. Hackl, Inelastic light scattering from correlated electrons, *Rev. Mod. Phys.* **79**, 175 (2007).

Evidence of spin-phonon coupling in CrSiTe₃A. Milosavljević,¹ A. Šolajić,¹ J. Pešić,¹ Yu Liu (刘育),² C. Petrovic,² N. Lazarević,^{1,*} and Z. V. Popović^{1,3}¹*Center for Solid State Physics and New Materials, Institute of Physics Belgrade, University of Belgrade, Pregrevica 118, 11080 Belgrade, Serbia*²*Condensed Matter Physics and Materials Science Department, Brookhaven National Laboratory, Upton, New York 11973-5000, USA*³*Serbian Academy of Sciences and Arts, Knez Mihailova 35, 11000 Belgrade, Serbia*

(Received 12 July 2018; published 18 September 2018; corrected 28 March 2019)

We present Raman scattering results on the layered semiconducting ferromagnetic compound CrSiTe₃. Four Raman-active modes, predicted by symmetry, are observed and assigned. The experimental results are supported by density functional theory calculations. The self-energies of the A_g^3 and the E_g^3 symmetry modes exhibit unconventional temperature evolution around 180 K. In addition, the doubly degenerate E_g^3 mode shows a clear change of asymmetry in the same temperature region. The observed behavior is consistent with the presence of the previously reported short-range magnetic order and strong spin-phonon coupling.

DOI: [10.1103/PhysRevB.98.104306](https://doi.org/10.1103/PhysRevB.98.104306)

I. INTRODUCTION

Trichalcogenides CrXTe₃ ($X = \text{Si, Ge}$) belong to a rare class of quasi-two-dimensional semiconducting materials with a ferromagnetic order, band gaps of 0.4 eV for Si and 0.7 eV for Ge compounds, and Curie temperatures (T_C) of 32 and 61 K, respectively [1–6]. Because of their layered structure, due to van der Waals bonding, they can be exfoliated to mono- and few-layer nanosheets, which, together with their semiconducting and magnetic properties, make an ideal combination for applications in optoelectronics and nanospintronics [7–11]. This was further supported by the observation of giant resistivity modulation of CrGeTe₃-based devices [12].

From an x-ray diffraction study [1], it was revealed that CrSiTe₃ crystals are twined along c axes, the thermal expansion is negative at low temperatures, and the thermal conductivity shows strong magnon-phonon scattering effects. A very small single-ion anisotropy favoring magnetic order along c axes and spin waves was found in CrSiTe₃ by elastic and inelastic neutron scattering [13]. Spin-wave measurements suggest the absence of three-dimensional correlations above T_C , whereas in-plane dynamic correlations are present up to 300 K. First-principles calculations suggested the possibility of graphenelike mechanical exfoliation for CrXTe₃ ($X = \text{Si, Ge}$) single crystals with conserved semiconducting and ferromagnetic properties [14]. The exfoliation of CrSiTe₃ bulk to mono- and few-layer two-dimensional crystals onto a Si/SiO₂ substrate has been achieved [15] with a resistivity between 80 and 120 K, depending on the number of layers. Critical exponents for CrSiTe₃ were also determined from theoretical analysis [16].

Spin-phonon coupling in CrGeTe₃ was investigated in Raman scattering experiments [17]. Splitting of the two lowest-energy E_g modes in the ferromagnetic phase has been observed and ascribed to time-reversal symmetry breaking by

the spin ordering. Furthermore, the significant renormalization of the three higher-energy modes' self-energies below T_C provided additional evidence of spin-phonon coupling [17]. The external pressure-induced effect on lattice dynamics and magnetization in CrGeTe₃ has also been studied [18].

The Raman spectrum of CrSiTe₃ single crystals was reported in Ref. [1], where three Raman-active modes have been observed. Similar results have also been presented in Ref. [15] for ultrathin nanosheets of CrSiTe₃. Here, we report a Raman scattering study of CrSiTe₃ single crystals, with the main focus on phonon properties in the temperature range between 100 and 300 K. Our experimental results are qualitatively different from those previously reported [1,15] but consistent with the results obtained for CrGeTe₃ [17,18]. Furthermore, our data reveal the asymmetry of the E_g^3 mode, which is suppressed at higher temperatures. The A_g^3 and E_g^3 symmetry modes exhibit nonanharmonic self-energy temperature dependence in the region around 180 K, related to the strong spin-lattice interaction due to short-range magnetic order [1]. Energies and symmetries of the observed Raman-active modes are in good agreement with theoretical calculations.

II. EXPERIMENT AND NUMERICAL METHOD

Single crystals of CrSiTe₃ and CrGeTe₃ were grown as described previously [19]. For a Raman scattering experiment, a Tri Vista 557 spectrometer was used in the backscattering micro-Raman configuration with a 1800/1800/2400 grooves/mm diffraction grating combination. A coherent Verdi G solid-state laser with a 532-nm line was used as the excitation source. The direction of the incident (scattered) light coincides with a crystallographic c axis. Right before being placed in the vacuum, the samples were cleaved in the air. All measurements were performed in a high vacuum (10^{-6} mbar) using a KONTI CryoVac continuous-helium-flow cryostat with a 0.5-mm-thick window. Laser-beam focusing was achieved through a microscope objective with $\times 50$ magnification, a spot size of approximately 8 μm , and a power

*nenadl@ipb.ac.rs

TABLE I. Calculated and experimental crystallographic lattice parameters for CrSiTe₃ ($|a| = |b|$), bond lengths, interlayer distance (d), and van der Waals (vdW) gap.

CrSiTe ₃	Calculation (Å)	Experiment (Å) [20]
a	6.87	6.76
c	19.81	20.67
Si-Si	2.27	2.27
Si-Te	2.52	2.51
Cr-Te	2.77	2.78
d	6.86	6.91
vdW gap	3.42	3.42

<2 mW on the surface of a sample. All spectra were corrected for the Bose factor.

Density functional theory calculations were performed in the Quantum Espresso software package [21], using the PBE exchange-correlation functional [22], PAW pseudopotentials [23,24], and energy cutoffs for wave functions and the charge density of 85 and 425 Ry, respectively. For k -point sampling, the Monkhorst-Pack scheme was used, with a Γ -centered $8 \times 8 \times 8$ grid. Optimization of the atomic positions in the unit cell was performed until the interatomic forces were minimized down to 10^{-6} Ry/Å. In order to obtain the parameters accurately, treatment of the van der Waals interactions was included using the Grimme-D2 correction [25]. Phonon frequencies were calculated at the Γ point

within the linear response method implemented in Quantum Espresso. Calculated crystallographic properties obtained by relaxing the structures are in good agreement with x-ray diffraction measurements [20]. A comparison between our, calculated, and experimental results is presented in Table I.

III. RESULTS AND DISCUSSION

A. Polarization dependence

CrSiTe₃ crystallizes in the rhombohedral crystal structure, described by $R\bar{3}$ (C_{3i}^2) [26]. Wyckoff positions of atoms, together with each site's contribution to phonons at the Γ point and corresponding Raman tensors, are listed in Table II. The phonon mode distribution obtained by factor-group analysis for the $R\bar{3}$ space group is as follows:

$$\Gamma_{\text{Raman}} = 5A_g + 5E_g,$$

$$\Gamma_{\text{IR}} = 4A_u + 4E_u,$$

$$\Gamma_{\text{Acoustic}} = A_u + E_u.$$

Since the plane of incidence is ab , where $|a| = |b|$ [$\angle(a, b) = 120^\circ$], and the direction of light propagation is along c axes, from the selection rules, it is possible to observe all Raman-active modes, i.e., five A_g modes and five doubly degenerate E_g modes. According to the Raman tensors presented in Table II, A_g symmetry modes are observable only in the parallel polarization configuration, whereas E_g symmetry

TABLE II. (a) Type of atoms, Wyckoff positions, each site's contribution to the phonons at the Γ point, and corresponding Raman tensors for the $R\bar{3}$ space group of CrSiTe₃. (b) Phonon symmetry, calculated optical phonon frequencies at 0 K, and experimental values for Raman-active (at 100 K) and infrared (IR)-active (at 110 K) [1] CrSiTe₃ phonons.

(a) Space group $R\bar{3}$ (No. 148)					
Atom(s) (Wyckoff positions)			Irreducible representations		
Cr, Si (6 <i>c</i>)			$A_g + E_g + A_u + E_u$		
Te (18 <i>f</i>)			$3A_g + 3E_g + 3A_u + 3E_u$		
(b) Raman tensors					
$A_g = \begin{pmatrix} a & 0 & 0 \\ 0 & b & 0 \\ 0 & 0 & c \end{pmatrix}$		$E_g^1 = \begin{pmatrix} c & d & e \\ d & -c & f \\ e & f & 0 \end{pmatrix}$		$E_g^2 = \begin{pmatrix} d & -c & -f \\ -c & -d & e \\ -f & e & 0 \end{pmatrix}$	
Raman active			IR active [1]		
Symmetry	Calc. (cm ⁻¹)	Expt. (cm ⁻¹)	Symmetry	Calc. (cm ⁻¹)	Expt. (cm ⁻¹)
A_g^1	88.2	–	A_u^1	91.8	91.0
E_g^1	93.5	88.9	E_u^1	93.7	–
E_g^2	96.9	–	A_u^2	116.8	–
E_g^3	118.3	118.2	E_u^2	117.1	–
A_g^2	122.0	–	A_u^3	202.4	–
A_g^3	148.0	147.4	E_u^3	206.2	207.9
A_g^4	208.7	–	A_u^4	243.7	–
E_g^4	219.5	217.2	E_u^4	365.8	370.4
E_g^5	357.4	–			
A_g^5	508.8	–			

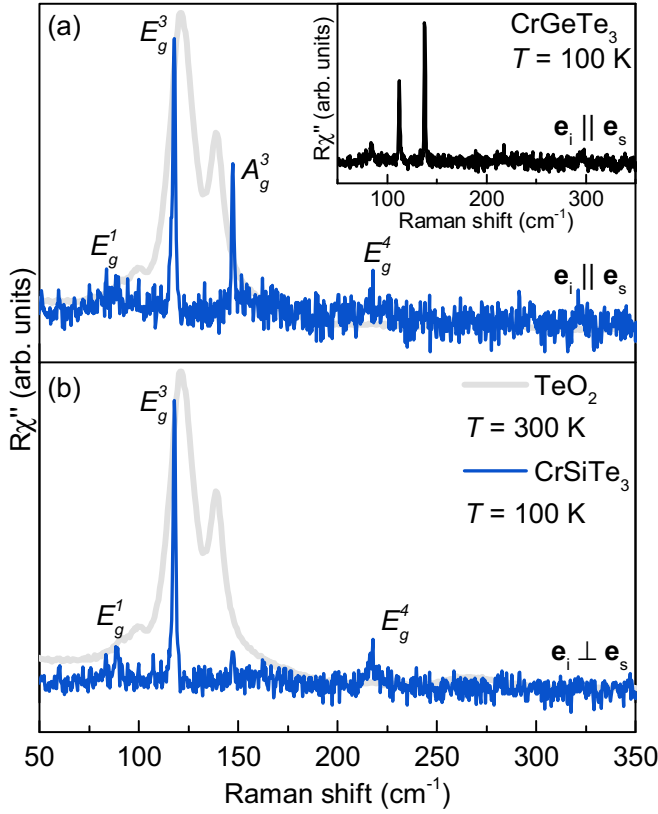


FIG. 1. Raman spectra of CrSiTe₃ single crystals measured at 100 K in (a) parallel and (b) cross polarization configurations. The gray line represents the TeO₂ spectrum measured at 300 K. Inset: Raman spectrum of CrGeTe₃ in the parallel polarization configuration measured at 100 K.

modes can be expected to appear for both in-parallel and cross polarization configurations.

The Raman spectra of CrSiTe₃ for two main linear polarization configurations, at 100 K, are shown in Fig. 1. Four peaks can be observed in the spectra, at energies of 88.9, 118.2, 147.4, and 217.2 cm⁻¹. Since only the peak at 147.4 cm⁻¹ vanishes in the cross polarization configuration, it corresponds to the A_g symmetry mode. The other three modes appear in both parallel and cross polarization configurations and, thereby, can be assigned as E_g symmetry modes (Fig. 1).

In order to exclude the possibility that any of the observed features originate from the TeO₂ [17,27], its Raman spectrum is also presented in Fig. 1. It can be noted that no TeO₂ contribution is present in our CrSiTe₃ data. Furthermore, the observed CrSiTe₃ Raman spectra are also consistent with the CrGeTe₃ Raman spectra (see inset in Fig. 1), isostructural to CrSiTe₃. Five Raman-active modes have been observed for CrGeTe₃, two A_g modes, at 137.9 and 296.6 cm⁻¹, and three E_g modes, at 83.5, 112.2, and 217.5 cm⁻¹, in agreement with the previously published data [17,18]. The main difference in the spectra of CrSiTe₃ and CrGeTe₃ arises from the change in mass and lattice parameter effects that cause the peaks to shift.

Calculated and observed Raman-active phonon energies are compiled in Table II, together with the experimental energies of the infrared (IR)-active phonons [1], and are found to be in good agreement. Displacement patterns of the A_g

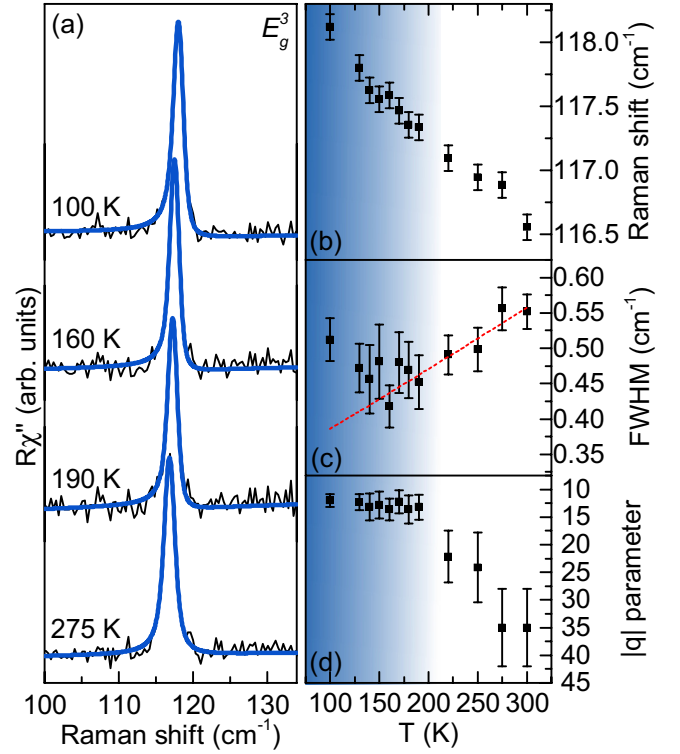


FIG. 2. (a) The E_g^3 mode Raman spectra of CrSiTe₃ at four temperatures measured in the cross polarization configuration. Blue lines represent line shapes obtained as a convolution of the Fano line shape and Gaussian, calculated to fit the experimental data. Temperature dependence of (b) the energy, (c) the line width, and (d) the Fano parameter q of the E_g^3 mode. The dashed red line represents standard anharmonic behavior [28,29]. All the parameters show a change in tendency around 180 K.

and E_g symmetry modes are presented in Fig. 4, in the Appendix.

B. Temperature dependence

After proper assignment of all the observed CrSiTe₃ Raman-active modes we proceeded with temperature evolution of their properties, focusing on the most prominent ones, E_g^3 and A_g^3 . Figure 2(a) shows the spectral region of the doubly degenerate E_g^3 mode at an energy of 118.2 cm⁻¹, at four temperatures. Closer inspection of the 100 K spectra revealed clear asymmetry of the peak on the low-energy side. The presence of defects may result in the appearance of the mode asymmetry [30], however, they would also contribute to the mode line width and, possibly, the appearance of phonons from the edge of the Brillouin zone in the Raman spectra [29]. The very narrow lines and absence of additional features in the Raman spectra of CrSiTe₃ do not support this scenario. The asymmetry may also arise when the phonon is coupled to a continuum [31]. Such a coupling of the E_g^3 phonon mode would result in a line shape given by the convolution of a Fano function and a Gaussian, the latter representing the resolution of the spectrometer [29]. Comparison between the Fano line shape convoluted with a Gaussian, the Voigt line shape, and the experimental data at 100 K is presented in Fig. 5, in the

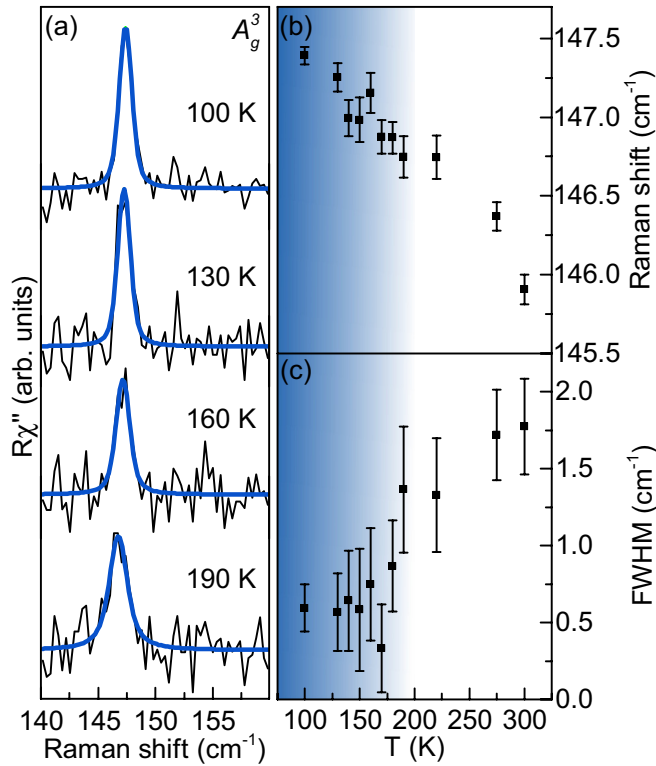


FIG. 3. (a) A_g^3 mode Raman spectra of CrSiTe_3 at four temperatures measured in the parallel polarization configuration. Blue lines represent Voigt line shapes. (b) Energy and (c) line-width temperature dependence of the A_g^3 mode.

Appendix, with the former yielding better agreement with the experimental data. Furthermore, it fully captures the E_g^3 mode line shape at all temperatures under investigation [Figs. 2(a) and 6].

Upon cooling of the sample, the E_g^3 mode energy hardens [Fig. 2(b)] with a very small discontinuity in the temperature range around 180 K. Down to the same temperature, the line width monotonically narrows in line with the standard anharmonic behavior [dashed red line in Fig. 2(c)]. Upon further cooling, the line width increased, deviating from the expected anharmonic tendency. This indicates activation of an additional scattering mechanism, e.g., spin-phonon interaction. Figure 2(d) shows the evolution of the Fano parameter, $|q|$. Whereas in the region below 180 K, it increases slightly but continuously, at higher temperatures it promptly goes to lower values and the mode recovers a symmetric line shape. We believe that the observed behavior of the E_g^3 mode can be traced back to the short-range magnetic correlations, which, according to Ref. [1], persist up to 150 K, and the strong spin-phonon coupling in CrSiTe_3 . Similar behavior of the energy and line width, which differs from the conventional anharmonic, as well as the E_g mode Fano-type line shape, was recently reported in $\alpha\text{-RuCl}_3$ and was interpreted as a consequence of the spin-phonon interaction [32].

Unlike the E_g^3 mode, no pronounced asymmetry was observed for the A_g^3 mode. As can be seen from Figs. 3(b) and 3(c) both the energy and the line width of the A_g^3 mode showed

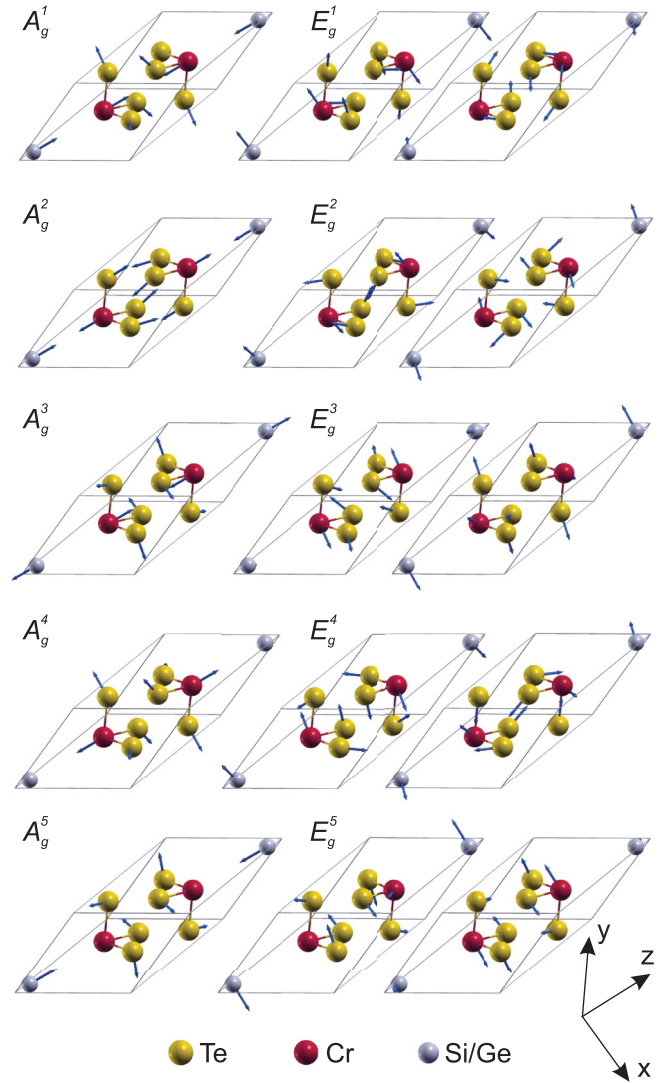


FIG. 4. Unit cell of a CrSiTe_3 single crystal (solid lines) with the displacement patterns of the A_g and E_g symmetry modes. Arrow lengths are proportional to the square root of the interatomic forces.

a similar change in tendency in the same temperature region as the E_g^3 mode, most likely due to the spin-phonon coupling.

IV. CONCLUSION

The lattice dynamics of CrSiTe_3 , a compound isostructural to CrGeTe_3 , is presented. An A_g and three E_g modes were observed and assigned. The experimental results are well supported by theoretical calculations. The temperature dependences of the energies and line widths of the A_g^3 and E_g^3 modes deviate from the conventional anharmonic model in the temperature range around 180 K. In addition, the E_g^3 mode shows clear Fano resonance at lower temperatures. This can be related to the previously reported short-range magnetic correlations at temperatures up to 150 K [1] and the strong spin-phonon coupling.

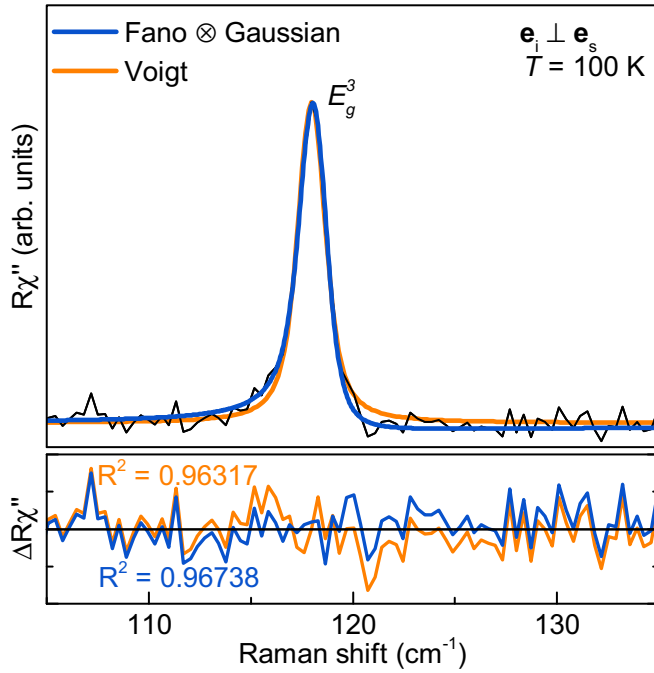


FIG. 5. Analysis of the E_g^3 asymmetry. Measured data are shown as the black line. The solid blue line represents the line shape obtained as a convolution of the Fano line shape and a Gaussian, whereas the orange line represents a Voigt line shape, both calculated to fit the experimental data. The Voigt profile deviates from the experimental data at the peak flanks.

ACKNOWLEDGMENTS

The work was supported by the Serbian Ministry of Education, Science and Technological Development under Projects III45018 and OI171005. DFT calculations were performed using computational resources at Johannes Kepler University, Linz, Austria. Work at Brookhaven was supported by the US Department of Energy, Office of Basic Energy Sciences as part of the Computation Material Science Program (material synthesis and characterization).

A.M. and N.L. conceived and performed the experiment, analyzed and discussed data, and wrote the paper; A.S. and J.P. calculated phonon energies, analyzed and discussed data, and wrote the paper; Y.L. and C.P. synthesized and characterized the samples; Z.V.P. analyzed and discussed data and wrote the paper. All authors commented on the manuscript.

APPENDIX

1. Eigenvectors of Raman-active modes

Figure 4 summarizes the A_g and E_g symmetry mode displacement patterns of a CrSiTe₃ single crystal ($R\bar{3}$ space group). Arrow lengths are proportional to the square root of the interatomic forces.

2. Asymmetry of the E_g^3 line

The peak at 118.2 cm^{-1} , which we assigned as the E_g^3 symmetry mode, at low temperatures shows a significant asymmetry towards lower energies. The possibility of additional

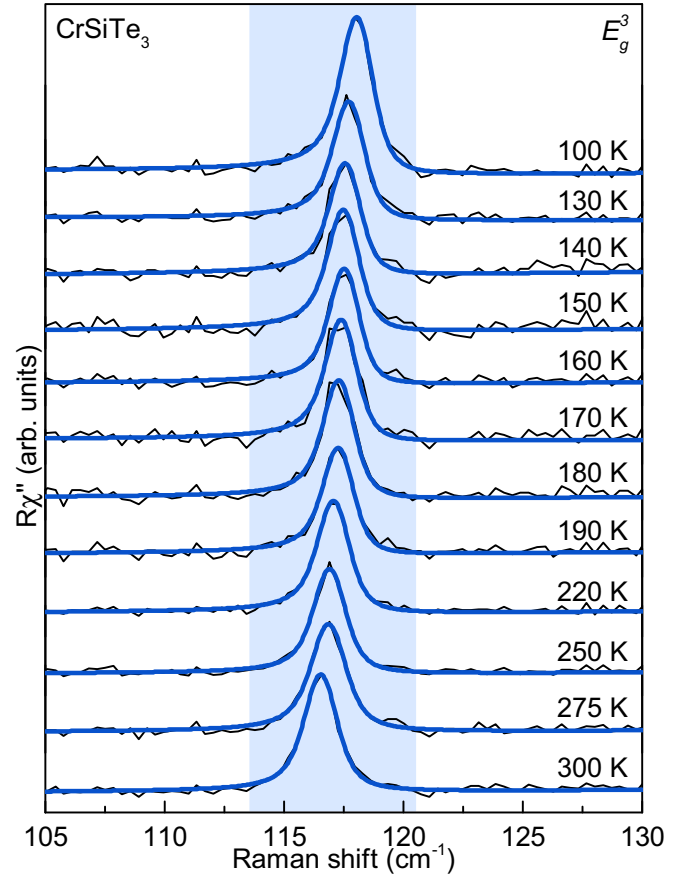


FIG. 6. The E_g^3 mode Raman spectra of CrSiTe₃ at all temperatures measured in the cross polarization configuration. Blue lines represent calculated spectra obtained as the convolution of the Fano line shape and Gaussian.

defect-induced features in Raman spectra can be excluded, since the modes are very narrow, suggesting high crystallinity of the sample. Also, the theoretical calculations do not predict additional Raman-active modes in this energy region. On the other hand, coupling of the phonon mode to a continuum may result in an asymmetric line shape described with the Fano function. Due to the finite resolution of the spectrometer it has to be convoluted with a Gaussian ($\Gamma_G = 1 \text{ cm}^{-1}$). In Fig. 5 we present a comparison of the line obtained as a convolution of the Fano line shape and a Gaussian (blue line) and a Voigt line shape (orange line) fitted to the experimental data. Whereas the Voigt line shape deviates at the peak flanks, excellent agreement has been achieved for convolution of the Fano line shape and a Gaussian.

3. E_g^3 mode temperature dependence

Figure 6 shows Raman spectra of CrSiTe₃ in the region of the E_g^3 mode in the cross polarization configuration at various temperatures. Solid blue lines represent the convolution of the Fano line shape and Gaussian fitted to the experimental data. The asymmetry is the most pronounced below 190 K. Above this temperature, the asymmetry is decreasing, and at high temperatures the peak recovers the fully symmetric line shape.

- [1] L. D. Casto, A. J. Clune, M. O. Yokosuk, J. L. Musfeldt, T. J. Williams, H. L. Zhuang, M.-W. Lin, K. Xiao, R. G. Hennig, B. C. Sales, J.-Q. Yan, and D. Mandrus, Strong spin-lattice coupling in CrSiTe₃, *APL Mater.* **3**, 041515 (2015).
- [2] X. Zhang, Y. Zhao, Q. Song, S. Jia, J. Shi, and W. Han, Magnetic anisotropy of the single-crystalline ferromagnetic insulator Cr₂Ge₂Te₆, *Jpn. J. Appl. Phys.* **55**, 033001 (2016).
- [3] T. Leineweber and H. Kronmüller, Micromagnetic examination of exchange coupled ferromagnetic nanolayers, *J. Magn. Magn. Mater.* **176**, 145 (1997).
- [4] G. Ouvrard, E. Sandre, and R. Brec, Synthesis and crystal structure of a new layered phase: The chromium hexatellurosilicate Cr₂Si₂Te₆, *J. Solid State Chem.* **73**, 27 (1988).
- [5] B. Siberchicot, S. Jobic, V. Carreaux, P. Gressier, and G. Ouvrard, Band structure calculations of ferromagnetic chromium tellurides CrSiTe₃ and CrGeTe₃, *J. Phys. Chem.* **100**, 5863 (1996).
- [6] V. Carreaux, F. Moussa, and M. Spiesser, 2D Ising-like ferromagnetic behaviour for the lamellar Cr₂Si₂Te₆ compound: A neutron scattering investigation, *Europhys. Lett.* **29**, 251 (1995).
- [7] N. Sivasdas, M. W. Daniels, R. H. Swendsen, S. Okamoto, and D. Xiao, Magnetic ground state of semiconducting transition-metal trichalcogenide monolayers, *Phys. Rev. B* **91**, 235425 (2015).
- [8] K. S. Novoselov, A. K. Geim, S. V. Morozov, D. Jiang, Y. Zhang, S. V. Dubonos, I. V. Grigorieva, and A. A. Firsov, Electric field effect in atomically thin carbon films, *Science* **306**, 666 (2004).
- [9] Q. H. Wang, K. Kalantar-Zadeh, A. Kis, J. N. Coleman, and M. S. Strano, Electronics and optoelectronics of two-dimensional transition metal dichalcogenides, *Nat. Nanotechnol.* **7**, 699 (2012), review Article.
- [10] C. Gong, L. Li, Z. Li, H. Ji, A. Stern, Y. Xia, T. Cao, W. Bao, C. Wang, Y. Wang, Z. Q. Qiu, R. J. Cava, S. G. Louie, J. Xia, and X. Zhang, Discovery of intrinsic ferromagnetism in two-dimensional van der Waals crystals, *Nature* **546**, 265 (2017).
- [11] B. Huang, G. Clark, E. Navarro-Moratalla, D. R. Klein, R. Cheng, K. L. Seyler, D. Zhong, E. Schmidgall, M. A. McGuire, D. H. Cobden, W. Yao, D. Xiao, P. Jarillo-Herrero, and X. Xu, Layer-dependent ferromagnetism in a van der Waals crystal down to the monolayer limit, *Nature* **546**, 270 (2017).
- [12] W. Xing, Y. Chen, P. M. Odenthal, X. Zhang, W. Yuan, T. Su, Q. Song, T. Wang, J. Zhong, S. Jia, X. C. Xie, Y. Li, and W. Han, Electric field effect in multilayer Cr₂Ge₂Te₆: A ferromagnetic 2D material, *2D Mater.* **4**, 024009 (2017).
- [13] T. J. Williams, A. A. Aczel, M. D. Lumsden, S. E. Nagler, M. B. Stone, J.-Q. Yan, and D. Mandrus, Magnetic correlations in the quasi-two-dimensional semiconducting ferromagnet CrSiTe₃, *Phys. Rev. B* **92**, 144404 (2015).
- [14] X. Li and J. Yang, CrXTe₃ (X = Si, Ge) nanosheets: Two dimensional intrinsic ferromagnetic semiconductors, *J. Mater. Chem. C* **2**, 7071 (2014).
- [15] M.-W. Lin, H. L. Zhuang, J. Yan, T. Z. Ward, A. A. Piretzky, C. M. Rouleau, Z. Gai, L. Liang, V. Meunier, B. G. Sumpter, P. Ganesh, P. R. C. Kent, D. B. Geohegan, D. G. Mandrus, and K. Xiao, Ultrathin nanosheets of CrSiTe₃: A semiconducting two-dimensional ferromagnetic material, *J. Mater. Chem. C* **4**, 315 (2016).
- [16] B. Liu, Y. Zou, S. Zhou, L. Zhang, Z. Wang, H. Li, Z. Qu, and Y. Zhang, Critical behavior of the van der Waals bonded high T_C ferromagnet Fe₃GeTe₂, *Sci. Rep.* **7**, 6184 (2017).
- [17] Y. Tian, M. J. Gray, H. Ji, R. J. Cava, and K. S. Burch, Magneto-elastic coupling in a potential ferromagnetic 2D atomic crystal, *2D Mater.* **3**, 025035 (2016).
- [18] Y. Sun, R. C. Xiao, G. T. Lin, R. R. Zhang, L. S. Ling, Z. W. Ma, X. Luo, W. J. Lu, Y. P. Sun, and Z. G. Sheng, Effects of hydrostatic pressure on spin-lattice coupling in two-dimensional ferromagnetic Cr₂Ge₂Te₆, *Appl. Phys. Lett.* **112**, 072409 (2018).
- [19] Y. Liu and C. Petrovic, Critical behavior of quasi-two-dimensional semiconducting ferromagnet Cr₂Ge₂Te₆, *Phys. Rev. B* **96**, 054406 (2017).
- [20] G. T. Lin, H. L. Zhuang, X. Luo, B. J. Liu, F. C. Chen, J. Yan, Y. Sun, J. Zhou, W. J. Lu, P. Tong, Z. G. Sheng, Z. Qu, W. H. Song, X. B. Zhu, and Y. P. Sun, Tricritical behavior of the two-dimensional intrinsically ferromagnetic semiconductor CrGeTe₃, *Phys. Rev. B* **95**, 245212 (2017).
- [21] P. Giannozzi, S. Baroni, N. Bonini, M. Calandra, R. Car, C. Cavazzoni, D. Ceresoli, G. L. Chiarotti, M. Cococcioni, I. Dabo, A. D. Corso, S. de Gironcoli, S. Fabris, G. Fratesi, R. Gebauer, U. Gerstmann, C. Gougousis, A. Kokalj, M. Lazzeri, L. Martin-Samos, N. Marzari, F. Mauri, R. Mazzarello, S. Paolini, A. Pasquarello, L. Paulatto, C. Sbraccia, S. Scandolo, G. Sclauzero, A. P. Seitsonen, A. Smogunov, P. Umari, and R. M. Wentzcovitch, Quantum espresso: A modular and open-source software project for quantum simulations of materials, *J. Phys.: Condens. Matter* **21**, 395502 (2009).
- [22] J. P. Perdew, K. Burke, and M. Ernzerhof, Generalized Gradient Approximation Made Simple, *Phys. Rev. Lett.* **77**, 3865 (1996).
- [23] P. E. Blöchl, Projector augmented-wave method, *Phys. Rev. B* **50**, 17953 (1994).
- [24] G. Kresse and D. Joubert, From ultrasoft pseudopotentials to the projector augmented-wave method, *Phys. Rev. B* **59**, 1758 (1999).
- [25] G. Stefan, Semiempirical GGA-type density functional constructed with a long-range dispersion correction, *J. Comput. Chem.* **27**, 1787 (2006).
- [26] R. E. Marsh, The crystal structure of Cr₂Si₂Te₆: Corrigendum, *J. Solid State Chem.* **77**, 190 (1988).
- [27] N. Lazarević, E. S. Bozin, M. Šćepanović, M. Opačić, Hechang Lei, C. Petrovic, and Z. V. Popović, Probing IrTe₂ crystal symmetry by polarized Raman scattering, *Phys. Rev. B* **89**, 224301 (2014).
- [28] M. Opačić, N. Lazarević, M. Šćepanović, H. Ryu, H. Lei, C. Petrovic, and Z. V. Popović, Evidence of superconductivity-induced phonon spectra renormalization in alkali-doped iron selenides, *J. Phys.: Condens. Matter* **27**, 485701 (2015).
- [29] A. Baum, A. Milosavljević, N. Lazarević, M. M. Radonjić, B. Nikolić, M. Mitschek, Z. Inanloo Maranloo, M. Šćepanović, M. Grujić-Brožćin, N. Stojilović, M. Opel, Aifeng Wang, C. Petrovic, Z. V. Popović, and R. Hackl, Phonon anomalies in FeS, *Phys. Rev. B* **97**, 054306 (2018).

- [30] N. Lazarević, M. Radonjić, M. Šćepanović, Hechang Lei, D. Tanasković, C. Petrovic, and Z. V. Popović, Lattice dynamics of KNi₂Se₂, [Phys. Rev. B **87**, 144305 \(2013\)](#).
- [31] N. Lazarević, Z. V. Popović, Rongwei Hu, and C. Petrovic, Evidence for electron-phonon interaction in Fe_{1-x}M_xSb₂ ($M = \text{Co and Cr}$; $0 \leq x \leq 0.5$) single crystals, [Phys. Rev. B **81**, 144302 \(2010\)](#).
- [32] L. J. Sandilands, Y. Tian, K. W. Plumb, Y.-J. Kim, and K. S. Burch, Scattering Continuum and Possible Fractionalized Excitations in α -RuCl₃, [Phys. Rev. Lett. **114**, 147201 \(2015\)](#).

Correction: Missing support information in the Acknowledgment section has been inserted.

Lattice dynamics and phase transition in CrI₃ single crystals

S. Djurdjic-Mijin,¹ A. Šolajić,¹ J. Pešić,¹ M. Šćepanović,¹ Y. Liu (刘育),² A. Baum,^{3,4} C. Petrovic,²
N. Lazarević,¹ and Z. V. Popović^{1,5}

¹Center for Solid State Physics and New Materials, Institute of Physics Belgrade, University of Belgrade,
Pregrevica 118, 11080 Belgrade, Serbia

²Condensed Matter Physics and Materials Science Department, Brookhaven National Laboratory, Upton, New York 11973-5000, USA

³Walther Meissner Institut, Bayerische Akademie der Wissenschaften, 85748 Garching, Germany

⁴Fakultät für Physik E23, Technische Universität München, 85748 Garching, Germany

⁵Serbian Academy of Sciences and Arts, Knez Mihailova 35, 11000 Belgrade, Serbia



(Received 9 July 2018; published 18 September 2018; corrected 28 March 2019)

The vibrational properties of CrI₃ single crystals were investigated using Raman spectroscopy and were analyzed with respect to the changes of the crystal structure. All but one mode are observed for both the low-temperature $R\bar{3}$ and the high-temperature $C2/m$ phase. For all observed modes the energies and symmetries are in good agreement with DFT calculations. The symmetry of a single layer was identified as $p\bar{3}1/m$. In contrast to previous studies we observe the transition from the $R\bar{3}$ to the $C2/m$ phase at 180 K and find no evidence for coexistence of both phases over a wide temperature range.

DOI: [10.1103/PhysRevB.98.104307](https://doi.org/10.1103/PhysRevB.98.104307)

I. INTRODUCTION

Two-dimensional layered materials have gained attention due to their unique properties, the potential for a wide spectrum of applications, and the opportunity for the development of functional van der Waals heterostructures. CrI₃ is a member of the chromium-trihalide family which are ferromagnetic semiconductors [1]. Recently they have received significant attention as candidates for the study of magnetic monolayers. The experimental realization of CrI₃ ferromagnetic monolayers [1] motivated further efforts towards their understanding. CrI₃ features electric field controlled magnetism [2] as well as a strong magnetic anisotropy [3,4]. With the main absorption peaks lying in the visible part of the spectrum, it is a great candidate for low-dimensional semiconductor spintronics [5]. In its ground state, CrI₃ is a ferromagnetic semiconductor with a Curie temperature of 61 K [1,6] and a band gap of 1.2 eV [6]. It was demonstrated that the magnetic properties of CrI₃ mono- and bilayers can be controlled by electrostatic doping [2]. Upon cooling, CrI₃ undergoes a phase transition around 220 K from the high-temperature monoclinic ($C2/m$) to the low-temperature rhombohedral ($R\bar{3}$) phase [3,7]. Although the structural phase transition is reported to be first order, it was suggested that the phases may coexist over a wide temperature range [3]. Raman spectroscopy can be of use here due to its capability to simultaneously probe both phases in a phase-separated system [8–10].

A recent theoretical study predicted the energies of all Raman active modes in the low-temperature and high-temperature structure of CrI₃ suggesting a near degeneracy between the A_g and B_g modes in the monoclinic ($C2/m$) structure. Their energies match the energies of E_g modes in the rhombohedral ($R\bar{3}$) structure [7].

In this article we present an experimental and theoretical Raman scattering study of CrI₃ lattice dynamics. In both phases all but one of the respective modes predicted by

symmetry were observed. The energies for all modes are in good agreement with the theoretical predictions for the assumed crystal symmetry. Our data suggest that the first-order transition occurs at $T_s \approx 180$ K without evidence for phase coexistence over a wide temperature range.

II. EXPERIMENT AND NUMERICAL METHOD

The preparation of the single crystal CrI₃ sample used in this study is described elsewhere [11]. The Raman scattering experiment was performed using a Tri Vista 557 spectrometer in backscattering micro-Raman configuration with a 1800/1800/2400 grooves/mm diffraction grating combination. The 532 nm line of a Coherent Verdi G solid state laser was used for excitation. The direction of the incident light coincides with the crystallographic c axis. The sample was oriented so that its principal axis of the $R\bar{3}$ phase coincides with the x axis of the laboratory system. A KONTI CryoVac continuous helium flow cryostat with a 0.5-mm-thick window was used for measurements at all temperatures under high vacuum (10^{-6} mbar). The sample was cleaved in air before being placed into the cryostat. The obtained Raman spectra were corrected by the Bose factor and analyzed quantitatively by fitting Voigt profiles to the data whereby the Gaussian width $\Gamma_{\text{Gauss}} = 1 \text{ cm}^{-1}$ reflects the resolution of the spectrometer.

The spin polarized density functional theory (DFT) calculations have been performed in the Quantum Espresso (QE) software package [12] using the Perdew-Burke-Ernzerhof (PBE) exchange-correlation functional [13] and PAW pseudopotentials [14,15]. The energy cutoffs for the wave functions and the charge density were set to be 85 and 425 Ry, respectively, after convergence tests. For k -point sampling, the Monkhorst-Pack scheme was used with a $8 \times 8 \times 8$ grid centered around the Γ point. Optimization of the atomic positions in the unit cell was performed until the interatomic forces

were smaller than 10^{-6} Ry/Å. To treat the van der Waals (vdW) interactions a Grimme-D2 correction [16] is used in order to include long-ranged forces between the layers, which are not properly captured within LDA or GGA functionals. This way, the parameters are obtained more accurately, especially the interlayer distances. Phonon frequencies were calculated at the Γ point using the linear response method implemented in QE. The phonon energies are compiled in Table III together with the experimental values. The eigenvectors of the Raman active modes for both the low- and high-temperature phase are depicted in Fig. 5 of the Appendix.

III. RESULTS AND DISCUSSION

CrI₃ adopts a rhombohedral $R\bar{3}$ (C_{3i}^2) crystal structure at low temperatures and a monoclinic $C2/m$ (C_{2h}^3) crystal structure at room temperature [3], as shown in Fig. 1. The main difference between the high- and low-temperature crystallographic space groups arises from different stacking sequences with the CrI₃ layers being almost identical. In the rhombohedral structure the Cr atoms in one layer are placed above the center of a hole in the Cr honeycomb net of the two adjacent layers. When crossing the structural phase transition at T_s to the monoclinic structure the layers are displaced along the a direction so that every fourth layer is at the same place as the first one. The interatomic distances, mainly the interlayer distance, and the vdW gap, are slightly changed by the structural transition. The crystallographic parameters for both phases are presented in Table I. The numerically obtained values are in good agreement with reported x-ray diffraction data [11].

The vibrational properties of layered materials are typically dominated by the properties of the single layers composing the crystal. The symmetry of a single layer can be described by one of the 80 diperiodic space groups (DG) obtained by

TABLE I. Calculated and experimental [11] parameters of the crystallographic unit cell for the low-temperature $R\bar{3}$ and high-temperature $C2/m$ phase of CrI₃.

T (K)	Space group $R\bar{3}$		Space group $C2/m$	
	Calc.	Expt. [11]	Calc.	Expt. [11]
a (Å)	6.87	6.85	6.866	6.6866
b (Å)	6.87	6.85	11.886	11.856
c (Å)	19.81	19.85	6.984	6.966
α (deg)	90	90	90	90
β (deg)	90	90	108.51	108.68
γ (deg)	120	120	90	90

lifting translational invariance in the direction perpendicular to the layer [17]. In the case of CrI₃, the symmetry analysis revealed that the single layer structure is fully captured by the $p\bar{3}1/m$ (D_{3d}^1) diperiodic space group DG71, rather than by $R\bar{3}2/m$ as proposed in Ref. [7].

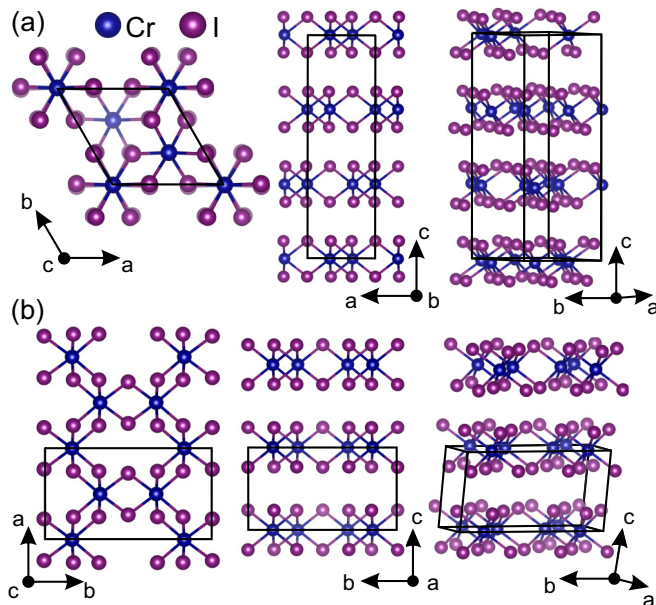


FIG. 1. Schematic representation of (a) the low-temperature $R\bar{3}$ and (b) the high-temperature $C2/m$ crystal structure of CrI₃. Black lines represent unit cells.

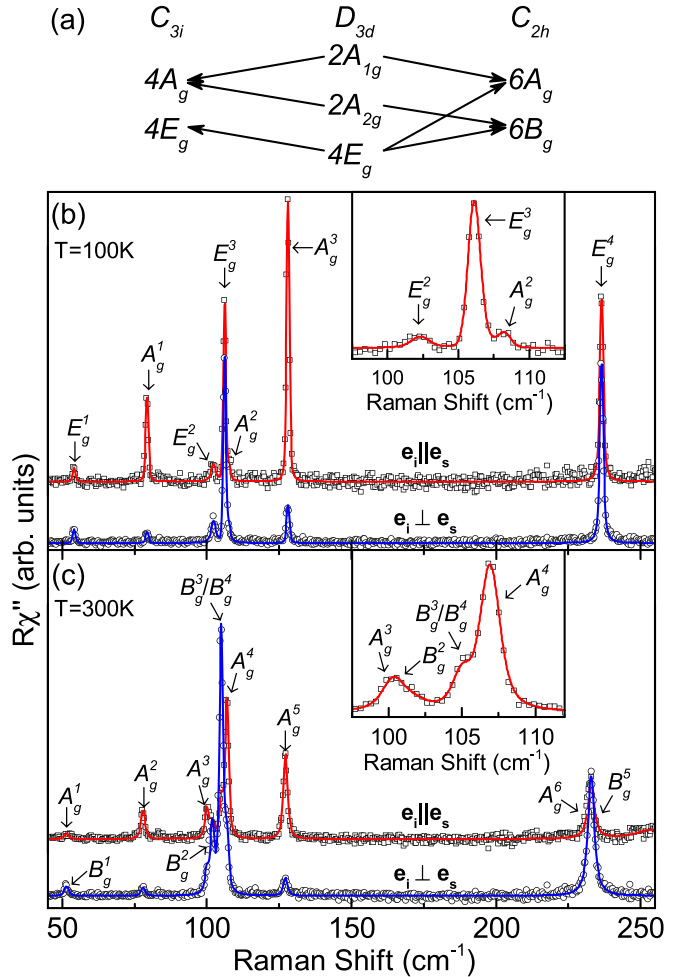


FIG. 2. (a) Compatibility relations for the CrI₃ layer and the crystal symmetries. Raman spectra of (b) the low-temperature $R\bar{3}$ and (c) the high-temperature $C2/m$ crystal structure measured in parallel (open squares) and crossed (open circles) polarization configurations at 100 and 300 K, respectively. Red and blue solid lines represent fits of Voigt profiles to the experimental data.

TABLE II. Wyckoff positions of the two types of atoms and their contributions to the Γ -point phonons for the $R\bar{3}$ and $C2/m$ as well as the $p\bar{3}1/m$ diperiodic space group. The second row shows the Raman tensors for the corresponding space groups.

Space group $R\bar{3}$		Diperiodic space group $p\bar{3}1/m$		Space group: $C2/m$	
Atoms	Irreducible representations	Atoms	Irreducible representations	Atoms	Irreducible representations
Cr (6c)	$A_g + A_u + E_g + E_u$	Cr (2c)	$A_{2g} + A_{2u} + E_g + E_u$	Cr (4g)	$A_g + A_u + 2B_g + 2B_u$
I (18f)	$3A_g + 3A_u + 3E_g + 3E_u$	I (6k)	$2A_{1g} + A_{1u} + A_{2g} + 2A_{2u} + 3E_g + 3E_u$	I (4i)	$2A_g + 2A_u + B_g + B_u$
				I (8j)	$3A_g + 3A_u + 3B_g + 3B_u$
$A_g = \begin{pmatrix} a & & \\ & a & \\ & & b \end{pmatrix}$		$A_{1g} = \begin{pmatrix} a & & \\ & a & \\ & & b \end{pmatrix}$		$A_g = \begin{pmatrix} a & d \\ & c & \\ d & & b \end{pmatrix}$	
${}^1E_g = \begin{pmatrix} c & d & e \\ d & -c & f \\ e & f & \end{pmatrix}$		${}^1E_g = \begin{pmatrix} c & & \\ -c & d & \\ d & & \end{pmatrix}$		$B_g = \begin{pmatrix} e & & \\ & e & \\ e & f & f \end{pmatrix}$	
${}^2E_g = \begin{pmatrix} d & -c & -f \\ -c & -d & e \\ -f & e & \end{pmatrix}$		${}^2E_g = \begin{pmatrix} -c & -c & -d \\ -c & & e \\ -d & e & \end{pmatrix}$			

According to the factor group analysis (FGA) for a single CrI_3 layer, six modes ($2A_{1g} + 4E_g$) are expected to be observed in the Raman scattering experiment (see Table II). By stacking the layers the symmetry is reduced and, depending on the stacking sequence, FGA yields a total of eight Raman active modes ($4A_g + 4E_g$) for the $R\bar{3}$ and 12 Raman active modes ($6A_g + 6B_g$) for the $C2/m$ crystal symmetry. The correlation between layer and crystal symmetries for both cases is shown in Fig. 2(a) [18,19].

Figure 2(b) shows the CrI_3 single crystal Raman spectra measured at 100 K in two scattering channels. According to the selection rules for the rhombohedral crystal structure (Table II) the A_g modes can be observed only in the parallel polarization configuration, whereas the E_g modes appear in both parallel and crossed polarization configurations. Based on the selection rules the peaks at about 78, 108, and 128 cm^{-1} were identified as A_g symmetry modes, whereas the peaks at about 54, 102, 106, and 235 cm^{-1} are assigned as E_g symmetry. The weak observation of the most pronounced A_g modes in crossed polarizations [Fig. 2(b)] is attributed to

the leakage due to a slight sample misalignment and/or the presence of defects in the crystal. The energies of all observed modes are compiled in Table III together with the energies predicted by our calculations and by Ref. [7], and are found to be in good agreement for the E_g modes. The discrepancy is slightly larger for the low energy A_g modes. Our calculations in general agree with those from Ref. [7]. The A_g^4 mode of the rhombohedral phase, predicted by calculation to appear at about 195 cm^{-1} , was not observed in the experiment, most likely due to its low intensity.

When the symmetry is lowered in the high-temperature monoclinic $C2/m$ phase [Fig. 2(c)] the E_g modes split into an A_g and a B_g mode each, whereas the rhombohedral A_g^2 and A_g^4 modes are predicted to switch to the monoclinic B_g symmetry. The correspondence of the phonon modes across the phase transition is indicated by the arrows in Table III. The selection rules for $C2/m$ (see Table II) predict that A_g and B_g modes can be observed in both parallel and crossed polarization configurations. Additionally, the sample forms three types of domains which are rotated with respect to each other. We

TABLE III. Phonon symmetries and phonon energies for the low-temperature $R\bar{3}$ and high-temperature $C2/m$ phase of CrI_3 . The experimental values were determined at 100 and 300 K, respectively. All calculations were performed at zero temperature. Arrows indicate the correspondence of the phonon modes across the phase transition.

Space group $R\bar{3}$				Space group $C2/m$			
Symm.	Expt. (cm^{-1})	Calc. (cm^{-1})	Calc. (cm^{-1}) [7]	Symm.	Expt. (cm^{-1})	Calc. (cm^{-1})	Calc. [7] (cm^{-1})
E_g^1	54.1	59.7	53	B_g^1	52.0	57.0	52
				A_g^1	53.6	59.8	51
A_g^1	73.33	89.6	79	A_g^2	78.6	88.4	79
E_g^2	102.3	99.8	98	A_g^3	101.8	101.9	99
				B_g^2	102.4	101.8	99
E_g^3	106.2	112.2	102	B_g^3	106.4 ^a	108.9	101
				A_g^4	108.3	109.3	102
A_g^2	108.3	98.8	88	B_g^4	106.4 ^a	97.8	86
A_g^3	128.1	131.1	125	A_g^5	128.2	131.7	125
A_g^4	—	195.2	195	B_g^5	—	198.8	195
E_g^4	236.6	234.4	225	A_g^6	234.6	220.1	224
				B_g^6	235.5	221.1	225

^aObserved as two peak structure.

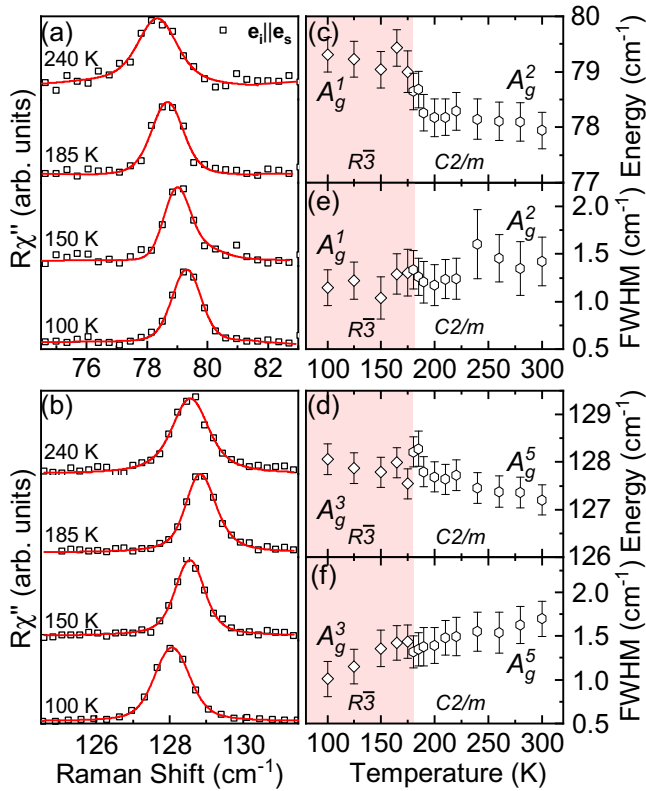


FIG. 3. Temperature dependence of the A_g^1 and A_g^3 phonon modes of the rhombohedral structure and the corresponding A_g^2 and A_g^5 modes of the monoclinic structure, respectively. (a) and (b) Raman spectra at temperatures as indicated. The spectra are shifted for clarity. Solid red lines represent Voigt profiles fitted to the data. (c) and (d) and (e) and (f) Temperature dependence of the phonon energies and linewidths, respectively. Both modes show an abrupt change in energy at the phase transition at 180 K.

therefore identify the phonons in the $C2/m$ phase in relation to the calculations and find again good agreement of the energies. The B_g^3 and B_g^4 modes overlap and therefore cannot be resolved separately. As can be seen from the temperature dependence shown below [Fig. 4(b)] the peak at 106 cm^{-1} broadens and gains spectral weight in the monoclinic phase in line with the expectation that two modes overlap. The missing rhombohedral A_g^4 mode corresponds to the monoclinic B_g^5 mode, which is likewise absent in the spectra.

The temperature dependence of the observed phonons is shown in Figs. 3 and 4. In the low-temperature rhombohedral phase all four E_g modes as well as A_g^1 and A_g^2 soften upon warming, whereas A_g^3 hardens up to $T \approx 180\text{ K}$ before softening again. Crossing the first-order phase transition from $R\bar{3}$ to $C2/m$ crystal symmetry is reflected in the spectra as a symmetry change and/or renormalization for the non-degenerate modes and lifting of the degeneracy of the E_g modes as shown in Table II. In our samples, this transition is observed at $T_s \approx 180\text{ K}$. The splitting of the E_g phonons into A_g and B_g modes at the phase transition is sharp (Fig. 4). The rhombohedral A_g^1 and A_g^3 phonons show a jump in energy and a small discontinuity in the linewidth at T_s (Fig. 3). Our spectra were taken during warming in multiple runs after

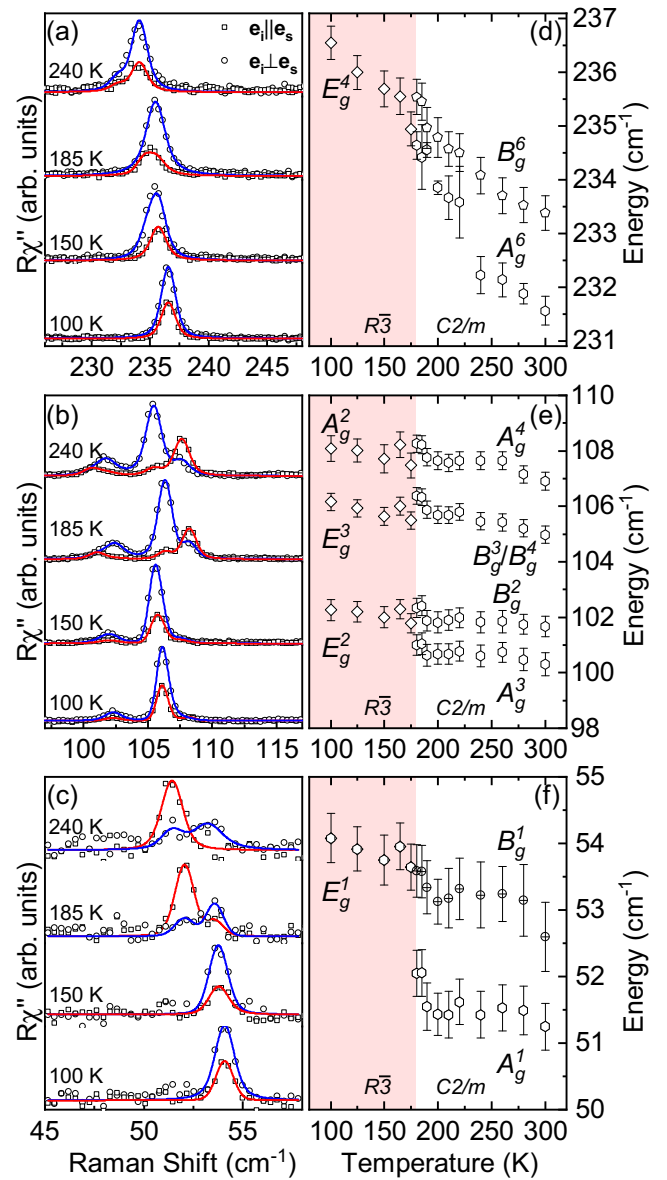


FIG. 4. Temperature dependence of the rhombohedral A_g^4 and E_g modes. (a)–(c) Raman spectra in parallel (open squares) and crossed (open circles) light polarizations at temperatures as indicated. The spectra are shifted for clarity. Blue and red solid lines are fits of Voigt profiles to the data. Two spectra were analyzed simultaneously in two scattering channels with the integrated intensity as the only independent parameter. (d)–(f) Phonon energies obtained from the Voigt profiles. Each E_g mode splits into an A_g and a B_g mode above 180 K.

cooling to 100 K each time. We found that the temperature dependence for the phonon modes obtained this way was smooth in each phase. McGuire *et al.* [3,20] reported T_s in the range of 220 K, a coexistence of both phases and a large thermal hysteresis. However, they also noted that the first and second warming cycle showed identical behavior and only found a shift of the transition temperature to higher values for cooling cycles. We therefore consider the difference between the reported transition around 220 K and our $T_s \approx 180\text{ K}$ significant. To some extent this difference may be attributed

to local heating by the laser. More importantly, we find no signs of phase coexistence in the observed temperature range. The spectra for the low-temperature and high-temperature phases are distinctly different (Fig. 2) and the E_g modes exhibit a clearly resolved splitting which occurs abruptly at T_S . We performed measurements in small temperature steps (see Figs. 3 and 4). This limits the maximum temperature interval where the phase coexistence could occur in our samples to approximately 5 K, much less than the roughly 30 to 80 K reported earlier [3,20]. We cannot exclude the possibility that a small fraction of the low-temperature phase could still

coexist with the high-temperature phase over a wider temperature range, whereby weak peaks corresponding to the remains of the low-temperature $R\bar{3}$ phase might be hidden under the strong peaks of the $C2/m$ phase.

IV. CONCLUSION

We studied the lattice dynamics in single crystalline CrI_3 using Raman spectroscopy supported by numerical calculations. For both the low-temperature $R\bar{3}$ and the high-temperature $C2/m$ phase, all except one of the predicted

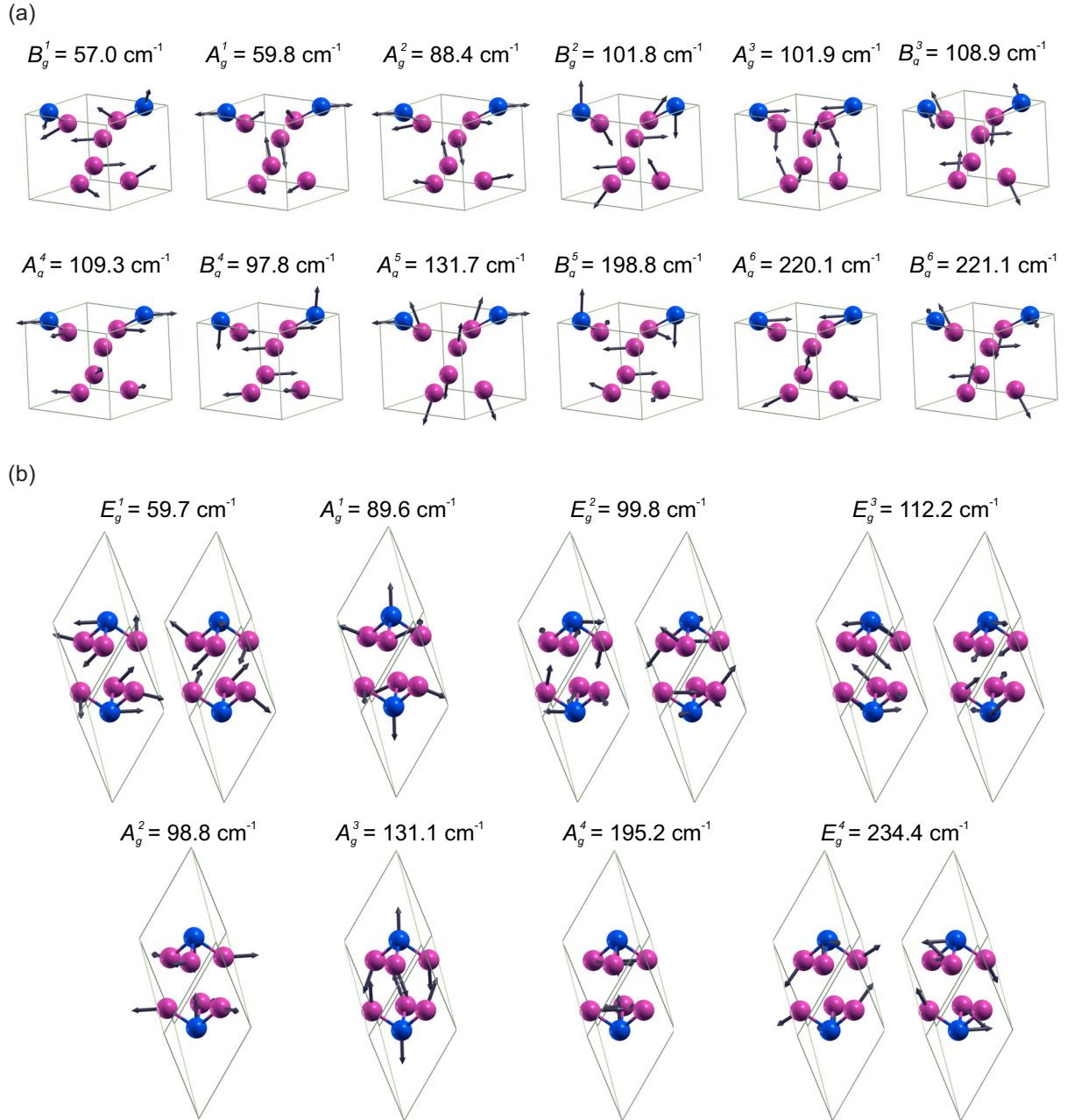


FIG. 5. Raman-active phonons in CrI_3 for (a) the monoclinic phase hosting A_g and B_g modes and for (b) the rhombohedral phase hosting A_g and E_g modes. Blue and violet spheres denote Cr and I atoms, respectively. Solid lines represent primitive unit cells. Arrow lengths are proportional to the square root of the interatomic forces. The given energies are calculated for zero temperature.

phonon modes were identified and the calculated and experimental phonon energies were found to be in good agreement. We determined that the symmetry of the single CrI_3 layers is $p\bar{3}1/m$. Abrupt changes to the spectra were found at the first-order phase transition which was located at $T_s \approx 180$ K, lower than in previous studies. In contrast to the prior reports we found no sign of phase coexistence over temperature ranges exceeding 5 K.

ACKNOWLEDGMENTS

The work was supported by the Serbian Ministry of Education, Science and Technological Development under Projects No. III45018 and No. OI171005. DFT calculations were performed using computational resources at Johannes Kepler University, Linz, Austria. Work at Brookhaven was supported by the US Department of Energy, Office of Basic Energy Sciences as part of the Computation Material Science Program (material synthesis and characterization).

S.Dj.M. and N.L. conceived the experiment, performed the experiment, analyzed and discussed the data, and wrote the paper. A.Š. and J.P. calculated the phonon energies, analyzed and discussed the data, and wrote the paper. Y.L. and C.P. synthesized and characterized the samples. M.Š. performed the experiment and analyzed and discussed the data. A.B. and Z.V.P. analyzed and discussed the data and wrote the paper. All authors commented on the manuscript.

APPENDIX: EIGENVECTORS

In addition to the phonon energies we also calculated the phonon eigenvectors which are shown in Fig. 5(a) for the high-temperature monoclinic phase and in Fig. 5(b) for the low-temperature rhombohedral phase. The energies, as given, are calculated for zero temperature. The relative displacement of the atoms is denoted by the length of the arrows.

-
- [1] E. Navarro-Moratalla, B. Huang, G. Clark *et al.*, Layer-dependent ferromagnetism in a van der Waals crystal down to the monolayer limit, *Nature (London)* **546**, 270 (2017).
 - [2] S. Jiang, L. Li, Z. Wang, K. F. Mak, and J. Shan, Controlling magnetism in 2D CrI_3 by electrostatic doping, *Nat. Nanotechnol.* **13**, 549 (2018).
 - [3] M. A. McGuire, H. Dixit, V. R. Cooper, and B. C. Sales, Coupling of crystal structure and magnetism in the layered, ferromagnetic insulator CrI_3 , *Chem. Mater.* **27**, 612 (2015).
 - [4] J. L. Ladno and J. Fernández-Rossier, On the origin of magnetic anisotropy in two dimensional CrI_3 , *2D Mater.* **4**, 035002 (2017).
 - [5] W.-B. Zhang, Q. Qu, P. Zhu, and C.-H. Lam, Robust intrinsic ferromagnetism and half semiconductivity in stable two-dimensional single-layer chromium trihalides, *J. Mater. Chem. C* **3**, 12457 (2015).
 - [6] J. F. Dillon, Jr. and C. E. Olson, Magnetization, resonance, and optical properties of the ferromagnet CrI_3 , *J. Appl. Phys.* **36**, 1259 (1965).
 - [7] D. T. Larson and E. Kaxiras, Raman Spectrum of CrI_3 : An *ab initio* study, *Phys. Rev. B* **98**, 085406 (2018).
 - [8] N. Lazarević, M. Abeykoon, P. W. Stephens, H. Lei, E. S. Bozin, C. Petrovic, and Z. V. Popović, Vacancy-induced nanoscale phase separation in $\text{K}_x\text{Fe}_{2-y}\text{Se}_2$ single crystals evidenced by Raman scattering and powder x-ray diffraction, *Phys. Rev. B* **86**, 054503 (2012).
 - [9] H. Ryu, M. Abeykoon, K. Wang, H. Lei, N. Lazarevic, J. B. Warren, E. S. Bozin, Z. V. Popovic, and C. Petrovic, Insulating and metallic spin glass in Ni-doped $\text{K}_x\text{Fe}_{2-y}\text{Se}_2$ single crystals, *Phys. Rev. B* **91**, 184503 (2015).
 - [10] H. Ryu, K. Wang, M. Opacic, N. Lazarevic, J. B. Warren, Z. V. Popovic, E. S. Bozin, and C. Petrovic, Sustained phase separation and spin glass in Co-doped $\text{K}_x\text{Fe}_{2-y}\text{Se}_2$ single crystals, *Phys. Rev. B* **92**, 174522 (2015).
 - [11] Y. Liu and C. Petrovic, Three-dimensional magnetic critical behavior in CrI_3 , *Phys. Rev. B* **97**, 014420 (2018).
 - [12] P. Giannozzi, S. Baroni, N. Bonini, M. Calandra, R. Car, C. Cavazzoni, D. Ceresoli, G. L. Chiarotti, M. Cococcioni, I. Dabo, A. D. Corso, S. de Gironcoli, S. Fabris, G. Fratesi, R. Gebauer, U. Gerstmann, C. Gougousis, A. Kokalj, M. Lazzeri, L. Martin-Samos, N. Marzari, F. Mauri, R. Mazzarello, S. Paolini, A. Pasquarello, L. Paulatto, C. Sbraccia, S. Scandolo, G. Sclauzero, A. P. Seitsonen, A. Smogunov, P. Umari, and R. M. Wentzcovitch, Quantum espresso: A modular and open-source software project for quantum simulations of materials, *J. Phys. Condens. Matter* **21**, 395502 (2009).
 - [13] J. P. Perdew, K. Burke, and M. Ernzerhof, Generalized Gradient Approximation Made Simple, *Phys. Rev. Lett.* **77**, 3865 (1996).
 - [14] P. E. Blöchl, Projector augmented-wave method, *Phys. Rev. B* **50**, 17953 (1994).
 - [15] G. Kresse and D. Joubert, From ultrasoft pseudopotentials to the projector augmented-wave method, *Phys. Rev. B* **59**, 1758 (1999).
 - [16] S. Grimme, Semiempirical GGA-type density functional constructed with a long-range dispersion correction, *J. Comput. Chem.* **27**, 1787 (2006).
 - [17] E. A. Wood, The 80 diperiodic groups in three dimensions, *Bell Syst. Tech. J.* **43**, 541 (1964).
 - [18] W. G. Fateley, N. T. McDevitt, and F. F. Bentley, Infrared and raman selection rules for lattice vibrations: The correlation method, *Appl. Spectrosc.* **25**, 155 (1971).
 - [19] N. Lazarević, Z. V. Popović, R. Hu, and C. Petrovic, Evidence of coupling between phonons and charge-density waves in ErTe_3 , *Phys. Rev. B* **83**, 024302 (2011).
 - [20] M. A. McGuire, G. Clark, S. KC, W. M. Chance, G. E. Jellison, V. R. Cooper, X. Xu, and B. C. Sales, Magnetic behavior and spin-lattice coupling in cleavable van der Waals layered CrCl_3 crystals, *Phys. Rev. Mater.* **1**, 014001 (2017).
- Correction:* Missing support information in the Acknowledgment section has been inserted.



Ab-initio calculations of electronic and vibrational properties of Sr and Yb intercalated graphene

Andrijana Šolajić¹ · Jelena Pešić¹ · Radoš Gajić¹

Received: 14 October 2017 / Accepted: 14 June 2018 / Published online: 20 June 2018
© Springer Science+Business Media, LLC, part of Springer Nature 2018

Abstract

Since the 1960s, Graphite intercalation compounds (GIC) have been extensively studied, showing many new properties and exotic physics. This inspired many to investigate a single or few-layer intercalated graphene. Intercalated graphene has many extraordinary properties and it is different compared to pristine graphene or bulk GICs, with great spectra of characteristics induced by various intercalants. This method opens new possibilities for research and applications in electronics and photonics. Here we present the results of a DFT study on electronic and vibrational properties of the graphene doped with Sr and Yb adatoms, taking into account that only their corresponding bulk compounds have been investigated so far. The calculations were performed in Quantum Espresso software package.

Keywords Graphene · DFT · Electronic properties · 2D materials

1 Introduction

Since the experimental discovery in Novoselov et al. (2004), graphene has been attracting enormous attention. The relativistic behaviour of the low-energy excitations (the so-called *Dirac fermions*) leads to many interesting effects and the linear electronic dispersion of graphene in the vicinity of the K-point mimics the physics of the massless fermions in quantum electrodynamics, at speed 300 times smaller than the speed of light. Therefore, many unusual properties can be observed in graphene, such are the Klein paradox (Katsnelson et al. 2006) or the anomalous integer quantum Hall effect (Gusynin and Sharapov 2005; Neto et al. 2006) which can be observed at room temperatures (Novoselov et al. 2007).

This article is part of the Topical Collection on Focus on Optics and Bio-photonics, Photonica 2017.

Guest Edited by Jelena Radovanovic, Aleksandar Krmpot, Marina Lekic, Trevor Benson, Mauro Pereira, Marian Marciniak.

✉ Andrijana Šolajić
solajic@ipb.ac.rs

¹ Laboratory for Graphene, Other 2D Materials and Ordered Nanostructures, Center for Solid State Physics and New Materials, Institute of Physics Belgrade, University of Belgrade, Pregrevica 118, Belgrade 11080, Serbia

Graphene has excellent thermal conductivity, high electron mobility (Bolotin et al. 2008) and transparency, and at the same time it is one of the strongest materials known (Lee et al. 2008), about 200 times stronger than structural steel, yet very flexible and stretchable. With all its unique properties, graphene has various potential applications in almost all research fields, especially in electronics and optoelectronics (Ferrari 2015; Blake et al. 2008; Todorović et al. 2015). With high electrical and optical conductivity, it is promising candidate for applications in energy storage (Bonaccorso et al. 2015), detectors (Sassi et al. 2017; Liu et al. 2014), or even for the flexible touch screen technology (Ahn and Hong 2014; Bae et al. 2010). Ultra-thin graphitic films are also well researched for applications in photonics with high transparency and electrical conductivity (Matković et al. 2016).

Already extraordinary characteristics of graphene can be tailored and enhanced in many ways—by various types of disorders, controlling the type of edges (Peres et al. 2006; Wakabayashi et al. 1996, 2009), number of layers, by doping, applying the strain (Levy et al. 2010; Choi et al. 2010; Settnes et al. 2016; Masir et al. 2013), etc. Among them, doping graphene is an excellent way to make graphene suitable for various applications (Sharma and Ahn 2013; Wang et al. 2010; Qu et al. 2010; Jeong et al. 2011; Cui et al. 2011). Especially interesting is intercalation of various species in a few layer graphene (or doping a single layer graphene with adatoms), in a similar manner to the graphite intercalation compounds (GIC). This provides very high level of doping and leads to many interesting effects that are not present in pristine graphene, offering a new way to design various materials with magnetic, highly conductive or superconducting properties. Doping via adsorption is also very convenient, as the graphene can host various adatoms or small molecules while preserving its own structure, and at the same time drastically change its electronic properties. By covering the graphene sheet with the layer of adatoms, significant structural changes are avoided, as the dopant atoms are not fitted in the graphene lattice instead of the carbon atoms. However, adsorbed atoms can strongly affect the electronic properties of graphene, dominantly through the p_z orbitals. Therefore, it is an excellent tool for tuning the properties of graphene in a wide range and obtain new effects. GIC have been extensively researched since the 1960s (Rüdorff 1959; Enoki et al. 2003; Dresselhaus and Dresselhaus 2002), but the interest for them has significantly raised with discovery of the superconductivity in some of the alkali or alkaline earth metal intercalated graphite structures, among which are CaC_6 and YbC_6 (Weller et al. 2005) with relatively high critical temperatures of $T_c = 11.5$ K and $T_c = 6.5$ K. As research of 2D materials has raised in the last decade, the superconductivity in GIC imposed a question of investigating the monolayer graphene doped with alkali and alkaline earth metal adatoms, searching for the atomically thin superconductors. The electrical characteristics of the doped graphene depend strongly on the species of the used adatom. Reports on related structures suggest the occurrence of superconductivity in some of them, usually with alkali or alkaline earth metals doping, similar to the GICs. The explanation for the emergence of the superconductivity in the alkali doped graphene lies in the electron-phonon coupling that arises from the new intercalant-derived band and the graphene π -bands at the Fermi level. Among first researched doped graphene structures was Li decorated graphene (Profeta et al. 2012; Pešić et al. 2015), which is superconducting with the critical temperature of $T = 5.9$ K. It can also be enhanced by applying the strain (Pešić et al. 2014). The experimental evidence of superconductivity in the Li doped graphene (Ludbrook 2015) inspired many to search for other 2D superconducting structures (Calandra et al. 2012; Penev et al. 2016; Shimada et al. 2017; Saito et al. 2016). Graphene doped with the Ca atoms is also reported to be superconducting as the doped monolayer (Profeta et al. 2012) and bilayer intercalated graphene (Mazin and Balatsky 2010; Margine et al. 2016), there are also reports for a

few-layer potassium doped graphene (Xue et al. 2012). Among other similar structures, the heavily n-doped graphene was also predicted to be superconducting (Margine and Giustino 2014), the combination of biaxial strain with charge doping, which leads to the superconductor with T_c estimated to be up to 30 K (Si et al. 2013), or the hole-doped graphene which was predicted to be a high T_c superconductor, with a critical temperature in range 60–80 K (Durajski 2015). However, many possible structures based on doped graphene with potential superconducting properties are not considered yet.

In this paper we studied the electronic and vibrational properties of Sr and Yb doped graphene using the density functional theory approach. We were motivated by the fact that both structures are known as superconductors in their corresponding bulk compounds, YbC₆ with critical temperature of $T_c = 6.5$ K (Weller et al. 2005) and SrC₆ with up to $T_c = 3.03$ K (Calandra and Mauri 2006). We are first to report the results for a monolayer graphene doped with those adatoms.

2 Computational details

All calculations were performed using the Quantum Espresso software package (Giannozzi et al. 2009), based on the plane waves and pseudopotentials. We used norm-conserving pseudopotentials (Perdew and Zunger 1981) and LDA exchange-correlation functional. The plane wave energy cutoff is 120 Ry for SrC₆-mono and 160 Ry for YbC₆-mono. The unit cell for both structures is modelled as $\sqrt{3} \times \sqrt{3}R30^\circ$ supercell of the graphene unit cell, with adatoms positioned in the H-site. This is the favorable adsorption site for both adatoms, according to the DFT study (Nakada and Ishii 2011). The value of the hexagonal cell parameter a is 4.26 Å taken theoretically, as there are no experimental realization of those structures. The top and side view of the structures are shown in Fig. 1. In order to avoid interactions between layers, the hexagonal cell parameter c of the unit cell was chosen to be sufficiently large, $c = 11.4$ Å for SrC₆-mono and 11.3 Å for YbC₆-mono. Prior to any calculations, the ionic positions in systems are fully relaxed to their minimum energy configuration, using the Broyden-Fletcher-Goldfarb-Shanno (BFGS) algorithm. Obtained vertical distance between graphene layer and the adsorbed atom is $h = 2.22$ Å for SrC₆-mono and $h = 2.25$ Å for YbC₆-mono. Phonon properties are obtained with the Density

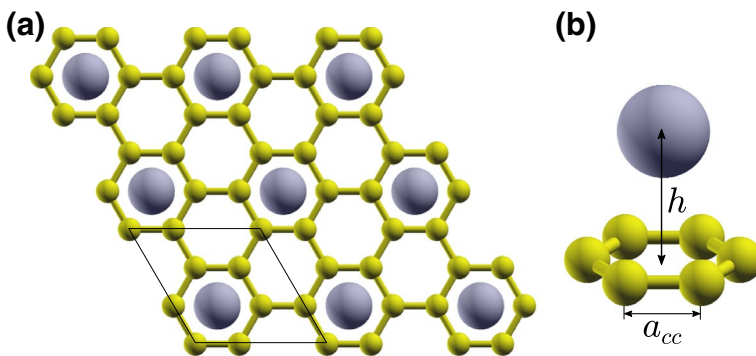


Fig. 1 **a** Top view of the graphene structure with the adatoms adsorbed in the H-site. Unit cell is marked with the black line, **b** side view of the one hexagon with the adatom above

Functional Perturbation Theory (DFPT) implemented in the PHonon part of the Quantum Espresso software.

3 Results and discussion

As we said in Sect. 2, the unit cell for our H-site doped structures is enlarged compared to the pristine graphene. Due to the increase in the size of the primitive cell in direct space, basis vector lengths in reciprocal space are reduced. As a consequence, the K-point of the Brillouin zone of graphene is folded to the Γ point of the Brillouin zone of H-site doped graphene. Brillouin zones of the graphene unit cell and the H-site doped graphene are shown in Fig. 2.

3.1 Electronic properties

Electronic dispersions along Γ -M-K- Γ high symmetry points for SrC_6 -mono and YbC_6 -mono are shown in Fig. 3. Fermi level is set to zero in all figures. Folding the π and π^* bands of graphene from K-point to Γ -point, the inner and outer carbon π and π^* bands are obtained, crossing at the Γ point. For both structures, lower bands from the σ bonds in the valence band are almost unaffected, as expected, and they are not shown in figures. The Fermi level is shifted up in both structures. By deposition of adatoms on top of graphene, new interlayer band derived from the Yb or Sr adatoms is formed around the Fermi level, showing a nearly free-electron-like dispersion. They are placed at 2.2 and 1.5 eV below the Fermi level in the YbC_6 -mono and SrC_6 -mono, respectively, being partially occupied. The density of states on Fermi level is also raised. The carbon π bands are not affected by the presence of the adatoms. Previously unoccupied π^* bands now intersect the new up-shifted Fermi level and are strongly hybridized with the new band derived from the adsorbed atoms. In YbC_6 -mono, 4f orbitals coming from the Yb atoms form a set of flat non-dispersive bands, similar to the bulk YbC_6 (Csányi et al. 2005). Those flat bands are characteristic for most lanthanides. They are localized at 0.7 eV below the Fermi level with the corresponding peak clearly observed in the density of states. As reported for the bulk YbC_6 , calculations with the Hubbard+U corrections do not give significant changes and result only in slightly shifting down those bands, so the same is expected for the monolayer. The Dirac points from graphene are folded to the Γ point in the H-site doped graphene, and

Fig. 2 Brillouin zones of graphene (black) and the H-site doped graphene (red). (Color figure online)

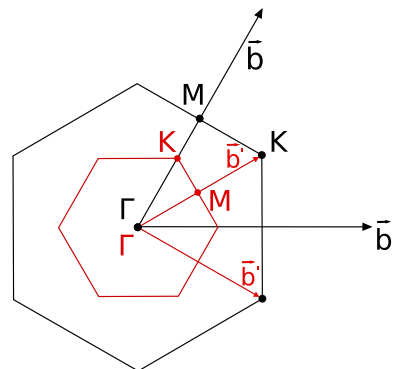
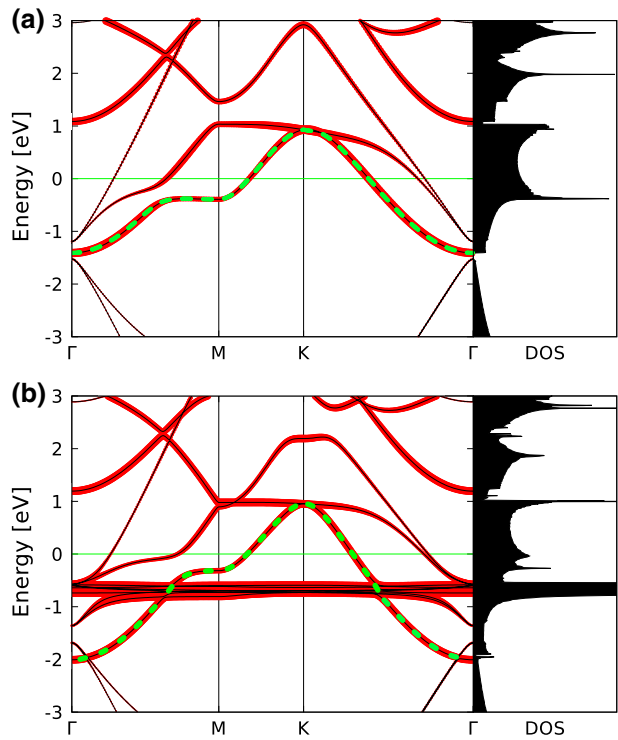


Fig. 3 Electronic dispersions of **a** SrC_6 -mono and **b** YbC_6 -mono. Thickness of the red lines is proportional to the Sr/Yb character and the interlayer band is marked in green dotted line. (Color figure online)



they are now below the Fermi level. Due to the adatom presence, the symmetry is broken and a gap is opened. In the SrC_6 , interlayer band is placed between the π and π^* and a very small gap can be observed in the density of states, while in the YbC_6 -mono, the new interlayer band intersect the π band and the gap is closed.

3.2 Phonon properties

The symmetry group of graphene with adatoms adsorbed in the H-site is $Dg77 = T' C_{6v}$, which is a subgroup of the diperiodic group of graphene, $Dg80 = TD_{6h}$ (Damljanović et al. 2014). In order to connect the phonon modes of the H-site doped graphene with the corresponding phonon modes of graphene, the corresponding irreducible representation of group $Dg77$ of graphene to its subgroup $Dg80$ (Damljanović et al. 2014). The modes from the Γ point, ΓE_{2g} and ΓB_{1g} correspond to ΓE_2 and ΓB_1 . For the modes of graphene in the K point, KA'_1 corresponds to the modes A_1 and B_2 , KA'_2 to A_2 and B_1 , KE' and KE'' to E_1 and E_2 (Altmann and Herzig 1994; Damljanović and Gajić 2012). The modes A_1 and E_1 are both infrared and Raman active, while E_2 modes are only Raman active. The symmetry classification of optical modes and Raman tensors for H-site doped graphene are given in Table 1. The displacement patterns of the SrC_6 -mono and YbC_6 -mono, in the Γ point are shown in Fig. 4. Those modes have displacement patterns similar to those of graphene phonons at Γ and K points, which happens due to the Brillouin zone folding. As the K point of graphene is folded to the Γ point of the new Brillouin zone in the H-site doped graphene, the phonon modes in graphene at the Γ and K points correspond to the Γ modes in the H-site doped

Table 1 Raman tensors and symmetry classification of optical modes

Raman tensors			
Graphene	A_{1g}	E_{1g}	E_{2g}
$Dg80 = TD_{6h}$	$\begin{pmatrix} a & 0 & 0 \\ 0 & a & 0 \\ 0 & 0 & b \end{pmatrix}$	$\begin{pmatrix} 0 & 0 & 0 \\ 0 & 0 & c \\ 0 & c & 0 \end{pmatrix}$	$\begin{pmatrix} d & 0 & 0 \\ 0 & -d & 0 \\ 0 & 0 & 0 \end{pmatrix}$
$O_z \parallel C_6$		$\begin{pmatrix} 0 & 0 & -c \\ 0 & 0 & 0 \\ c & 0 & 0 \end{pmatrix}$	$\begin{pmatrix} 0 & -d & 0 \\ -d & 0 & 0 \\ 0 & 0 & 0 \end{pmatrix}$
$O_x \parallel C_2$			
$A\alpha$	A_1	E_1	E_2
$Dg77 = TC_{6v}$	$\begin{pmatrix} a & 0 & 0 \\ 0 & a & 0 \\ 0 & 0 & b \end{pmatrix}$	$\begin{pmatrix} 0 & 0 & c \\ 0 & 0 & 0 \\ c & 0 & 0 \end{pmatrix}$	$\begin{pmatrix} d & 0 & 0 \\ 0 & -d & 0 \\ 0 & 0 & 0 \end{pmatrix}$
$O_z \parallel C_6$		$\begin{pmatrix} 0 & 0 & c \\ 0 & 0 & c \\ 0 & c & 0 \end{pmatrix}$	$\begin{pmatrix} 0 & -d & 0 \\ -d & 0 & 0 \\ 0 & 0 & 0 \end{pmatrix}$
$O_x \parallel \sigma_v$			
Optical modes			
$A\alpha$	$\Gamma_{opt} = 2A_1 + A_2 + 2B_1 + B_2 + 3E_1 + 3E_2$		

structures. This is valid for all H-site doped graphene structures as the unit cell is the type. As the Kohn anomaly is present in graphene at Γ and K points in E_{2g} and KA'_1 modes, we expect it to be present in the H-site doped graphene structures for the modes related to these two. Modes with Kohn anomaly can not be calculated precisely using the density functional theory as the DFT is based on the adiabatic Born-Oppenheimer approximation which is in this case broken. Comparing the calculated phonon modes for graphene at K and Γ point, with the corresponding phonon modes at the Γ point of the SrC_6 and YbC_6 monolayers, we can observe small differences in the corresponding frequencies. Some of these are lower than in pristine graphene and some frequencies are split. For example, frequencies of E_2 mode in Sr and Yb doped graphene are 1470 cm^{-1} and 1488 cm^{-1} , respectively, while the frequency of E_{2g} in pristine graphene is 1550 cm^{-1} ; Frequency of E' mode in graphene is 1200 cm^{-1} , and corresponding modes in doped graphene are E_2 at 1180 cm^{-1} and E_1 at 1200 cm^{-1} ; E'' mode in graphene is at 580 cm^{-1} , and corresponding modes in doped graphene are E_2 at 495 cm^{-1} and E_1 at 510 cm^{-1} for SrC_6 -mono and E_2 at 477 cm^{-1} and E_1 at 500 cm^{-1} for YbC_6 -mono. This can be ascribed to the adatoms impact, and in general, it depends on the type of the adatom.

4 Conclusion

Using the density functional theory approach, we calculated the electronic and phonon properties of the Sr and Yb doped graphene, in a similar manner to the GICs. Their corresponding bulk compounds have been studied so far and we are first to investigate the monolayer graphene doped with those adatoms. The electronic and phonon properties are of essential interest for electron-phonon coupling as well as the guidelines for experimental research. From the electronic band structure calculations, we can observe a new adatom-derived interlayer band crossing the Fermi level in both structures, which hybridize strongly with the carbon p_z orbitals. Density of states on the Fermi level is also raised. Those results can be indicating a possible superconductivity and can be inspiring for further research of those structures. Displacement patterns calculated in the Γ point are similar to those in the K and Γ point of the pristine graphene, as a consequence of the zone folding effect, but due to the adatoms impact we can observe some differences in frequencies and the splitting of

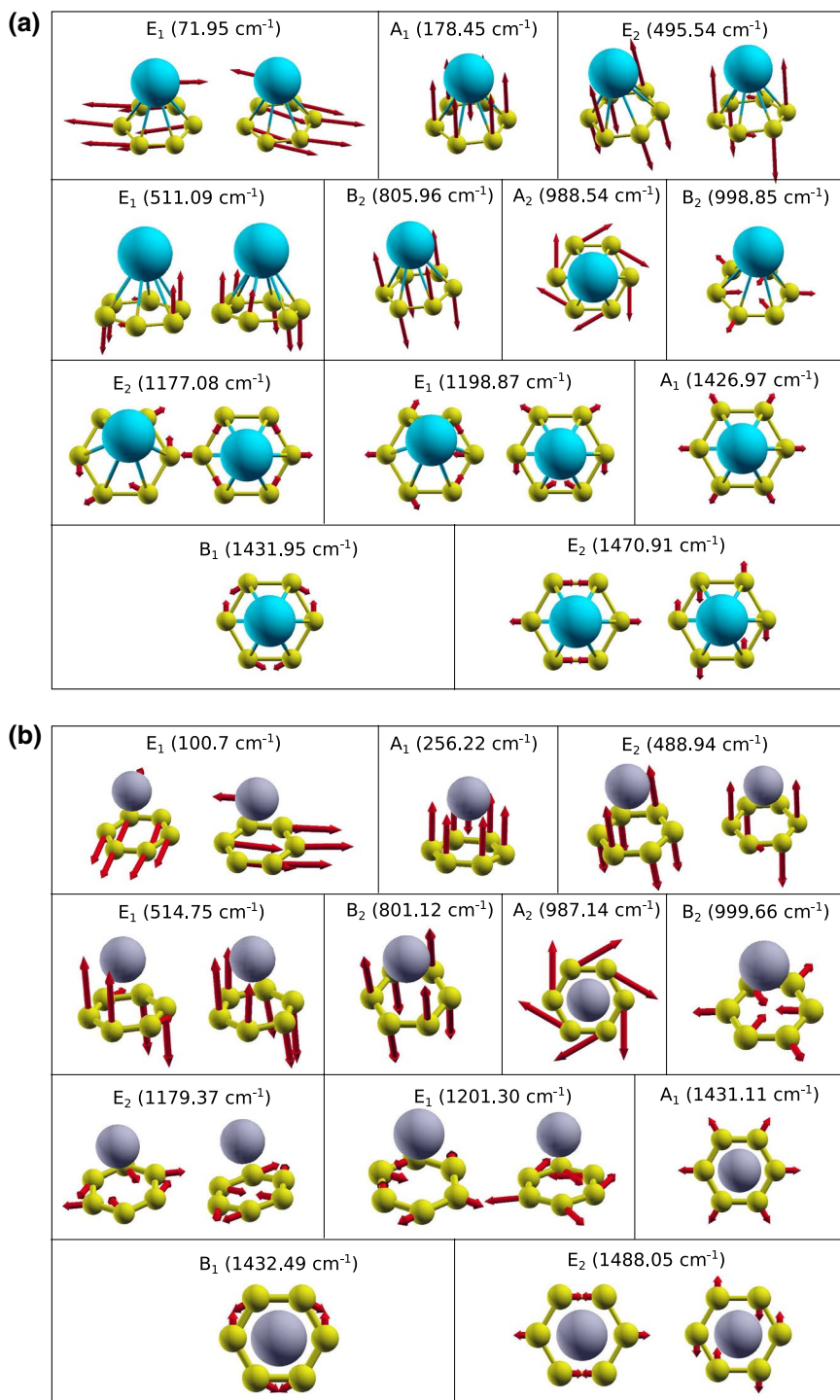


Fig. 4 Displacement patterns of **a** SrC_6 -mono and **b** YbC_6 -mono. Acoustic modes ($\omega = 0$) are not shown in pictures

some modes. The results obtained in this paper are important base for further theoretical and experimental research of those two structures, as well for future research of similar structures of graphene doped with other metal adatoms.

Acknowledgements This work is supported by the Serbian MPNTR through Project OI 171005 and by Qatar National Research Foundation through Project NPRP 7-665-1-12.

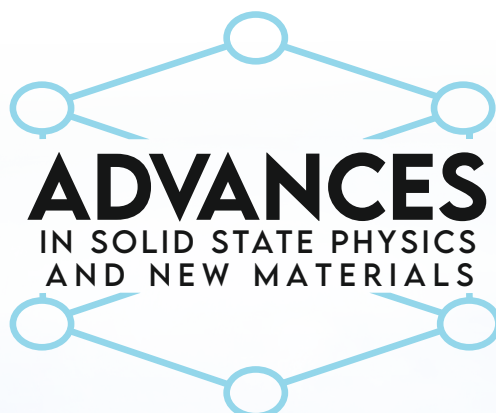
References

- Ahn, J.H., Hong, B.H.: Graphene for displays that bend. *Nat. Nanotechnol.* **9**(10), 737–738 (2014)
- Altmann, S., Herzog, P.: *Point-Group Theory Tables*. Oxford Science Publications, Clarendon Press, Oxford (1994)
- Bae, S., Kim, H., Lee, Y., Xu, X., Park, J.S., Zheng, Y., Balakrishnan, J., Lei, T., Kim, H.R., Song, Y.I., et al.: Roll-to-roll production of 30-inch graphene films for transparent electrodes. *Nat. Nanotechnol.* **5**(8), 574–578 (2010)
- Blake, P., Brimicombe, P.D., Nair, R.R., Booth, T.J., Jiang, D., Schedin, F., Ponomarenko, L.A., Morozov, S.V., Gleeson, H.F., Hill, E.W., Geim, A.K., Novoselov, K.S.: Graphene-based liquid crystal device. *Nano Lett.* **8**(6), 1704–1708 (2008)
- Bolotin, K., Sikes, K., Jiang, Z., Klima, M., Fudenberg, G., Hone, J., Kim, P., Stormer, H.: Ultrahigh electron mobility in suspended graphene. *Solid State Commun.* **146**(9), 351–355 (2008)
- Bonaccorso, F., Colombo, L., Yu, G., Stoller, M., Tozzini, V., Ferrari, A.C., Ruoff, R.S., Pellegrini, V.: Graphene, related two-dimensional crystals, and hybrid systems for energy conversion and storage. *Science* **347**(6217), 1246501 (2015)
- Calandra, M., Mauri, F.: Possibility of superconductivity in graphite intercalated with alkaline earths investigated with density functional theory. *Phys. Rev. B* **74**, 094507 (2006)
- Calandra, M., Profeta, G., Mauri, F.: Superconductivity in metal-coated graphene. *Physica Status Solidi (B)* **249**(12), 2544–2548 (2012)
- Choi, S.M., Jhi, S.H., Son, Y.W.: Effects of strain on electronic properties of graphene. *Phys. Rev. B* **81**, 081407 (2010)
- Csányi, G., Littlewood, P., Nevidomskyy, A.H., Pickard, C.J., Simons, B.: The role of the interlayer state in the electronic structure of superconducting graphite intercalated compounds. *Nat. Phys.* **1**(1), 42–45 (2005)
- Cui, T., Lv, R., Huang, Z.H., Zhu, H., Zhang, J., Li, Z., Jia, Y., Kang, F., Wang, K., Wu, D.: Synthesis of nitrogen-doped carbon thin films and their applications in solar cells. *Carbon* **49**(15), 5022–5028 (2011)
- Damljanović, V., Kostić R., Gajić R.: Characters of graphenes symmetry group dg80. *Physica Scr.* **2014**(T162), 014022 (2014)
- Damljanović, V., Gajić, R.: Phonon eigenvectors of graphene at high-symmetry points of the brillouin zone. *Physica Scr.* **2012**(T149), 014067 (2012)
- Dresselhaus, M.S., Dresselhaus, G.: Intercalation compounds of graphite. *Adv. Phys.* **51**(1), 1–186 (2002)
- Durajski, A.P.: Influence of hole doping on the superconducting state in graphane. *Supercond. Sci. Technol.* **28**(3), 035002 (2015)
- Enoki, T., Suzuki, M., Endo, M.: *Graphite Intercalation Compounds and Applications*, pp. 1–456. Oxford University Press, Oxford (2003)
- Ferrari, A.C., et al.: Science and technology roadmap for graphene, related two-dimensional crystals, and hybrid systems. *Nanoscale* **7**, 4598–4810 (2015)
- Gianozzi, P., et al.: Quantum espresso: a modular and open-source software project for quantum simulations of materials. *J. Phys. Condens. Matter* **21**(39), 395–502 (2009)
- Gusynin, V.P., Sharapov, S.G.: Unconventional integer quantum hall effect in graphene. *Phys. Rev. Lett.* **95**, 146801 (2005)
- Jeong, H.M., Lee, J.W., Shin, W.H., Choi, Y.J., Shin, H.J., Kang, J.K., Choi, J.W.: Nitrogen-doped graphene for high-performance ultracapacitors and the importance of nitrogen-doped sites at basal planes. *Nano Lett.* **11**(6), 2472–2477 (2011)
- Katsnelson, M., Novoselov, K., Geim, A.: Chiral tunnelling and the klein paradox in graphene. *Nat. Phys.* **2**(9), 620–625 (2006)

- Lee, C., Wei, X., Kysar, J.W., Hone, J.: Measurement of the elastic properties and intrinsic strength of monolayer graphene. *Science* **321**(5887), 385–388 (2008)
- Levy, N., Burke, S.A., Meaker, K.L., Panlasigui, M., Zettl, A., Guinea, F., Neto, A.H.C., Crommie, M.F.: Strain-induced pseudo-magnetic fields greater than 300 tesla in graphene nanobubbles. *Science* **329**(5991), 544–547 (2010)
- Liu, C.H., Chang, Y.C., Norris, T.B., Zhong, Z.: Graphene photodetectors with ultra-broadband and high responsivity at room temperature. *Nat. Nanotechnol.* **9**(4), 273–278 (2014)
- Ludbrook, B.M., et al.: Evidence for superconductivity in li-decorated monolayer graphene. *Proc. Nat. Acad. Sci.* **112**(38), 11795–11799 (2015)
- Margine, E.R., Giustino, F.: Two-gap superconductivity in heavily *n*-doped graphene: Ab initio migdal-eliasberg theory. *Phys. Rev. B* **90**, 014518 (2014)
- Margine, E., Lambert, H., Giustino, F.: Electron-phonon interaction and pairing mechanism in superconducting ca-intercalated bilayer graphene. *Sci. Rep.* **6**, 21414 (2016)
- Masir, M.R., Moldovan, D., Peeters, F.: Pseudo magnetic field in strained graphene: revisited. *Solid State Commun.* **175**, 76–82 (2013)
- Matković, A., Milošević, I., Milićević, M., Tomašević-Ilić, T., Pešić, J., Musić, M., Spasenović, M., Jovanović, D., Vasić, B., Deeks, C., Panajotović, R., Belić, M.R., Gajić, R.: Enhanced sheet conductivity of Langmuir-Blodgett assembled graphene thin films by chemical doping. *2D Mater.* **3**(1), 015002 (2016)
- Mazin, I., Balatsky, A.: Superconductivity in Ca-intercalated bilayer graphene. *Philos. Mag. Lett.* **90**(10), 731–738 (2010)
- Nakada, K., Ishii, A.: DFT calculation for adatom adsorption on graphene. In: Gong, J.R. (ed.) *Graphene Simulation*. InTech, Rijeka, Croatia (2011)
- Neto, A.H.C., Guinea, F., Peres, N.M.R.: Edge and surface states in the quantum hall effect in graphene. *Phys. Rev. B* **73**, 205408 (2006)
- Novoselov, K.S., Geim, A.K., Morozov, S.V., Jiang, D., Zhang, Y., Dubonos, S.V., Grigorieva, I.V., Firsov, A.A.: Electric field effect in atomically thin carbon films. *Science* **306**(5696), 666–669 (2004)
- Novoselov, K.S., Jiang, Z., Zhang, Y., Morozov, S.V., Stormer, H.L., Zeitler, U., Maan, J.C., Boebinger, G.S., Kim, P., Geim, A.K.: Room-temperature quantum hall effect in graphene. *Science* **315**(5817), 1379–1379 (2007)
- Penev, E.S., Kutana, A., Yakobson, B.I.: Can two-dimensional boron superconduct? *Nano Lett.* **16**(4), 2522–2526 (2016)
- Perdew, J.P., Zunger, A.: Self-interaction correction to density-functional approximations for many-electron systems. *Phys. Rev. B* **23**, 5048–5079 (1981)
- Peres, N.M.R., Neto, A.H.C., Guinea, F.: Conductance quantization in mesoscopic graphene. *Phys. Rev. B* **73**, 195411 (2006)
- Pešić, J., Gajić, R., Hingerl, K., Belić, M.: Strain-enhanced superconductivity in li-doped graphene. *EPL (Europhys. Lett.)* **108**(6), 67005 (2014)
- Pešić, J., Damljanović, V., Gajić, R., Hingerl, K., Belić, M.: Density functional theory study of phonons in graphene doped with Li, Ca and Ba. *EPL (Europhys. Lett.)* **112**(6), 67006 (2015)
- Profeta, G., Calandra, M., Mauri, F.: Phonon-mediated superconductivity in graphene by lithium deposition. *Nat. Phys.* **8**(2), 131–134 (2012)
- Qu, L., Liu, Y., Baek, J.B., Dai, L.: Nitrogen-doped graphene as efficient metal-free electrocatalyst for oxygen reduction in fuel cells. *ACS Nano* **4**(3), 1321–1326 (2010)
- Rüddorff, W.: *Graphite Intercalation Compounds*. Advances in Inorganic Chemistry and Radiochemistry, pp. 223–266. Academic Press, Cambridge (1959)
- Saito, Y., Nojima, T., Iwasa, Y.: Highly crystalline 2d superconductors. *Nat. Rev. Mater.* **2**, 16094 (2016)
- Sassi, U., Parret, R., Nanot, S., Bruna, M., Borini, S., De Fazio, D., Zhao, Z., Lidorikis, E., Koppens, F., Ferrari, A., et al.: Graphene-based mid-infrared room-temperature pyroelectric bolometers with ultra-high temperature coefficient of resistance. *Nature Commun.* **8**, 14311 (2017)
- Settnes, M., Power, S.R., Jauho, A.P.: Pseudomagnetic fields and triaxial strain in graphene. *Phys. Rev. B* **93**, 035456 (2016)
- Sharma, B.K., Ahn, J.H.: Graphene based field effect transistors: efforts made towards flexible electronics. *Solid-State Electron.* **89**(Supplement C), 177–188 (2013)
- Shimada, N.H., Minamitani, E., Watanabe, S.: Theoretical prediction of phonon-mediated superconductivity with $T_c = 25K$ in Li-intercalated hexagonal boron nitride bilayer. *Appl. Phys. Express* **10**(9), 093101 (2017)
- Si, C., Liu, Z., Duan, W., Liu, F.: First-principles calculations on the effect of doping and biaxial tensile strain on electron-phonon coupling in graphene. *Phys. Rev. Lett.* **111**, 196802 (2013)

- Todorović, D., Matković, A., Milićević, M., Jovanović, D., Gajić, R., Salom, I., Spasenović, M.: Multilayer graphene condenser microphone. *2D Mater* **2**(4), 045013 (2015)
- Wakabayashi, K., Fujita, M., Kusakabe, K., Nakada, K.: Magnetic structure of graphite ribbon. *Czech J. Phys.* **46**(4), 1865–1866 (1996)
- Wakabayashi, K., Takane, Y., Yamamoto, M., Sigrist, M.: Edge effect on electronic transport properties of graphene nanoribbons and presence of perfectly conducting channel. *Carbon* **47**(1), 124–137 (2009)
- Wang, Y., Shao, Y., Matson, D.W., Li, J., Lin, Y.: Nitrogen-doped graphene and its application in electrochemical biosensing. *ACS Nano* **4**(4), 1790–1798 (2010)
- Weller, T.E., Ellerby, M., Saxena, S.S., Smith, R.P., Skipper, N.T.: Superconductivity in the intercalated graphite compounds C_6Yb and C_6Ca . *Nat. Phys.* **1**(1), 39–41 (2005)
- Xue, M., Chen, G., Yang, H., Zhu, Y., Wang, D., He, J., Cao, T.: Superconductivity in potassium-doped few-layer graphene. *J. Am. Chem. Soc.* **134**(15), 6536–6539 (2012)

BOOK OF ABSTRACTS



ДОСТИГНУЋА У ФИЗИЦИ ЧВРСТОГ СТАЊА И НОВИХ МАТЕРИЈАЛА

*30 година Центра за физику чврстог стања и нове материјале
Института за физику у Београду*

ADVANCES IN SOLID STATE PHYSICS AND NEW MATERIALS

*30 years of the Center for Solid State Physics and New Materials at the
Institute of Physics Belgrade*

19 - 23 May 2025
Belgrade, Serbia



Strain Engineering in hBN/M^{III}X^{VI} Heterostructures for Enhanced Optoelectronic Performance

Andrijana Šolajić^a, Jelena Pešić^a

^aLaboratory for 2D materials, Center for Solid State Physics and New Materials, Institute of Physics Belgrade, University of Belgrade, Pregrevica 118, 11080 Belgrade, Serbia

Abstract. Group IIIa monochalcogenides (M^{III}X^{VI}, M = Ga, In; X = S, Se, Te) are promising 2D materials due to their high electron mobility, tunable bandgaps, and strong light absorption. However, their chemical sensitivity, particularly oxidation in ambient conditions, limits their stability and device integration. Encapsulation with hexagonal boron nitride (hBN) provides an effective solution, offering both mechanical protection and enhanced electronic and optical properties [1]. This study investigates the structural, electronic, and optical properties of hBN/M^{III}X^{VI} heterostructures (HS), with a particular focus on the role of mechanical strain in tuning their performance. Using biaxial strain, we demonstrate precise bandgap modulation and improved optical absorption while preserving material symmetry [2,3]. Our results highlight hBN/InTe and hBN/GaTe as particularly promising HSs due to their excellent lattice matching, enhanced mechanical stability, and broad-spectrum absorption in the visible range [2]. These findings not only advance fundamental understanding of strain-engineered HSs but also provide design strategies for integrating these materials into next-generation optoelectronic devices, including flexible photodetectors and absorbers.

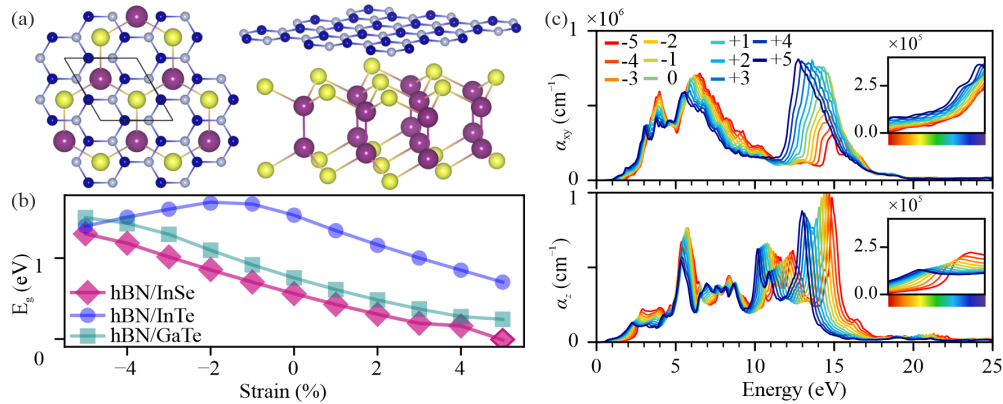


FIGURE 1. (a) Top and side view of hBN/M^{III}X^{VI} HS, (b) calculated bandgap of hBN/InSe, hBN/InTe and hBN/GaTe for different strain intensities, (c) Absorption of hBN/GaTe HS under strain.

REFERENCES

1. Šolajić, A., Pešić, J., *Journal of Physics: Condensed Matter*, **34**(34):345301, 2022.
2. Šolajić, A., Pešić, J., *Scientific Reports*, **14**(1):1081, 2024.
3. Šolajić, A., Pešić, J., *Optical and Quantum Electronics*, **56**(7):1186, 2024.

Advances in Solid State Physics and New Materials (5; 2025; Beograd)

Book of abstracts / Advances in Solid State Physics and New Materials - 30 years of the Center for Solid State Physics and New Materials at the Institute of Physics Belgrade, 19 – 23 May 2025, Belgrade, Serbia; editors Bojana Višić and Andrijana Šolajić. – Belgrade: Center for Solid State Physics and New Materials, Institute of Physics, 2025 (Belgrade: SASA).

ISBN 978-86-82441-65-6

1. Advances in Solid State Physics and New Materials

а) Физика чврстог стања - Апстракти

BOOK OF ABSTRACTS



ДОСТИГНУЋА У ФИЗИЦИ ЧВРСТОГ СТАЊА И НОВИХ МАТЕРИЈАЛА

*30 година Центра за физику чврстог стања и нове материјале
Института за физику у Београду*

ADVANCES IN SOLID STATE PHYSICS AND NEW MATERIALS

*30 years of the Center for Solid State Physics and New Materials at the
Institute of Physics Belgrade*

19 - 23 May 2025
Belgrade, Serbia



Raman Signatures Of Instabilities In InSiTe₃

T. Belojica^a, A. Milosavljević^a, S. Djurdjić Mijin^{ba}, J. Blagojević^a, A. Šolajić^a, J. Pešić^a, B. Višić^a, V. Damjanović^a, M. O. Ogunbunmi^c, S. Bobev^{cd}, Yu Liu^d, C. Petrović^{def}, Z. Popović^g, R. Hackl^{hi}, and N. Lazarević^a

^a*Institute of Physics Belgrade, University of Belgrade, Pregrevica 118, 11080 Belgrade, Serbia*

^b*Departamento de Física de Materiales, Facultad de Ciencias, Universidad Autónoma de Madrid, 28049 Madrid, Spain*

^c*Department of Chemistry and Biochemistry, University of Delaware, Newark, Delaware 19716, USA*

^d*Condensed Matter Physics and Materials Science Department, Brookhaven National Laboratory, Upton, NY 11973-5000, USA*

^e*Department of Nuclear and Plasma Physics, Vinca Institute of Nuclear Sciences, University of Belgrade, Belgrade 11001, Serbia*

^f*Shanghai Advanced Research in Physical Sciences (SHARPS), Shanghai 201203, China*

^g*Serbian Academy of Sciences and Arts, Knez Mihailova 35, 11000 Belgrade, Serbia*

^h*School of Natural Sciences, Technische Universität München, Garching 85748, Germany*
ⁱ*IFW Dresden, Helmholtzstrasse 20, Dresden 01069, Germany*

Abstract. Layered van der Waals materials have gained considerable interest for their unique physical properties, yet InSiTe₃ remains largely unexplored due to uncertainties surrounding its crystal structure. In this work, we present a comprehensive experimental and theoretical investigation of InSiTe₃, confirming a rhombohedral structure with $P\bar{3}$ space group symmetry via single-crystal X-ray diffraction. Polarization-resolved Raman scattering reveals nine out of ten Raman-active modes expected for this symmetry, further validating the structural assignment. Beyond conventional phonon behavior, we identify strong anharmonicity and the emergence of a self-organized coherent phonon state associated with a high-energy A_g mode near 500 cm⁻¹. Analysis of phonon-phonon coupling parameters indicates that A_g modes exhibit coupling strengths up to eight times greater than E_g modes. Temperature-dependent Raman measurements from 80 to 300 K reveal notable changes in A_g mode intensities around 200 K and the appearance of broad spectral features in the phonon gap region, attributed to overtone excitations. Our findings point to an intrinsic lattice instability in InSiTe₃, driven by strong anharmonic interactions. However, further studies are required to fully uncover the microscopic origin of these instabilities and their implications for the material's physical properties.

*This research was supported by the Science Fund of the Republic of Serbia, 10925, Dynamics of CDW transition in strained quasi-1D systems – DYNAMIQS

Advances in Solid State Physics and New Materials (5; 2025; Beograd)

Book of abstracts / Advances in Solid State Physics and New Materials - 30 years of the Center for Solid State Physics and New Materials at the Institute of Physics Belgrade, 19 – 23 May 2025, Belgrade, Serbia; editors Bojana Višić and Andrijana Šolajić. – Belgrade: Center for Solid State Physics and New Materials, Institute of Physics, 2025 (Belgrade: SASA).

ISBN 978-86-82441-65-6

1. Advances in Solid State Physics and New Materials

а) Физика чврстог стања - Апстракти

BOOK OF ABSTRACTS



ДОСТИГНУЋА У ФИЗИЦИ ЧВРСТОГ СТАЊА И НОВИХ МАТЕРИЈАЛА

*30 година Центра за физику чврстог стања и нове материјале
Института за физику у Београду*

ADVANCES IN SOLID STATE PHYSICS AND NEW MATERIALS

*30 years of the Center for Solid State Physics and New Materials at the
Institute of Physics Belgrade*

19 - 23 May 2025
Belgrade, Serbia



Anisotropic Strain Response in FeSe

A. Milosavljević^a, J. Blagojević^a, T. Belojica^a, B. Višić^a, S. Djurdjić Mijin^{a, b}, M. Opačić^a, A. Šolajić^a, J. Pešić^a, A. Wang^c, C. Petrović^{c, d, e}, R. Hackl^{f, g} and N. Lazarević^a

^a*Institute of Physics Belgrade, University of Belgrade, Pregrevica 118, 11080 Belgrade, Serbia*

^b*Departamento de Física de Materiales, Facultad de Ciencias, Universidad Autónoma de Madrid, 28049 Madrid, Spain*

^c*Condensed Matter Physics and Material Science Department, Brookhaven National Laboratory, Upton, NY 11973-5000, USA*

^d*Shanghai Advanced Research in Physical Sciences (SHARPS), Shanghai 201203, China*

^e*Department of Nuclear and Plasma Physics, Vinca Institute of Nuclear Sciences, University of Belgrade, Belgrade 11001, Serbia*

^f*School of Natural Sciences, Technische Universität München, Garching 85748, Germany*

^g*IFW Dresden, Helmholtzstrasse 20, Dresden 01069, Germany*

Abstract.

Unconventional superconductivity often arises in materials with complex interactions, where competing ordered states such as magnetism, nematicity, and superconductivity, interact and sometimes overlap, making their nature elusive. Among iron-based superconductors, the isostructural FeSe and FeS may appear similar but they differ significantly in their physical properties. While FeSe undergoes a nematic and structural phase transition, FeS shows no structural transition even at the lowest temperatures, with its critical temperature (T_c) halved compared to FeSe. Interestingly, substituting selenium with sulfur in FeSe suppresses the nematic transition temperature to zero near a quantum critical point (QCP), which coincides with a significant drop in T_c . It has been suggested that while spin-fluctuations dominate below the QCP and significantly affect electron-phonon interactions, nematic fluctuations become prominent above the QCP. Here, we present a detailed Raman scattering study of FeSe under uniaxial strain applied along two high-symmetry crystallographic directions, $\langle 110 \rangle$ and $\langle 100 \rangle$, to investigate how symmetry-breaking perturbations affect its lattice dynamics. Our results reveal a pronounced anisotropy in the phonon response to strain: orthorhombic distortion along the $\langle 110 \rangle$ direction leads to a moderate narrowing of the temperature window over which phonon anomalies occur, while strain along $\langle 100 \rangle$ which introduces rhombohedral distortion, results in a significant broadening of the temperature range over which phonon mode splitting, and energy and linewidth anomalies are observed. We find that the fully symmetric A_{1g} phonon mode is particularly sensitive to symmetry-breaking perturbations, while the B_{1g} phonon mode remains largely unaffected.

*This research was supported by the Science Fund of the Republic of Serbia, 10925, Dynamics of CDW transition in strained quasi-1D systems - DYNAMIQS

Advances in Solid State Physics and New Materials (5; 2025; Beograd)

Book of abstracts / Advances in Solid State Physics and New Materials - 30 years of the Center for Solid State Physics and New Materials at the Institute of Physics Belgrade, 19 – 23 May 2025, Belgrade, Serbia; editors Bojana Višić and Andrijana Šolajić. – Belgrade: Center for Solid State Physics and New Materials, Institute of Physics, 2025 (Belgrade: SASA).

ISBN 978-86-82441-65-6

1. Advances in Solid State Physics and New Materials

а) Физика чврстог стања - Апстракти

**TWENTY-SECOND YOUNG RESEARCHERS'
CONFERENCE
MATERIALS SCIENCE AND ENGINEERING**

December 4 – 6, 2024, Belgrade, Serbia

Program and the Book of Abstracts

**Materials Research Society of Serbia
&
Institute of Technical Sciences of SASA**

2024

Book title:

Twenty-Second Young Researchers' Conference - Materials Science and Engineering:
Program and the Book of Abstracts

Publisher:

Institute of Technical Sciences of SASA
Kneza Mihaila 35/IV, 11000 Belgrade, Serbia
Tel: +381-11-2636994, 2185263, <http://www.itn.sanu.ac.rs>

Conference organizers:

Materials Research Society of Serbia, Belgrade, Serbia
Institute of Technical Sciences of SASA, Belgrade, Serbia

Editor:

Dr. Smilja Marković

Technical Editor:

Aleksandra Stojičić and Dr. Ivana Dinić

Cover page: Dr. Smilja Marković

Cover photo: Dr. Nebojša Labus

Printing:

Gama digital centar
Otona Župančića No. 19, 11070 Belgrade, Serbia
Tel: +381-63 8616734
<http://www.gdc.rs>

Publication year: 2024

Print-run:

120 copies

CIP - Каталогизација у публикацији

Народна библиотека Србије, Београд

66.017/.018(048)

YOUNG Researchers Conference Materials Sciences and Engineering (22 ; 2024 ; Beograd)

Program ; and the Book of abstracts / Twenty-Second Young Researchers' Conference Materials Science and Engineering, December 4 – 6, 2024, Belgrade, Serbia ; [organizers] Materials Research Society of Serbia & Institute of Technical Sciences of SASA ; [editor Smilja Marković]. - Belgrade : Institute of Technical Sciences of SASA, 2024 (Belgrade : Gama digital centar). - XXII, 89 str. ; 23 cm
Tiraž 120. - Registar.

ISBN 978-86-80321-39-4

а) Наука о материјалима -- Апстракти б) Технички материјали -- Апстракти
COBISS.SR-ID 157262345

8-5

Effect of metal atoms doping on magnetism in talc - 2D natural material

Ayan Khasiyeva, Andrijana Solajic, Jelena Pesic

Laboratory for 2D materials, Center for Solid State Physics and New Materials, Institute of Physics Belgrade, University of Belgrade

2D materials with intrinsic magnetic properties enable opportunities for many technological applications, including in the fields of spintronics, data storage, and magnetoelectronics. However, most of the known magnetic 2D materials suffer from a lack of ambient stability. This makes the usage of natural 2D materials, such as talc, advantageous when it comes to stability. Talc is a mineral found abundantly in nature with the chemical formula $\text{Mg}_3\text{Si}_4\text{O}_{10}(\text{OH})_2$. It belongs to the group of phyllosilicates. In nature, iron-rich phyllosilicates, such as minnesotaite (iron-rich talc) and annite, are present, which inspires the search for similarly magnetic materials. A single layer of talc consists of $[\text{MgO}_4(\text{OH})_2]$ octahedra in between parallel sheets of tetrahedral $[\text{Si}_2\text{O}_5]$. Monolayers of talc can be obtained through processes of chemical vapour deposition or mechanical and liquid phase exfoliation. While talc is naturally non-magnetic, doping by substitution of the Mg cation for those of ferromagnetic metals allows for magnetic properties to be exhibited.

In this research, we use computational techniques based on density functional theory, as implemented in the Quantum Espresso software package, in order to analyse the stability and electronic properties of metal doped talc. Talc possesses two inequivalent Mg substitution sites. Cell optimizations were performed for Fe, Ni, Co substitutions, with the goal of finding the most energetically favourable structure for both of the distinct substitution sites. After optimization, band structures were calculated and magnetic moments were compared in all possible candidates. Air-stable natural 2D materials with long-range magnetic ordering at room temperature would represent a major breakthrough in the field of advanced technologies, for applications such as magnetoresistant tunnelling junctions and magnetooptic devices. Metal-doped talc would represent a novel material that would not only exhibit magnetism in low dimension, but also remain stable in ambient conditions and ecologically friendly.

**TWENTY-SECOND YOUNG RESEARCHERS'
CONFERENCE
MATERIALS SCIENCE AND ENGINEERING**

December 4 – 6, 2024, Belgrade, Serbia

Program and the Book of Abstracts

**Materials Research Society of Serbia
&
Institute of Technical Sciences of SASA**

2024

Book title:

Twenty-Second Young Researchers' Conference - Materials Science and Engineering:
Program and the Book of Abstracts

Publisher:

Institute of Technical Sciences of SASA
Kneza Mihaila 35/IV, 11000 Belgrade, Serbia
Tel: +381-11-2636994, 2185263, <http://www.itn.sanu.ac.rs>

Conference organizers:

Materials Research Society of Serbia, Belgrade, Serbia
Institute of Technical Sciences of SASA, Belgrade, Serbia

Editor:

Dr. Smilja Marković

Technical Editor:

Aleksandra Stojičić and Dr. Ivana Dinić

Cover page: Dr. Smilja Marković

Cover photo: Dr. Nebojša Labus

Printing:

Gama digital centar
Otona Župančića No. 19, 11070 Belgrade, Serbia
Tel: +381-63 8616734
<http://www.gdc.rs>

Publication year: 2024

Print-run:

120 copies

CIP - Каталогизација у публикацији

Народна библиотека Србије, Београд

66.017/.018(048)

YOUNG Researchers Conference Materials Sciences and Engineering (22 ; 2024 ; Beograd)

Program ; and the Book of abstracts / Twenty-Second Young Researchers' Conference Materials Science and Engineering, December 4 – 6, 2024, Belgrade, Serbia ; [organizers] Materials Research Society of Serbia & Institute of Technical Sciences of SASA ; [editor Smilja Marković]. - Belgrade : Institute of Technical Sciences of SASA, 2024 (Belgrade : Gama digital centar). - XXII, 89 str. ; 23 cm
Tiraž 120. - Registar.

ISBN 978-86-80321-39-4

а) Наука о материјалима -- Апстракти б) Технички материјали -- Апстракти
COBISS.SR-ID 157262345

6-2

Study of crystal phases and temperature dependence of InSiTe₃

T. Belojica¹, J. Blagojević¹, S. Djurđić Mijin^{1,2}, A. Šolajić¹, J. Pešić¹, B. Višić¹, V. Damljanović¹, M. O. Ogunbunmi³, S. Bobev^{3,4}, Yu Liu⁴, C. Petrovic^{4,5,6}, Z.V. Popović⁷, A. Milosavljević¹, N. Lazarević¹

¹Center for Solid State Physics and New Materials, Institute of Physics Belgrade, University of Belgrade, Pregrevica 118, 11080 Belgrade, Serbia, ²Departamento de Fisica de Materiales, Facultad de Ciencias, Universidad Autonoma de Madrid, 28049 Madrid, Spain, ³Department of Chemistry and Biochemistry, University of Delaware, Newark, Delaware 19716, U.S.A., ⁴Condensed Matter Physics and Materials Science Department, Brookhaven National Laboratory, Upton, NY 11973-5000, USA, ⁵Shanghai Advanced Research in Physical Sciences (SHARPS), Shanghai 201203, China, ⁶Department of Nuclear and Plasma Physics, Vinca Institute of Nuclear Sciences, University of Belgrade, Belgrade 11001, Serbia, ⁷Serbian Academy of Sciences and Arts, Knez Mihailova 35, 11000 Belgrade, Serbia

In recent years, quasi-low-dimensional materials have attracted significant attention due to their distinctive properties and possible applications in nanoelectronics and spintronics. The material of a specific interest within this group is InSiTe₃. Unlike related compounds, such as CrSiTe₃ and CrGeTe₃, research results InSiTe₃ are limited, most likely due to the unclear nature of its crystal structure. Detailed experimental and theoretical investigation was conducted to determine the crystal structure of InSiTe₃. Inelastic light scattering experiment performed on the InSiTe₃ reveals presence of six ($3A_{1g} + 3E_g$) out of eight and seven ($5A_g + 2E_g$) out of ten Raman active modes for proposed $P\bar{3}1m$ and $P\bar{3}$ space groups, respectively. These findings suggest a coexistence of two trigonal crystal phases: a high symmetry one corresponding to $P\bar{3}1m$ and a lower symmetry one that corresponds to $P\bar{3}$ space group. Additional excitations were detected in parallel scattering configuration; two broad features in the gap of PDOS that can be a consequence of two-phonon processes and a third one, at about 500 cm⁻¹ that might indicate local symmetry breaking at nano scale. Temperature dependent measurements from 80 K to 300 K show monotonous decrease in energy and increase in linewidth up to 200 K at which point discontinuities appear across all analyzed modes. However, this anomaly overcomes the scope of this research and remains an open question.

**TWENTY-SECOND YOUNG RESEARCHERS'
CONFERENCE
MATERIALS SCIENCE AND ENGINEERING**

December 4 – 6, 2024, Belgrade, Serbia

Program and the Book of Abstracts

**Materials Research Society of Serbia
&
Institute of Technical Sciences of SASA**

2024

Book title:

Twenty-Second Young Researchers' Conference - Materials Science and Engineering:
Program and the Book of Abstracts

Publisher:

Institute of Technical Sciences of SASA
Kneza Mihaila 35/IV, 11000 Belgrade, Serbia
Tel: +381-11-2636994, 2185263, <http://www.itn.sanu.ac.rs>

Conference organizers:

Materials Research Society of Serbia, Belgrade, Serbia
Institute of Technical Sciences of SASA, Belgrade, Serbia

Editor:

Dr. Smilja Marković

Technical Editor:

Aleksandra Stojičić and Dr. Ivana Dinić

Cover page: Dr. Smilja Marković

Cover photo: Dr. Nebojša Labus

Printing:

Gama digital centar
Otona Župančića No. 19, 11070 Belgrade, Serbia
Tel: +381-63 8616734
<http://www.gdc.rs>

Publication year: 2024

Print-run:

120 copies

CIP - Каталогизација у публикацији

Народна библиотека Србије, Београд

66.017/.018(048)

YOUNG Researchers Conference Materials Sciences and Engineering (22 ; 2024 ; Beograd)

Program ; and the Book of abstracts / Twenty-Second Young Researchers' Conference Materials Science and Engineering, December 4 – 6, 2024, Belgrade, Serbia ; [organizers] Materials Research Society of Serbia & Institute of Technical Sciences of SASA ; [editor Smilja Marković]. - Belgrade : Institute of Technical Sciences of SASA, 2024 (Belgrade : Gama digital centar). - XXII, 89 str. ; 23 cm
Tiraž 120. - Registar.

ISBN 978-86-80321-39-4

а) Наука о материјалима -- Апстракти б) Технички материјали -- Апстракти
COBISS.SR-ID 157262345

8-7

Investigation of electronic properties of 1T and 2H phases of 2D GaS

Lenka Filipović, Andrijana Šolajić, Jelena Pešić

Laboratory for 2D Materials, Center for Solid State Physics and New Materials, Institute of Physics Belgrade, University of Belgrade, Pregrevica 118, 11080 Belgrade, Serbia

Two-dimensional materials offer unique electronic, optical, and mechanical properties, making them ideal candidates for next-generation technologies in electronics, energy storage, and sensing applications. Gallium sulfide (GaS) is a layered, two-dimensional material belonging to the group-III metal chalcogenides. In its monolayer form, GaS exhibits a hexagonal structure and notable electronic and optoelectronic properties. It has a wide bandgap, making it suitable for applications in optoelectronics, such as photodetectors, light-emitting devices, and potential uses in flexible and transparent electronics. Due to its stability and tunable properties, GaS is a focus of research for next-generation semiconductor technology. This study emphasizes potential of 2D GaS in advanced technological application. The main motivation of the research is investigation of the solid-solid phase transition (2H->1T) in two-dimensional GaS and possibility of inducing this phase transition by application of the mechanical strain. Research consists of detail computational analysis of crystal structures and properties of 1T and 2H phases of GaS, using formalism based on Density Functional Theory. Our calculations demonstrate energetical stability of both phases with 2H phase being more stabile. We study electronic properties presenting band structures and electronic DOS and dielectric function for both phases. Density functional theory calculations are based on plane waves basis and pseudopotential as implemented in Quantum Espresso software package. Calculations are employing the PBE exchange-correlation functional and PAW pseudopotentials. For accurate treatment of interlayer interactions, the Van der Waals interactions is treated using the Grimme-D2 correction. The results of this study enhance understanding of structural properties and highlight the potential to induce solid-solid phase transitions, paving the way for new applications based on phase-switching effects.

Scientific Program ICP2DC 2024 - International Conference on Physics of Two-Dimensional Crystals 2024

Tuesday 2nd July 2024	9:30	Welcome and introduction			
	10:00	INVITED TALK 1	Durnev	Mikhail	Intervalley mixing of interface excitons at TMDC-based lateral heterojunctions
	10:30	INVITED TALK 2	Lazic	Snezana	Cost-efficient deterministic engineering of quantum light sources in 2D semiconductors
	11:00	Coffee			
	11:30	INVITED TALK 3	Toropov	Alexey	Single-exciton photoluminescence spectroscopy in a GaN monolayer in AlN
	12:00	INVITED TALK 4	Shubina	Tatiana	Excitons and exciton-polaritons in mono- and dichalcogenide nanostructures
	12:30	ORAL 1	De Simoni	Beatriz	Optical Transitions of Some MPS3 Layered Compounds Under Hydrostatic Pressure
	12:50	Lunch			
	14:30	INVITED TALK 5	Djurdjic Mijin	Sanja	Raman Spectroscopy Study of Two-Dimensional van der Waals magnets
	15:00	INVITED TALK 6	Nestoklon	Mikhail	Landé Factors in Lead Halide Perovskites and their nanostructures
	15:30	Oral 2	Rybak	Milosz	Magneto-optical anisotropies of two-dimensional antiferromagnetic MPX
	15:50	Panel Discussion/Talk 7	Speaker 1st da	All	Optical properties of 2D materials
	16:20	Coffee			
	17:00	Round Table Discussion	All	All	The use of Artificial Intelligence for material discovery
	18:00	End of the I day			
Wednesday 3rd July 2024	9:30	INVITED TALK 8	Holleitner	Alexander	Spatially coherent many-body exciton ensembles in 2D heterostructures
	10:00	INVITED TALK 9	Volkov	Valentyn	Giant optical anisotropy in van der Waals materials: perspectives and challenges
	10:30	INVITED TALK 10	Zendejdel	Mahmoud	Advances in low-dimensional perovskite structures for high-performance perovskite solar cells and modules
	11:00	Coffe			
	11:30	INVITED TALK 11	Saranin	Danila	Advances for interface engineering for inverted perovskite solar modules and testing in ambient conditions
	12:00	INVITED TALK 12	Anichini	Cosimo	Solution-processed two-dimensional materials for energy applications
	12:30	ORAL 3	Ciesiolkiewicz	Karolina	Optical Transmission and Photomodulated Spectra Analysis of VdWs crystals placed on Fiber Tips
	12:50	Lunch			
	14:30	INVITED TALK 13	Portnoi	Mikhail	Momentum alignment of photoexcited carriers and optical valley separation in two-dimensional Dirac materials
	15:00	INVITED TALK 14	Cordero	Francesco	Phase transition in thick metallic films of Ti3C2Tx MXene: possible sliding ferroelectricity
	15:30	INVITED TALK 15	Kusmartsev	Fedor	Electron-hole and clustered liquids and crystals in 2D materials
	16:00	ORAL 4	Kravchenko	Sergey	Collective depinning and sliding of a quantum Wigner crystal in a two-dimensional electron system
	16:20	Coffee			
	17:00	Round Table Discussion			The physics of 2D materials: what is still open ?
	18:00	End of the II day			
Thursday 4th July 2024 EXCURSION					
Friday 5th July 2024	9:30	INVITED TALK 16	Stratakis	Emmanuel	Pulsed Laser Assisted Generation of Novel Materials and Related Applications
	10:00	INVITED TALK 17	Illarionov	Yury	Recent progress in understanding and improvement the reliability of 2D electronic devices
	10:30	INVITED TALK 18	Ifor	Samuel	Organic Optoelectronics: Faster and Brighter
	11:00	Coffee			
	11:30	INVITED TALK 19	Kymakis	Emmanuel	Perovskite PV industrialization via 2D materials interface engineering
	12:00	INVITED TALK 20	Di Carlo	Aldo	MXenes and othe 2D materials in new generation photovoltaics
	12:30	ORAL 5	Nikbakht	Hafez	Low-temperature encapsulation approach for perovskite solar panels based on two-dimensional hexagonal boron nitride
	12:50	Lunch			
	14:30	INVITED TALK 21	Reale	Andrea	Printable thermoelectric devices based on graphene nanoplatelets and organic semiconductor composites for low temperature grade energy harvesting
	15:00	ORAL 6	Budkin	Grigory	Shift photocurrents in transition metal dichalcogenide monolayers taking account of Coulomb interaction
	15:20	ORAL 7	Król	Konrad	Single-layer Mo(SXSe1-X)2 FET: Effect of temperature on electrical properties
	15:40	Round Table Discussion	all	All	The role of 2D materials in technology. The and hat will be next
	17:00	End of the conferenc /Coffee.			



21th International Workshop on Computational Physics and Materials Science: Total Energy and Force Methods | (SMR 3814)

11 Jan 2023 - 13 Jan 2023
ICTP, Trieste, Italy

P01 - ABDURRAZAQ Abdulgaffar

Tricking germanium to open the band gap

P02 - ACHEHBOUNE Mohamed

Atomic scale nucleation and formation mechanism of hexagonal boron nitride (hBN) on graphene and Germanium : A DFT study

P03 - ADAK Abhishek Kumar

Insights from density functional theory into the formation and rotation of an enantiospecific assembly of molecular raffle wheels

P04 - ARTACHO CORTÉS Martin Emilio Martin

Floquet Theory of Electronic Stopping of nuclei projectiles in solids

P05 - ASHANI Mitonji Timothy

Exploring plasmon properties of the Dirac compound LiNa₂Bi using TDDFT.

P06 - ATAEL Seyedeh Samaneh

Interlayer Excitons in 2D TMD Heterostructures

P07 - ATTIA Mahmoud Mostafa Elsayed

Li vs. Na Solid-State based Batteries : Modelling of Diffusion in Solid Electrolytes

P08 - AZIZI Khatereh

Investigation of the structural complexity of aqueous systems through machine learning

P09 - BANERJEE Debarshi

Development of a computational toolbox to analyse first-passage times and diffusion coefficients in heterogeneous soft-matter systems

P10 - BHATTACHARYA Sanchari

Signature of cubic and linear Rashba in LaAlO₃/KTaO₃ (0 0 1) heterostructure

P11 - BIDOGGIA Davide

Ab-initio characterization of CoTPyP and CoTPyP-Co metalorganic monolayers for catalytic application

P12 - BINCI Luca

Noncollinear relativistic Hubbard parameters and DFT+U with ultrasoft pseudopotentials

P13 - BONACCI Miki

Automated Many-Body Perturbation Theory

P14 - BORGHESI Costanza

Tailoring High-Entropy Oxides (HEOs) as Emerging Radiative Materials for Green Energy Buildings

P15 - BOUCHRIT Abir

The effect of vacancies on the thermoelectric properties of half-Heusler materials

The Evolution of Vibrational Modes of FeSe Under Uniaxial Strain

Jelena Pešić, Andrijana Šolajić, Ana Milosavljević, Sanja Đurđić Mijin, Borislav Vasić, Novica Paunović and Nenad Lazarević

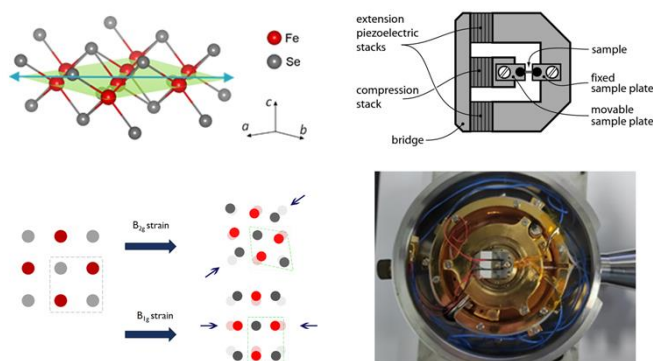
Center for Solid State Physics and New Materials, Institute of Physics Belgrade, Serbia

Application of strain is one of the effective ways to engineer the various properties of materials. Iron-based superconductors are suitable materials to study the strain dependence of physical properties due to their high sensitivity to variations in the local crystal structure. Among the iron-based superconductor family, FeSe is a prominent example of the interplay between superconductivity, magnetism, and electronic nematicity, which can be tuned both by chemical substitution and by application of physical pressure and consequent lattice distortions [1].

Here we present a first principle study of evolution of vibrational modes of the strained FeSe. We performed a systematic computational study, using density functional theory formalism, on bulk FeSe crystals with applying the in-plane uniaxial strain in B_{1g} and B_{2g} symmetry channels, in the range -1.5% to 1.5%. For the calculation, we used the experimental parameters and the volume cell of the unit cell is conserved under applied uniaxial strain [2].

We focus on the effect of the modification of the lattice constant, and the consequent symmetry distortion, on characteristic A_{1g} and B_{1g} modes of FeSe. These findings are compared with experimental data from Raman measurements, studying the trend of changes of A_{1g} and B_{1g} modes with applied strain using a piezoelectric strain device. The sample was mounted in such a way that the strain was applied in the ab -crystallographic plane and that the direction of incident light propagation is along the crystallographic c -axes. The sample orientations were set so that $[110]$ (B_{2g}) and $[100]$ (B_{1g}) crystallographic directions were orthogonal to a gap between the holder plates.

The work was supported by the Science Fund of the Republic of Serbia, PROMIS, No. 6062656, StrainedFeSC [3].



Left: Schematic representation of applied strain, Right: piezoelectric strain device, schematic and photography

[1] M. Ghini et al. Strain tuning of nematicity and superconductivity in single crystals of FeSe, *Physical Review B*, 103, 205139 (2021)

[2] Willa, R. et al. Strain tuning and anisotropic spin correlations in iron-based systems. *Physical Review B*, 100(8) (2019).

[3] <http://strainedfesc.ipb.ac.rs/>

Vienna Ab-initio Simulation Package (VASP) Ecosystem

Book of Abstracts

HPC Centre, University of Évora, Portugal
06-07 February 2023

Lattice Dynamics in Ferrimagnetic Layered van der Waals Material $\text{Mn}_3\text{Si}_2\text{Te}_6$ (CT)

Jelena Pešić¹, Andrijana Šolajić¹, Sanja Djurdžić¹, Yu Liu², Cedomir Petrovic², Michel Bockstedte³, Alberta Bonanni⁴, Zoran Popović⁵, & Nenad Lazarević¹

¹ Institute of Physics Belgrade, University of Belgrade, Serbia

² Condensed Matter Physics and Materials Science Department, Brookhaven National Laboratory, Upton, USA

³ Institute for Theoretical Physics, Johannes Kepler University Linz, Austria

⁴ Institute of Semiconductor and Solid-State Physics, Johannes Kepler University Linz, Austria

⁵ Serbian Academy of Sciences and Arts, Belgrade, Serbia

Email: yelena@ipb.ac.rs

$\text{Mn}_3\text{Si}_2\text{Te}_6$ single crystals were first synthesized in 1985 [1], however, few studies were carried out on this compound since. It was only recently that the attention has shifted to them, mainly through the comparisons with quasi-two-dimensional materials, specifically CrSiTe_3 . Layered magnetic van der Waals materials have lately received widespread attention due to their relevance for spintronics, magneto-electronics and data storage.

$\text{Mn}_3\text{Si}_2\text{Te}_6$ crystallizes in a trigonal $P\bar{3}1c$ crystal structure (No. 163 space group) [2]. First principle calculations suggested a competition between ferrimagnetic ground state and three additional magnetic configurations, originating from antiferromagnetic exchange for the three nearest Mn-Mn pairs [2]. Here we present a first principle study with the focus on the phonon properties [3]. We compare our computational results with experimental Raman scattering of $\text{Mn}_3\text{Si}_2\text{Te}_6$ single crystals. Eighteen Raman-active modes are identified, fourteen of which are assigned according to the trigonal symmetry. Five A_{1g} modes and nine E_g modes are observed and assigned according to the $P\bar{3}1c$ symmetry group. Four additional peaks to the ones ascribed to the $P\bar{3}1c$ symmetry group and obeying the A_{1g} selection rules, are attributed to overtones. A pronounced asymmetry of the A_{1g}^5 phonon mode is evidenced at 100K and 300 K. The unconventional temperature evolution of the A_{1g}^5 Raman mode reveals three successive, possibly magnetic, phase transitions that are expected to have significant impact on the strength of the spin-phonon interaction in $\text{Mn}_3\text{Si}_2\text{Te}_6$. These are suggested to be caused by the competition between the various magnetic states, which are close in energy.

This study provides a comprehensive insight into the lattice properties of the considered system and shows arguments for the emergence of competing short-range magnetic phases in $\text{Mn}_3\text{Si}_2\text{Te}_6$.

The calculations are based on the density functional theory formalism as implemented in the Vienna Ab-initio Simulation Package (VASP) [4-7], with the plane wave basis truncated at a kinetic energy of 520 eV, using the Perdew-Burke-Ernzerhof (PBE) exchange-correlation functional [8] and the projector augmented wave (PAW) method [9,10]. The Monkhorst and Pack scheme of the k point sampling is employed to integrate over the first Brillouin zone with $12 \times 12 \times 10$ at the Γ -centered grid. The convergence criteria for energy and force have been set to 10^{-6} eV and $0.001 \text{ eV}\text{\AA}^{-1}$, respectively. The DFT-D2 method of Grimme is employed for van der Waals corrections [11]. The vibrational modes are calculated applying the density functional perturbation theory implemented in VASP and Phonopy [12].

Application of MXenes in heterogeneous catalysis: A computational perspective (CT)

José D. Gouveia & José R. B. Gomes

CICECO-Aveiro Institute of Materials, University of Aveiro, Portugal

Email: jrgomes@ua.pt

The catalytic activities of several different heterogeneous catalysts, ranging from planar extended surfaces to clusters and particles with different shapes, sizes or compositions, have been experimentally determined for a long time. However, a fully understanding of the catalytic mechanisms is a defiant task because of the large number of variables that determine the performance of the catalyst. Therefore, to isolate the effect of each variable, studies using well-controlled conditions that allow separating the influence of different parameters in the global catalytic processes are required. Computer modelling arises as a very adequate strategy since the composition of the systems can be fully controlled, with relevant information being retrieved when combined with electronic structure methods. In this communication, we will present results

**21. СИМПОЗИЈУМ ФИЗИКЕ
КОНДЕНЗОВАНЕ МАТЕРИЈЕ**
**THE 21st SYMPOSIUM ON
CONDENSED MATTER PHYSICS**

BOOK OF ABSTRACTS



Probing charge density wave phases and the Mott transition in 1T-TaS₂ by Raman scattering

S. Djurdjić Mijin,¹ A. Baum,² J. Bekaert,³ A. Šolajić,¹ J. Pešić,¹ Y. Liu,⁴ Ge He,² M. V. Milošević,³ C. Petrovic,⁴ Z. V. Popović,⁵ R. Hackl,² and N. Lazarević¹

¹*Center for Solid State Physics and New Materials, Institute of Physics Belgrade, University of Belgrade, Pregrevica 118, RS-11080, Belgrade, Serbia*

²*Walther Meissner Institut, Bayerische Akademie der Wissenschaften, D-85748 Garching, Germany*

³*Department of Physics, University of Antwerp, Groenenborgerlaan 171, B-2020 Antwerp, Belgium*

⁴*Condensed Matter Physics and Materials Science Department, Brookhaven National Laboratory, Upton, New York 11973-5000, USA*

⁵*Serbian Academy of Sciences and Arts, Kneza Mihaila 35, RS-11000 Belgrade, Serbia*

Abstract. We present a polarization-resolved, high-resolution inelastic light scattering study consecutive CDW regimes in 1T-TaS₂ single crystals, supported by ab initio calculations. The analysis of the spectra within the low-temperature C-CDW regime suggests $P\bar{3}$ symmetry of the system. The spectra of the high-temperature IC-CDW phase directly project the phonon density of states due to the breaking of the translational invariance, supplemented by sizable electron-phonon coupling. Between 200 and 352 K, our Raman spectra show contributions from both the IC-CDW and the C-CDW phases, indicating their coexistence in the NC-CDW phase. The temperature dependence of the symmetry-resolved Raman conductivity indicates the stepwise reduction of the density of states in the CDW phases, followed by a Mott transition within the C-CDW phase. By means of inelastic light scattering, we were able to determine the size of the Mott gap at 170–190 meV, and to track its temperature dependence.

REFERENCES

1. S. Djurdjić Mijin, A. Baum, J. Bekaert, A. Šolajić, J. Pešić, Y. Liu, Ge He, M. V. Milošević, C. Petrovic, Z. V. Popović, R. Hackl, and N. Lazarević, Phys. Rev. B 103, 245133 (2021).

**21. СИМПОЗИЈУМ ФИЗИКЕ
КОНДЕНЗОВАНЕ МАТЕРИЈЕ**
**THE 21st SYMPOSIUM ON
CONDENSED MATTER PHYSICS**

BOOK OF ABSTRACTS



Crystal structure and phase transitions in InSiTe_3

T. Belojica^a, A. Milosavljević^a, S. Đurđić Mijin^a, A. Šolajić^a, J. Pešić^a, B. Višić^a, Yu Liu^b, C. Petrovic^b, Z. V. Popović^{a,c} and N. Lazarević^a

^aCenter for Solid State Physics and New Materials, Institute of Physics Belgrade, University of Belgrade, Pregrevica 118, 11080 Belgrade, Serbia

^bCondensed Matter Physics and Materials Science Department, Brookhaven National Laboratory, Upton, NY 11973-5000, USA

^cSerbian Academy of Sciences and Arts, Knez Mihailova 35, 11000 Belgrade, Serbia

Abstract. Although first report of InSiTe_3 single crystal synthesis and its structure dates nearly 30 years ago, only a few studies are available up till today. Unlike its related compounds (CrSiTe_3 , CrGeTe_3) which have been intensively studied, and their high and low temperature physical properties are well established, only resistivity and thermal conductivity, as well as theoretical predictions of thermodynamical and mechanical stability of InSiTe_3 were investigated. Probably, one of the main issues causing lack of research data is the proper determination of InSiTe_3 crystal structure, since the literature predicts three different space groups for this material, $P3$, $P\bar{3}$, and $P\bar{3}1m$.

In order to properly investigate InSiTe_3 crystal structure we employed inelastic light scattering technique, and DFT calculations for all suggested crystal structures. Six out of eight and seven out of ten Raman active modes for proposed $P\bar{3}1m$ and $P\bar{3}$ space groups, respectively, are observed and assigned, in agreement with numerical calculations. The theoretical calculations for $P3$ crystal structure are in a strong discrepancy with theoretical results, hence this proposed space group can be neglected. The obtained results suggest the coexistence of two trigonal crystal phases, high symmetry one, $P\bar{3}1m$ and low symmetry $P\bar{3}$ space group. Additionally, to the modes that are theoretically predicted, at around 500 cm^{-1} the A_{1g}/A_g “splitting” mode is detected. The appearance of this peak might be a consequence of local symmetry breaking due to a small difference in lattice parameters of both crystal phases. The temperature dependence of energies and linewidths of the most prominent Raman active modes show a monotonous decrease in energy and increase in linewidth when the material is heated from 80 K. At around 200 K discontinuities in phonon properties can be observed. Above the same temperature, additional features in Raman spectra between 175 and 300 cm^{-1} only in parallel scattering configuration are present, and may be a consequence of two-phonon processes. The phonon temperature dependence and these additional excitations indicate the presence of some kind of phase transition above 200 K. Due to the lack of theoretical and experimental studies the origin and type of this transition remains an open question and requires further analysis.

**21. СИМПОЗИЈУМ ФИЗИКЕ
КОНДЕНЗОВАНЕ МАТЕРИЈЕ**
**THE 21st SYMPOSIUM ON
CONDENSED MATTER PHYSICS**

BOOK OF ABSTRACTS



Uniaxial Strain-Induced Changes in Vibrational Modes of FeSe

J. Pešić^a, A. Šolajić^a, A. Milosavljević^a and N. Lazarević^a

*^aCenter for Solid State Physics and New Materials, Institute of Physics Belgrade,
University of Belgrade, Pregrevica 118, 11080 Belgrade, Serbia*

Abstract. Strain application is an effective method for manipulating the characteristics of materials, and it proves particularly valuable in investigating the impact of local crystal structure changes on physical properties. Iron-based superconductors are ideal candidates for studying this strain dependence due to their heightened sensitivity to variations in crystal structure. Among these superconductors, FeSe stands out as a notable example that showcases the intricate relationship between superconductivity, magnetism, and electronic nematicity. This interplay can be adjusted through both chemical substitution and the application of physical pressure. In this study, we present a comparison between first-principle calculations and Raman spectroscopy to examine the evolution of vibrational modes in strained FeSe superconductors. Using density functional theory, we conducted a comprehensive computational investigation on bulk FeSe crystals, subjecting them to in-plane uniaxial strain ranging from -2% to 2%. Our primary focus was to analyze the impact of straining the lattice constant and the resulting symmetry distortion on the distinctive A_{1g} and B_{1g} modes of FeSe. These numerical findings were then compared to experimental data obtained from Raman measurements, which allowed us to study the trends in changes of the A_{1g} and B_{1g} modes with applied strain.

**21. СИМПОЗИЈУМ ФИЗИКЕ
КОНДЕНЗОВАНЕ МАТЕРИЈЕ**
**THE 21st SYMPOSIUM ON
CONDENSED MATTER PHYSICS**

BOOK OF ABSTRACTS



Strain-Controlled Electronic and Optical Properties of hBN/InTe and hBN/GaTe Heterostructures

Andrijana Šolajić^a, Jelena Pešić^a

*^aCenter for Solid State Physics and New Materials, Institute of Physics Belgrade,
University of Belgrade, Pregrevica 118, 11080 Belgrade, Serbia*

Abstract. Van der Waals heterostructures have been extensively researched recently, as their rich physics and new effects not present in their component materials alone, make them prominent for applications in modern nanodevices [1,2]. The application of strain provides more flexibility to tune the properties of such structures, as well as to utilize them in devices such as precise sensors and detectors [3]. Here we present the study of novel hBN/InTe and hBN/GaTe heterostructures under biaxial strain, which are previously shown as an excellent broad-spectrum absorbers [4]. Using density functional theory, we investigate the effect of strain on their electrical and optical properties. We demonstrate how the strain can influence the electronic structure and allow the fine-tuning of the band gap. The absorption spectrum changes accordingly, enhancing specific parts of the absorption function with different strain intensities.

REFERENCES

1. Geim A. K. and Grigorieva I. V. 2013 *Nature* 499 419–425
2. Liu Y., Weiss N. O., Duan X, Cheng H. C., Huang Y., 2016, *Nature Reviews Materials* 1 1–17
3. Zhang J., Lang X., Zhu Y. and Jiang Q., 2018, *Physical Chemistry Chemical Physics* 20 17574–17582.
4. Solajic A. and Pesic J., 2022, *Journal of Physics: Condensed Matter* 34 345301

**21. СИМПОЗИЈУМ ФИЗИКЕ
КОНДЕНЗОВАНЕ МАТЕРИЈЕ**
**THE 21st SYMPOSIUM ON
CONDENSED MATTER PHYSICS**

BOOK OF ABSTRACTS



Lattice dynamics and phase transitions in $\text{Mn}_3\text{Si}_2\text{Te}_6$

S. Djurdjić Mijin^{1,2}, A. Šolajić¹, J. Pešić¹, Y. Liu^{3,*}, C. Petrovic³, M. Bockstedte⁴, A. Bonanni⁵, Z. V. Popović^{1,6} and N. Lazarević¹

¹*Institute of Physics Belgrade, University of Belgrade, Pregrevica 118, 11080 Belgrade, Serbia*

²*Departamento de Física de Materiales, Facultad de Ciencias, Universidad Autónoma de Madrid (UAM), 28049 Madrid, Spain*

³*Condensed Matter Physics and Materials Science Department, Brookhaven National Laboratory, Upton, New York 11973-5000, USA*

⁴*Institute for Theoretical Physics, Johannes Kepler University Linz, Altenbergerstrasse 69, 4040 Linz, Austria*

⁵*Institute of Semiconductor and Solid-State Physics, Johannes Kepler University Linz, Altenbergerstrasse 69, 4040 Linz, Austria*

⁶*Serbian Academy of Sciences and Arts, Knez Mihailova 35, 11000 Belgrade, Serbia*

**Present address: Los Alamos National Laboratory, Los Alamos, New Mexico 87545, USA*

Abstract. Quasi-two-dimensional materials, known for their easy exfoliation to a monolayer and unique optical and transport properties, create a platform for experimental investigation of various low-dimensional phenomena, such as low-dimensional magnetism. This, together with their potential application in spintronics, nanoelectronics, data storage, biomedicine, and as a platform for magneto-optoelectronic devices puts these materials in the center of extensive experimental studies. Aiming to provide much needed deeper insight into these systems, we have investigated the vibrational properties of ferrimagnetic $\text{Mn}_3\text{Si}_2\text{Te}_6$ single crystals using Raman spectroscopy. Fourteen out of eighteen Raman-active modes were observed in our spectra and assigned according to the trigonal symmetry. Additional peaks, which obey the A_{1g} selection rules, were attributed to the overtones. The obtained experimental results were compared to the density functional theory calculations and found to be in a good agreement. The temperature evolution of phonon properties of the two most prominent peaks reveal three subsequent, possible magnetic, phase transitions at $T_1=142.5$ K, $T_2=190$ K, and $T_3=285$ K which have significant impact on the strength of the spin-phonon interaction in $\text{Mn}_3\text{Si}_2\text{Te}_6$. These are likely caused by the competition between the various magnetic states, close in energy. This research provides comprehensive insight into the lattice dynamics, and gives arguments to support the existence of competing short-range magnetic phases in $\text{Mn}_3\text{Si}_2\text{Te}_6$.

Abstract book of the International meeting on superconducting quantum
materials and nanodevices

17 to 21 April 2023



**Friday 21 April
08:55-09:20 Jelena Pešić**

EVOLUTION OF VIBRATIONAL MODES OF FeSe UNDER UNIAXIAL STRAIN

J. Pešić*, A. Šolajić, A. Milosavljević and N. Lazarević

Center for Solid State Physics and New Materials, Institute of Physics Belgrade, University of Belgrade, Pregrevica 118, 11080 Zemun, Serbia

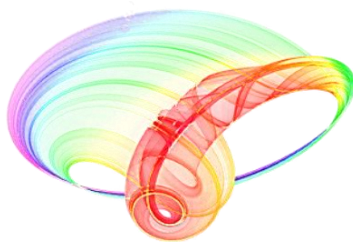
**Presenting author: yelena@ipb.ac.rs*

Application of strain is one of the effective ways to engineer the various properties of materials. Iron-based superconductors are suitable materials to study the strain dependence on physical properties due to their high sensitivity to variations in the local crystal structure. Among the iron-based superconductor family, FeSe is prominent example of the interplay between superconductivity, magnetism, and electronic nematicity, which can be tuned both by chemical substitution and application of physical pressure.

Here we present the first principle study compared with Raman spectroscopy of evolution of vibrational modes of the strained FeSe superconductor. We performed systematic computational study on bulk FeSe crystals with applying in-plane uniaxial strain ranging from -2% to 2% using density functional theory formalism. We focus on the effect of the straining of the lattice constant, and consequent symmetry distortion, on characteristic A_{1g} and B_{1g} modes of FeSe. These numerical findings are compared with experimental data from Raman measurements studying the trend of changes of A_{1g} and B_{1g} modes with applied strain.

The authors acknowledge funding provided by the Institute of Physics Belgrade, through a grant from the Ministry of Science, Technological Development and Innovations of the Republic of Serbia. The work was supported by the Science Fund of the Republic of Serbia, PROMIS, No. 6062656, StrainedFeSC.

Book of abstracts



IX International School and Conference on Photonics

PHOTONICA2023

with joint events:

Understanding interaction light - biological surfaces: possibility for new electronic materials and devices

&

Biological and bioinspired structures for multispectral surveillance

&

Quantum sensing integration within microfluidic Lab-on-a Chips for biomedical applications

&

Advanced Biophysical Methods for Soil Targeted Fungi-Based Biocontrol Agents

August 28 - September 01, 2023, Belgrade, Serbia

Editors

Jelena Potočnik, Maja Popović, Dušan Božanić

Vinča Institute of Nuclear Sciences – National Institute of the Republic of Serbia, University of Belgrade

Belgrade, 2023

ABSTRACTS OF TUTORIAL, KEYNOTE, INVITED LECTURES,
PROGRESS REPORTS AND CONTRIBUTED PAPERS

of

IX International School and Conference on Photonics

PHOTONICA2023

August 28 - September 01, 2023, Belgrade, Serbia

Editors

Jelena Potočnik, Maja Popović, Dušan Božanić

Publisher

Vinča Institute of Nuclear Sciences – National Institute of the Republic of
Serbia, University of Belgrade
Mike Petrovića Alasa 12-14
11351 Vinča, Belgrade, Serbia

Printed by

Serbian Academy of Sciences and Arts

Number of copies

200

ISBN 978-86-7306-165-8

ISBN 978-86-7306-168-9 (Online)



This work is licensed under a Creative Commons Attribution-NonCommercial-NoDerivatives 4.0 International License, <http://creativecommons.org/licenses/by-nc-nd/4.0/>

Strain-induced modulation of electronic and optical properties in hBN/group III monochalcogenide heterostructures

A. Solajic and J. Pesic

*Laboratory for 2D Materials, Center for Solid State Physics and New Materials, Institute of Physics Belgrade,
University of Belgrade, Pregrevica 118, 11080 Belgrade, Serbia
e-mail: solajic@ipb.ac.rs*

Van der Waals heterostructures, an intriguing class of materials composed of stacked two-dimensional layers held together by weak van der Waals (vdW) forces, have garnered significant attention in recent research. These structures exhibit a plethora of unique physics and novel effects that are absent in their constituent materials alone, rendering them highly promising for applications in modern nanodevices [1,2]. One of notable advantage lies in their remarkable manipulability – the weak nature of the vdW forces enables the easy manipulation of individual layers, offering precise control over their electronic and optical properties. This unprecedented level of control opens up a vast realm of possibilities for designing and fabricating materials with tailored characteristics, paving the way for numerous cutting-edge applications in modern nanodevices, including high performance transistors, solar cells, advanced lithium-ion batteries, and state-of-the-art light-emitting devices and photodetectors.

The application of strain provides even greater flexibility in tuning the properties of such structures, as well as exploiting them in devices such as highly precise sensors and detectors [3]. In this study, we focus on investigating novel heterostructures based on hBN and group III monochalcogenides (MX) subjected to biaxial strain. Some of them have shown exceptional potential for broad-spectrum absorbers [4], while the inclusion of hBN layer offers an excellent protection from oxidation, a common issue faced by MX materials when exposed to air. Using density functional theory, we investigate the effect of strain on their electrical and optical properties. Our findings reveal the profound impact of strain on the electronic structure, enabling precise fine-tuning of the band gap. Moreover, the absorption spectrum undergoes significant changes in response to different strain intensities, thereby enhancing specific regions of the absorption function.

REFERENCES

- [1] A.K. Geim, I.V. Grigorieva, *Nature* 499, 419 (2013).
- [2] Y. Liu, *Nat. Rev. Mater.* 1, 1 (2016).
- [3] J. Zhang *et al.*, *Phys. Chem. Chem. Phys.* 20, 17574 (2018).
- [4] A. Solajic, J. Pesic, *J. Phys. Condens. Matter* 34, 345301 (2022).

INSTITUTE OF TECHNICAL SCIENCES OF SASA
MATERIALS RESEARCH SOCIETY OF SERBIA

Programme and the Book of Abstracts

**TWENTIETH YOUNG RESEARCHERS' CONFERENCE
MATERIALS SCIENCE AND ENGINEERING**

Belgrade, November 30 – December 2, 2022



Book title:

Twentieth Young Researchers' Conference - Materials Science and Engineering:
Programme and the Book of Abstracts

Publisher:

Institute of Technical Sciences of SASA

Knez Mihailova 35/IV, 11000 Belgrade, Serbia

Tel: +381-11-2636994, 2185263, <http://www.itn.sanu.ac.rs>

Conference organizers:

Materials Research Society of Serbia, Belgrade, Serbia

Institute of Technical Sciences of SASA, Belgrade, Serbia

Editor:

Dr. Smilja Marković

Technical Editor:

Aleksandra Stojičić and Dr. Ivana Dinić

Cover page: Ivana Stojković Simatović and Smilja Marković

Cover: Nebojša Labus

Printing:

Gama Digital Centar doo

Adresa: Otona Zupančiča 19 - Grafičko medijska škola, 11070 Belgrade, Serbia

Tel: +381-62 880 06 71

<http://www.gdc.rs>

Publication year: 2022

Print-run:

120 copies

CIP - Каталогизacija у публикацији - Народна библиотека Србије, Београд

66.017/.018(048)

YOUNG Researchers' Conference Materials Science and Engineering (20 ; 2022 ; Beograd)

Programme ; and the Book of Abstracts / Twentieth Young Researchers' Conference Materials Science and Engineering, November 30 % December 2, 2022, Belgrade, Serbia ; [organized by] Materials Research Society of Serbia [and] Institute of Technical Sciences of SASA ; [editor Smilja Marković]. - Belgrade : Institute of Technical Sciences of SASA, 2022 (Beograd : Gama digital centar). - XXI, 98 str. ; 23 cm

Tiraž 120. - Registar.

ISBN 978-86-80321-37-0

1. Društvo za istraživanje materijala Srbije (Beograd) 2. Institut
tehničkih nauka SANU (Beograd)

a) Наука о материјалима - Апстракти b) Технички материјали - Апстракти

COBISS.SR-ID 80584457

7-1

Crystal structure of InSiTe_3 studied by Raman spectroscopy

Ana Milosavljević¹, Sanja Đurđić¹, Tea Belojica¹, Andrijana Šolajić¹, Jelena Pešić¹, Bojana Višić¹, Yu Liu², Cedomir Petrović², Zoran V. Popović^{1,3}, Nenad Lazarević¹

¹*Center for Solid State Physics and New Materials, Institute of Physics Belgrade, University of Belgrade, Pregrevica 118, 11080 Belgrade, Serbia,* ²*Condensed Matter Physics and Materials Science Department, Brookhaven National Laboratory, Upton, NY 11973-5000, USA,* ³*Serbian Academy of Sciences and Arts, Knez Mihailova 35, 11000 Belgrade, Serbia*

Even though the first report of InSiTe_3 single crystal synthesis and its structure dates from about 30 years ago, unlike its related compounds (CrSiTe_3 , CrGeTe_3), there has been only a few studies available. One of the reasons behind the lack of research data is the fact that its crystal structure is not unambiguously determined. Raman scattering study of InSiTe_3 reveals presence of six ($3A_{1g} + 3E_g$) out of eight and seven ($5A_g + 2E_g$) out of ten Raman active modes for proposed $P\bar{3}1m$ and $P\bar{3}$ space groups, respectively. These results suggest the coexistence of two trigonal crystal phases, high symmetry one, $P\bar{3}1m$ and a lower symmetry one, which corresponds to $P\bar{3}$ space group. The theoretical predictions obtained by DFT calculations for both space group support this scenario. In addition to the symmetry predicted modes, at around 500 cm^{-1} a mode ascribed to the A_{1g}/A_g mode „splitting“ is detected. The emergence of additional peak could be a consequence of local symmetry breaking due to a small difference in lattice parameters of both crystal phases. The temperature dependence of energies and linewidths of most prominent Raman active modes is also presented in the temperature range from 80 to 300 K. Monotonous decrease in energy and increase in linewidth is present upon heating up to 200 K. Around this temperature discontinuities in properties of all analyzed modes are detected. Yet, due to lack of theoretical and experimental studies of this material this anomaly still remains an open question.

MATERIALS RESEARCH SOCIETY OF SERBIA
INSTITUTE OF TECHNICAL SCIENCES OF SASA

Programme and the Book of Abstracts

**NINETEENTH YOUNG RESEARCHERS' CONFERENCE
MATERIALS SCIENCE AND ENGINEERING**

Belgrade, December 1-3, 2021



Book title:

Nineteenth Young Researchers' Conference - Materials Science and Engineering:
Program and the Book of Abstracts

Publisher:

Institute of Technical Sciences of SASA

Knez Mihailova 35/IV, 11000 Belgrade, Serbia

Tel: +381-11-2636994, 2185263, <http://www.itn.sanu.ac.rs>

Conference organizers:

Materials Research Society of Serbia, Belgrade, Serbia

Institute of Technical Sciences of SASA, Belgrade, Serbia

Editor:

Dr. Smilja Marković

Technical Editor:

Aleksandra Stojičić

Cover page: Aleksandra Stojičić and Milica Ševkušić

Cover: Milica Ševkušić

Printing:

Gama digital centar

Autoput No. 6, 11070 Belgrade, Serbia

Tel: +381-11-6306992, 6306962

<http://www.gdc.rs>

Publication year: 2021

Print-run:

120 copies

CIP - Каталогизација у публикацији

Народна библиотека Србије, Београд

66.017/.018(048)

YOUNG Researchers Conference Materials Sciences and Engineering (19 ; 2021 ; Beograd)

Program ; and the Book of abstracts / Nineteenth Young Researchers' Conference Materials Science and Engineering, December 1-3, 2021, Belgrade, Serbia ; [organized by] Materials Research Society of Serbia & Institute of Technical Sciences of SASA ; [editor Smilja Marković]. - Belgrade : Institute of Technical Sciences of SASA, 2021 (Belgrade : Gama digital centar). - XVIII, 86 str. : ilustr. ; 23 cm

Tiraž 120. - Registar.

ISBN 978-86-80321-36-3

а) Наука о материјалима -- Апстракти б) Технички материјали – Апстракти

COBISS.SR-ID 51231241

12-1

Raman Spectroscopy of Quasi-two-dimensional transition metal trihalides

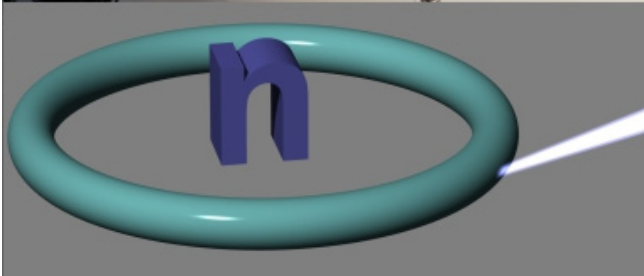
S. Djurdjić Mijin¹, AM Milinda Abeykoon², A. Solajić¹, A. Milosavljević¹, J. Pešić¹, M. Šćepanović¹, Y. Liu³, A. Baum^{4,5}, C. Petrović³, N. Lazarević¹, Z. V Popović^{1,6}

¹*Center for Solid State Physics and New Materials, Institute of Physics Belgrade, University of Belgrade, Pregrevica 118, 11080 Belgrade, Serbia,* ²*National Synchrotron Light Source II, Brookhaven National Laboratory, Upton, New York 11973,* ³*Condensed Matter Physics and Materials Science Department, Brookhaven National Laboratory, Upton, New York 11973-5000, United States,* ⁴*Walther Meissner Institut, Bayerische Akademie der Wissenschaften, 85748 Garching, Germany,* ⁵*Fakultät für Physik E23, Technische Universität München, 85748 Garching, Germany,* ⁶*Serbian Academy of Sciences and Arts, Knez Mihailova 35, 11000 Belgrade, Serbia*

Theoretically speaking, the restriction of only one dimension in a three-dimensional material could result in its layered quasi-two-dimensional (2D) analog which has completely unpredictable properties and therefore hosts various unexpected physical phenomena. Successful exfoliation of quasi-2D grapheme by A. Geim's group in 2004 did not only confirm these expectations and create a platform for experimental investigation of low-dimensional phenomena, but also paved the way for the next-generation nanoelectronic devices. All of the above mentioned strongly contributed to the extensive research on the fundamental properties of quasi-2D materials. Great effort has been put towards realization of a magnetic atomically thin crystals which would open up the opportunities of exploring, or even exploiting, of different 2D magnetic states, expand the scope of their possible applications, and point to the possible emergence of a new quantum state of matter. That being said, it is not surprising that the experimental confirmation of 2D magnetism in transition-metal-trihalides (TMTs) caused a stir in scientific community. In an effort to better understand fundamental properties of these materials we have performed the Raman Spectroscopy Study of the two TMT members – CrI₃ and VI₃, both of which have been confirmed to host low-dimensional magnetism. This experimental technique was used to probe a reported phase transition in CrI₃ and crystal structure of VI₃. The phase transition, which transforms the low-temperature $R\bar{3}$ structure into the high-temperature C2/m structure, with potential co-existence, has been observed at 220 K. Our findings confirm the mentioned phase transition but at much lower temperature of 180 K, and no co-existence has been tracked. Our investigation into the crystal structure of VI₃ tried to give an answer to the long unsolved mystery whether at room temperatures VI₃ crystallizes into a $P3\bar{1}c$, $R\bar{3}$ or C2/m crystal structure. Interestingly, what we have observed points to the coexistence of short-range ordered $P3\bar{1}c$ and long-range ordered $R\bar{3}$ phases.

NESY Winterschool & Symposium

25/02–01/03, 2024



Organizing Committee (MU Leoben)

Rainer T. Lechner, Chair of Physics
Oskar Paris, Chair of Physics
Gerhard Popovski, Chair of Physics
H. Noll & N. Aichberger, Chair of Physics

Program Committee

Roland Resel, TU Graz
Erwin Jericha, TU Wien
Klaudia Hradil, XRC, TU Wien
Ronald Miletich-Pawliczek, Univ. Wien
Rainer T. Lechner, MU Leoben
Oskar Paris, MU Leoben

Infos & Registration:

nesy.unileoben.ac.at

12th European NESY Winterschool & Symposium on Neutron and Synchrotron Radiation

including topical highlight lectures on

Crystallographic Methods

&

The 1st Austrian Crystallography Days ACD' 24

Bad Aussee (Austria), 25.02–01.03, 2024



The school & symposium will cover introductory tutorials in the morning, **contributed scientific talks** in the late afternoon, **topical highlight lectures** in the evening, and a **continuous poster session**. Graduate students and young scientists just starting to work in this field are particularly encouraged to register and to submit an abstract.



The school venue, the **JUFA Bad Aussee** in Styria, is located near the winter resort *Loser* in the *Salzkammergut*, which is quite the **center of Austria's Alps**. Thus excellent possibilities for winter activities are nearby, but also the thermal spa *Narzisstherme*!

 Bundesministerium
Bildung, Wissenschaft
und Forschung

Novel hBN/In(Ga)Te Heterostructures For Wide Spectrum Light Absorbers

Andrijana Solajic and Jelena Pesic

Institute of Physics Belgrade, University of Belgrade, Serbia

yelena@ipb.ac.rs

In recent years, enormous attention given to the exploration and researching of two-dimensional materials has started a whole new era in materials science and countless possibilities for novel devices emerged. Two dimensional group III monochalcogenides have recently attracted quite attention for their wide spectrum of optical and electric properties, being promising candidates for optoelectronic and novel electrical applications¹. However major obstacle in using them in various application arises from the fact they are strongly sensitive and vulnerable to oxygen in air in their pristine form, especially as thin films or single layer. Many studies reveal that monolayers are oxidized fast, almost instantly, after exposure to the air^{2,3}. Here we present two newly designed vdW heterostructures based on hBN (hexagonal boron nitride) and GaTe or InTe monolayer, in order to make them more robust and resistant to mechanical influences while enhancing their optoelectronic properties. Using density functional theory we investigate electronic and optical properties of those heterostructures. Our study reveals them as an excellent candidates for various optoelectronic devices with great capabilities of absorption from visible light to far UV part of spectrum, being exceptionally good for absorbing the UV light. The hBN layer is beneficial⁴ for mechanical protection of sensitive and vulnerable single layers of monochalcogenides like InTe and GaTe, while as we showed, in our heterostructures, electronic and optical properties are not only preserved but even enhanced. Importantly, we demonstrate type of stacking does not affect properties of the heterostructure, making them convenient for experimental realization.

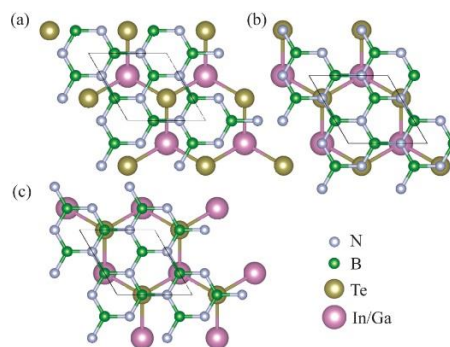


FIG 1. hBN/In(Ga)Te heterostructures. Top view of three possible stacking types, (a) H-top, (b) N-top and (c) B-top

- [1] C. Ren, S. Wang, H. Tian, Y. Luo, J. Yu, Y. Xu, and M. Sun, First principles investigation on electronic properties and band alignment of group III monochalcogenides, *Scientific reports* 9, 1 (2019)
- [2] M. Rahaman, R. D. Rodriguez, M. Monecke, S. A. Lopez-Rivera, and D. R. T. Zahn, GaSe oxidation in air: from bulk to monolayers, *Semiconductor Science and Technology* 32, 105004 (2017).
- [3] Y. Guo, S. Zhou, and J. Zhao, Oxidation behaviors of two-dimensional metal chalcogenides, *ChemNanoMat* 6, 838 (2020).
- [4] D. A. Bandurin, A. V. Tyurnina, L. Y. Geliang, A. Mishchenko, V. Zolotarev, S. V. Morozov, R. K. Kumar, R. V. Gorbachev, Z. R. Kudrynskyi, S. Pezzini, et al., High electron mobility, quantum hall effect and anomalous optical response in atomically thin InSe, *Nature nanotechnology* 12, 223 (2017)



<http://www.sfkm.ac.rs/>

The 20th Symposium on Condensed Matter Physics

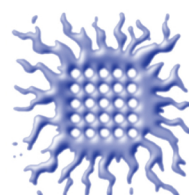
BOOK OF ABSTRACTS



University of Belgrade,
Faculty of Physics



Institute of Physics Belgrade



Vinca Institute
of Nuclear Sciences



Serbian Academy
of Sciences and Arts



Ministry of Education, Science and
Technological Development,
Republic of Serbia

Strain effects on vibrational properties in hexagonal 2D materials from the first principles – doped graphene and MgB₂- monolayer study

Jelena Pešić^a, Andrijana Šolajić^a and Radoš Gajić^a

^aCenter for Solid State Physics and New Materials,
Institute of Physics Belgrade, University of Belgrade, Serbia

Abstract. We present computational study within the density functional theory framework of the effects of application of the (equi) biaxial strain on the two isostructural two-dimensional materials, Li-intercalated graphene and magnesium-diboride monolayer, both electron-phonon mediated superconductors [1-4]. The application of the tensile biaxial strain causes softening of the phonons, enhancing the total electron-phonon interaction and resulting in significantly a higher critical temperature. By application of the strain, we achieve the increase of the density of states at the Fermi level and softening of the modes [2,4,5]. Without drastically modifying the structure, with experimentally achievable strain [2,5], we significantly affect the electron-phonon coupling strength.

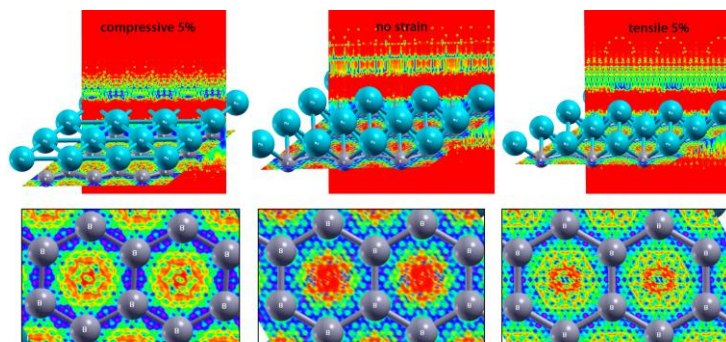


FIGURE 1. Electron localization function (ELF) for MgB₂-mono nonstrained and compressively (left) and tensely (right) strained. Top: 3D projection of ELF with focus on the Mg layer. Bottom: ELF projection on the B layer.

REFERENCES

1. G. Profeta, M. Calandra, F. Mauri, *Nature Physics* **8**, 131–134 (2012).
2. J. Pešić, R. Gajić, K. Hingerl, M. Belić, *Europhysics Letters*, **108** (6), 67005, (2014)
3. J. Bekaert, A. Aperis, B. Partoens, P.M. Oppeneer, M.V. Milošević, *Physical Review B* **96** (9), 094510, (2017)
4. J. Pešić, I. Popov, A. Šolajić, V. Damjanović, K. Hingerl, M. Belić, R. Gajić, *Condensed Matter* **4** (2), 37 (2019)
5. V. Čelebonović, J. Pešić, R. Gajić, B. Vasić, A. Matković, *Journal of Applied Physics* **125** (15), 154301 (2019)

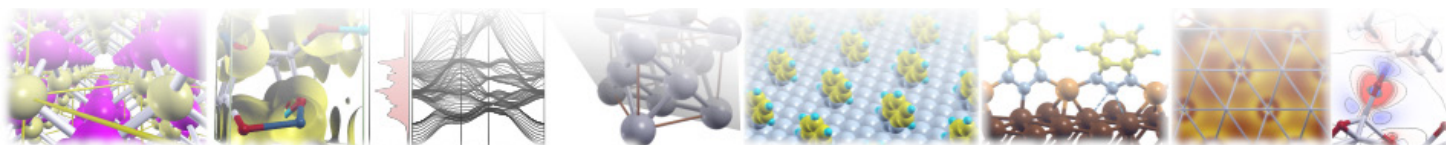


QUANTUM ESPRESSO

September 15–20, 2019

Ljubljana, Slovenia

Summer School on Advanced Materials and Molecular Modelling



BOOK OF ABSTRACTS

September 15 – 20, 2019

Jožef Stefan Institute, Ljubljana



QUANTUM ESPRESSO
FOUNDATION



DRIVING
THE EXASCALE
TRANSITION



Jožef Stefan
Institute
Ljubljana, Slovenia



Centre Européen de Calcul Atomique et Moléculaire



EUROTECH

Imagine. Build. Succeed.

BOOK OF ABSTRACTS: Quantum ESPRESSO Summer School on Advanced Materials and Molecular Modelling

Publisher:
Jožef Stefan Institute, Jamova 39, Ljubljana, Slovenia

Edited by:
Anton Kokalj and Matjaž Dlouhy

Layout by Matjaž Dlouhy and Anton Kokalj
Authors of the front page: Anton Kokalj and Matjaž Dlouhy

Katalogni zapis o publikaciji (CIP) pripravili v Narodni in univerzitetni knjižnici v Ljubljani
COBISS.SI-ID=301641728
ISBN 978-961-264-154-2 (pdf)

This book of abstracts is available online at <http://qe2019.ijs.si/qe2019-book-of-abstracts.pdf>

Ljubljana, Slovenia, 2019

Poster session (part I) / **15**

Electron-phonon interaction and superconductivity in graphene doped with metal atoms

Author: Ms. ŠOLAJIĆ, Andrijana ¹

Co-Author: Dr. PESIC, Jelena ¹

¹ *Institute of Physics Belgrade, University of Belgrade*

Corresponding Author: solajic@ipb.ac.rs

With its outstanding mechanical and electrical properties [1,2], graphene is predicted to have a plenty of applications and has gained enormous research focus in last years. Furthermore, its already superb properties can easily be tuned by various structure manipulations including the applied strain, controlled defects, exposure to electrical or magnetic field, or doping. As opposed to pristine graphene, when doped with some alkali metal atoms adsorbed on its surface in a manner similar to the graphite intercalation compounds, graphene becomes superconducting, with critical temperatures up to 11K [3,4]. This raised an interest in research of superconductivity in graphene, which is not present in its pristine form. Here we investigate the electron-phonon interaction several structures based on graphene doped with metal atoms. In the framework of density functional theory and Eliashberg theory, we calculate the electron-phonon coupling and estimate the superconducting critical temperatures.

References:

- [1] Katsnelson, M., Novoselov, K., Geim, A., Nat. Phys. 2(9), 620–625 (2006)
- [2] Bolotin, K., Sikes, K., Jiang, et al., Solid State Commun. 146(9), 351–355 (2008)
- [3] Profeta, G., Calandra, M., Mauri, F., Nat. Phys. 8(2), 131–134 (2012)
- [4] Pešić, J., Gajić, R., Hingerl, K., Belić, M., EPL 108(6), 67005 (2014)

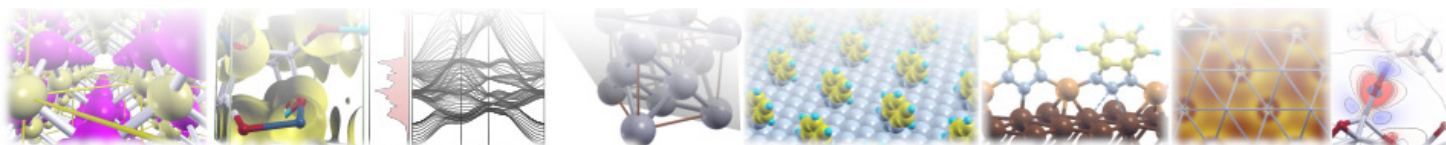


QUANTUM ESPRESSO

September 15–20, 2019

Ljubljana, Slovenia

Summer School on Advanced Materials and Molecular Modelling



BOOK OF ABSTRACTS

September 15 – 20, 2019

Jožef Stefan Institute, Ljubljana



QUANTUM ESPRESSO
FOUNDATION



DRIVING
THE EXASCALE
TRANSITION



Jožef Stefan
Institute
Ljubljana, Slovenia



Centre Européen de Calcul Atomique et Moléculaire



EUROTECH

Imagine. Build. Succeed.

BOOK OF ABSTRACTS: Quantum ESPRESSO Summer School on Advanced Materials and Molecular Modelling

Publisher:
Jožef Stefan Institute, Jamova 39, Ljubljana, Slovenia

Edited by:
Anton Kokalj and Matjaž Dlouhy

Layout by Matjaž Dlouhy and Anton Kokalj
Authors of the front page: Anton Kokalj and Matjaž Dlouhy

Kataložni zapis o publikaciji (CIP) pripravili v Narodni in univerzitetni knjižnici v Ljubljani
COBISS.SI-ID=301641728
ISBN 978-961-264-154-2 (pdf)

This book of abstracts is available online at <http://qe2019.ijs.si/qe2019-book-of-abstracts.pdf>

Ljubljana, Slovenia, 2019

Poster session (part II) / 14

Computational study of vibrational properties of chemically exfoliated titanium carbide MXenes - Ti₃C₂ and TiC₂Author: Dr. PEŠIĆ, Jelena¹Co-Author: Ms. ŠOLAJIĆ, Andrijana²¹ *Institute of Physics Belgrade, University of Belgrade*² *Institute of Physics Belgrade, University of Belgrade*

Corresponding Author: yelena@ipb.ac.rs

With the increased attention to 2D materials beyond graphene a new large family extending the world of 2D materials was discovered in 2011 [1]. This is the group of early transition metal carbides and/or carbo-nitrides labeled as MXenes. MXenes are synthesized by exfoliating MAX phase ternary carbides, nitrides, or carbonitrides: $Mn+1AX_n$, where M is an early transition metal, A is a III or IV A-group element and X is carbon/nitrogen. Acid etching is used to remove the A layer, resulting in the formation of $Mn+1X_n$ MXene [2]. The rich chemistries and unique morphologies of MXenes, in addition to their good electronic conductivities, render them strong candidates for many applications that range from sensors and electronic device materials, conductive reinforcement additives to polymers, electrochemical energy storage materials, among many others [3, 4]. MXenes can potentially be used as additives to polymers to fabricate composites with outstanding mechanical properties and good electrical conductivities [5].

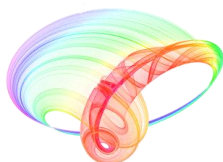
We present a comparative study on the vibrational properties of Ti₃C₂ and TiC₂ using density functional theory (DFT) calculations. Both Raman and infrared-active vibrational modes are predicted and conclusively assigned to experimental spectra as a guide for characterization. After the synthesis, HF etched MXenes were characterized using Raman spectroscopy and then further processed as additive to poly(methyl methacrylate) (PMMA) [6].

The computational analysis enabled proper assignation of MXenes modes in spectra but also modes of residual products of synthesis, TiO₂ and amorphous carbon. Further comparative analysis of DFT calculations with Raman spectra of MXene/PMMA composite offers insight in effects of PMMA matrices on MXenes modes.

References:

- [1] M. Naguib, et al., Two-Dimensional Nanocrystals Produced by Exfoliation of Ti₃AlC₂, *Advanced Materials*, 23, 4248 (2011)
- [2] A. Alhabeib, et al., Guidelines for Synthesis and Processing of Two-Dimensional Titanium Carbide (Ti₃C₂T_xMXene), *Chemistry of Materials*, 29, 7633 (2017)
- [3] B. Anasori, et al., 2D Metal Carbides and Nitrides (MXenes) for Energy Storage, *Nature Reviews Materials*, 2, 16098 (2017)
- [4] K. Hantanasirisakul, et al., Fabrication of Ti₃C₂T_x MXene Transparent Thin Films with Tunable Optoelectronic Properties, *Advanced Electronic Materials*, 2, 1600050 (2016)
- [5] X. Zhang et al. Ultrathin nanosheets of MAX phases with enhanced thermal and mechanical properties in polymeric compositions: Ti₃Si(0.75)Al(0.25)C₂ *Angew. Chem. Int. Ed.* 52, 4361, (2013)
- [6] J. Pešić et al., Structural and Optical Characterization of MXene Ti₃C₂ /PMMA (Polymethyl methacrylate) nanocomposite, manuscript in preparation

Book of abstracts



PHOTONICA2019

**The Seventh International School and Conference on
Photonics, 26 August – 30 August 2019, Belgrade, Serbia**

**& Machine Learning with Photonics Symposium
(ML-Photonica 2019)**



& ESUO Regional Workshop



& COST action CA16221



Editors: Milica Matijević, Marko Krstić and Petra Beličev

Belgrade, 2019

ABSTRACTS OF TUTORIAL, KEYNOTE, INVITED LECTURES,
PROGRESS REPORTS AND CONTRIBUTED PAPERS

of

The Seventh International School and Conference on Photonics
PHOTONICA2019, 26 August – 30 August 2019, Belgrade, Serbia

and

Machine Learning with Photonics Symposium

and

ESUO Regional Workshop

Editors

Milica Matijević, Marko Krstić and Petra Beličev

Technical Assistance

Danka Stojanović and Goran Gligorić

Publisher

Vinča Institute of Nuclear Sciences

Mike Petrovića Alasa 12-14, P.O. Box 522

11000 Belgrade, Serbia

Printed by

Serbian Academy of Sciences and Arts

Number of copies

300

ISBN 978-86-7306-153-5

Optical and mechanical properties and electron-phonon interaction in graphene doped with metal atoms

A. Šolajić¹, J. Pešić¹ and R. Gajić¹

¹*Institute of Physics Belgrade, University of Belgrade, Pregrevica 118, 11080 Belgrade, Serbia*
e-mail: solajic@ipb.ac.rs

Graphene, the first experimentally realized 2D material with outstanding mechanical and electrical properties as well an excellent optical transparency [1, 2, 3], is predicted to have many applications in various scientific fields [4, 5]. Furthermore, there are numerous ways for modifications of pure graphene that allow precise tuning of its properties or observation of some new effects, including the applied strain, various types of controlled defects, exposure to electrical or magnetic field, or doping. It is known that graphene with alkali metal atoms adsorbed on its surface becomes superconducting with critical temperatures up to 11K [6, 7, 8].

The question remains what happens with optical and mechanical properties of such structures, can we preserve or enhance these superb properties while making graphene superconducting at the same time.

Here we investigate structures based on graphene doped with several metal atoms. Using the Density Functional Theory, we analyze the optical and elastic properties of those structures and calculate the electron-phonon interaction. We discuss the influence of adsorbed atoms on these properties.

REFERENCES

- [1] M. Katsnelson, K. S. Novoselov, A. K. Geim, *Nat. Phys.* 2, 620 (2006).
- [2] K. I. Bolotin et al., *Solid State Commun.* 146, 351 (2008).
- [3] C. Lee et al., *Science* 321, 385 (2008).
- [4] A. C. Ferrari et al., *Nanoscale* 7, 4598 (2015).
- [5] D. Todorović et al., *2D Mater.* 2, 045013 (2015).
- [6] G. Profeta, M. Calandra, F. Mauri, *Nat. Phys.* 8, 131 (2012).
- [7] J. Pešić et al., *EPL* 108, 67005 (2014).
- [8] A. P. Durajski, K. M. Skoczylas, R. Szczeniński, *Phys. Chem. Chem. Phys.* 21, 5925 (2019).



<http://www.sfkm.ac.rs/>

The 20th Symposium on Condensed Matter Physics

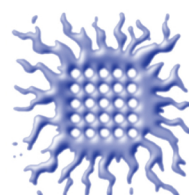
BOOK OF ABSTRACTS



University of Belgrade,
Faculty of Physics



Institute of Physics Belgrade



Vinca Institute
of Nuclear Sciences



Serbian Academy
of Sciences and Arts



Ministry of Education, Science and
Technological Development,
Republic of Serbia

Lattice dynamics and phase transitions in $\text{Fe}_{3-x}\text{GeTe}_2$

A. Milosavljević^a, A. Šolajić^a, S. Djurdjić Mijin^a, J. Pešić^a, B. Višić^a, Y. Liu^b, C. Petrovic^b, N. Lazarević^a and Z. V. Popović^c

^aCenter for Solid State Physics and New Materials, Institute of Physics Belgrade, University of Belgrade, Pregrevica 118, 11080 Belgrade, Serbia

^bCondensed Matter Physics and Materials Science Department, Brookhaven National Laboratory, Upton, New York 11973-5000, USA

^cCenter for Solid State Physics and New Materials, Institute of Physics Belgrade, University of Belgrade, Pregrevica 118, 11080 Belgrade, Serbia and Serbian Academy of Sciences and Arts, Knez Mihailova 35, 11000 Belgrade, Serbia

Abstract. A new class of magnetic van der Waals bonded materials has recently become of great interest, as a suitable candidates for various applications. Whereas CrXTe_3 ($X = \text{Si, Ge, Sn}$) and CrX_3 ($X = \text{Cl, Br, I}$) classes maintain low phase transition temperatures even in a monolayer regime, $\text{Fe}_{3-x}\text{GeTe}_2$ has a high bulk transition temperature, between 220 and 230 K, making it a promising applicant.

Here we present DFT calculations of lattice dynamics and Raman spectroscopy measurements of the van der Waals bonded ferromagnet $\text{Fe}_{3-x}\text{GeTe}_2$ [1]. Four out of eight Raman active modes are observed and assigned, in agreement with numerical calculations. The energies and linewidths of the observed modes display an unconventional temperature dependence at about 150 and 220 K, followed by the nonmonotonic evolution of the Raman continuum. Whereas the former can be related to the magnetic phase transition, the origin of the latter anomaly remains an open question.

REFERENCES

1. A. Milosavljević, A. Šolajić, S. Djurdjić-Mijin, J. Pešić, B. Višić, Yu Liu, C. Petrovic, N. Lazarević, and Z. V. Popović. "Lattice dynamics and phase transitions in $\text{Fe}_{3-x}\text{GeTe}_2$." *Physical Review B* 99, no. 21 (2019): 214304.



The Abdus Salam
**International Centre
for Theoretical Physics**



SMR.3191

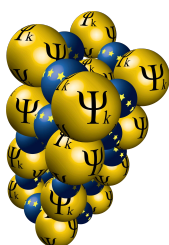
School on Electron-Phonon Physics from First Principles

19 - 23 March 2018

Webpage: <http://indico.ictp.it/event/8301/>

ABSTRACTS OF POSTERS

(in alphabetical order of presenting author)



Electron-Phonon Interaction in Monolayer MgB_2 from the First Principles

Jelena Pešić, Andrijana Šolajić, Radoš Gajić

*Laboratory for graphene, other two-dimensional materials and ordered nanostructures,
Institute of Physics, University of Belgrade, Pregrevica 118, 11080 Zemun, Belgrade Serbia*

In this study magnesium diboride is explored in low-dimensional limit and here are presented structural, electronic, vibrational properties of MgB_2 as a monolayer. Using density functional theory and the isotropic Eliashberg approach we study the electron-phonon interaction in the single layer of MgB_2 showing it is superconductive, presenting it as a two-dimensional materials with a highest critical temperature. We showed that the low-frequency vibrations contribute more in the low-dimensional structures however not to overcome a decrease of coupling in high-frequency region. The calculated critical temperature of 18K, can be further enhanced with application of biaxial strain or by adding one more layer of boron atoms. Further we compare properties of MgB_2 monolayer with structurally and electronically similar superconducting 2D materials, Li and Sr doped graphene.

MATERIALS RESEARCH SOCIETY OF SERBIA
INSTITUTE OF TECHNICAL SCIENCES OF SASA

Programme and the Book of Abstracts

**SEVENTEENTH YOUNG RESEARCHERS' CONFERENCE
MATERIALS SCIENCE AND ENGINEERING**

Belgrade, December 5–7, 2018

Materials Research Society of Serbia

<http://www.mrs-serbia.org.rs/index.php/young-researchers-conference>

Book title:

Seventeenth Young Researchers' Conference - Materials Science and Engineering:
Program and the Book of Abstracts

Publisher:

Institute of Technical Sciences of SASA
Knez Mihailova 35/IV, 11000 Belgrade, Serbia
Tel: +381-11-2636994, 2185263, <http://www.itn.sanu.ac.rs>

Editor:

Dr. Smilja Marković

Technical Editor:

Aleksandra Stojičić

Cover page: Aleksandra Stojičić and Milica Ševkušić

Cover: Modified Photo by Dani Lavi 0007; Wikimedia Commons

(https://commons.wikimedia.org/wiki/File:Belgrade_at_night.jpg); CC BY-SA
4.0

Printer:

Gama digital centar
Autoput No. 6, 11070 Belgrade, Serbia
Tel: +381-11-6306992, 6306962
<http://www.gdc.rs>

Edition:

130 copies

CIP - Каталогизација у публикацији - Народна библиотека Србије, Београд
66.017/.018(048)

YOUNG Researchers Conference Materials Sciences and Engineering (17 ; 2018; Beograd)

Program ; and the Book of Abstracts / Seventeenth Young Researchers' Conference
Materials Sciences and Engineering, December 5-7, 2018, Belgrade, Serbia ; [organized by]
Materials Research Society of Serbia & Institute of Technical Sciences of SASA ; [editor
Smilja Marković]. -Belgrade : Institute of Technical Sciences of SASA, 2018 (Beograd :
Gama digital centar). - XX, 100 str. ; 23 cm

Tiraž 130. - Registar.
ISBN 978-86-80321-34-9

1. Društvo za istraživanje materijala Srbije (Beograd) 2. Institut
tehničkih nauka SANU (Beograd)

a) Наука о материјалима - Апстракт б) Технички материјали - Апстракт
COBISS.SR-ID 270509836

10-6

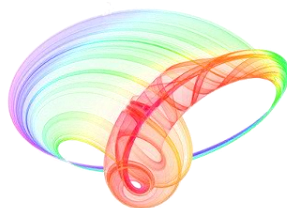
Raman Spectroscopy Study on phase transition in CrI_3 single crystals

Sanja Đurđić¹, Andrijana Šolajić¹, Jelena Pešić¹, Maja Šćepanović¹, Y. Liu²,
Andreas Baum^{3,4}, Čeda Petrović², Nenad Lazarević¹, Zoran V. Popović^{1,5}

¹*Institute of Physics, Pregrevica 118, Belgrade, Serbia,* ²*Brookhaven National Laboratory, Upton, New York 11973-5000, USA,* ³*Walther Meissner Institut, Bayerische Akademie der Wissenschaften, 85748 Garching, Germany,* ⁴*Fakultät für Physik E23, Technische Universität München, 85748 Garching, Germany,* ⁵*Serbian Academy of Sciences and Arts, Knez Mihailova 35, 11000 Belgrade, Serbia*

By virtue of their unique properties and the potential for a wide spectrum of applications, such as the development of functional van der Waals heterostructures, CrI_3 among the other two dimensional materials, has received significant attention in the most recent studies on the ferromagnetic semiconductors. In this study we represent the vibrational properties of CrI_3 single crystals investigated using Raman spectroscopy together with the density functional theory (DFT) calculations. Experimental results show that first-order phase transition from the low-temperature ($R\bar{3}$) to the high-temperature ($C2/m$) phase occurs at 180K with no evidence of the two-phase coexistence. All observed modes, in both phases, are in good agreement with DFT calculations.

Book of abstracts



PHOTONICA2017

The Sixth International School and Conference on Photonics

& COST actions: MP1406 and MP1402



&H2020-MSCA-RISE-2015 CARDIALLY workshop



28 August – 1 September 2017

Belgrade, Serbia

Editors

Marina Lekić and Aleksandar Krmpot

Institute of Physics Belgrade, Serbia

Belgrade, 2017

ABSTRACTS OF TUTORIAL, KEYNOTE, INVITED LECTURES,
PROGRESS REPORTS AND CONTRIBUTED PAPERS

of

The Sixth International School and Conference on Photonics
PHOTONICA2017

28 August – 1 September 2017
Belgrade Serbia

Editors

Marina Lekić and Aleksandar Krmpot

Technical assistance

Marko Nikolić and Danica Pavlović

Publisher

Institute of Physics Belgrade
Pregrevica 118
11080 Belgrade, Serbia

Printed by

Serbian Academy of Sciences and Arts

Number of copies

300

ISBN 978-86-82441-46-5

Ab-initio calculations of electronic and vibrational properties of Sr and Yb-intercalated graphene

A. Šolajić¹, J. Pešić¹ and R. Gajić¹

¹*Institute of Physics, Center for Solid State and New Materials, Belgrade, Serbia*
e-mail: solajic@ipb.ac.rs

In the last couple of years, 2D materials have gained a leading role in material science and have been attracting a great attention due to their unique physical and chemical properties. Intercalation is one of the powerful tools for making 2D materials even more exciting by providing an additional doping and tunable properties.

Graphene, a two-dimensional honeycomb lattice of carbon atoms, possess various fascinating physical, structural and electronic properties, which make it an excellent candidate for applications in electronics and photonics. Structures based on intercalated graphite have been extensively studied, showing many new properties and exotic physics [1,2]. This inspired many to investigate a single or few-layer intercalated graphene.

Intercalated graphene has many extraordinary properties that are not present in pristine graphene [3-6]. It is also different compared to bulk intercalated graphite materials and has great spectra of characteristics induced by various intercalants, usually alkali or alkaline earth metals. This opens new possibilities for further research and a wide range of applications. Although some of those structures have even been realised experimentally [7,8], there are many more to come, with a great potential for both theoretical and experimental investigations. Based on the first principle calculations, such as Density Functional Theory (DFT) and Density Functional Perturbation Theory (DFPT), it is possible to calculate various electronic and optical properties as well as to simulate some of the most used spectroscopic techniques (like IR and Raman spectroscopy). Those methods enable a comparison with existing experimental data, as well as for getting directions for a new research and experiments.

In this paper, we present the results of a DFT study on electronic and vibrational properties of the graphene intercalated with Sr and Yb, taking into account that their corresponding bulk compounds have been mostly investigated so far. The calculations were performed in Quantum Espresso software package [9].

This work is supported by the Serbian MPNTR through Project OI 171005 and by Qatar National Research Foundation through Projects NPRP 7-665-1-12.

REFERENCES

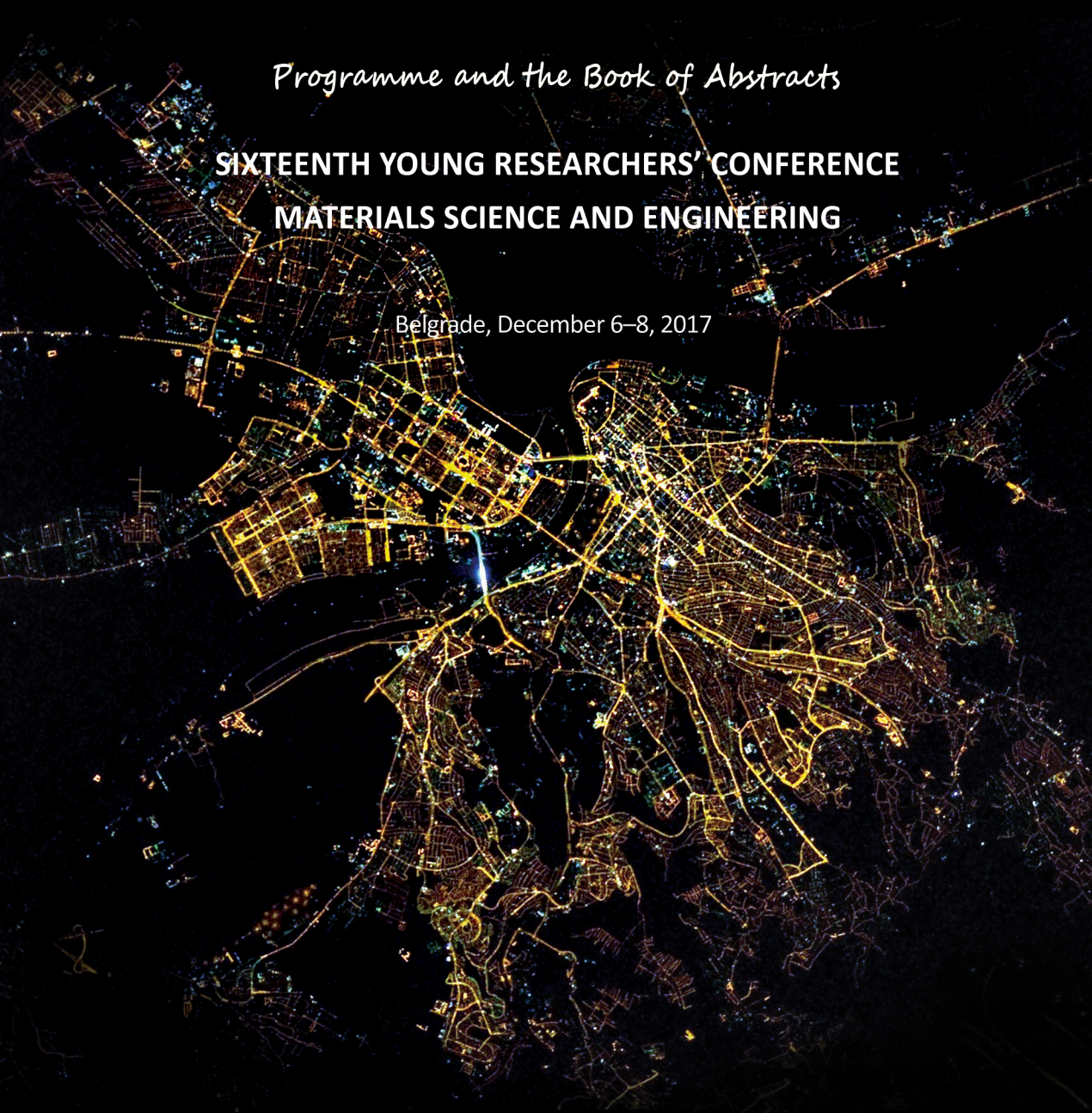
- [1] T. E. Weller, M. Ellerby, S. S. Saxena, R. P. Smith, and N. T. Skipper, *Nat. Phys.* 1, 39 (2005).
- [2] Csányi, G., Littlewood, P. B., Nevidomskyy, A. H., Pickard, C. J., Simons, B. D. *Nat. Phys.* 1, 42–45 (2005).
- [3] Pešić J., Gajić R., Hingerl K. and Belić M., *EPL* 108 67005 (2014).
- [4] J. Chapman, Y. Su, C. A. Howard, D. Kundys, A. N. Grigorenko, F. Guinea, A. K. Geim, I. V. Grigorieva & R. R. Nair, *Scientific Reports* 6, 23254 (2016).
- [5] G. Profeta, M. Calandra, F. Mauri, *Nat. Phys.*, 8, 131 (2012).
- [6] Pešić J., Damjanović V., Gajić R., Hingerl K. and Belić M., *EPL*, 112 6 67006 (2015).
- [7] Kanetani K, Sugawara K, Sato T, Shimizu R, Iwaya K, Hitosugi T, Takahashi T, *PNAS* 109, 19610–19613 (2012).
- [8] Ludbrook, B.M. et al., *PNAS* 112, 11795–11799 (2015).
- [9] P. Giannozzi, et al *J.Phys.:Condens.Matter*, 21, 395502 (2009).

MATERIALS RESEARCH SOCIETY OF SERBIA
INSTITUTE OF TECHNICAL SCIENCES OF SASA

Programme and the Book of Abstracts

**SIXTEENTH YOUNG RESEARCHERS' CONFERENCE
MATERIALS SCIENCE AND ENGINEERING**

Belgrade, December 6–8, 2017



Book title:

Sixteenth Young Researchers' Conference - Materials Science and Engineering:
Program and the Book of Abstracts

Publisher:

Institute of Technical Sciences of SASA
Knez Mihailova 35/IV, 11000 Belgrade, Serbia
Tel: +381-11-2636994, 2185263, <http://www.itn.sanu.ac.rs>

Editor:

Dr. Smilja Marković

Technical Editor:

Aleksandra Stojičić

Cover page: Aleksandra Stojičić and Milica Ševkušić

Front cover: Modified photo by Anatoly Alekseyevich Ivanishin, Exploration 30 ISS Mission, NASA;
Wikimedia Commons

(https://commons.wikimedia.org/wiki/File:Warp_Belgrade_Nightscene_April_2012spatial_subset.jpg);
Public domain

Back cover: Modified Photo by Hons084; Wikimedia Commons

(https://commons.wikimedia.org/wiki/File:Widoki_z_twierdzy_Forte_Mare_na_Herceg_Novi_03.jpg);
CC BY-SA 4.0

Printer:

Gama digital centar
Autoput No. 6, 11070 Belgrade, Serbia
Tel: +381-11-6306992, 6306962, <http://www.gdc.rs>

Edition:

130 copies

CIP - Каталогизација у публикацији - Народна библиотека Србије, Београд

66.017/.018(048)

YOUNG Researchers Conference Materials Sciences and Engineering (16 ; 2017 ; Beograd)

Program ; and the Book of Abstracts / Sixteenth Young Researchers' Conference Materials Sciences and Engineering, December 6-8, 2017, Belgrade, Serbia ; [organized by] Materials Research Society of Serbia & Institute of Technical Sciences of SASA ; [editor Smilja Marković]. - Belgrade : Institute of Technical Sciences of SASA, 2017 (Beograd : Gama digital centar). - XVIII, 78 str. ; 23 cm

Tiraž 130. - Registar.

ISBN 978-86-80321-33-2

1. Društvo za istraživanje materijala Srbije (Beograd) 2. Institut tehničkih nauka SANU (Beograd)

a) Наука о материјалима - Апстрактни b) Технички материјали - Апстрактни

COBISS.SR-ID 250864908

6-1

Nitrogen-doped graphene nanoribbons for oxygen reduction reaction – DFT insights

Ana S. Dobrota, Igor A. Pašti

*University of Belgrade, Faculty of Physical Chemistry,
Studentski trg 12-16, 11158 Belgrade, Serbia*

Increasing energy demands and the need for pollution reduction require development of new energy conversion and storage systems. Fuel cells are thought to be the next generation of chemical power sources, but demand cheap and effective oxygen reduction reaction (ORR) catalysts. Many experimental studies have reported excellent performance of N-doped graphene towards ORR. However, the reasons for such an improvement are still under debate. We investigate how various N-containing groups alter the reactivity of graphene and graphene nanoribbons towards the reactants and intermediates of ORR by means of Density Functional Theory calculations. We discuss which N-groups on graphene promote ORR, and in what way. Based on the obtained results we reveal which N-functional groups provide improved ORR catalytic activity and enhanced selectivity. The importance of including graphene edges into such considerations is emphasized.

6-2

First principle study of Yb and Sr doped monolayer graphene

Andrijana Šolajić, Jelena Pešić, Radoš Gajić

*Graphene Laboratory (GLAB), Center for Solid State Physics and New Materials,
University of Belgrade, Pregrevica 118, 11080, Belgrade, Serbia*

Since the experimental discovery in 2004, graphene is attracting enormous attention due to many unusual effects and extraordinary properties. By doping, those properties can be tailored and even new effects can be obtained that pristine graphene lacks. Graphite intercalation compounds (GIC) have been studied since the 1960s, showing many new properties that are not present in pristine graphite, but the interest for them has significantly raised with the discovery of the superconductivity in some of those structures. By intercalating with the alkali or alkaline earth metal atoms, the superconductivity can be achieved. In the last few years, as the interest for 2D materials has raised, the question of the superconductivity in the atomically thin materials has appeared again. In a similar manner to GICs, the structures based on alkali/alkaline earth metal adatoms doped graphene have been investigated. Superconductivity in graphene was first experimentally verified in the Li-doped graphene. Therefore, the Li-doped graphene has inspired many to search similar structures, such as the Ca or K doped graphene. Motivated by superconductivity in the bulk SrC_6 and YbC_6 compounds, we studied electronic and vibrational properties of Sr and Yb doped monolayer graphene, using the density functional theory. We are first to report the results for those structures. The calculations were performed using Quantum Espresso software package, based on the plane waves and pseudopotentials.